申报	系列：教师系列教学科研并重型
	专业：控制理论与控制工程
	职称：副教授

业绩成果材料

（申报人的业绩成果材料包括论文、科研项目、获奖以及其他成果等）

单　位（二级单位） 工程学院

姓　名 施琳琳

材料核对人:　　单位盖章:

核对时间:

华南农业大学制

目　录

一、教学研究业绩

1.教学研究项目

1.1 关于2024年度校级教学改革项目青年项目的立项通知及有关佐证材料.....1

1.2 关于2025年度课程思政示范项目课程思政典型案例项目的立项通知及有关佐证材料.....4

2.教改论文:“理论前沿知识—实践应用能力”融合下混合式教学模式探索—以智能控制课程为例检索证明与论文..... 7

3.教学比赛证书

3.1 2024年度华南农业大学十佳教师.....12

3.2 华南农业大学2023-2024学年青年教师教学优秀奖.....13

二、科研项目

1.主持:

1.1 关于国家自然科学基金青年科学基金项目（C类）的项目计划书佐证材料.....14

1.2 关于广东省自然科学基金面上项目任务书佐证材料.....22

1.3 关于广州市科技计划项目任务书佐证材料.....33

1.4 关于农业装备技术全国重点实验室开放课题项目任务书佐证材料.....43

2.主参:

2.1 关于国家重点研发计划子课题主要参与人项目任务书佐证材料..... 46

2.2 关于省重点研发计划项目课题主要参与人项目任务书佐证材料..... 70

三、论文、著作等

1.检索证明.....89

2.以第一作者发表本专业论文情况

2.1.C 类: 车载式无人机簇状水果采摘系统设计与试验.....92

3.以通讯作者发表本专业论文情况

3.1.A 类: Simultaneous Task Execution and Formation Re-configuration in Multi-Robot Systems 100

3.2. A 类: YOLOv8s-Longan: a lightweight detection method for the longan fruit-picking UAV.....112

3.3. A 类: HPS-RRT*: An Improved Path Planning Algorithm for a Nonholonomic Orchard Robot in Unstructured Environments.....132

3.4. 中科院二区: An autonomous obstacle avoidance and path planning method for fruit-picking UAV in orchard environments.....158

四、科研成果

1.知识产权-发明专利授权证书

1.1.一种水果采摘无人机以及作业方法.....172

1.2.一种基于采摘无人机的减振平衡装置.....173

五、其他业绩

1.指导大学生创新训练计划

1.1. 2025 年大学生创新训练计划国家级立项佐证材料....174

2.指导学生学科竞赛

2.1.第一指导教师 T2 类: 2025 年第七届全球校园智能算法精英赛全国总决赛优秀奖.....175

2.2. 第一指导教师 A 类： 2025 首届全国人工智能应用创新大赛一等奖.....176
2.3. 第一指导教师 B 类：广东省第二十七届中国机器人及人工智能大赛三等奖.....177
2.4. 第一指导教师 B 类：2025 年第七届全球校园智能算法精英赛省级选拔赛二等奖.....178
2.5. 第二指导教师 T2 类：2025 年睿抗机器人开发者大赛（RAICOM）全国总决赛一等奖.....179

华南农业大学文件

华南农教〔2024〕52号

关于公布华南农业大学2024年度校级本科教学质量与教学改革工程项目立项名单的通知

各学院、部处、各单位:

根据《关于开展2024年度校级本科教学质量与教学改革工程项目申报工作的通知》精神,经项目负责人申报、所在单位推荐和学校组织专家评审、公示等程序,决定立项“基于大湾区新能源汽车人才需求的智能网联技术课程改革”等121个项目为2024年度校级本科教学改革项目;立项“涉外法治人才培养实验班”等36个项目为2024年度校级本科质量工程项目;根据学校年度人才培养工作重点及本年度申报项目质量,立项“‘长基计划’下新文科历史学课程体系的改革与实践”等11个项目为2024年度“长基计划”教学质量和教学改革工程专项项目(经

费由“长基计划”专业专项资金资助）。具体名单见附件。

请各项目负责人按照项目建设任务及要求，及时开展各项工作，加快推进学校人才培养改革，并力争取得高水平的教学成果。各单位要切实履行项目建设主体责任，加强对项目建设的督促、指导，以确保项目能如期高质量完成建设任务。

特此通知。

附件：1. 华南农业大学2024年度校级本科教学改革立项名单

2. 华南农业大学2024年度校级本科质量工程立项名单

3. 华南农业大学2024年度校级“长基计划”教学质量和教学改革工程专项立项名单

华南农业大学

2024年8月15日

（联系人：孙齐胜；电话：85288020）

公开方式：主动公开

华南农业大学党政办公室　　2024年8月20日印发

序号	项目编号	项目类别	单位	项目名称	负责人	项目组成员
60	JG2024060	一般项目	农学院	“知农爱农”核心素养导向的《主要农作物识别》课程设计与实践	程雄	朱海涛、段美洋、王树丽
61	JG2024061	一般项目	林学与风景园林学院	《森林经理学》课程体系教学改革研究与实践	林娜	陈世清、李玉玲、王本洋
62	JG2024062	一般项目	农学院	教育数字化背景下AI赋能新农科专业教学模式探索与实践——以《试验统计学实验》课程为例	布素红	刘桂富、冯发强、宋瑞凤、陈志雄、
63	JG2024063	一般项目	园艺学院	《茶叶生物化学》课程教学评价改革的研究与实践	张灵枝	张凌云、孙彬妹、孟慧
64	JG2024064	一般项目	艺术学院	新媒体类课程融入思政元素的探索与实践	梁松清	胡辉、胡年春、赵娜、王新锋
65	JG2024065	一般项目	图书馆	新时代高校图书馆阅读推广服务育人机制研究	刘丽葵	刘月秀、郑雯
66	JG2024066	一般项目	体育教学研究部	大学体育课程思政“微实践”体验式课例实践研究 ——以跆拳道为例	黄海峰	朱红梅，赵燕，李嘉鹏，赵东升
67	JG2024067	一般项目	基础实验与实践训练中心	AI交互化学实验智能平台建设研究	葛春玉	林碧敏、刘小波、龚正想、张芸
68	JG2024068	一般项目	经济管理学院	新文科背景下会计专业改造与提升的研究与实践	于健南	周小春、易智敏、张京心
69	JG2024069	青年项目	工程学院	基于理论前沿与实践应用相融合的混合式案例教学模式探索与实践——以《智能控制》课程为例	施琳琳	李君、马瑞峻、李继宇、邢航
70	JG2024070	青年项目	马克思主义学院	“习近平用典”融入高校思政课教学的路径探究——以《习近平新时代中国特色社会主义思想概论》课为例	韩谦	何艳玲、陈洁、李俊宏、梁辉、李萌萌
71	JG2024071	青年项目	数学与信息学院、软件学院	农业院校"计算机网络"课程教学创新与实践探索	邱少健	周敏、祝胜林、李舜鹏
72	JG2024072	青年项目	人文与法学学院	“双一流”背景下农林院校“农文化+文学”教育模式新探索	张吕坤	王瑛、孙宗美、李飞
73	JG2024073	青年项目	经济管理学院	数字化时代背景下《人力资源管理》教学内容与教学模式改革	徐光毅	杨学儒、郭萍、冯江洪
74	JG2024074	青年项目	马克思主义学院	田野调查在思政育人中的创新与运用	张慧慧	王敏、李若衡、杨琳
75	JG2024075	青年项目	食品学院	新工科背景下基于OBE理念的“畜产品加工学”混合式教学模式探究	郭宗林	郑华、吴绍宗
76	JG2024076	青年项目	马克思主义学院	问题链教学法在“马克思主义基本原理”课程教学的创新与运用	林逸云	林晓希、周轩宇
77	JG2024077	青年项目	水利与土木工程学院	中华水文化融入高校课程思政的探索与实践	陈文杰	周浩澜、姜俊红
78	JG2024078	青年项目	国际教育学院（广州都柏林国际生命科学与技术学院）	农业院校基于产出导向法的英语口语课程思政教学实践研究	邱倩	陈喜华
79	JG2024079	青年项目	兽医学院	“兽医寄生虫学实验”课程思政改革研究	许瑞	冯耀宇、夏宁波

华南农业大学文件

华南农教〔2025〕48号

关于公布2025年度华南农业大学课程思政示范项目立项名单的通知

各学院、部处、各单位:

结合学校新时代立德树人机制综合改革试点高校工作安排，依据《关于开展2025年度校级课程思政示范建设项目申报工作的通知》要求，学校组织开展了2025年度课程思政示范项目评选工作。

经项目负责人申请、所在单位推荐、学校组织专家评审及校内公示等程序，决定立项建设华南农业大学2025年度课程思政示范项目61项，其中包括试点学院2个、示范团队2个、示范课程8门、示范课堂14个、典型案例35个（名单详见附件）。

本次立项的课程思政示范项目建设期至2027年9月。在建设期内，原则上不允许更换负责人或变更项目团队成员。各项目

负责人须严格依据申报通知要求，落实立德树人根本任务，强化改革创新和智能化技术应用，确保高质量完成各项建设目标与任务。

特此通知。

附件：华南农业大学2025年度课程思政示范项目立项名单

华南农业大学

2025年9月29日

（联系人：孙航；联系电话：85280052）

16	课程思政示范课堂	《高等数学 AI（理工类）》第三章第 3 节（洛必达法则）	曾庆茂	马立华	数学与信息学院、软件学院
17	课程思政示范课堂	产品优化设计课程思政示范课堂	徐宁	熊巍、郭涵	工程学院
18	课程思政示范课堂	台湾问题与国家安全	张春苑	欧阳娟、伍鹏、钟晓雄、王向方	马克思主义学院
19	课程思政示范课堂	中国茶产业概况	刘少群	曹潘荣、张凌云	园艺学院
20	课程思政示范课堂	《土力学》第六章第一节地基沉降计算	姜俊红	黄金林、余长洪、胡威	水利与土木工程学院
21	课程思政示范课堂	《食品机械与设备》无菌包装机（第四章第一节）	司徒文贝	罗树灿、宋贤良	食品学院
22	课程思政示范课堂	大学英语 II Unit 6 War and Peace	王世龙	邵爱琴、张金萍	外国语学院
23	课程思政示范课堂	游泳提高班	李梅	张俊龙、郑壮荣、田甜	体育教学研究部
24	课程思政示范课堂	《食品包装安全》第四章第 4 节（食品包装货架期）	曹黎明	范小平、岳淑丽	食品学院
25	课程思政示范课堂	植物病原线虫	徐春玲	饶雪琴	植物保护学院
26	课程思政示范课堂	与乡村建设实践相结合的《建筑设计》课程思政	许媛媛	周彝馨、陈方慧	水利与土木工程学院
27	课程思政典型案例	计算平面机构自由度的注意事项	程碧懿	王红军	工程学院
28	课程思政典型案例	《智能控制》第四章第一节——神经网络概述	施琳琳	邢航	工程学院
29	课程思政典型案例	《财务管理》第一章第二节——财务管理目标思政案例	周小春	龙思颖，喻子秦	经济管理学院
30	课程思政典型案例	金相试样的制备与显微观察	胡航	曹巧英	材料与能源学院
31	课程思政典型案例	糖酵解中间产物的鉴定	许燕珍	李亚娟	基础实验与实践训练中心
32	课程思政典型案例	德语 III-Deutsche und Ausländer 跨文化交际中的刻板印象	杜文婷	苏君	外国语学院
33	课程思政典型案例	大学物理实验-液体表面张力系数的测定	徐军	无	基础实验与实践训练中心
34	课程思政典型案例	经济学-第一章第五节弹性和收入	胡焕玲	刘伟章、陈炜颖	数学与信息学院、软件学院
35	课程思政典型案例	手球	麦粤徽	刘建涛	体育教学研究部
36	课程思政典型案例	无机及分析化学“课程思政”教学案例	刘伟鹏	刘伟鹏	材料与能源学院

SCAULIB202625968

检索证明

根据委托人提供的论文材料，委托人华南农业大学工程学院 施琳琳(学科类型:自然科学) 1 篇论文收录情况如下表。

序号	论文名称	发表刊物及发表的年月卷期/页码等	作者排名	论文等级	作者文中单位	收录情况	影响因子	中科院大类分区
1	“理论前沿知识—实践应用能力”融合下混合式教学模式探索——以智能控制课程为例	中国现代教育装备 出版年：2025 卷期：11 页码：82-84+92 文献号： 文献类型：	第一作者	普刊类	华南农业大学工程学院	CNKI	无	无

说明：论文等级和中科院大类分区按《华南农业大学学术论文评价方案（试行）》划分。

报告免责声明:如未盖章,报告无效

检索员：田成

华南农业大学图书馆

2026-03-12

2025年6月

中国现代教育装备

CHINA MODERN EDUCATIONAL EQUIPMENT

中华人民共和国教育部主管　　中国高等教育学会主办
国内刊号：CN11-4994/T　　国际刊号：ISSN 1672-1438

北京林业大学超薄切片制样技术示范培训

知识图谱与大模型赋能教育教学典型应用
学科交融视域下大设计学科实践平台的构建研究
“双一流”背景下高校实验室安全文化建设创新路径探析
高校专业教学改革项目竞争性磋商采购风险与防范策略
“放管服”背景下高校采购管理研究

2025 · 6
（高教版）
ISSN 1672-1438

中国现代教育装备

主　管：中华人民共和国教育部
主　办：中国高等教育学会

中国现代教育装备
CHINA MODERN EDUCATIONAL EQUIPMENT

半月刊·高教版
2025年6月 第11期（总第459期）

编辑出版：《中国现代教育装备》杂志社有限责任公司
国内刊号：CN11-4994/T
国际刊号：ISSN 1672-1438
邮发代号：82-651（国内）M1802（国际）
国内发行：北京市报刊发行局
发行范围：国内外公开发行

地　址：北京市海淀区学院路35号世宁大厦一层108室
邮　编：100191
电　话：010-82098610
网　址：www.zgxdjyzb.com
投稿信箱：cn11_4994@263.net
印　刷：中国文联印刷厂

开户名称：《中国现代教育装备》杂志社有限责任公司
开户银行：北京银行金融街支行
账　号：01090848000120109024074

出刊日期：2025年6月20日
每册定价：24.00元

规範　嚴謹　特質　出新

目　录

撷萃有期
1 知识图谱与大模型赋能教育教学典型应用 …… 郝　佳　牛红伟　杜　钧　等
6 学科交融视域下大设计学科实践平台的构建研究 …… 卢　静　陈倩芸
9 “双一流”背景下高校实验室安全文化建设创新路径探析 …… 马美倩　刘　钊

高校采购招标工作
12 高校专业教学改革项目竞争性磋商采购风险与防范策略 …… 王　峰　郑淮毅　单心如　等
15 “放管服”背景下高校采购管理研究 …… 辛　娟
18 基于住宅专项维修资金采购的案例分析 …… 胡玉环　陈尚聪

技术前沿与教学应用
21 基于数字孪生的皮带机分拣教学系统设计与开发 …… 张文超　王明伟　张　尧
25 基于光声显微成像装备的本科实验教学设计 …… 彭东青

教育信息化与智能化
28 信息管理与信息系统专业结构优化研究 …… 刘　升　游晓明
31 基于人工智能的新能源并网发电技术课程创新与教学转型 …… 李从善　王延峰　和　萍　等
34 基于“互联网+”的工程实训教学体系改革探索与实践 …… 刘可宁　姜　旭　孙建华
37 教育数字化转型背景下职业本科院校数据治理研究 …… 杨盈图　马朝霞　郭治豪　等

实验实训实践平台建设
40 基于虚拟技术的电路实验平台设计 …… 崔双喜　马百强
44 超薄切片制样技术示范培训体系的构建 …… 尹丽丽　刘颖儒　耿亚茹
47 “双碳”目标下高校实验室低碳转型管理模式研究 …… 张　芳　麻军亮
49 学生助理参与应用型高校实验室管理的“2S-2I”运行机制研究 …… 任作琳　郭　薇
52 高职院校生化类实训室“6S”管理的应用探究 …… 方志惠　何曼文　陈云霞　等

“四新”建设研究与实践
55 新工科背景下基于“双平台+双引擎”的材料类创新型人才培养模式探索 …… 赵红亮　翁康荣　张书亚　等
59 新工科背景下电路课程和工程教育的融合创新 …… 田　葳　徐丹旸　闫青源　等
62 新工科视域下3D打印课程教学改革与探索 …… 余竹玛　贺　军　龚育超
65 面向新工科的应用型本科机械设计基础课程案例教学实践 …… 任晓莉　刘吉轩　王国平　等
68 新农科视域下无人机林业遥感实验教学改革初探 …… 喻素芳　苏　凯

工程教育专业认证
72 基于OBE理念的电路原理课堂教学设计与实践 …… 朱　广　史艳琼　张润梅　等
75 工程教育专业认证背景下材料力学性能课程教学改革 …… 满田囡　张洪亮　刘　腾　等

期刊基本参数：CN11-4994/T*1998*b*A4*154*zh*P*￥24.00*4000*48*2025-6

收录本刊内容的数据信息库：中国期刊全文数据库、中文科技期刊数据库、中国核心期刊遴选数据库。

作者如不同意文章被上列数据信息库收录，请在来稿时向本刊声明。

本刊所付稿酬已包含上列数据信息库著作权使用费。

本刊载文，作者文责自负。

关注我们：

扫描二维码或搜索
中国现代教育装备

封面图片由北京林业大学尹丽丽老师提供

目　录

混合式教学模式研究

78 桥梁抗震与抗风课程融合 OBE 和 PBL 的混合式教学改革方法探究 ..... 巫志文　孟勇军　彭林欣

82 “理论前沿知识—实践应用能力”融合下混合式教学模式探索 ..... 施琳琳　李　君　马瑞峻　等

85 基于数字教育的“四融合”式教学探究 ..... 其木格

课程建设与教学研究

88 科教融合理念下的电子信息类专业课程改革实践 ..... 刘晨曦　查　淞　张继宏

93 阈概念视域下的新工科课程改革探究 ..... 郭　强　王雨琦　禹　昱

96 传热学课程混合式教学模式探索 ..... 张井志　周乃香　袁学良　等

99 金属增材制造专创融合实践体系构建与应用 ..... 刘婷婷　张百成　章　林　等

102 海洋保护课程“一体两翼”教育教学科研体系建设 ..... 张　伟　熊　竹　张高生　等

105 “三位一体”教学目标下的流体力学实验教学探索 ..... 陈春美　李国建　张文婷

108 基于数字化立体课堂的电工与电子技术课程建设策略探究 ..... 陈　月　梁春英　韩　静　等

111 电子信息类专业软件技术基础课程精准教学模式探索 ..... 宋颖超　张丽丽　白　玉　等

115 医学科研素养培养的微课程模式研究 ..... 包芳军　王清雅　刘美辰

119 基于三维信息化工具的消防制图教学改革 ..... 汤　旻　周延豪　王丽娟

122 智慧教学背景下步兵武器原理课程教学模式探索 ..... 宋　坤　安纯尧　张军挪　等

创新创业教育实践研究

125 “双碳”目标下能源动力专业创新教育开展情况研究 ..... 邵志鹏　刘忠宝　孙　晗

128 “四链”融合下机械专业创新人才培养探析 ..... 杨　潇　杜彦斌

131 进阶式创新创业教育：模式构建、实践探索与未来展望 ..... 袁　侃

134 新质生产力视阈下高校创新创业教育路径探索 ..... 刘颂迪

高职教育研究与实践

136 BOPPPS-OMO 教学模式在职业本科仪器分析教学中的实践 ..... 丁　丽　王淑君　杜玲玲　等

140 1+X 证书制度下高职数控实训室的创新与挑战 ..... 范登胜　钟国坚

数字化图书馆建设

143 “三融”视域下高职院校图书馆建设与服务创新研究 ..... 陈嘉慧

中国高等教育学会课题专栏

146 基于创新能力培养的海洋资源开发与利用综合实验研究 ..... 樊　燕　侯　虎

149 线上线下混合式教学模式在外科基本技能教学中的应用研究 ..... 陈晓云　李　翔　刘　攀　等

152 “岗课赛证”融合的高职院校机械设计与制造专业人才培养模式探索与实践 ..... 任清海　孙祖东

“理论前沿知识—实践应用能力”融合下混合式教学模式探索
——以智能控制课程为例

施琳琳　李　君*　马瑞峻　李继宇　邢　航
华南农业大学工程学院 广东广州 510640

摘　要：面对人工智能技术快速发展的现状，为满足机器人工程专业创新能力培养的需求，围绕“理论前沿知识—实践应用能力”相融合的培养理念，从理论教学框架、实践案例库、课程考核方式等方面开展探索。从课程内容架构体系出发，基于理论前沿知识重构层次化理论教学框架，结合农业高校特色协同构建多元项目案例，探索“导入—分析—解决—拓展”的混合式教学模式，形成以学生为中心的考核机制，以提升学生解决实际问题的能力，构建以创新能力培养为导向的机器人工程专业人才培养模式。

关键词：智能控制；混合式教学；教学模式；理论前沿；实践应用
中图分类号：G642.0　**文献标识码**：A　**文章编号**：1672-1438(2025)11-0082-03
DOI:10.13492/j.cnki.cmee.2025.11.025

机器人工程专业是顺应国家建设需求和国际发展趋势而设立的新工科专业，是2016年教育部批准的本科新专业。华南农业大学机器人工程专业于2021年开始招生，以系统科学、控制科学、信息科学、机器人学等为理论基础，以各类先进技术为主要技术手段，实现机器人的环境感知、运动规划、智能决策、驱动控制，是典型的实践综合性专业。随着我国机器人产业的迅速发展，产业规模和市场潜力持续扩大，对实践应用型人才的需求也随之增加[1]。而机器人工程作为新工科专业还处于起步阶段，以创新能力为导向的专业课程和人才培养模式仍在不断探索中[2]。

智能控制作为机器人实现自动化、信息化和智能化的关键桥梁，在机器人工程专业的人才培养过程中扮演着至关重要的角色。随着被控对象的非线性化和复杂化，以及控制任务的多目标要求，智能控制作为一种新兴的控制理论，代表了自动控制理论发展的高级阶段。该课程结合了人工智能和控制理论，具有理论性和实践性强的特点，涵盖了广泛的专业知识，包含控制、计算机、通信等多个领域，呈现明显的学科交叉特征[3]。该课程涉及多种智能控制算法，如专家系统、模糊理论、神经网络技术在控制中的应用。在人工智能快速发展的背景下，如何针对智能控制课程特点，探索以学生为中心、以创新能力培养为导向的机器人工程专业人才培养模式有着重要的意义。

1　对智能控制课程中存在问题的剖析

随着人工智能的兴起，各高校智能控制课程的开设呈现扩增的趋势，其教学方式以理论讲授为主，以软件编程为辅[4]。该教学方式可满足基本的课程教学要求，但对以机器人工程专业为代表的新工科专业而言，无法满足实践型和创新型人才培养的要求。

1.1　课程教材重理论现象突出，教学内容未能与时俱进

智能控制课程涵盖了模糊理论、神经网络、专家系统以及强化学习等多个学科的内容，而且其内容相互独立，但在应用中相互交叉[5]。学生学习该课程时普遍面临知识点散乱、概念晦涩难懂、公式复杂、内容枯燥等困扰，以教师为主的“精讲+略讲”的授课方式，削弱了学生学习的内驱力。

此外，该课程结合了人工智能和控制理论。随着这两个学科的迅速发展，出现了许多新兴的智能算法，如深度学习、强化学习等。虽然本科生对这些算法有所了解，但通常仅停留在浅层认知层面，缺乏对

作者简介：施琳琳，博士，讲师；李君(通讯作者)，博士，教授；马瑞峻，博士，教授；李继宇，博士，教授；邢航，博士，讲师。

基金项目：2024年华南农业大学教育教学研究和改革项目“基于理论前沿与实践应用相融合的混合式案例教学模式探索与实践——以《智能控制》课程为例”(编号：JG2024069)；2023年广东省研究生教育创新计划项目“农业机器人教学案例库建设”(编号：2023ANLK_016)。

荣誉证书

HONORARY CREDENTIAL

施琳琳 老师：

被评为2024年度华南农业大学十佳教师。

特发此证，以资鼓励！

华南农业大学

2025年7月1日

荣誉证书

HONORARY CREDENTIAL

施琳琳 老 师：

在华南农业大学 2023-2024 学年青年教师教学优秀奖评选中荣获

三等奖

特发此证，以资证明！

华南农业大学

2025 年 1 月 6 日

项目批准号	62303188
申请代码	F0311
归口管理部门	
依托单位代码	51064208A0499-0932

623031881001209

国家自然科学基金

资助项目计划书

（包干制项目）

资助类别：青年科学基金项目

亚类说明：

附注说明：

项目名称：动态未知海流环境下多AUV的分布式目标围捕控制研究

资助经费：30万元　　执行年限：2024.01-2026.12

负 责 人：施琳琳

通讯地址：广东省广州市天河区五山路483号华南农业大学工程学院

邮政编码：510642　　电　　话：

电子邮件：

依托单位：华南农业大学

联 系 人：唐家林　　电　　话：

填表日期：2023年08月28日

国家自然科学基金委员会制

Version：1.001.209

国家自然科学基金资助项目计划书填报说明

（包干制项目）

一、项目负责人收到《国家自然科学基金资助项目批准通知》（以下简称《批准通知》）后，请认真阅读本填报说明，参照国家自然科学基金相关项目管理办法和新修订的《国家自然科学基金资助项目资金管理办法》（以下简称《资金管理办法》，请查阅国家自然科学基金委员会官方网站首页“政策法规”栏目），按《批准通知》的要求认真填写和提交《国家自然科学基金资助项目计划书》（以下简称《计划书》）。

二、填写《计划书》时要科学严谨、实事求是、表述清晰、准确。《计划书》经国家自然科学基金委员会相关项目管理部门审核批准后，将作为项目研究计划执行、检查和验收的依据。

三、《计划书》各部分填写要求如下：

（一）简表：由系统自动生成。

（二）摘要及关键词：各类获资助项目都应当填写中、英文摘要及关键词。

（三）正文：

1. 青年科学基金项目：如果《批准通知》所附“项目评审意见及修改意见表”中“修改意见”栏目没有修改要求的，只需选择“研究内容和研究目标按照申请书执行”即可；如果《批准通知》中上述栏目明确要求调整研究期限或研究内容等的，须选择“根据研究方案修改意见更改”并填报相关修改内容。

2. 国家杰出青年科学基金项目和优秀青年科学基金项目按下列提纲撰写：

（1）研究方向；

（2）结合国内外研究现状，说明研究工作的学术思想和科学意义（限两个页面）；

（3）研究内容、研究方案及预期目标（限两个页面）；

（4）年度研究计划；

3. 科技管理专项项目按下列提纲撰写：

（1）科技战略研究领域方向；

（2）结合该领域国内外研究现状及发展趋势，分析科学基金资助战略与政策（限两个页面）；

（3）研究内容、研究方案及预期目标（限两个页面）；

（4）年度研究与实践计划。

四、资助经费相关要求：

1. 资助经费批准时不再区分直接费用和间接费用。

2. 项目负责人在提交计划书时需签署承诺书，承诺尊重科研规律，弘扬科学家精神，遵守科研伦理道德和作风学风诚信要求，认真开展科学研究工作；承诺项目经费全部用于与本项目研究工作相关的支出，不得用于与本项目研究无关的支出。

3. 项目负责人提交计划书时，无需编制项目预算。项目资金由项目负责人自主决

定使用，按照《资金管理办法》第九条规定的开支范围列支。有关管理费用的补助支出，由依托单位根据实际管理需要，在充分征求项目负责人意见基础上合理确定。绩效支出由项目负责人根据实际科研需要和相关薪酬标准自主确定，依托单位按照工资制度进行管理。其余用途经费无额度限制，由项目负责人根据实际需要自主决定使用。

4. 项目结题时，项目负责人根据实际使用情况编制项目经费决算，经依托单位财务、科研管理部门审核后，报自然科学基金委。依托单位应当在单位内部公开非涉密项目立项、主要研究人员、资金使用（重点是间接费用、外拨资金、结余资金使用等）、决算、大型仪器设备购置以及项目研究成果等情况，接受内部监督。

5. 自然科学基金委结合项目管理，对经费使用情况和依托单位管理情况定期开展抽查。

简表

项目负责人信息	姓　　名	施琳琳	性 别	女	出生年月		民 族	汉族
	学　　位	博士			职称	讲师		
	是否在站博士后	否			电子邮件			
	电　　话				个人网页			
	工 作 单 位	华南农业大学						
	所 在 院 系 所	工程学院						
依托单位信息	名　　称	华南农业大学					代码	51064208A0499
	联 系 人	唐家林			电子邮件			
	电　　话				网站地址			
合作单位信息	单 位 名 称							
项目基本信息	项 目 名 称	动态未知海流环境下多AUV的分布式目标围捕控制研究						
	资 助 类 别	青年科学基金项目			亚 类 说 明			
	附 注 说 明							
	申 请 代 码	F0311:新兴领域的自动化理论与技术			F0301:控制理论与技术			
	基 地 类 别							
	执 行 年 限	2024.01-2026.12						
	资 助 经 费	30万元						

项目摘要

中文摘要：

自主水下航行器(Autonomous Underwater Vehicle, AUV)作为新型智能化海洋作业装备已成为实现水下目标监测的必备工具。多AUV协同作业的时间并行性和空间分布性可有效应对水下目标的突发性和多样性。本项目围绕动态未知海流环境开展水下移动目标的分布式围捕控制研究：构建运动积分误差约束，揭示动态海洋流场的三维时空变化与AUV未知航行路径的映射关系，提出分布式网络下的协同估计算法以实现高精度的海流估计；针对部分航行器目标信息缺失的情况，提出基于局部信息的分布式控制并设计辅助变量的自适应更新方法，以实现动态海流环境下移动目标的围捕控制；研究动态多目标实时变化的运动形态，基于弱时限下任务分配方法提出快速切换控制策略，以实现集群运动和四散逃跑的多目标协同围捕。本项目力图突破多AUV在动态未知海流环境中协同围捕的技术瓶颈，为其在现代海洋防御系统的发展提供理论基础和关键技术支撑。

Abstract:

Autonomous Underwater Vehicle (AUV), as a new intelligent oceanic equipment, has been playing an increasingly important role in monitoring underwater moving targets. The temporal parallelism and spatial distribution by multi-AUV cooperation can effectively deal with the variability and suddenness of underwater targets. This project aims at the moving target enclosing in the dynamic unknown ocean environment. The mapping relationship between the three-dimensional dynamic flow fields and unknown navigation path is established as the motion-integration error constraints, which is introduced to achieve the high-precision flow field estimation under a distributed network; For the problem of a moving target enclosing when some vehicles cannot detect the target, a target enclosing control method based on local information is proposed and the designed auxiliary variables are introduced into the proposed controller to eliminate the influence of the flow field on trajectories; Considering the real-time changing movements of multiple targets, a fast switching control strategy is proposed based on the task assignment method with a weak time limit, which will achieve the dynamic targets enclosing by multi-AUV cooperation in a clustered or dispersed movement. This project tries to break the technical bottleneck of the cooperative control for multi-AUV in a dynamic and unknown ocean environment, and provide a theoretical basis and key technical support for its development in modern marine defense systems.

关键词(用分号分开)： 系统控制；分布式控制；目标围捕；协同估计；多自主水下航行器

Keywords(用分号分开)： system control; distributed control; target enclosing; cooperative estimation; multi-AUV system

报告正文

研究内容和研究目标按照申请书执行。

国家自然科学基金项目负责人、依托单位承诺书

国家自然科学基金项目负责人承诺书

本人郑重承诺：我接受国家自然科学基金的资助，严格遵守中共中央办公厅、国务院办公厅《关于进一步加强科研诚信建设的若干意见》《关于进一步弘扬科学家精神加强作风和学风建设的意见》《关于加强科技伦理治理的意见》等规定，及国家自然科学基金委员会关于资助项目管理、项目资金管理等各项规章，在《计划书》填写及项目执行过程中：

（一）按照《批准通知》《国家自然科学基金资助项目计划书填报说明》的要求填写《计划书》，未自行降低、更改目标任务或约定要求，或缩减研究（研制）内容；

（二）树立“红线”意识，严格履行科研合同义务，按照《计划书》负责实施本项目（批准号：62303188），切实保证研究工作时间，按时报送有关材料，及时报告重大情况变动，不违规将科研任务转包、分包他人，不以项目实施周期外或不相关成果充抵交差；

（三）遵守科研诚信、科技伦理规范和学术道德，认真开展研究工作，对资助项目发表的论著和取得的研究成果按规定进行标注，不在非本项目资助的成果或其他无关成果上标注本项目批准号，反对无实质学术贡献者“挂名”，不在成果署名、知识产权归属等方面侵占他人合法权益，并如实报告本人及项目组成员发生的违背科研诚信要求的任何行为；

（四）尊重科研规律，弘扬科学家精神，严谨求实，追求卓越，反对浮夸浮躁、投机取巧，不人为夸大学术或技术价值，不传播未经科学验证的现象和观点；

（五）将项目资金全部用于与本项目研究工作相关的支出，并结合科研活动需要，科学合理安排项目资金支出进度；

（六）做好项目组成员的教育和管理，确保遵守以上相关要求。

如违背上述承诺，本人愿接受国家自然科学基金委员会和相关部门做出的各项处理决定。

项目负责人（签字）施琳琳

2023年 9月 6日

国家自然科学基金项目依托单位承诺书

我单位同意承担上述国家自然科学基金项目，将保证项目负责人及其研究队伍的稳定和研究项目实施所需的条件，严格遵守国家自然科学基金委员会有关资助项目管理、项目资金管理、科研诚信管理和科技伦理管理等各项规定，并督促实施。

依托单位（公章）

2023年 9月 18日

国家自然科学基金资助项目签批审核表

本栏目由自然科学基金委填写

科学处审查意见：

同意按照计划执行

负责人（签章）：

年 月 日

2023年 11月 13日

科学部审查意见：

同意

负责人（签章）：

年 月 日

2023年 11月 13日

受理编号：c24140500000806

项目编号：2024A1515010135

文件编号：粤基金字〔2024〕7号

广东省基础与应用基础研究基金项目

任务书

项目名称：面向海洋监测的多AUV协同估计与控制研究

项目类别：广东省自然科学基金-面上项目

项目起止时间：2024-01-01 至 2026-12-31

管理单位（甲方）：广东省基础与应用基础研究基金委员会

依托单位（乙方）：华南农业大学

通讯地址：广东省广州市天河区五山路483号

邮政编码：510642 单位电话：

项目负责人：施琳琳 联系电话：

（广东科技微信公众号） （查看任务书信息） （受理纸质材料二维码）

广东省基础与应用基础研究
基金委员会
二〇二〇年制

填写说明

一、项目任务书内容原则上要求与申报书相关内容保持一致，不得无故修改。

二、项目承担单位通过广东省科技业务管理阳光政务平台下载项目任务书，按要求完成签名盖章后扫描上传到广东省科技业务管理阳光政务平台。

三、签名盖章说明。请分别在单位工作分工及经费分配情况页、人员信息页、签约各方页等地方按要求签字或盖章，签章不合规或错漏将不予受理。其中，人员信息页要求所有参与人员本人亲笔签名，代签或印章无效，漏签将不予受理。

四、本任务书自签字并加盖公章之日起生效，各方均应负本任务书的法律责任，不应受机构、人事变动影响。

五、根据《广东省科学技术厅广东省财政厅关于深入推进省基础与应用基础研究基金项目经费使用“负面清单+包干制”改革试点工作的通知》（粤科规范字〔2022〕2号），2022年度及以后立项资助的全部省基金项目(包括省自然科学基金、省市联合基金、省企联合基金项目等)均适用“负面清单+包干制”，项目提交申请书和任务书时无需编制费用明细科目预算。

一、主要研究内容和要达到的目标

一、主要研究内容

自主水下航行器作为一种新型智能化海洋作业装备已成为实现高效便捷海洋监测的必备工具。面对日益多样化的海洋监测作业需求，实现对海洋环境精确、实时、大范围的立体监测，本项目利用多AUV系统展开协同估计与控制研究。具体研究内容如下：

（1）考虑到执行海洋监测任务时，初始工作空间模型的非完整性和动态不确定性，研究如何通过高效局部信息共享机制实现多AUV系统的在线任务重规划。利用分布式一致性的策略，各AUV基于局部信息共享实现对协同任务规划的在线调整；同时，根据运动控制反馈的信息设计事件触发机制，降低多AUV系统的通信要求，实现了顶层任务规划和底层运动控制信息的融合。

（2）考虑到海洋流场的高复杂度和动态变化特性，以及AUV绝对位置信息未知，研究多AUV系统是如何通过相互配合实现高精度的三维时空流场估计。通过建立三维时空分解的流场模型，在不依赖局部流速测量的前提下，通过非线性误差约束关系提出行迭代形式下的协同流场估计算法，突破流场估计精度低的技术瓶颈；设计低通信成本的树型网络，实现分布式流场估计提高了估计算法求解速度。

（3）考虑到由于传感器灵敏度，或是水下障碍物遮挡等原因导致目标信息丢失的情况，研究如何利用局部信息估计移动目标的轨迹信息实现多AUV的协同控制。进一步，利用AUV间的协同控制以应对多目标发生形态变化，并设计并提出一组三维辅助变量的自适应更新方法以消除海流对航行器轨迹的影响，实现海流影响下的移动多目标围捕控制。

二、要达到的目的

本项目研究大范围海洋监测中的多AUV协同估计与控制问题，从多个角度拟解决海洋环境特殊性所带来的问题，构建面向海洋监测应用需求的多AUV协同估计与控制理论，提高海洋监测的估计精度，扩展立体监测范围，以及提升应对敌对目标入侵的技术能力。本项目的具体目标如下：

（1）针对动态未知的海洋环境，设计基于运动控制反馈信息的动态任务规划方法，通过局部信息共享设计一致性算法，实现多AUV在海洋监测中高效与可容错任务规划；

（2）考虑到海洋流场的高复杂度和动态变化特性，设计基于三维时空分解模型的多AUV协同流场估计算法以提高估计精度，并设计低通信成本的树型网络，实现分布式流场估计；

（3）针对水下目标的运动特性以及多样性，融合海洋环境的流场、未知障碍物等信息，提出水下目标轨迹的精准预测，实现三维空间中基于局部信息的移动目标围捕控制。

二、项目预期获得的研究成果及形式

<table>
<tr><td rowspan="3">论文及专著情况</td><td colspan="2">国家统计源刊物以上刊物发表论文（篇）</td><td colspan="2">4</td><td colspan="2">科技报告（篇）</td><td colspan="2">1</td></tr>
<tr><td colspan="2">其中被SCI/EI/ISTP收录论文数（篇）</td><td colspan="2">4</td><td colspan="2">培养人才（人）</td><td colspan="2"></td></tr>
<tr><td colspan="2">专著（册）</td><td colspan="2"></td><td colspan="2">引进人才（人）</td><td colspan="2"></td></tr>
<tr><td rowspan="3">专利情况(项)</td><td colspan="2">发明专利</td><td colspan="2">实用新型专利</td><td colspan="2">外观设计专利</td><td colspan="2">国外专利</td></tr>
<tr><td>申请</td><td>授权</td><td>申请</td><td>授权</td><td>申请</td><td>授权</td><td>申请</td><td>授权</td></tr>
<tr><td>1</td><td></td><td></td><td></td><td></td><td></td><td></td><td></td></tr>
</table>

三、项目进度和阶段目标

（一）项目起止时间： 2024-01-01 至 2026-12-31		
（二）项目实施进度及阶段主要目标：		
开始日期	结束日期	主要工作内容
2024-01-01	2024-12-31	（1）研究动态未知海洋模型下的复杂协同任务规划问题； （2）在MATLAB软件平台完成任务规划算法的仿真； （3）完成会议论文1-2篇； （4）参加学术交流活动或学术会议1-2次；
2025-01-01	2025-12-31	（1）研究基于多AUV平台的三维时空海洋流场协同估计问题； （2）搭建基于MATLAB/ROS的软件平台完成水下流场估计仿真； （3）完成期刊及会议论文1-2篇，申请发明专利1项； （4）在室内水池或湖面上构建人工试验环境；
2026-01-01	2026-12-31	（1）研究目标信息部分缺失下的水下移动目标围捕控制问题； （2）在MATLAB/GAZEBO软件平台完成围捕控制算法的仿真并在人工试验环境进行验证； （3）完成期刊及会议论文1-2篇； （4）项目总结，完成科技报告和结题报告。

四、项目总经费及省基金委经费预算

1.省基金委经费下达总额： （大写）壹拾伍万圆整；（小写 ）15万元；					
2.省基金委经费年度下达计划：					
年度	2024 年	年	年	年	年
经费(万元)	15.00				

五、人员信息

项目负责人								
姓名	证件号码	年龄	性别	职称	学历	在项目中承担的任务	所在单位	签名
施琳琳			女	讲师	博士研究生	项目负责人	华南农业大学	施琳琳

项目组主要成员								
姓名	证件号码	年龄	性别	职称	学历	在项目中承担的任务	所在单位	签名
李君			男	教授	博士研究生	多机器人协同估计	华南农业大学	李君
肖博一			男	副教授	博士研究生	协同任务规划	华南农业大学	肖博一
黄光文			男	讲师	博士研究生	目标定位算法	华南农业大学	黄光文
曹亚超			男	讲师	博士研究生	多机器人协同控制	华南农业大学	曹亚超
陈恒旭			男	未取得	硕士研究生	分布式估计算法	华南农业大学	陈恒旭
周浩波			男	未取得	本科	动态规划算法	华南农业大学	周浩波
曾晔			男	未取得	硕士研究生	目标围捕算法	华南农业大学	曾晔

六、工作分工及财政经费分配

承担/参与单位名称（盖章）	工作分工	省级财政科技资金分配（万元）
华南农业大学	全面负责项目实施和计划管理	15.00
	合计	15.00

七、任务书条款

第一条 甲方与乙方根据《中华人民共和国民法典》及国家有关法规和规定，按照《广东省科学技术厅关于广东省基础与应用基础研究基金（省自然科学基金、联合基金等）项目管理的实施细则（试行）》《省级科技计划项目任务书管理细则》《广东省省级科技计划项目验收结题工作规程（试行）》等规定，为顺利完成（2024）年面向海洋监测的多AUV协同估计与控制研究专项项目（项目编号：2024A1515010135）经协商一致，特订立本任务书，作为甲乙双方在项目实施管理过程中共同遵守的依据。

第二条 甲方的权利义务：

1.按任务书规定进行经费核拨的有关工作协调。

2.根据甲方需要，在不影响乙方工作的前提下，定期或不定期对乙方项目的实施情况和经费使用情况进行检查或抽查。

3.根据《广东省科研诚信管理办法(试行)》等规定对乙方进行科技计划信用管理。

第三条 乙方的权利义务：

1.确保落实自筹经费及有关保障条件。

2.按任务书规定，对甲方核拨的经费实行专款专用，单独列账，并随时配合甲方进行监督检查。

3.经费使用按照广东省级财政科研项目经费使用等有关规定进行管理。

4.项目依托单位应制定经费使用“负面清单+包干制”内部管理制度并报甲方备案。

5.使用财政资金采购设备、原材料等，按照《广东省实施〈中华人民共和国招标投标法〉办法》有关规定，符合招标条件的须进行招标。

6.项目任务书任务完成后，或任务书规定的任务、指标及经费投入等提前完成的，乙方可提出验收结题申请，并按甲方要求做好项目验收结题工作。

7.若项目发生需要终止结题的情况，乙方须提出终止结题申请，并按甲方要求做好项目终止结题工作。

8.在每年规定时间内向甲方如实提交上年度工作情况报告，报告内容包含上年度项目进展情况、经费决算和取得的成果等。

9.按照国家和省有关规定，提交科技报告及其他材料。

10.利用甲方的经费获得的研究成果，项目负责人和参与者应当注明获得“广东省基础与应用基础研究基金（英文：Guangdong Basic and Applied Basic Research Foundation）（项目编号）”资助或作有关说明。

11.乙方要恪守科学道德准则，遵守科研活动规范，践行科研诚信要求，不得抄袭、剽窃他人科研成果或者伪造、篡改研究数据、研究结论；不得购买、代写、代投论文，虚构同行评议专家及评议意见；不得违反论文署名规范，擅自标注或虚假标注获得科技计划（专项、基金等）等资助；不得弄虚作假，骗取科技计划（专项、基金等）项目、科研经费以及奖励、荣誉等；不得有其他违背科研诚信要求的行为。

12.确保本项目开展的研究工作符合我国科技伦理管理相关规定。

第四条 在履行本任务书的过程中，如出现广东省相关政策法规重大改变等不可抗力情况，甲方有权对所核拨经费的数量和时间进行相应调整。

第五条 在履行本任务书的过程中，当事人一方发现可能导致项目整体或部分失败的情形时，应及时通知另一方，并采取适当措施减少损失，没有及时通知并采取适当措施，致使损失扩大的，应当就扩大的损失承担责任。

第六条 本项目技术成果的归属、转让和实施技术成果所产生的经济利益的分享，除双方另有约定外，按国家和广东省有关法规执行。

第七条 根据项目具体情况，经双方另行协商订立的附加条款，作为本任务书正式内容的一部分，与本任务书具有同等效力。

第八条 本任务书一式三份，各份具有同等效力。甲、乙方及项目负责人各执一份，三方签字、盖章后即生效，有效期至项目结题后一年内。各方均应负任务书的法律责任，不应受机构、人事变动的影响。

第九条 乙方必须接受甲方聘请的本项目任务书监理单位的监督和管理。监理单位按照甲方赋予的权利对本项目任务书的履行进行审核、进度调查，对项目任务书变更、经费使用情况进行监督管理及组织项目验收。

说明：1.本任务书中，凡是当事人约定无需填写的内容，应在空白处划（/）。

2.委托代理人签订本任务书的，应出具合法、有效的委托书。

八、本任务书签约各方

管理单位（甲方）：　　广东省基础与应用基础研究基金委员会　（盖章）

法定代表人（或法人代理）：曾路　（签章）

2024 年　05 月　22 日

依托单位（乙方）：　华南农业大学　（盖章）

法定代表人（或法人代理）：　薛红卫　（签章）

联系人（项目主管）姓名：　倪慧群　（签章）

Email：

电话：

开户单位名称：　华南农业大学

开户银行名称：　广东广州工行五山支行

开户银行账号：　3602002609000310520

2024年 5月 31日

联系人（项目负责人）姓名：　施琳琳　（签名）

Email：

电话：

2024 年 5月 31日

任务书编号：2024A04J4141

广州市科技计划项目

任务书

项目名称：	基于局部信息的多水下机器人协同目标围捕控制研究
承担单位：	华南农业大学
项目负责人：	施琳琳
计划类别：	基础研究计划
专题名称：	2024年度基础与应用基础研究专题
支持方向：	青年博士“启航”项目
组织单位：	华南农业大学
起止时间：	2024-01-01 至 2025-12-31
主管处室：	基础研究处

广州市科学技术局制

二〇二四年

填写说明

1.任务书甲方为广州市科学技术局；乙方为项目承担单位；丙方为项目组织单位。

2.任务书基于项目申报书转换而成，请按照“广州科技大脑”提示在线填写核实，若存在不填写内容的栏目，请用“无”表示；任务书中的单位名称应为规范全称，并与单位公章一致。

3.乙方与合作单位的合作协议自动从项目申报书中读取，如需变化调整，须待任务书签订后，按要求及时办理重大变更。

4.乙方完成项目任务书在线填写，依次提交丙方和甲方审核确认后，按要求登录“穗好办”APP完成电子签章。不具备电子签章条件的单位，经与业务主管处室沟通对接后，可下载电子版项目任务书用A4纸双面打印装订签章；一式六份报甲方和丙方签章，其中甲方两份丙方两份，项目承担单位和项目负责人各一份。

5.涉密项目请在“广州科技大脑”下载项目任务书模板，按保密要求离线填写报送。

6.项目申报书是项目任务书填报的重要依据，未经甲方许可，乙方不得修改考核指标，调整主要研究内容。项目任务书将作为项目实施管理、验收结题和监督评估的重要依据。

7.项目任务书中的“备注”，包括重要的必须补充的内容。

8.“广州科技大脑”是项目管理过程中重要通知和文书的电子送达平台。为确保电子送达渠道畅通，乙方和项目负责人应及时更新维护“广州科技大脑”的单位和个人信息。

9.根据相关要求，项目涉及人体临床研究的，项目需经医学伦理委员会审查通过并在任务书附件栏上传相关佐证材料。

一、项目基本信息

项目基本信息	项目名称	基于局部信息的多水下机器人协同目标围捕控制研究
	申请市财政科技经费	5(万元)
	研究期限	2（年）
项目摘要	水下机器人作为新型智能化海洋作业装备已成为实现水下目标监测的必备工具。多水下机器人协同作业的时间并行性和空间分布性可有效应对水下目标的突发性和多样性。本项目针对部分目标信息缺失的情况，提出基于局部信息的分布式控制并设计辅助变量的自适应更新方法，以实现动态海流环境下移动目标的围捕控制；研究动态多目标实时变化的运动形态，基于弱时限下任务分配方法提出快速切换控制策略，以实现不同形态下多目标的协同围捕。	

二、项目单位情况

项目承担单位	单位名称	华南农业大学	统一社会信用代码	12440000455416563 4
	注册时间	1952-01-01	单位类型	高等院校
	注册地址	广东省广州市天河区五山路483号		
	办公地址	广东省广州市天河区五山路483号		
	联系人	姓名	倪慧群	
		手机号码		
		电子邮箱		
	开户银行	广东广州工行五山支行		
	开户户名	华南农业大学		
	银行账号	3602002609000310520		

三、项目负责人信息

姓名	施琳琳	证件类型	身份证
证件号码		性别	女
出生日期		民族	汉族
国籍	中国	学历	博士研究生
学位	博士	学位授予国家（或地区）	中国
职务	无	职称	中级
所学专业	控制理论与控制工程	手机号码	
办公电话		电子邮箱	

四、项目经费信息

本项目总投入：¥（5）万元，其中，市财政科技经费：¥（5）万元，自筹经费：¥（0）万元。

经费下达计划			
资金来源	小计	市财政科技经费	自筹经费
2024	5	5	0
总计	5	5	0

（单位：万元）

注：本专题纳入“包干制”，市财政科技经费按市科技计划项目经费“包干制”相关规定执行。

五、预期代表性成果

项目负责人在项目实施期内，以该项目作为资助项目获得以下5种情形之一且经费使用符合规定的，由组织单位审核后通过验收。

（一）项目实施期内，以第一作者/通讯作者发表论文1篇或以上（须标注资助项目编号）；

（二）项目实施期内，以第一完成人申请或授权专利、软件著作1项或以上；

（三）项目实施期内，获省级以上科技计划项目或人才项目支持1项或以上；

（四）项目实施期内，获省级以上科技奖励（含列入获奖团队成员名单）1项或以上；

（五）项目实施期内，获得职称晋升。

六、备注

专题补充约定条款：

甲方对未履行勤勉尽责义务的相关责任主体，自作出处理结论之日起，依照法律法规规定或任务书约定实施惩戒5年，取消相关责任主体申报市科技计划项目、申领市科技计划项目经费的资格。

预期代表性成果需在实施期内获得。

项目承担单位（乙方）及项目负责人承诺书

承诺书

本单位/本人作为广州市科技计划项目承担单位/项目负责人，将严格遵守广州市科技计划管理相关规定，严格履行自身责任，加强对项目组人员及合作单位的管理，在此郑重承诺：

（一）确保与本项目有关的全部材料真实、合法、有效，未侵犯其他方知识产权等权利，不存在多头申报、重复申报行为；

（二）严格遵守《广州市科技创新条例》《广州市科技计划项目管理办法》《广州市科技计划项目经费管理办法》《广州市科技计划科技报告管理办法》等相关规定，实施项目和经费管理；

（三）严格遵守国家、省、市关于科研诚信和科技伦理的有关法律、法规，相关政策以及各项规定，加强项目实施过程中的科研诚信及科技伦理管理，恪守科研道德准则。

如有违反，本单位/本人愿意接受相关部门做出的各项处理决定，包括但不限于终止项目、停拨经费、核减经费、追回经费，取消一定期限广州市科技计划项目申报资格，记入科研失信行为数据库，将不良行为向社会公开等。

项目承担单位：华南农业大学

日期：2023年12月16日

项目负责人：施琳琳

日期：2023年12月15日

任务书签署

甲乙丙三方根据《广州市科技计划项目管理办法》《广州市科技计划项目经费管理办法》《广州市科技计划科技报告管理办法》等有关文件规定，以及有关法律、政策和管理要求，签署本任务书。

签订地点：广州市越秀区

广州市科学技术局（甲方）：广州市科学技术局
局项目经办人：蒋韬略　　联系电话：83124150
责任处室负责人：麦胜文

2024年01月17日

项目承担单位（乙方）：华南农业大学
二级部门：华南农业大学工程学院
项目负责人：施琳琳
项目经费汇入账号
账户名：华南农业大学　　账号：3602002609008310520
开户银行：广东广州工行五山支行
财务负责人：肖斐

2023年12月16日

组织单位（丙方）：华南农业大学
项目经办人：倪慧群

2023年12月18日

课题任务书编号：SKL-2025-009

农业装备技术全国重点实验室
开放课题任务书

课题名称： 面向柑橘采摘的多无人机视觉感知与作业规划研究

课题委托单位：农业装备技术全国重点实验室

（中国农业机械化科学研究院集团有限公司）

课题承担单位：华南农业大学

课题负责人： 施琳琳

起止年限： 2025 年 06 月至 2026 年 12 月

农业装备技术全国重点实验室编制

二〇二五年一月

五、课题承担单位及主要研究人员

姓　名	性别	年龄	职 称	专　业	工 作 单 位	在本课题中的分工	签字
施琳琳	女		讲师	控制科学与工程	华南农业大学	感知与规划	施琳琳
李　君	男		教授	车辆工程	华南农业大学	果园测试	李君
曹亚超	男		讲师	机械工程	华南农业大学	机器人控制	曹亚超
黄成杰	男		副教授	控制科学与工程	华南农业大学	协同规划	黄成杰
韩振浩	男		高级工程师	机械设计及理论	中国农业机械化科学研究院集团有限公司	视觉感知	
韩亚芬	女		高级工程师	机械设计及理论	中国农业机械化科学研究院集团有限公司	任务分配	

六、任务书双方签章

课题委托单位（甲方）：农业装备技术全国重点实验室

（中国农业机械化科学研究院集团有限公司）

负责人（签字）：

（公　章）

20　年　月　日

课题承担单位（乙方）：华南农业大学

单位负责人（签字）：

课题负责人（签字）：

（公　章）

20　年　月　日

子课题编号： 2025YFD1700504-01 密　级：公开

国家重点研发计划
子课题任务书

子课题名称： 水田施药装备无人化控制装置研发与示范

所属课题： 水田系列化智能施药装备集成与示范应用

所属项目： 智能精准农药施用装备研发与产业化

课题牵头承担单位： 华南农业大学

子课题承担单位： 华南农业大学

子课题负责人： 黄成杰

执行期限： 2025 年 12 月 至 2028 年 11 月

2025 年 12 月 29 日

填 写 说 明

一、任务书甲方即课题牵头承担单位，乙方即子课题承担单位。

二、任务书中的单位名称，请按规范全称填写，并与单位公章一致。

三、任务书中文字须用宋体小四号字填写。

四、凡不填写内容的栏目，请用“无”表示。

五、乙方完成任务书的填写，甲方审核确认后，用 A4 纸在线打印、装订、签章。一式六份报课题牵头承担单位签章，其中子课题承担单位一份，子课题负责人一份，作为课题任务书附件四份。

子课题基本信息表

<table>
<tr><td>子课题名称</td><td colspan="5">水田施药装备无人化控制装置研发与示范</td></tr>
<tr><td>子课题编号</td><td colspan="5">2025YFD1700504-01</td></tr>
<tr><td>所属课题</td><td colspan="5">水田系列化智能施药装备集成与示范应用</td></tr>
<tr><td>所属项目</td><td colspan="5">智能精准农药施用装备研发与产业化</td></tr>
<tr><td>密级</td><td colspan="2">■公开 □秘密 □机密</td><td>单位总数</td><td colspan="2">1</td></tr>
<tr><td>子课题类型</td><td colspan="5">□基础前沿 □重大共性关键技术 ■应用示范研究 □其他</td></tr>
<tr><td>子课题活动类型</td><td colspan="5">□基础前沿 ■应用研究 □试验发展</td></tr>
<tr><td>子课题研究所属学科</td><td colspan="5">农业工程</td></tr>
<tr><td>子课题成果应用的主要国民经济行业</td><td colspan="5">农、林、牧、渔业
农业
谷物种植
稻谷种植</td></tr>
<tr><td>子课题的社会经济目标</td><td colspan="5">环境保护、生态建设及污染防治
环境污染预防</td></tr>
<tr><td>经费预算</td><td colspan="5">总经费 80.00 万元，其中中央财政专项资金 80.00 万元</td></tr>
<tr><td rowspan="2">子课题周期节点</td><td>起始时间</td><td>2025 年 12 月</td><td>结束时间</td><td colspan="2">2028 年 11 月</td></tr>
<tr><td>实施周期</td><td>共 36 个月</td><td>预计中期时间点</td><td colspan="2">2027 年 06 月</td></tr>
<tr><td rowspan="9">子课题承担单位</td><td>单位名称</td><td colspan="2">华南农业大学</td><td>单位法定代表人姓名</td><td>薛红卫</td></tr>
<tr><td>单位性质</td><td colspan="2">大专院校/私营企业/事业型研究单位/其他事业单位</td><td>组织机构代码</td><td></td></tr>
<tr><td>单位主管部门</td><td colspan="2"></td><td>隶属关系</td><td>地方</td></tr>
<tr><td>单位所属地区</td><td colspan="2">广东省</td><td>地市（市、自治州、盟）</td><td>广州市</td></tr>
<tr><td>通信地址</td><td colspan="2">广州市天河区五山路 483 号</td><td>邮政编码</td><td>510642</td></tr>
<tr><td>单位开户名称</td><td colspan="4">华南农业大学</td></tr>
<tr><td>开户银行（全称）</td><td colspan="2">中国工商银行股份有限公司广州五山支行</td><td>汇入地点</td><td>广东省广州市</td></tr>
<tr><td>银行账号</td><td colspan="2">3602002609000310520</td><td>银行机构代码</td><td>102581000546</td></tr>
</table>

<table>
<tr><td rowspan="6">子课题负责人</td><td>姓 名</td><td>黄成杰</td><td>性 别</td><td>■男□女</td><td>出生日期</td><td></td></tr>
<tr><td>证件类型</td><td>身份证</td><td>证件号码</td><td colspan="3"></td></tr>
<tr><td>所在单位</td><td colspan="5">华南农业大学</td></tr>
<tr><td>最高学位</td><td colspan="5">■博士 □硕士 □学士 □其他</td></tr>
<tr><td>职 称</td><td colspan="3">□正高级 □副高级 ■中级 □初级 □其他</td><td>职务</td><td>无</td></tr>
<tr><td>电子邮箱</td><td colspan="2"></td><td>移动电话</td><td colspan="2"></td></tr>
<tr><td rowspan="3">子课题联系人</td><td>姓 名</td><td>肖博一</td><td>电子邮箱</td><td colspan="3">b</td></tr>
<tr><td>固定电话</td><td>无</td><td>移动电话</td><td colspan="3">1</td></tr>
<tr><td>证件类型</td><td>身份证</td><td>证件号码</td><td colspan="3">3</td></tr>
<tr><td rowspan="3">子课题财务负责人</td><td>姓 名</td><td>肖斐</td><td>电子邮箱</td><td colspan="3"></td></tr>
<tr><td>固定电话</td><td></td><td>移动电话</td><td colspan="3"></td></tr>
<tr><td>证件类型</td><td>身份证</td><td>证件号码</td><td colspan="3"></td></tr>
<tr><td rowspan="2">其他参与单位</td><td>序号</td><td colspan="2">单位名称</td><td>单位性质</td><td>组织机构代码</td></tr>
<tr><td>无</td><td colspan="2">无</td><td>无</td><td>无</td></tr>
<tr><td rowspan="2">子课题参加人数</td><td rowspan="2">10 人。其中：</td><td colspan="5">高级职称 3 人，中级职称 1 人，初级职称 0 人，其他 6 人；</td></tr>
<tr><td colspan="5">博士学位 4 人，硕士学位 3 人，学士学位 3 人，其他 0 人。</td></tr>
<tr><td>子课题简介(限 500 字以内)</td><td colspan="6">子课题针对水田泥脚深浅变化、硬底层高低不平等引起喷雾机侧滑、轨迹偏差的瓶颈问题，开展喷雾机行驶特性估计与侧滑状态预测控制技术研究，提出预测前馈与抗干扰融合的无人化轨迹跟踪控制方法，实现多工况水田环境下轨迹精准跟踪作业。</td></tr>
</table>

一、目标及考核指标、考核方式/方法

请填写下表。

子课题目标、预期成果与考核指标表

<table>
<tr><td rowspan="2">子课题目标[1]</td><td colspan="2" rowspan="2">预期成果</td><td colspan="4">考核指标[2]</td><td rowspan="2">考核方式（方法）及评价手段[4]</td></tr>
<tr><td>预期成果名称</td><td>预期成果类型</td><td>指标名称</td><td>立项时已有指标值/状态</td><td>中期指标值/状态[3]</td><td>完成时指标值/状态</td></tr>
<tr><td rowspan="3">针对水田泥脚深浅变化、硬底层高低不平等引起喷雾机侧滑、轨迹偏差的瓶颈问题，开展喷雾机行驶特性估计与侧滑状态预测控制技术研究，提出预测前馈与抗干扰融合的无人化轨迹跟踪控制方法，实现多工况水田环境下轨迹精准跟踪作业。</td><td rowspan="3">主要成果</td><td rowspan="3">1：侧滑状态预测与无人化轨迹跟踪控制</td><td rowspan="3">☐新理论 ☐新原理 ☐新产品 ☑新技术 ☐新方法 ☐关键部件 ☐数据库 ☐软件 ☐应用解决方案 ☑实验装置/系统 ☐临床指南/规范 ☐工程工艺 ☐标准 ☐论文 ☑发明专利 ☐其他</td><td>1.1 数量指标</td><td>无</td><td>/</td><td>无人化水田喷雾机的高精度轨迹跟踪控制装置1套；
申请专利1~2件</td><td>提供相关佐证材料，通过专家论证或第三方评价，专利授权证书或受理证明</td></tr>
<tr><td>1.2 技术指标</td><td>无</td><td>/</td><td>面向水田施药的防侧滑高精度轨迹跟踪控制技术</td><td>提供相关佐证材料，通过专家论证或第三方评价</td></tr>
<tr><td>1.3 推广应用指标</td><td>无</td><td>/</td><td>示范应用面积≥0.5万亩</td><td>提供示范应用面积证明</td></tr>
<tr><td rowspan="6">科技报告考核指标</td><td colspan="2">序号</td><td>报告类型[5]</td><td>数量</td><td colspan="2">提交时间</td><td>公开类别及时限[6]</td></tr>
<tr><td colspan="2">1</td><td>年度科技报告</td><td>3</td><td colspan="2">2026年12月、2027年12月、2028年12月</td><td>延期公开，3年</td></tr>
<tr><td colspan="2">2</td><td>年度执行情况报告</td><td>3</td><td colspan="2">2026年12月、2027年12月、2028年12月</td><td>延期公开，3年</td></tr>
<tr><td colspan="2">3</td><td>中期进展报告</td><td>1</td><td colspan="2">2027年10月</td><td>延期公开，3年</td></tr>
<tr><td colspan="2">4</td><td>最终科技报告</td><td>1</td><td colspan="2">2028年12月</td><td>延期公开，3年</td></tr>
<tr><td colspan="2">5</td><td>最终执行情况报告</td><td>1</td><td colspan="2">2028年12月</td><td>延期公开，3年</td></tr>
<tr><td colspan="8">其他目标与考核指标</td></tr>
</table>

备注：

1.**“子课题目标”**，应从以下方面明确描述：（1）研发主要针对什么问题和需求；（2）将要解决哪些科学问题、突破哪些核心/共性/关键技术；（3）预期成果；（4）成果将以何种方式应用在哪些领域/行业/重大工程等，并拟在科技、经济、社会、环境或国防安全等方面发挥何种的作用和影响。（5）所列主要成果原则上不超过5项，如有其他重要成果放在“其他”成果中表述。

2.**“考核指标”**，指相应成果的数量指标、技术指标、质量指标、应用指标和产业化指标等，其中，数量指标可以为专利、产品等的数量，论文代表作应注重质量，不以数量作为评价标准；技术指标可以为关键技术、产品的性能参数等；质量指标可以为产品的耐震动、高低温、无故障运行时间等；应用指标可以为成果应用的对象、范围和效果等；产业化指标可以为成果产业化的数量、经济效益等。同时，对各项考核指标需填写立项时已有的指标值/状态以及子课题完成时要到达的指标值/状态。同时，考核指标也应包括支撑和服务其他重大科研、经济、社会发展、生态环境、科学普及需求等方面的直接和间接效益。如对国家重大工程、社会民生发展等提供了关键技术支撑，成果转让并带动了环境改善、实现了销售收入等。若某项成果属于开创性的成果，立项时已有指标值/状态可填写“无”，若某项成果在立项时已有指标值/状态难以界定，则可填写“/”。

3.**“中期指标”**，各专项根据管理特点，确定是否填写，鼓励阶段目标明确的项目子课题填写中期指标。

4.**“考核方式方法”**，应提出符合相关研究成果与指标的具体考核技术方法、测算方法等。

5.**“科技报告类型”**，包括项目综合绩效评价（验收）前撰写的全面描述研究过程和技术内容的最终科技报告、项目年度或中期检查时撰写的描述本年度研究过程和进展的年度技术进展报告以及在项目实施过程中撰写的包含科研活动细节及基础数据的专题科技报告（如实验报告、试验报告、调研报告、技术考察报告、设计报告、测试报告等）。其中，每个项目在综合绩效评价（验收）前应撰写一份最终科技报告；研究期限超过2年（含2年）的项目，应根据管理要求，每年撰写一份年度技术进展报告；每个项目可根据研究内容、期限和经费强度，撰写数量不等的专题科技报告。科技报告应按国家标准规定的格式撰写。

6.**“公开类别及时限”**，公开项目科技报告分为公开或延期公开，内容需要发表论文、申请专利、出版专著或涉及技术诀窍的，可标注为“延期公开”。需要发表论文的，延期公开时限原则上在2年（含2年）以内；需要申请专利、出版专著的，延期公开时限原则上在3年（含3年）以内；涉及技术诀窍的，延期公开时限原则上在5年（含5年）以内。涉密项目科技报告按照有关规定管理。

二、子课题研究内容、研究方法及技术路线

（一）子课题的主要研究内容

拟解决的关键科学问题、关键技术问题，针对这些问题拟开展的主要研究内容。

1、拟解决的关键科学问题、关键技术问题

（1）行驶特性估计与侧滑状态预测技术

研究融合多源传感信息的行驶特性估计与在线识别方法，构建适应泥脚深浅变化与硬底层起伏的侧滑状态预测器，实现水田多工况条件下行驶状态的高精度预测与动态更新。

（2）基于预测前馈与抗干扰的轨迹跟踪控制技术

提出融合状态预测前馈与抗干扰补偿的控制方法，提前修正施药装备行驶路径，有效抑制侧滑造成的轨迹偏差，实现水田复杂环境下的高精度无人化轨迹跟踪控制。

2、主要研究内容

针对水田泥脚深浅不一、硬底层起伏不平导致施药装备侧滑与轨迹跟踪精度下降的问题，综合离线数据人工标注先验知识与水田农机运动姿态在线信息，研究基于数据驱动的侧滑位姿状态估计方法；构建基于侧滑位姿修正的喷雾机运动学模型，综合农机动力学特性、喷杆受激振动（水田及喷雾动态激励）及环境因素，研究基于侧滑状态前馈与模型预测控制的抗干扰轨迹跟踪控制方法，补偿侧滑引起的横向位姿偏差并抑制喷杆扰动引起的二次滑移，研制基于高精度轨迹跟踪的无人化水田喷雾控制装置。

（二）子课题采取的研究方法

针对子课题研究拟解决的问题，拟采用的方法、原理、机理、算法、模型等

采用数据驱动与物理模型结合方法，利用 IMU、RTK 与轮速传感器构建多源融合的侧滑位姿估计模型，通过时序深度网络或 Kalman 滤波整合离线标注先验知识，实现泥脚差异条件下的侧滑识别。建立基于侧滑修正的喷雾机运动学模型，引入模型预测控制与前馈补偿策略，抑制轨迹误差及喷杆振动引发的二次滑移。

三、主要创新点

围绕基础前沿、共性关键技术或应用示范等层面，简述子课题的主要创新点。具体内容应包括该项创新的基本形态及其前沿性、时效性等，并说明是否具备方法、理论和知识

产权特征。

1、创新点 1：水田智能喷雾机防侧滑轨迹跟踪控制技术

研究喷雾机在水田行驶时土壤硬底层不平度的位姿响应机制，提出侧滑状态预测的观测器设计方法，构建水田喷雾机动力学模型，基于非线性控制理论开发一种状态预测前馈方法与模型预测控制的喷雾机自动驾驶控制器，提升无人化作业的水田抗侧 滑能力，确保导航路径跟踪精度。

四、预期经济社会效益

子课题的科学、技术、产业预期指标及科学价值、社会、经济、生态效益。

1、 子课题的科学、技术、产业预期指标

子课题旨在突破水田复杂环境下的侧滑动态感知与补偿难题，通过构建耦合动力学模型及前馈-预测控制策略，形成核心的面向水田施药的防侧滑高精度轨迹跟踪控制技术。在此基础上，研制具有侧滑修正与二次滑移抑制功能的无人化喷雾控制装置，验证其在泥脚深浅不一、硬底层起伏条件下的作业稳定性。在预期产出方面，将围绕侧滑位姿估计与抗干扰控制算法申请发明专利 1～2 件；在产业推广方面，将在典型水田作业区开展规模化应用验证，完成示范推广面积≥0.5 万亩，为水田植保机械的智能化升级提供关键技术与装备支撑。

2、 子课题的科学价值、社会、经济、生态效益

子课题通过解决非结构化水田环境下的多源扰动感知与鲁棒控制难题，提高水田无人化喷雾复杂环境适应性，具有显著的科学价值。在社会效益方面，无人化作业可替代传统人工施药，减少作业人员农药暴露风险，有效缓解农村劳动力短缺矛盾。在经济效益方面，高精度跟踪技术能精准规避因侧滑导致的压苗减产，消除重喷漏喷现象，显著提升农药利用率与作业效率，降低综合种植成本。在生态效益方面，基于侧滑补偿的精准施药从源头减少了因路径偏差造成的农药过量投入与流失，降低了水土面源污染风险，有力推动水田农业向绿色化、智能化、可持续方向发展。

五、子课题年度计划

按每 6 个月制定形成子课题的计划进度，应将子课题的考核指标分解落实到年度计划中。

1、年度：2025 年 12 月—2026 年 5 月

任务：形成无人化施药装备侧滑感知模块的初步技术方案；

考核指标：完成水田侧滑感知的关键技术调研、方案设计与技术论证；

成果形式：技术方案报告、初步设计图纸、照片等。

2、年度：2026 年 6 月—2026 年 11 月

任务：开展水田无人化施药装备侧滑特性数据采集及位姿识别模块调试；

考核指标：突破关键技术 1 项；

成果形式：实验报告、检测报告、示范记录、照片等。

一、年度：2026 年 12 月—202“ 年 5 月

任务：在典型水田场景下开展侧滑工况下的路线跟踪测试、喷杆扰动响应评估与装备田间适应性试验；

考核指标：申请发明专利 1 件；

成果形式：照片、申请专利、新闻报道等。

4、年度：202“ 年 6 月—202“ 年 11 月

任务：推进无人化施药装备在多地水田开展侧滑补偿、轨迹跟踪与路径规划综合验证，实现稳定无人化作业；

考核指标：突破关键技术 1 项；

成果形式：实验报告、检测报告、专利和软著、新闻报道等。

5、年度：202“ 年 12 月—202” 年 5 月

任务：进一步完善无人化施药装备侧滑补偿与抗扰控制策略，使其适应规模化水田作业；

考核指标：示范面积≥1 万亩；

成果形式：照片、新闻报道等。

6、年度：202” 年 6 月—202” 年 11 月

任务：准备并提交验收所需材料；

考核指标：完成子课题最终验收报告；

成果形式：子课题验收报告、实验与监测报告等。

六、子课题组织实施机制及保障措施

1、子课题的内部组织管理方式、协调机制等，限 500 字以内。

子课题将严格遵循《国家重点研发计划管理暂行办法》《国家重点研发计划资金管理办法》《国家重点研发计划项目综合绩效评价工作规范（试行）》等要求，强化规范化与科学化管理，完善相关管理制度。

（1）子课题组织管理方式

组建完善管理研发团队，明确了各骨干与参与人员的职责与分工，组建由专家领衔的工作组，进一步确保研究目标明确、技术方案路径可行、实施过程风险可控。同时，制定项目监管制度，确定各项任务时间节点，定期通报项目研发进程，在关键节点对照目标要求，评价技术指标完成情况，评价阶段性工作情况，发现问题及时讨论解决，并根据项目实施需要调整下一阶段研究工作和资金使用计划。

（2）子课题管理协调机制

会同各课题参与单位推荐农业智能装备、人工智能、自动化控制、植保无人机、农药学等领域专家（尤其针对水田场景），构建子课题专家咨询智库，为研究方案制定与关键技术问题提供专业指导。

在子课题推进过程中，各研究团队建立资源共享和快速响应机制，积极协作共享信息与技术资源，及时提供所需资料并反馈研究进展及存在问题。

2、子课题实施的相关政策，已有的组织、技术基础，支撑保障条件，限500字以内。

（1）政策支撑

建立子课题联合攻关与示范推广机制，强化与其他参与单位在技术体系上的有效衔接，通过优势互补统筹成果落地、人才培养及示范点建设。进一步完善资金、设备、材料和技术规范等日常管理制度，形成覆盖子课题组织、实施与监督的全流程管理机制。

（2）技术支撑

子课题团队在路径跟踪控制方面具备扎实积累，已开展水田装备轨迹控制技术研究，具备数据驱动、辨识和模型预测控制等技术与方法积累。

（—）组织支撑

子课题汇聚智能水田植保机械、控制装置与自主导航等领域优势力量，配备匹配的研发人员，形成责任明确、分工清晰、协同高效的组织体系。

3、对实现课题总目标的支撑作用，及与课题内其他子课题的协同机制，限500字以内。

子课题重点攻克水田侧滑状态估计与抗干扰轨迹跟踪核心技术，研制具有通用性的无人化控制装置，解决了水田复杂环境下施药装备“走得准、控得稳”的关键共性难题，为构建系列化智能施药装备体系提供核心控制中枢与硬件基础。

在协同方面，子课题负责向整机研制与集成环节输出核心控制模块及算法，支撑各类施药装备的智能化升级；同时依托整机平台开展算法实地验证与数据迭代，同时依据

作业质量评价环节的反馈数据，动态修正控制策略以满足农艺要求；与其他类型施药技术形成互补，共同构建“空-地”立体化施药模式，协同推进课题的示范应用。

七、知识产权对策、成果管理及合作权益分配

限 500 字以内。

（一）知识产权对策

课题实施前单位独立获得的知识产权归本单位所有。课题实施后，在课题资助下产生的论文、专利、标准、规程及其他科技成果，应及时进行知识产权保护。单位独立承担任务所产生的成果，其知识产权归承担单位所有；双方共同参与研发的科技成果，知识产权归双方共同所有，课题组享有使用权。

（二）成果管理

子课题执行期间产生的所有成果，由第一完成单位负责知识产权申请与后续维护，费用由该单位承担。课题组内按协议实现资源共享。成果产权方须及时在课题组内登记注册，课题组负责最终成果统计，确保登记与统计客观、准确、及时和完整。

（三）合作权益分配

子课题执行期间，单位有权对合作完成科技成果的知识产权权利分配，在不违反公平原则和国家强制性规定以外，做出符合自身利益和意愿的约定。约定可以是某一方单独享有，也可以是双方共有。对于双方共有的知识产权，根据各方对该成果的贡献大小进行确权，成果转化收益分配按照确权比例进行分配，具体比例遵照执行《中华人民共和国科技进步法》《中华人民共和国促进科技成果转化法》《国家科技重大专项知识产权管理暂行规定》执行。

八、需要约定的其他内容

限 500 字以内。

1. 项目经费须专款专用，不得挪用。超支部分由乙方自筹解决，且不得影响项目执行。

2. 甲方有权对乙方经费使用情况进行监督，并对不符合规定的支出提出调整意见。

3. 乙方如需调整任务，须依规向甲方提交变更申请，经甲方审核并报科技部等主管部门批准后方可实施。批准前，双方应继续按原任务书执行，擅自调整造成的后果由调整方承担。

4. 若乙方因故无法继续执行任务并要求中止，应视情况部分或全部退还拨付经费；如乙方未提出中止，甲方有权根据调查情况提出中止建议，报主管部门批准后执行。

5. 乙方因不可抗力无法履行任务时，应及时通知甲方并在合理期限内提供证明。

6. 乙方应保持任务负责人及主要人员的稳定，确需调换须经甲方同意。因人员变动导致项目无法实施的，损失由乙方承担，项目予以撤销。

7. 乙方应严格履行任务书约定，并于每年年底前提交年度执行总结、经费决算及下一年度计划。

8. 项目结束后，乙方应按要求向甲方提交验收申请，由甲方组织专家依据任务书进行验收。

9. 双方均须履行本任务书约定的责任。如发生争议，依任务书相关条款及有关规定处理。

九、子课题参加人员基本情况表

填表说明： 1.专业技术职称：A、正高级　B、副高级　C、中级　D、初级　E、其他；
2.投入本子课题的全时工作时间（人月）是指在子课题实施期间该人总共为子课题工作的满月度工作量；累计是指子课题组所有人员投入人月之和；
3.子课题固定研究人员需填写人员明细；
4.是否有工资性收入：Y、是　N、否；
5.人员分类代码：B、子课题负责人　C、课题/子课题骨干　D、其他研究人员；
6.工作单位：填写单位全称，其中高校要具体填写到所在院系。

序号	姓名	性别	出生日期	证件类型	证件号码	专业技术职称	职务	最高学位	专业	投入本子课题的全时工作时间（人月）	人员分类代码	在子课题中分担的任务	是否有工资性收入	工作单位
1	黄成杰	男				B、副高级	无	博士	控制科学与工程	18	B、子课题负责人	负责子任务“水田施药装备无人化控制装置研发与示范”；承担面向水田无人化施药的高精度轨迹跟踪控制技术研究	是	华南农业大学
2	肖博一	男				B、副高级	无	博士	机械工程	18	C、课题/子课题骨干	参加子任务“水田施药装备无人化控制装置研发与示范”，承担滑移位姿估计研究	是	华南农业大学
3	施琳琳	女				C、中级	无	博士	控制科学与工程	18	C、课题/子课题骨干	参加子任务“水田施药装备无人化控制装置研发与示	是	华南农业大学

												范”，承担水田地面施药装备滑移估计		
4	李庆	男				3、副高级	无	博士	农业机械化及其自动化	18	C、课题/子课题骨干	参加子任务“水田施药装备无人化控制装置研发与示范”，承担水田地面施药装备滑移预测	是	华南农业大学
5	龚林立	男				E、其他	无	硕士	农业工程	18	D、其他研究人员	参加子任务“水田施药装备无人化控制装置研发与示范”，承担水田无人化施药装备关键技术的研究	否	华南农业大学
6	李茂鑫	男				E、其他	无	学士	机器人工程	18	D、其他研究人员	参加子任务“水田施药装备无人化控制装置研发与示范”，承担水田无人化施药装备关键技术的研究	否	华南农业大学
7	李俞浩	男				E、其他	无	硕士	机械	18	D、其他研究人员	参加子任务“水田施药装备无人化控制装置研发与示范”，承担水田无人化施药装备关键技术的研究	否	华南农业大学
8	陈铿	男				E、其他	无	学士	机械工程	18	D、其他研究人员	参加子任务“水田施药装备无人化控制装置研发与示	否	华南农业大学

												范”，承担水田无人化施药装备关键技术的研究		
9	潘惜园	女	[redacted]			E、其他	无	学士	机械工程	18	D、其他研究人员	参加子任务“水田施药装备无人化控制装置研发与示范”，承担水田施药装备跟踪及轨迹预测研究	否	华南农业大学
10	曾晔	男				E、其他	无	硕士	农业工程	18	D、其他研究人员	参加子任务“水田施药装备无人化控制装置研发与示范”，承担水田施药装备跟踪及轨迹预测研究	否	华南农业大学
固定研究人员合计										108	/	/	/	/
流动人员或临时聘用人员合计										0	/	/	/	/
累计										108	/	/	/	/

十、经费预算

子课题预算表

表 B1 子课题编号：2025YFD1700504-01　子课题名称：水田施药装备无人化控制装置研发与示范

金额单位：万元

序号	预算科目名称	金额
	(1)	(2)
1	**一、中央财政专项资金**	**80.00**
2	（一）直接费用	66.50
3	1.设备费	0
4	其中：购置设备费	0
5	2.业务费	55.10
6	3.劳务费	11.40
7	（二）间接费用（自动计算）	13.50
8	**二、其他来源资金**	**0**
9	**三、合计**	**80.00**

注：1.间接费用无需编制预算说明；2.绩效支出在间接费用中无比例限制。承担单位在统筹安排间接费用时，要处理好合理分摊间接成本和对科研人员激励的关系，绩效支出安排与科研人员在子课题工作中的实际贡献挂钩。

设备费——购置/试制设备预算明细表

表 B2　　子课题编号：2025YFD1700504-01　　子课题名称：水田施药装备无人化控制装置研发与示范　　金额单位：万元

填表说明：1.设备分类：购置、试制；
2.购置设备类型：通用、专用；
3.试制设备不需填列本表（9）列、（10）列、（11）列、（12）列；
4.设备单价的单位为万元/台套，设备数量的单位为台套；
5.单价 50 万元以下的设备不用填写；
6.本表只填写中央财政资金购置（试制）的设备。

序号	设备名称	设备分类	功能和技术指标	单价	数量	金额	购置或试制单位	安置单位	购置设备类型	主要生产厂家及国别	规格型号	拟开放共享范围
	（1）	（2）	（3）	（4）	（5）	（6）	（7）	（8）	（9）	（10）	（11）	（12）
无												
单价 50 万元以上购置设备合计							/	/	/	/	/	/
单价 50 万元以上试制设备合计							/	/	/	/	/	/
累计							/	/	/	/	/	/

子课题单位经费预算明细表

表 B3　子课题编号：　2025YFD1700504-01　　子课题名称：水田施药装备无人化控制装置研发与示范　　金额单位：万元

填表说明：1.单位类型分子课题承担单位、子课题参与单位；
2.组织机构代码指企事业单位国家标准代码，单位若已三证合一请填写单位统一社会信用代码，无组织机构代码的单位填写“000000000”。

序号	单位名称	组织机构代码-统一社会信用代码		单位类型	任务分工	研究任务负责人	合计	中央财政专项资金		其他来源资金
								小计	其中：间接费用	
	（1）	（2）	（3）	（4）	（5）	（6）	（7）	（8）	（9）	（10）
1	华南农业大学	统一社会信用代码	124400004554165634	课题承担单位	面向无人化水田施药的高精度轨迹跟踪控制技术研究	黄成杰	80.00	80.00	13.50	0
累计							80.00	80.00	13.50	0

预算说明

一、中央财政资金

预算的编制要坚持任务相关性、政策相符性和经济合理性，实事求是编制提出课题预算。填报时，直接费用应按设备费、业务费、劳务费三个类别填报，每个类别结合科研任务按支出用途进行说明。除 50 万元以上的设备外，其他费用只提供基本测算说明，不需要提供明细。

中央财政资金预算总经费 80.00 万元，直接经费 66.50 万元，其中设备费 0 万元，业务费 55.10 万元，劳务费 11.40 万元；间接经费 13.50 万元。

1.设备费 0 万元

1.1 购置设备费 0 元

1.2 试制设备费 0 万元

1.3 设备改造/租赁费 0 元

2.业务费 55.10 万元

2.1 材料费 16.40 万元

无人化施药装备研发与示范的材料费为 16.40 万元

根据研究内容需要，水田无人化施药高精度轨迹跟踪控制系统需集成高精度 RTK-GNSS 与工业级 IMU，实现厘米级定位与实时姿态测量；通过轨迹跟踪控制器与嵌入式计算单元运行模型预测控制算法，实现侧滑补偿与喷杆扰动抑制；配备轻量化喷杆、电磁阀、流量计等精准喷雾部件及防腐蚀储液与供液系统，确保稳定施药；利用激光雷达感知地形，结合数据通信模块实现远程监控与作业数据回传。具体购置材料费清单如下：

表 1 购置材料费清单

序号	设备名称	单价（万元）	单位	数量	总价（万元）
1	高精度 RTK-GNSS 导航定位与航向系统	3.20	套	1	3.20
2	工业级 IMU 姿态测量模块	1.50	套	1	1.50
3	轨迹跟踪控制器及嵌入式计算单元	2.80	套	1	2.80
4	喷雾执行单元（轻量化喷杆+电磁阀+流量计+喷头）	2.70	套	1	2.70
5	农药液储罐及供液系统	1.20	套	1	1.20
6	激光雷达传感器	1.60	套	1	1.60

7	数据采集与通信模块	1.10	套	1	1.10
8	线束、接插件、防水接头等	2.30	批	1	2.30
合计					16.40

2.2 测试化验加工费 7.12 万元

（1）针对无人化水田喷雾机在不同泥脚深浅、硬底层起伏条件下的运动特性与侧滑规律，对其姿态、速度、侧倾和俯仰等状态参数进行实地采集与对比验证。需对用于田间试验的测试平台进行基础加工，包括传感器安装支架、数据采集模块固定件及防水防泥保护结构等，预计加工费用 2.60 万元。

（2）为研究喷雾机喷杆在水田作业中受激振动对喷雾均匀性及轨迹精度的影响，对喷杆振动幅值、频谱特性及喷雾分布进行测试与分析。需加工喷杆振动监测夹具、喷雾沉积采样装置、喷头流量校准工装等试验器具，预计加工费用 2.72 万元。

（3）验证基于高精度轨迹跟踪控制的无人化水田喷雾装备的整机性能与作业效果，在广东、湖南等地典型水田开展轨迹精度、防效及农药利用率实地检测与示范。需加工示范作业样品采集器具、防效测定辅助装置及便携式喷雾性能测试工装等，预计加工费用 1.80 万元。

以上共计费用：2.60 万元+2.72 万元+1.80 万元=7.12 万元。

2.3 燃料动力费 0 万元。

2.4 出版/文献/信息传播/知识产权事务费：3.50 万元

（1）国内发明专利申请费 0.50 万元：专利申请费按平均 5000 元/篇，一共 1 篇，共计 5000 元/项*1 项=0.50 万元。

（2）印刷费 0.50 万元，用于项目和课题的研究报告以及科研资料复印、打印、彩扩、扫描、邮寄等费用，预计 3 年需要 0.50 万元。

（3）购买文件资料、书籍、技术成果查新、购买数据库等软件使用版权，共计 2.50 万元。

以上费用合计为：0.50 万元+0.50 万元+2.50 万元=3.50 万元。

2.5 会议/差旅/国际合作与交流费 27.60 万元

（1）会议费 14.85 万元

依据中央国家机关政府采购定点地点报价进行测算，课题支出中将严格控制会

议规模和会议标准。专项经费支出按照国管财行[2016] 214 号文件《中央和国家机关会议费管理办法》，三、四类会议费标准为 550 元/人天。

课题执行期间将开展课题启动会 1 次，用于邀请相关专家共同对项目关键技术难点方案进行论证；中期交流会 1 次，用于推进项目进度；课题验收总结会 1 次；示范会 2 次，用于促进水田无人化施药装备技术产业化，每年 18 人次，三年共计 54 人次，费用累计 3 年×18 人次×5 次×550 元/人天=14.85 万元。

（2）差旅费 6.97 万元

依照财政部关于印发《中央和国家机关工作人员赴地方差旅住宿费标准明细表》的通知（财行[2016]71 号）执行：

1）省外交通费、住宿费、补助等费用按平均每人次 0.30 万元预算，三年预计 34 人次，小计 34 人次×0.30 万元 =10.20 万元；市内交通 0.75 万元。主要用于课题组成员需要前往广东、湖南等试验基地进行田间试验，前往基地进行田间试验布置、野外试验样品采集、喷雾数据采集等工作。

2）用于参加课题骨干参加项目组织的交流会（广州-湖南），费用按平均每人次 0.20 万元预算，每年 3 人次，三年共计 9 人次，预计 3 年×3 人次×0.20 万元 =1.80 万元。

会议/差旅/国际合作与交流费用合计为：14.85 万元+10.20 万元+0.75 万元+1.80 万元=27.60 万元。

2.6 其他支出 0.48 万元

用于课题审计，按中央财政资金 6‰，预计 0.48 万元。

3. 劳务费 11.40 万元

劳务费包括劳务性费用 10.00 万元和专家咨询费 1.40 万元

3.1 劳务性费用：10.00 万元

用于硕博士生劳务费，具体测算如下：

①博士研究生：0.25 万元/人月×18 个月×1 人=4.50 万元；

②硕士研究生：0.15 万元/人月×18 个月×2 人=5.40 万元；

③临时工：5 人*200 元=0.1 万元；

劳务费用为： 4.50 万元+5.40 万元+0.1 万元=10.0 万元

3.2 专家咨询费：1.40 万元

依据关于印发《中央财政科研项目专家咨询费管理办法》的通知财科教〔2017〕128号，高级专业技术职称人员的专家咨询费标准为2000元/人/天。

课题召开课题启动会、中期总结、课题终期验收会，预计邀请专家7人次进行现场点评，以及实验过程中疑难问题临时请专家指导，预计7人次×2000元/人/天=1.40万元；

4. 间接经费13.50万元

课题间接经费13.50万元，主要用于课题管理费用的支出和课题执行期间一线科研人员的相关绩效支出。

二、其他来源资金（0万元）

对其他来源资金主要用途、支出预算做简要说明。

任务书签署

甲乙双方根据《国务院印发关于深化中央财政科技计划（专项、基金）管理改革方案的通知》（国发〔2014〕64号）、《国务院关于优化科研管理提升科研绩效若干措施的通知》（国发〔2018〕25号）、《国务院办公厅关于改革完善中央财政科研经费管理的若干意见》（国办发〔2021〕32号）、《科技部 财政部关于印发<国家重点研发计划管理暂行办法>的通知》（国科发资〔2017〕152号）、《财政部 科技部关于印发<国家重点研发计划资金管理办法>的通知》（财教〔2021〕178号）、《科技部财政部关于印发<中央财政科技计划（专项、基金等）监督工作暂行规定>的通知》（国科发政〔2015〕471号）等有关文件规定，以及有关法律、政策和管理要求，依据课题立项通知，签署本任务书。

同时，本单位和子课题负责人**郑重承诺**：对本子课题所有成果产出（包括但不限于新产品、新技术、标准、论文、专利等）的真实性、与课题（子课题）的关联性等负责，将按要求落实科研作风学风和科研诚信主体责任；项目经费全部用于与本项目研究工作相关的支出，不截留、挪用、侵占，不用于与科学研究无关的支出；接受并积极配合相关部门的监督检查。如有违反，本单位和子课题负责人以及相关成果产出者愿接受项目管理专业机构和相关部门做出的各项处理决定，包括但不限于终止子课题执行、追回子课题经费，取消一定期限国家科技计划项目（子课题）申报资格，记入科研诚信严重失信行为数据库以及主要负责人接受相应党纪政纪处理等。

课题牵头承担单位（甲方）：

法定代表人签字（签章）：薛红卫

（公章）

2025 年 12 月 31 日

课题负责人签字（签章）：李君

2025 年 12 月 31 日

子课题承担单位（乙方）：

法定代表人签字（签章）：薛红卫

（公章）

2025 年 12 月 31 日

子课题负责人签字（签章）：黄林杰

2025 年 12 月 31 日

受理编号：c252025040250100007　　项目编号：2025B0202100002

项目下达文号：粤科资字〔2025〕222号

广东省重点领域研发计划项目

课题任务书

项目名称：丘陵山区荔枝智能采收装备创制与应用

项目承担单位（甲方）：华南农业大学

项目负责人：李君

课题名称：荔枝机械化采收装备与多机协同作业技术研发

课题承担单位（乙方）：华南农业大学

课题负责人：曹亚超

起止时间：2025-11-01 至 2029-10-31

填写说明

一、课题任务书甲方即项目承担单位，乙方即课题承担单位。

二、任务书中的单位名称，请按规范全称填写，并与单位公章一致。

三、课题任务书中的单位名称，请按规范全称填写，并与单位公章一致。

四、任务书的起点时间不得早于项目申报时间（以申报书提交业务系统之日为准），不得迟于项目立项文件下达之日。

五、课题任务书内容须按照项目任务书据实填写，要遵循实事求是原则，无需凑够字数。

六、课题任务书填报不得降低双方约定好的考核指标，不得自行对主要研究内容作大的调整。任务书将作为项目与课题过程管理、综合绩效评价（验收）和监督评估的重要依据。

七、凡不填写内容的栏目，请用“无”表示。

八、乙方填写的任务书经甲方审核确认后，用A4纸打印、装订、签章。任务书一式六份，报课题承担单位和子课题承担单位的管理部门审核盖章后，分别由项目主持单位、课题承担单位和子课题负责人各保留2份。

九、本课题任务书自签字并加盖公章之日起生效，各方均应负本任务书的法律责任，不应受机构、人事变动的影响。

项目基本信息表

项目名称	丘陵山区荔枝智能采收装备创制与应用			
项目编号	2025B0202100002			
专项名称	精准农业及生态绿色技术（荔枝品质维持）			
专题名称	20250210--专题二：荔枝采收及质量安全监测关键技术、装备研发与应用		单位总数	5
经费预算	总投入 840.00 万元，其中省级财政科技资金投入 400 万元			
项目周期节点	起始时间	2025年 11月 01日	结束时间	2029年10月31日
	实施周期	共 47 个月	预计中期时间点	2027-10-31
项目牵头承担单位	单位名称	华南农业大学	单位性质	高等院校
	单位所在地	广东省-广州市-天河区	统一社会信用代码	124400004554165634
	通信地址	广东省-广州市-天河区五山路483号	邮政编码	510642
	银行账号	3602002609000310520	法定代表人姓名	薛红卫
	单位开户名称	华南农业大学		
	开户银行（全称）	广东广州工行五山支行		

课题负责人	姓名	曹亚超	性别		
	证件类型	身份证	证件号码		
	所在单位	华南农业大学			
	最高学位	博士			
	职称	讲师	职务	无	
	电子邮箱		移动电话		
课题联系人	姓名	施琳琳	电子邮箱		
	固定电话	/	移动电话		
	证件类型	身份证	证件号码		
课题财务负责人	姓名	科研财务科	电子邮箱		
	固定电话	020-85288032	移动电话		
	证件类型	身份证	证件号码		

一、任务书条款

第一条	甲乙两方根据《广东省人民政府关于印发广东省重点领域研发计划实施方案的通知 》（粤府〔2018〕84号）《广东省科学技术厅关于印发广东省重点领域研发计划“十四五”行动方案的通知》（粤科资字〔2022〕37号）《广东省人民政府办公厅关于改革完善省级财政科研经费使用管理的实施意见》（粤府办〔2022〕14号）《广东省财政厅广东省审计厅关于印发〈省级财政科研项目资金管理监督办法（2023年修订）〉的通知》（粤财规〔2023〕3号）等文件规定，以及有关法律、政策和管理要求，依据项目立项通知，为顺利完成（2025）年丘陵山区荔枝智能采收装备创制与应用专项项目（文件编号：粤科资字〔2025〕222号），特签署本任务书。
第二条	本项目以攻克关键核心技术、研发关键零部件和重大装备为目标，力争突破前沿性、引领性的技术，取得产业带动性强、技术自主可控的重大原创科技成果和自主知识产权。《项目申报书》和申报指南是本任务书填报的重要依据，任务书填报时不得降低考核指标，不得自行对主要研究任务作出调整。《项目申报书》、申报指南和本任务书将共同作为项目过程管理、验收结题和监督评估的重要依据。
第三条	甲方有权按照《广东省重点领域研发计划实施方案》进行资源整合，以目标为导向，合理优化课题承担单位、参与单位布局。甲方实行科技计划“放管服”改革，建立基于信任的管理制度,但有权按照有关规定采取日常监管、随机抽查、专项检查、中期评估、财务审计等方式对项目实施监督，并严格以本任务书中约定的任务、期限、目标和验收指标等具体内容作为监督依据。项目到期后，甲方依据本任务书对项目实施结果进行验收。甲方可根据《广东省科学技术厅科技计划项目科研诚信管理办法》（粤科规范字〔2024〕2号）对乙方进行科技计划信用管理。
第四条	乙方要建立以诚信为原则的自主管理制度，按如下要求执行项目：1.承担项目的核心研究任务。2.统筹协调做好资源分配和任务分工工作，履行项目组织实施和资金使用等方面的主体责任，对项目实施目标和财政资金绩效负责。3.完善单位内部控制制度和单位间监督制约机制。4.乙方负责协调落实项目自筹经费及有关保障条件，按照任务分工、任务量和时间进度合理分配和拨付财政资金，确保财政资金使用的安全有效,并签订单位间的合作协议。5.乙方及相关参与单位均应对财政资金实行专款专用，单独列账，并积极配合甲方（或委托专业机构等）进行的监督检查。6.乙方须积极配合甲方组织的评估检查；项目完成后，应主动申请验收结题。7.乙方应按照国家和省有关规定，提交科技报告及其他材料。8.项目负责人及主要研究开发成员应实质性参与项目组织实施，不得出现挂名现象。
第五条	项目经费可按单位性质、项目进展及评估情况分阶段拨付。
第六条	在履行本任务过程中，乙方及参与单位必须恪守科研道德准则、科研活动规范和科研诚信规定，严格遵守有关法律法规。涉及医学、生物技术和人工智能等敏感领域研究 ,应当按照国家有关规定设立伦理委员会，开展研究项目的伦理审查，遵循国际公认的科研伦理规范和生命伦理准则。
第七条	本项目主要研发活动应在广东省内开展，项目成果应优先在广东省内实施转化应用。项目形成的知识产权归属、使用和转移，按照国家和广东省有关法律、法规和政策执行。
第八条	按照《广东省科学技术厅关于科技成果登记与信息公开的实施办法》（粤科管字〔20 13〕127号）的规定，本项目产生的科技成果必须登记；登记完成后，科技管理部门根据文件要求，可在有关科技成果信息综合平台将登记信息（内容包括成果名称、成果完成单位、成果简介、成果完成人等）进行公开。
第九条	为促进职务科技成果转化，本项目形成的职务科技成果在项目验收完成后，自动纳入省职务科技成果“先用后转预备库”（经主管部门同意不纳入的除外）。成果完成方同意以“先用后转”方式转化的，成果自动从“先用后转预备库”进入“先用后转库 ”,予以公开发布；成果完成方不采取“先用后转”方式转化的，该成果3年内未完成转化，自动进入“先用后转库”予以公开发布。成果纳入“先用后转预备库”后完成转化的，成果完成人应及时提交佐证材料申请出库。对采取“先用后转”方式转化的，具体事宜由使用方与成果所有方另行约定。

第十条	各方应充分理解本任务书的内容并自愿签署本任务书。未尽事宜，协商解决或签订补充协议进一步明确，甲方拥有最终解释权。

二、项目验收指标

（一）技术及成果指标

1.核心考核指标

序号	成果名称	成果类型	验收指标	评测方式/方法
1	自适应仿形荔枝机械化采收装备	新产品	研制自适应仿形荔枝机械化采收装备1台，最大采收高度≥4m，采收作业效率相比人工提升200%以上，果实损伤率≤8%，并达到用人成本降低80%以上。硬件技术创新就绪度达到8级。	专家论证、用户评价、第三方评测等

2.高水平知识产权指标

序号	内容	类型	结题时状态	拟解决关键问题
1	荔枝自适应仿形围蔽采摘机	国内发明专利	授权	填补国内技术空白
2	荔枝机械化采收除杂协同作业方法	国内发明专利	授权	填补国内技术空白

对以上项目成果属于高质量知识产权的相关说明

发明专利1：创新性设计一种具有自适应仿形围蔽功能的荔枝机械化采摘装备。通过设计基于冠层仿形作业的两段式梳刷振动采摘机构和配套的一体化仿形围蔽装置，结合视觉感知算法获取果树冠层点云数据并对果实分布进行目标分割，突破传统机械式荔枝采收作业幅宽小、果实收集损失率高的关键痛点。部分结构及算法已在团队自研采摘原型机上完成部署，测试采收效率高。

发明专利2：创新提出一种荔枝机械化采收除杂协同作业方法。通过构建由采收装备与收集除杂装备组成的多机协同作业系统，设计分布式任务调度与协同控制算法，实现基于多机作业预测功能的一体化协同。该知识产权的落地将率先为行业低损高效采收除杂协同作业提供技术参考。

上述知识产权所用技术路径拥有高原创性，未构成与现有公开专利的重合；创新点集中、技术路线清晰完整，具有成为高质量知识产权的潜力。

3.技术创新就绪水平

当前技术创新就绪水平	中期评估时技术创新就绪水平	项目完成时技术创新就绪水平
5级	6级	8级

对项目实施后技术创新就绪水平提升情况的相关说明

项目实施后，总体技术就绪度从5级提升至8级，关键技术水平均有显著提升，达到应用或产业化水平，具体如下：自适应仿形荔枝机械化采收装备可实现荔枝的柔性采摘和围蔽收集功能。项目实施前研制了柔性梳刷采摘装置与配套仿形围蔽装置样机，开展了基于离散元的荔枝梳刷振动采摘果实损伤模拟，对荔

枝梳刷振动采摘试验验证和演示示范，达到了TRL5级；中期预计通过多源传感器对冠层轮廓与果实分布信息进行精准感知并优化采摘部件结构，提高采收作业幅宽，实现最大采收高度≥4m，采收作业效率相比人工提升200%以上，达到TRL6级；后期项目完成时，将进行基于采摘部件与自主作业性能优化的试验与推广示范，并在实际环境下充分使用，确保荔枝采净率≥90%，果实损伤率≤8%，达到TRL8级。

4.科技报告考核指标

序号	报告类型	提交时间	公开类别及时限
1	2026年度课题技术进展报告	2026-12	延期公开4年
2	2027年度课题技术进展报告	2027-12	延期公开4年
3	2028年度课题技术进展报告	2028-12	延期公开4年
4	2029年度课题技术进展报告	2029-10	延期公开4年

5.参考指标

（1）申请发明专利2件，授权发明专利2件，总计4件；（2）申请软件著作权3件；（3）发表学术论文4篇；（4）培养研究生12-14名。

（二）项目经济指标及社会效益

累计新增销售收入（万元，截至项目验收结题）	无
累计新增利税（万元，截至项目验收结题）	无

（三）项目其他经济指标说明

经济效益：相比现有机械采收技术，项目研究成果可减少果实损失20%以上，含杂率降低后节约保鲜分选人工成本50%，并有效延长商品货架期，间接经济效益可观。

（四）阶段性成果评价

序号	指标名称	立项时已有指标值/状态	中期指标值/状态	完成时指标值/状态	评估方式（方法）及评价手段
1	采收装备	爬坡度≥15°，荔枝采净率≥80%，含杂率≤10%，最大采收高度≥2.6m，采收作业效率相比人工提升80%以上，果实损伤率≤10%	爬坡度≥15°，荔枝采净率≥85%，含杂率≤5%，最大采收高度≥3.5m，采收作业效率相比人工提升150%以上，果实损伤率≤10%	爬坡度≥20°，荔枝采净率≥90%，含杂率≤5%，最大采收高度≥4m，采收作业效率相比人工提升200%以上，果实损伤率≤8%	专家论证意见、用户评价证明、第三方评测报告
2	发明专利	/	2件	4件	专利授权证书或受理通知书
3	论文	/	2篇	4篇	已发表论文全文或录用通知

4	软件著作权	/	1件	3件	软件著作权登记证书或受理通知书

三、项目研究内容、研究方法及技术路线、主要创新点

（一）项目拟解决的关键问题

（1）冠层接触式荔枝机械化采收的高效采收与围蔽减损问题

荔枝果树冠层结构复杂、果实分布均一化程度低，传统冠层接触式机械化采收装备多在开放空间作业，无法对果实的弹跳轨迹进行有效约束，导致漏果损失率较高。此外，采摘执行机构与冠层果实的空间包络度差、作业幅宽小，严重影响采摘效率。本项研究针对上述瓶颈，旨在研发可对目标树冠进行自适应仿形的荔枝机械化柔性采收与配套围蔽装置。如何根据冠层的三维形态特征与果实分布特性，结合振动采收装置的有效包络空间，实时决策仿形采收装置的空间位姿，同步实现采收区域冠层围蔽，是本项研究亟需解决的关键问题。

（二）项目的主要研究内容

（1）丘陵山地荔枝高效低损智能采收装备技术研发

① 荔枝冠层果实自适应仿形机械化采收装备创制

针对丘陵山地荔枝机械化采收装备作业幅宽小、冠层适应性差、果实收集损失率高等问题，开展自适应仿形围蔽的智能采收装备创制研究。基于果树冠层特征及果实分布特性，轻量化设计智能采收装备本体，创制具有冠层果实自适应仿形功能的两段式柔性梳刷振动采收装置和与之配套的一体化仿形围蔽装置；结合传感器实时获取的果实空间聚类信息，研究采摘部件空间位姿自适应仿形调控技术；构建基于冠层特征的仿形梳刷装置与围蔽收集装置的协同作业机制，限制采收过程中果实运动空间区域。集成并试制仿形围蔽式荔枝智能采收装备，以采净时间和损伤率为指标优化仿形结构与作业参数，开展整机可靠性及环境适应性等采收作业试验验证。

② 荔枝机械化采摘-收集-除杂多机协同作业技术研究

针对多机作业路径干扰大、协同效率低等问题，开展采摘-收集-除杂多机协同作业技术研究。构建由采收装备与收集除杂装备组成的多机协同作业系统，建立多机间状态感知与信息交互机制；融合果园环境高精度建图，研究多机作业路径规划与动态避让策略，设计分布式任务调度与协同控制算法，实现基于多机作业预测功能的一体化协同。以整机作业一致性、任务完成效率为评价指标，开展多机协同作业系统的可靠性与适应性试验验证。

（三）项目采取的研究方法及技术路线

（1）丘陵山地荔枝高效低损智能采收装备技术研发

设计具有冠层围蔽功能的可仿形两段式柔性梳刷振动采收装置，通过雷达和视觉传感器实时获取果树冠层点云数据以及果实分布图像，采用语义/实例分割算法对果实区域与果树冠层进行目标分割，拟合确定冠层轮廓特征，并基于果实空间聚类信息解算出振动采收机构空间姿态位置，进行采收围蔽装置的自适应仿形调整，根据试验结果优化结构与作业参数。

搭建半实物仿真平台，模拟采摘-收集-除杂作业场景，验证装置协同性。基于局部通信网络的信息交互机制，建立统一的多机状态描述协议与行为预测模型。结合作业任务与动态环境，设计分布式任务调度算法 。融合局部感知与全局环境，进行协同路径规划与避障作业试验验证。

（四）主要创新点

（1）基于冠层轮廓特征与果实分布特性的自适应仿形围蔽式荔枝机械化采收技术

突破现有荔枝振动采收机作业幅宽、冠形适应性的局限性，设计具有树冠自适应仿形功能的两段式宽幅柔性梳刷采收装置。通过雷达和视觉传感器实时获取果树冠层点云数据以及果实分布图像，确定冠层轮廓特征以及果实振动采收空间位置，基于采净时间和损伤率指标优化仿形作业参数，进行采收装置的姿态自适应调整，进一步提高采收作业效率；针对荔枝机械化采收过程中果实收集损失率高的问题，创制与采收装置配套的一体化仿形围蔽装置。通过感知围蔽部件与树冠的接触判断，自动对树冠结果区域进行采收围蔽 ，限制采收过程中果实运动方向，减少果实收集损失。该创新点革新了现有的水果振动式收获技术形态，形成具有自主知识产权的方法可引领簇状水果机械化采收技术的创新发展。

（2）丘陵山地荔枝机械采摘-折展收集-气力除杂的协同作业系统

为克服现有振动采摘机功能单一、多功能采收机结构复杂且体积大的局限性，采用仿形围蔽式荔枝采摘机与收集除杂一体化机的协同作业方案。通过路径规划与作业优化，实现丘陵山地荔枝园机械化采摘、收集、除杂环节的高效协同。该创新点形成的协同作业系统具有显著的原创性，针对荔枝树结果特性提出的机械采摘-折展收集-气力除杂的工作模式，作业效率高、集成度强、适应性好，有望解决荔枝产业机械化采收短板问题。

四、项目进度和阶段目标

（一）项目起止时间：2025年 11月 01日 至 2029年 10月 31日				
（二）项目实施进度及阶段主要目标				
开始日期	结束日期	主要工作内容	预期目标	成果形式
2025年 11月 01日	2026年 04月 30日	开展可仿形柔性梳刷振动采收装置的结构方案设计。	完成整体方案设计、可行性分析论证。	实施方案
2026年 05月 01日	2026年 10月 31日	开展仿形围蔽式振动执行机构关键部件的设计。	1）形成柔性梳刷振动采收装置和仿形围蔽装置。 2）申请专利1件。	专利，年度技术进展报告。
2026年 11月 01日	2027年 04月 30日	开展基于果实空间聚类信息的采收围蔽装置的自适应仿形调整研究。	1）形成采摘部件空间位姿自适应仿形调控技术。 2）申请专利1件，发表论文1篇。	论文、专利。
2027年 05月 01日	2027年 10月 31日	构建基于冠层特征的仿形梳刷装置与围蔽收集装置的协同作业机制研究，完成采收装备对果园信息的“感知-理解-决策”闭环系统集成测试。	1）形成仿形梳刷装置与围蔽收集装置的协同作业控制算法。 2）申请软件著作权1件，专利1件，发表论文1篇。	论文，软件著作权，年度技术进展报告。
2027年 11月 01日	2028年 04月 30日	开展仿形围蔽式荔枝智能采收装备技术模块与高适应性履带底盘的集成工作。	1）形成仿形围蔽式荔枝智能采收装备系统。 2）申请专利1件，发表论文1篇。	论文，专利

2028年 05月 01日	2028年 10月 31日	1）开展仿形围蔽式荔枝智能采收装备的果园环境功能试验，完成采收作业参数的优化工作。 2）开展采收装备与收集除杂装备的协同作业策略研究。开展丘陵山地荔枝机械化采收装备可靠性及环境适应性等采收作业试验验证。	1）形成荔枝机械化采摘-收集-除杂多机分布式任务调度与协同控制算法。 2）软件著作权1件，发表论文1篇。	论文，软件著作权，年度技术进展报告。
2028年 11月 01日	2029年 04月 30日	1）开展多机协同采收系统综合验证。 2）在基地生产应用，举办相关示范推广活动。	软件著作权1件。	软件著作权
2029年 05月 01日	2029年 10月 31日	1）环境适应性测试、动态避障试验等标准化流程。 2）整理项目成果资料，形成文档报告，准备项目验收。	完成项目的验收报告和项目成果资料的整理工作。	年度技术进展报告，验收报告。

五、知识产权对策、成果管理及合作权益分配

根据《中华人民共和国合同法》、《中华人民共和国专利法》、《中华人民共和国著作权法》等相关法律法规，以及科技部《关于加强与科技有关的知识产品保护和管理工作的若干意见》的规定，本项目各参与单位将遵循合作精神，针对项目申请和执行过程中涉及的知识产权、成果及合作权益分配，按照以下要求进行管理：

1.项目各方在申请项目之前所拥有的知识产权及相关权益归各自所有，不因共同申请项目而发生任何变更。

2.为项目申请所需，各方提供的未公开或已明确说明不得向第三方透露的与项目相关的技术资料、数据等信息，包括但不限于各自所有或合法持有的公式、流程、设计、产品、样品、发明、技术资料、版权、商标、研发计划等内容，未经提供方书面同意，禁止向第三方披露或使用。本条款在无论项目是否获得资助的情况下，均长期有效。

3.各方为项目申请提供的信息不应视为授予对方任何专利、著作权、商标等知识产权的许可。

4.在项目执行过程中，各方应及时对项目产生的科技成果采取以下知识产权保护措施：

对各方根据任务分工独立完成的科技成果及相应知识产权，归该方单独所有。

由多方共同完成的科技成果及其形成的知识产权则由各方共同所有。未经其他方同意，任何一方不得擅自向第三方转让共同科技成果的知识产权或技术资料。共同成果的精神权利，如身份权、荣誉称号、奖励证书及奖金等，由共同完成方共享。

5.对于共有科技成果，若实施许可或转让专利、非专利技术所产生的经济收益，将由各方共同分享。具体的收益分配方式应在相关行为实施前另行商定。

六、参与人员信息

课题负责人：							
姓名	性别	年龄	职务	职称	学位	在项目中承担的任务	所在单位
曹亚超	男		无	讲师	博士	荔枝机械化采收装备与多机协同作业技术研发	华南农业大学

主要研究开发人员：							
姓名	性别	年龄	职务	职称	学位	在项目中承担的任务	所在单位
施琳琳	女		院长助理	讲师	博士	分布式任务调度与协同控制算法设计	华南农业大学
黄成杰	男		无	副教授	博士	采收装备结构设计	华南农业大学
李钊	男		无	未取得	硕士	仿形围蔽装置结构设计	华南农业大学
李俞浩	男		无	未取得	硕士	机械化采收装备整机测试	华南农业大学
曾晔	男		无	未取得	硕士	多机作业路径规划算法设计	华南农业大学
罗明达	男		无	未取得	硕士	多机协同控制研究	华南农业大学
柯森蓝	男		无	未取得	学士	多机械臂路径规划研究	华南农业大学
刘盛龙	男		无	未取得	学士	多臂多机路径规划研究	华南农业大学
蔡佳敏	男		无	未取得	学士	多采收机器人路径规划与控制	华南农业大学
翁清林	男		无	未取得	学士	采摘部件空间位姿自适应仿形调控技术	华南农业大学
朱仲艺	男		无	未取得	学士	机械化采收装备试验验证	华南农业大学
韦标	男		无	未取得	学士	多机械化采收机器人协同控制研究	华南农业大学
黄明杰	男		无	未取得	学士	多采收机器人状态感知	华南农业大学
邓善鹏	男		无	未取得	学士	梳刷与围蔽收集装置协同作业	华南农业大学
麦煜炬	男		无	未取得	学士	自适应仿形调控技术	华南农业大学
王浩	男		无	未取得	学士	多机任务调度算法	华南农业大学
林晓婷	女		无	未取得	学士	轻量化采收装备	华南农业大学

詹茗杰	男		无	未取得	学士	整机可靠性及环境适应性测试	华南农业大学
钟柏洲	男		无	未取得	学士	整机可靠性及环境适应性测试	华南农业大学
马俊涛	男		无	未取得	学士	整机可靠性及环境适应性测试	华南农业大学

七、经费预算

课题承担单位基本情况表

<table>
<tr><td colspan="6">填表说明：1.组织机构代码指企事业单位国家标准代码，单位若已三证合一请填写单位社会信用代码无组织机构代码的单位填写“000000000”；
2.单位公章名称必须与单位名称一致。</td></tr>
<tr><td rowspan="9">课题承担单位</td><td>单位名称</td><td colspan="4">华南农业大学</td></tr>
<tr><td>组织机构代码</td><td colspan="4">10564</td></tr>
<tr><td>单位法定代表人姓名</td><td colspan="4">薛红卫</td></tr>
<tr><td rowspan="2">单位所属地区</td><td>省、直辖市、自治区等</td><td>地市（市、自治州、盟）</td><td colspan="2">县市（区、旗）</td></tr>
<tr><td>广东省</td><td>广州市</td><td colspan="2">天河区</td></tr>
<tr><td>电子邮箱</td><td colspan="4">[redacted]</td></tr>
<tr><td>通信地址</td><td colspan="4">广东省广州市天河区五山路483号</td></tr>
<tr><td>邮政编码</td><td colspan="4">510642</td></tr>
<tr><td>银行账号</td><td colspan="4">3602-0026-0900-0310-520</td></tr>
<tr><td>单位开户名称</td><td colspan="4">华南农业大学</td></tr>
<tr><td>开户银行（全称）</td><td colspan="4">中国工商银行广州五山支行</td></tr>
<tr><td rowspan="9">相关责任人</td><td rowspan="6">课题负责人</td><td>姓名</td><td colspan="3">曹亚超</td></tr>
<tr><td>身份证号码</td><td colspan="3">[redacted]</td></tr>
<tr><td>工作单位</td><td colspan="3">华南农业大学</td></tr>
<tr><td>电话号码</td><td>[redacted]</td><td>手机号码</td><td>[redacted]</td></tr>
<tr><td>电子邮箱</td><td>[redacted]n</td><td>邮政编码</td><td>[redacted]</td></tr>
<tr><td>通信地址</td><td colspan="3">广州市天河区五山路 483 号</td></tr>
<tr><td rowspan="3">财务部门负责人</td><td>姓名</td><td colspan="3">科研财务科</td></tr>
<tr><td>身份证号码</td><td colspan="3" rowspan="3">[redacted]</td></tr>
<tr><td>电话号码</td><td>手机号码</td><td>1[redacted]</td></tr>
<tr><td>电子邮箱</td><td></td></tr>
</table>

课题预算表

金额单位：万元

	项目总经费		省级财政科技资金	
支出经费	经费额	用途说明	经费额	用途说明
1、直接费用	82.00	用于项目设备费、业务费和直接人力资源成本支出	82.00	用于项目设备费、业务费和直接人力资源成本支出
（1）设备费	0.00	无设备费支出	0.00	无设备费支出
（2）业务费	68.86	用于材料、测试化验加工、燃料动力、出版文献/信息传播/知识产权事务、会议/差旅/国际合作与交流等支出	68.86	用于材料、测试化验加工、燃料动力、出版文献/信息传播/知识产权事务、会议/差旅/国际合作与交流等支出
（3）直接人力资源成本	13.14	用于参与项目的研究生及临聘科研辅助人员劳务费、专家咨询费、人员费以及项目聘用的研究人员劳务费等支出	13.14	用于参与项目的研究生及临聘科研辅助人员劳务费以及专家咨询费等支出
2、间接费用	18.00	用于绩效支出、管理费用和其他间接成本等费用支出	18.00	用于绩效支出、管理费用和其他间接成本等费用支出
（1）绩效支出	2.60	项目组绩效支出	2.60	项目组绩效支出
（2）管理费用	6.00	单位管理费用支出	6.00	单位管理费用支出
（3）其他间接费用	9.40	项目其他间接成本支出	9.40	项目其他间接成本支出
合计	100.00		100.00	

其他需说明的情况

1. 设备费、燃料动力费、人员费由自筹经费支出；

2. 专家咨询费由省级财政科技资金支出；

3. 材料费、测试化验加工费、出版文献/信息传播/知识产权事务费、会议/差旅/国际合作与交流费、劳务费由省级财政科技资金和自筹经费共同支出；

4. 省级财政科技资金中的间接经费按（直接费用-设备费）*20%预算，其中设备费为0.00万元。

自筹资金投入情况说明：

无。

八、签约各方

项目承担单位：　华南农业大学　　（盖章，单位法人章或单位法人授权章） 项目负责人：李君 签字：李君 2025 年 12 月 23 日
课题承担单位：　华南农业大学　　（盖章，单位法人章或单位法人授权章） 课题负责人：曹亚超 签字：曹亚超 2025 年 12 月 23 日

SCAULIB202625128

检索证明

根据委托人提供的论文材料，委托人华南农业大学工程学院 施琳琳(学科类型:自然科学) 4 篇论文收录情况如下表。

序号	论文名称	发表刊物及发表的年月卷期/页码等	作者排名	论文等级	作者文中单位	收录情况	影响因子	中科院大类分区
1	Simultaneous Task Execution and Formation Reconfiguration in Multirobot Systems	IEEE TRANSACTIONS ON INSTRUMENTATION AND MEASUREMENT 出版年：2025 卷期：74 页码：- 文献号：7505912 文献类型：Article	共同通信作者	A 类	华南农业大学工程学院	SCI	IF2-year=5.9 IF5-year=6.0 （2024）	工程技术 2 区 Top 期刊：否 OA 期刊：否 （2025）
2	YOLOv8s-Longan: a lightweight detection method for the longan fruit-picking UAV	FRONTIERS IN PLANT SCIENCE 出版年：2025 出版日期：JAN 22 卷期：15 页码：- 文献号：1518294 文献类型：Article	通信作者	A 类	华南农业大学工程学院	SCI	IF2-year=4.8 IF5-year=5.7 （2024）	生物学 2 区 Top 期刊：否 OA 期刊：是 标注：Mega-Journal （2025）
3	HPS-RRT*: An Improved Path Planning Algorithm for a Nonholonomic Orchard Robot in Unstructured Environments	AGRONOMY-BASEL 出版年：2025 出版日期：MAR 14 卷期：15 3 页码：-	通信作者	A 类	华南农业大学工程学院	SCI	IF2-year=3.4 IF5-year=3.8 （2024）	农林科学 2 区 Top 期刊：否 OA 期刊：是 标注：Mega-

		文献号：712 文献类型：Article						Journal （2025）
4	车载式无人机簇状水果采摘系统设计与试验	农机化研究 出版年：2026 出版日期：2025-10-15 15:25 卷期：48 05 页码：1-8 文献号： 文献类型：期刊论文	第一作者	C 类	华南农业大学工程学院	北大核心	无	无

说明：论文等级和中科院大类分区按《华南农业大学学术论文评价方案（试行）》划分。

报告免责声明:如未盖章,报告无效

检索员：刘汉忠

华南农业大学图书馆

2026-03-02

SCAULIB202626719

检索证明

根据委托人提供的论文材料，委托人华南农业大学工程学院 施琳琳(学科类型:自然科学) 1 篇论文收录情况如下表。

序号	论文名称	发表刊物及发表的年月卷期/页码等	作者排名	论文等级	作者文中单位	收录情况	影响因子	中科院大类分区
1	An autonomous obstacle avoidance and path planning method for fruit-picking UAV in orchard environments	Smart Agricultural Technology 出版年：2025 卷期： 页码：- 文献号： 文献类型：	通讯作者		华南农业大学工程学院	在线发表	IF2-year=5.7 IF5-year=5.7 （2024）	农林科学 2 区 Top 期刊：否 OA 期刊：是 （2025）

说明：论文等级和中科院大类分区按《华南农业大学学术论文评价方案（试行）》划分。

报告免责声明:如未盖章,报告无效

检索员：刘汉忠

华南农业大学图书馆

2026-03-27

农机化研究
Journal of Agricultural Mechanization Research

车载式无人机簇状水果采摘系统设计与试验

施琳琳[1]，巫凯旋[1]，周浩波[4]，麦煜炬[1]，林恒毅[1]，陈恒旭[1]，李　君[1,2,3]

(1. 华南农业大学 工程学院，广州　510642；2. 岭南现代农业科学与技术广东省实验室，广州　510642；
3. 农业装备技术全国重点实验室，北京　100083；4. 深圳市蓝禾技术有限公司，广东 深圳　518000)

摘　要： 由于现有以机械臂为代表的采摘机器人不适用于高大树冠或山地果园中荔枝、龙眼等簇状水果的采摘任务，引入以无人机为移动载体的空中采摘机器人，结合龙眼的生长特性和种植模式，提出了基于无人机的簇状水果采摘策略，设计了车载式无人机水果采摘系统。通过对无人机动力元件的计算和结构布局设计，减少了无人机重心偏移和低空飞行时下旋风产生扰流对采摘无人机飞行稳定的影响；同时根据实际作业需求，对运载无人车的结构设计进行优化；并结合基于YOLOv8s算法进行的目标识别、融合激光雷达与IMU数据进行的建图定位，以及基于改进A*算法进行的路径规划，使用PID控制器进行飞行控制等模块的协同，实现了该采摘系统的自动化作业。田间试验结果表明：该采摘系统在果园沙质土壤地表作业通过性好，最高作业半径可达3.2 m；在特定条件下平均往返采摘一串龙眼串果时长为66.78 s、平均采摘成功率为64%，验证了车载式无人机水果采摘系统自主作业的可行性，为空中采摘机器人的设计与应用提供了参考。

关键词： 丘陵果园；簇状水果；采摘执行器；无人车；自主作业

中图分类号： S225；S252　　**文献标志码：** A　　**文章编号：** 1003-188X(0000)00-0000-00

施琳琳，巫凯旋，周浩波，等. 车载式无人机簇状水果采摘系统设计与试验[J]. 农机化研究

SHI Linlin, WU Kaixuan, ZHOU Haobo, et al. Design and experiment of vehicle-mounted UAV cluster fruit harvesting system [J]. Journal of agricultural mechanization research

0　引　言

荔枝、龙眼等簇状水果是中国南部丘陵地区重要的经济作物，其采摘方式主要依赖于人工采摘和地面收获设备，随着人工成本的不断增加和劳动力短缺问题日益严重，迫切需要开发高效的自动化采摘机器人[1-2]。国内外研究者已经设计出多种类型的采摘机器人[3]，如中国农业大学开发的履带式黄瓜采摘机器人[4]、国家农业智能装备工程技术研究中心研制的轮式草莓采摘机器人[5]、松下公司开发的轨道式番茄采摘机器人[6]。当前的地面移动采摘机器人大多针对大棚果蔬和低矮果树，不适用于高大果树或丘陵山地果园的采摘任务。

近几年，无人机因其不受种植地形和作业对象等条件限制的优势，在植保施药、植物保护和作物监测等农业生产领域得到了广泛应用[7]。针对地面机器难以实现高大果树采摘的难题，利用无人机的高空作业优势，将其作为移动载体的空中采摘机器人成为一种可行的解决方案。昆明理工大学设计了一种用于采摘坚果的小型无人机、山东理工大学提出了一种山核桃采收一体无人机的设计、中航贵州飞机公司采用气吸式采摘无人机对蜂糖李进行采摘，但依赖搭载电源设备的采摘无人机无法满足长续航需求，限制了其在农业采摘中的应用。而且，国内外所设计的采摘无人机均采用气吸式末端执行器作为采摘机构完成对单目标水果的采摘，针对簇状水果采摘无人机的设计开发尚未实现。

为解决以机械臂为代表的地面移动采摘机器人难以对高大果树进行全树冠采摘的难题，采用长续航无人车作为采摘无人机的能量源，设计了一种车载式无人机水果采摘系统，实现对以龙眼为代表的簇状水果的采摘，以期为多无人机协同采摘作业的开发提供参考。

1　总体结构与工作原理

1.1　总体结构

车载式无人机水果采摘系统由采摘无人机和运载无人车组成，整体结构如图1所示。履带式运载无

收稿日期： 2025-02-14

基金项目： 国家自然科学基金项目(52375094,62303188)；岭南现代农业科学与技术广东省实验室科研项目(NT2021009)；国家荔枝龙眼产业技术体系项目(CARS-32)；“十四五”广东省农业科技创新十大主攻方向“揭榜挂帅”项目(2022SDZG03)；华南农业大学高校学科建设项目(2023B10564002)

作者简介： 施琳琳(
scau.edu

通信作者： 李　君(
scau.edu

人车为采摘无人机提供起降平台和电源,采摘无人机通过搭载的采摘执行器实现对龙眼等簇状水果的剪夹式采摘。系统通过有线通讯模块实现数据和控制命令的实时传输,以确保采摘无人机和运载无人车间的协同作业。

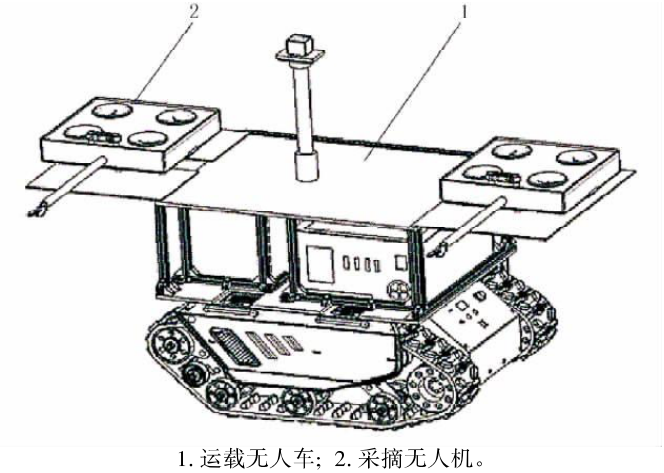

1. 运载无人车; 2. 采摘无人机。

图 1 车载式无人机水果采摘系统结构图

Fig. 1 Structure diagram of the vehicle-mounted unmanned aerial vehicle (UAV) fruit harvesting system

1.2 工作原理

作业时,履带式运载无人车通过搭载的激光雷达对果园环境信息建图,利用路径规划模块生成运动路线,引导其行走至目标果树下;接收上位机指令后,采摘无人机开始驻点采摘作业,从运载无人车的升降平台起飞,并结合目标识别定位算法对簇状果实进行识别和定位[8-9];通过路径规划算法生成航点,引导无人机靠近预定的目标簇果[10]。

当采摘无人机与目标簇果的距离小于预设的阈值 0.5 m 时,目标识别算法自动切换为对果实母枝的识别和定位,引导无人机飞至簇果结果母枝的正前方[11]。一旦采摘无人机到达预定位置,采摘执行机构将执行剪切动作,如图 2 所示。在结果母枝最上方的分枝节点(距离 2~5 cm)处,无人机剪断果枝并稳固夹持果枝后返航至果筐正上方,将采摘的果实放入果筐中,继续执行下一次采摘任务[12-13]。

(a) 单个串果 (b) 多个串果

图 2 结果母枝剪切部位

Fig. 2 The cutting point for clustered fruits

1.3 技术参数

整机技术参数如表 1 所示。

表 1 整机技术参数

Table 1 Machine technical parameters

参数	单位	数值
作业范围(半径)	mm	2 200
外形尺寸(长×宽×高)	mm	2 500×1 400×1 400
最大爬坡角度	(°)	26
无人车最大载荷	kg	45
最大摘果质量	kg	0.6
续航时间	min	18
作业高度	m	3.2

2 关键部件设计

2.1 采摘无人机

采摘无人机由多旋翼无人机、采摘执行器和感知定位等传感器所组成,如图 3 所示,用于实现对目标簇果的识别定位和采摘。

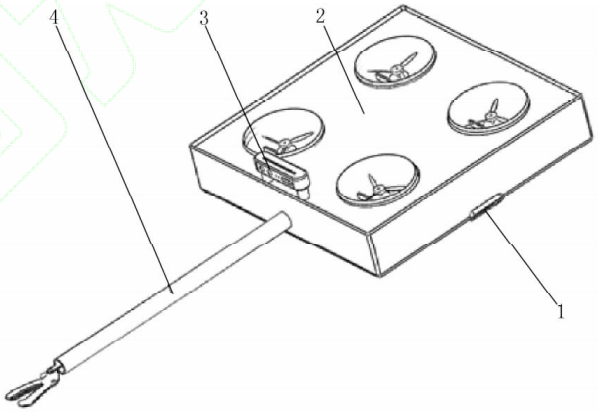

1. T265 相机; 2. 无人机; 3. RGB-D 相机; 4. 采摘执行器。

图 3 水果采摘无人机结构

Fig 3 Fruit harvesting UAV structure

2.1.1 多旋翼无人机结构

多旋翼无人机平台是采摘无人机的核心组成部分,包括机身、动力系统和控制系统[14]。

2.1.1.1 无人机的整体布局和结构

通过合理布局结构确保无人机重心位于中心位置,可以提高采摘无人机的飞行稳定性[15]。无人机的布局设计包括机体尺寸、重心位置、飞行控制器和其他传感器的安装位置,这些因素直接影响其飞行性能和稳定性。多旋翼无人机通常采用四旋翼和六旋翼布局,如图 4 所示。由图 4 可知,无人机的机体半径 R 与旋翼最大半径 r_{max} 关系为

$$R = \left(1 + \frac{1}{\sin(\theta/2)}\right) r_{max} \tag{1}$$

式中: θ 为相邻两旋翼轴间夹角的数值,单位(°)。

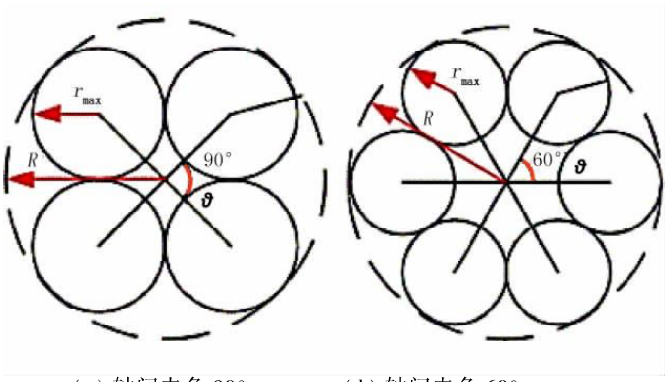

(a) 轴间夹角 90°　　(b) 轴间夹角 60°

图 4　多旋翼无人机整体布局

Fig. 4　Overall layout of multirotor UAV

根据研究数据表明,当两旋翼之间的距离从 0. 1 倍旋翼半径 r_p 变化到 1 倍旋翼半径 r_p 时,气流对飞行器的整体性能影响很小。因此,为了使飞行器布局紧凑,可令

$$r_{max} = 1.05r_p \sim 1.2r_p \quad (2)$$

对无人机进行布局计算,进一步确定旋翼之间的间距值[18],再通过计算模拟和实验验证来确定最佳重心位置,以提高无人机在前进飞行和受风干扰情况下的稳定飞行能力。

无人机在前进飞行的情况下受力如图 5(a) 所示。将重心设置在桨盘平面以下,由叶片柔性引起的诱导流阻力会产生一种力矩,这种力矩倾向于使多旋翼无人机的俯仰角度趋近于 0°,可提高其前进飞行的稳定性。风干扰情形的受力如图 5(b) 所示。当重心位于桨盘平面下方时,阵风引起的阻力可能造成不稳定力矩,使无人机俯仰角向不稳定方向倾斜,增加了翻转的可能性,而将重心置于桨盘平面以上,则可以有效抵抗风干扰引起的不稳定力矩。

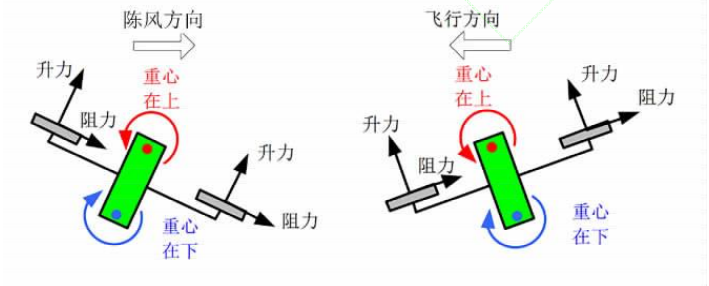

(a) 飞行器前飞情形　　(b) 风干扰情形

图 5　多旋翼无人机受力简化图

Fig. 5　Force diagram of multirotor UAV

将旋翼叶片直径为 177. 8 mm 代入式(1) 和式(2) ,计算可得无人机的机体半径 R 为 257. 5 mm,且在每个叶片外围安装有涵道,其直径为 210 mm。故该无人机整体尺寸为 515 mm×515 mm,对角桨心间距为 364 mm,且采摘执行器长度为 500 mm,质量为 291. 2 g,从无人机底部重心向前延伸; Allspark 处理器质量为 213 g,位于无人机后端顶部。上述无人机整体布局紧凑,可以忽略气流对飞行器的整体性能影响。

将无人机平衡并静止放在水平支架上,通过悬挂法多次测量与计算,确定无人机重心位于距离水平面中心前方 20 mm、垂直面中心下方 40 mm 的位置。

2.1.1.2　减振结构设计

无人机的位置和姿态主要依靠飞控加速度传感器来实现,而加速度传感器的精度受无人机机身振动影响,其中机架变形、电机和桨叶不对称等因素是机身振动的主要来源。

为减少无人机桨叶在高速旋转过程中对无人机机身造成的振动,选用 HQ7040 的 7 英寸三叶桨匹配尺寸为 515 mm×515 mm、对角桨心间距为 364 mm 的机架和 4 kg 机体,并确保 HQ7040 三叶桨在顺逆时针旋转时具有相同的韧性; 同时,通过采用碳纤维等刚性材料提高机架的抗扭特性和抗弯特性,减少机架变形产生的异步振动; 优化 T-Motor 的 F90 电机控制器参数保证电机平滑稳定运行,平衡电机和桨叶的安装减少偏心力的产生; 在飞控、电机等关键处安装泡沫胶等减振材料,以此降低机身振动对加速度传感器的影响,从而提高无人机飞行稳定性。

2.1.1.3　动力元件计算与分析

在近地飞行时,无人机产生的下洗气流对其飞行稳定性有较大影响。基于飞行器设计理论,优化计算动力元件,可以减少采摘无人机下洗气流的强度并提高近地飞行时稳定性[16]。

采摘无人机的总质量(包括采摘机构和最大挂果质量) 为 4 kg。在四轴飞行中,电机产生的升力 T 需要分配到上升下降、前后俯仰、左右横滚和抗风机动等多个方面。通常情况下,无人机的起飞质量不应超过整体升力 T 的 40%,超过 40%则可能导致续航性能急剧下降,超过 60%则可能导致电机震动加剧,影响无人机的飞行稳定性。升力是通过转子带动旋翼旋转产生[17],本文选取无人机的整体升力 T 为 100 N,并且用 40%升力以确保无人机的稳定上升下降,保留 60% 的升力来做俯仰、横滚和抗风运动。

在计算无人机动力元件参数时,需要通过整体升力 T 逆模型求解出转速 N,再通过转速 N 选取电机和旋翼型号。计算公式为

$$T = C_T \times \rho \times \left(\frac{N}{60}\right)^2 \times D^4 \quad (3)$$

式中: C_T 为旋翼拉力系数的数值,单位 N/(rad/s) ^{2},取 C_T = 5. 128e-6 N/(rad/s) ^{2}; ρ 为空气密度的数值,单位 kg/m^3,取 ρ = 1. 29 kg/m^3; N 为转速的数值,单位 r/s; D 为旋翼叶片直径的数值,单位

mm，取 D = 177.8 mm。

由式(1)计算可得转数 N 需满足 328 r/s，最终选取 T-Motor 的 F90 电机，该电机 KV 值为 1300 RPM/V，并搭配 HQ7040 的 7 英寸三叶桨。该电机与旋翼组合的最大升力可达 23.13 N，4 个电机总升力为 92.54 N，起飞质量占整体总升力 T 的 42%。F90 电机搭配 7 英寸三叶桨，满油门状态下的电流为 45.1 A，再增加 20%的电流阈值，最终选择 T-Motor 的 F45 电调，该电调峰值电流为 55 A。以上选型满足无人机基本动力需求，并保持了适当的续航能力。

能源效率 η 定义为旋翼输出功率与电池输出功率的比值，其在满油门状态下测定，是衡量能量利用效率的关键指标，其计算公式为

$$\eta = \frac{P_{\text{out}}}{P_{\text{in}}} = \frac{\pi n_r N M}{30 U_b I_b} \tag{4}$$

$$I_b = P / U_b \tag{5}$$

式中：P_{out} 为电机输出功率的数值，单位 W；P_{in} 为电池输出功率的数值，单位 W；U_b 为电池电压的数值，单位 V；I_b 为电池电流的数值，单位 A；P 为电机功率的数值，单位 W；n_r 为电调的数值，单位个；M 为旋翼转矩的数值，单位 N·m；

通过计算与实验测量，可得采摘无人机在满油门状态下的最大飞行时间为 3 min，总升力 T 为 87 N，电调电流 A 为 33.6 A，电机的输出功率 P_{out} 为 479.6 W，能源效率 η 为 58.9%。高能源效率意味着旋翼能更高效地转换能量，从而减少能量损失，对提高飞行器的续航时间至关重要。

2.1.2 采摘执行器

采摘执行器作为水果采摘无人机完成采摘任务的核心部件[19-20]，轻量化设计有助于降低无人机的整体质量并防止无人机产生的下洗流场影响飞行稳定性。采摘执行器主要包括一体化剪夹机构、连接杆、电源、底座和丝杆电机等组件，工作原理主要通过上位机驱动步进丝杆电机实现连接杆的伸缩，进而带动剪夹机构的伸开与闭合，从而实现对以龙眼为代表的簇状串果的剪夹。

采摘执行器的设计主要基于能否对龙眼结果母枝进行有效剪切，以及如何降低其对无人机重心不平衡的影响。

1) 龙眼果梗的剪切力计算。龙眼结果母枝截面近似圆形，则其剪刀强度计算公式[21]为

$$\tau = \frac{F_{\max}}{S/\sin\theta_1} = \frac{4F_{\max}\sin\theta_1}{\pi D_1^2} \tag{6}$$

式中：τ 为试样剪切强度的数值，单位 MPa；$F_{\max}$ 为峰值切割力的数值，单位 N；S 为截面面积的数值，单位 mm^2；θ_1 为切割角度的数值，单位(°)；D_1 为结果母枝直径的数值，单位 mm。

采摘执行器的切割速度与龙眼结果母枝的峰值切割力和剪切强度呈非线性关系，切割速度增加，峰值切割力和剪切强度减小；但随着切割速度不断增加，峰值切割力和剪切强度下降的趋势减弱。

通过查阅文献和试验采样可知，龙眼结果母枝直径为 10 ~20 mm [22]，所需的最大切割力约为 2.67 kN。本文通过增加步进丝杆电机的转速和推力来提高采摘执行器的切割速度和剪切力，以保证其对龙眼结果母枝的有效剪切。采摘执行器结构图如图 6 所示，剪刀开口度为 8.5 cm，剪切速度约为 500 mm/min，最大剪切力约为 3.12 kN。

1. 剪夹机构；2. 电源；3. 底座；4. 丝杆电机；5. 连接杆。

图 6 采摘执行器

Fig. 6 Harvesting actuator

2) 采摘无人机重心平衡计算。对采摘无人机摘果前后的两种受力状态进行受力分析，如图 7 所示。图中，O 点、E 点为无人机前后端点，A 点为配重块重心位置，B 点和 D 点为前后旋翼位置，C 点为无人机重心位置，H 点为剪夹结构重心位置，F 点为采摘连接杆重心位置，L_1(mm)为无人机后端到配重块的距离。L_2(mm)为配重块到后旋翼的距离，L_3(mm)为前后旋翼之间的距离，L_4(mm)为剪夹结构重心位置到无人机前端的距离，L_5(mm)为前旋翼到无人机前端的距离，G_1(N)为无人机所受的重力，G_2(N)为连接杆所受的重力，G_3(N)为剪夹机构所受的重力，G_4(N)为龙眼串果所受的重力，F_1(N)为平衡块所受的重力；F_2(N)、F_3(N)为无人机前后两端无人机的升力。通过调节采摘执行器的平衡块质量大小，以保持采摘无人机重心在中心位置 O，提高其飞行稳定性。

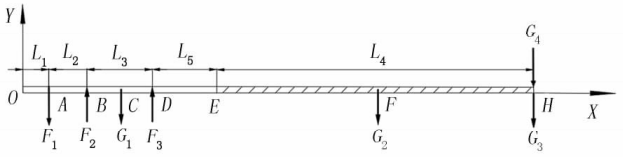

图 7 水果采摘无人机的受力分析图

Fig. 7 Force analysis diagram of fruit harvesting UAV

根据理论力学可以列出采摘无人机在摘果前的力系平衡方程为

$$\sum M_o = 0$$

$$F_2(L_1+L_2)+F_3(L_1+L_2+L_3)-F_1L_1-G_1\left(L_1+L_2+\frac{L_3}{2}\right)-G_2\left(L_1+L_2+L_3+\frac{L_4}{2}+L_5\right)-G_3(L_1+L_2+L_3+L_4+L_5)=0 \quad (7)$$

$$\sum M_H=0$$

$$-F_1(L_1+2L_2+L_3+L_4)-G_1\left(L_1+L_2+\frac{L_3}{2}+L_4\right)-\frac{G_2L_4}{2}+F_2(L_1+L_2+L_3+L_4)+F_3(L_1+L_2+L_4)=0 \quad (8)$$

$$\sum F_Y=0$$

$$F_1+G_1+G_2+G_3-F_2-F_3=0 \quad (9)$$

摘果后的力系平衡方程为

$$\sum M=0$$

$$F_2(L_1+L_2)+F_3(L_1+L_2+L_3)-F_1L_1-G_1\left(L_1+L_2+\frac{L_3}{2}\right)-G_2(2L_1+2L_2+L_3)-(G_3+G_4)(2L_1+2L_2+L_3+L_4)=0 \quad (10)$$

$$\sum M_H=0$$

$$-F_1(L_1+2L_2+L_3+L_4)-G_1\left(L_1+L_2+\frac{L_3}{2}+L_4\right)-\frac{G_2L_4}{2}+F_2(L_1+L_2+L_3+L_4)+F_3(L_1+L_2+L_4)=0 \quad (11)$$

$$\sum F_Y=0$$

$$F_1+G_1+G_2+G_3+G_4-F_2-F_3=0 \quad (12)$$

根据实验测得无人机所受重力 $G_1=32$ N、连杆所受重力 $G_2=3$ N、剪夹机构所受重力 $G_3=5$ N、预估最大挂果重力 $G_4=6$ N，结合无人机各结构尺寸，计算可得采摘无人机在水平轴方向的各端点距离 $L_1=24$ mm、$L_2=74$ mm、$L_3=257.5$ mm、$L_4=500$ mm，$L_5=159.5$ mm，求出采摘无人机在摘果前需在 A 点施加的平衡块重力 $F_1=3$ N，以及在摘果后无人机前后两端所需升力 $F_2=4.08$ N、$F_3=44.92$ N。

2.2 运载无人车

运载无人车由履带底盘和底盘舱组成。履带底盘作为行走装置，为运载无人车提供移动支持[23]；底盘舱集成了中央处理器模块和电源模块，用于控制运载无人车的运行并为其供电，从而延长采摘无人机作业时长。此外，底盘舱上方装有无人机的起降平台，为无人机提供稳定的起降环境；车顶安装的激光雷达作为环境感知模块，能够收集采摘无人机周围的环境信息，为无人机路径规划提供必要的障碍物信息。

2.2.1 底盘选型和底盘舱设计

鉴于龙眼果园大多分布于丘陵地区，运载无人车的设计必须考虑其在复杂地形中的稳定运行能力。履带底盘的选型主要从底盘的爬坡能力、载重量和控制稳定性等方面考虑[24]。本文选择松灵 BUNKER 车型作为运载无人车的履带底盘，如图 8 所示。其最大爬坡角度 30°、最大行驶速度 1.5 m/s、最大负载能力为 80 kg，能满足运载无人车在复杂丘陵地带的动力性能和负载需求。

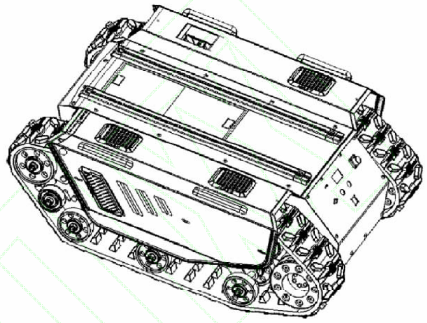

图 8 履带式底盘

Fig. 8 Tracked chassis

底盘舱的设计需要满足紧固和减振要求，设计的底盘舱整体尺寸为 2 500 mm×1 400 mm×1 400 mm，如图 9 所示。底部纵梁与履带底盘刚性连接，使用铝合金板加强了底部的支撑强度，其内部设备模块均通过固定结构与底盘舱连接，并通过海绵垫固定和隔离电源、中央处理器等模块，保护设备在运行中免受冲击和振动。通过选取具备防滑特性的复合材料，以提高降落平台的强度和防滑特性，确保无人机在降落时的安全与准确性。

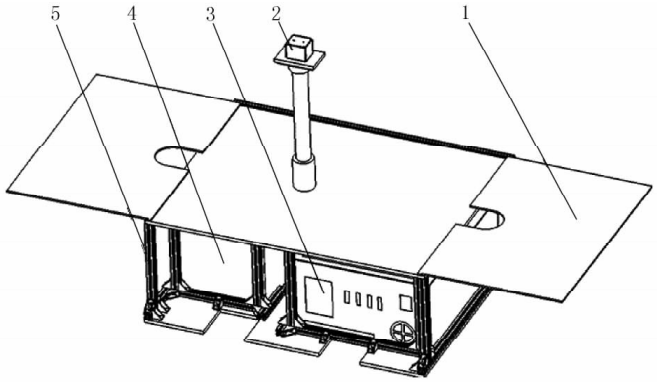

1. 升降平台; 2. 激光雷达; 3. 工控机;
4. 电源; 5. 底盘舱支架。

图 9 底盘舱

Fig. 9 Chassis compartment

2.2.2 动力设计

设计车载式无人机水果采摘系统时，首先对各个模块的耗电功率进行了详细测量和分析。由测量与计算可得 Intel RealSense 系列 RGB-D 相机平均耗电为 5 W，C-RTK 9P 的 RTK 接收器功率消耗为 1~2 W，Livox 激光雷达功率消耗通常为 15 W。采摘执行

器在空载时只需少量功率,而在高负载或频繁摘果运动时需要约 120 W,加上一台搭载 NVIDIA GeForce RTX 3090 显卡的电脑主机,其在负载较高时的总耗电量约为 600 W。基于以上,选择了输出规格为 220 W、50 Hz,最大持续输出电流为 8.18 A,持续输出功率为 1 800 W,峰值功率可达到 3 600 W 的便携式移动电源单元,以满足系统的运行需求。

2.3 软件系统

软件系统主要包括数据处理和决策模块、目标识别模块、定位导航模块、飞行控制模块、路径规划模块和采摘执行模块等,各个模块通讯传输方式如图 10 所示。

各个模块的具体功能:决策模块通过整体的任务调度和资源分配以确保各模块协同工作;目标识别模块通过 YOLOv8s 目标检测算法来识别和定位龙眼串果,以帮助无人机在较远距离准确找到目标果串,实现果实位置的精确识别[9, 25],并将定位数据反馈至决策模块,以指导后续采摘行动;融合激光雷达与 IMU 数据的定位导航模块通过激光雷生成有效的果园环境信息地图[26],以解决采摘无人机在果园环境下的定位问题,并生成有效的果园环境信息地图[27],为导航任务提供支持;基于改进 A* 算法的路径规划模块在规划最优采摘航线的同时考虑了动态避障策略,以增强无人机的行动自主性[28];使用 PID 控制器的飞行控制模块执行精确的姿态调整和路径跟踪,以保障飞行过程的稳定性[29],当无人机靠近目标串果(距离小于 0.7 m,即采摘杆的长度)时,将目标识别模块切换到关键点检测算法,以在近距离内精确定位采摘点;采摘执行模块完成具体的果实采摘任务,包括执行器的采摘动作[30]。

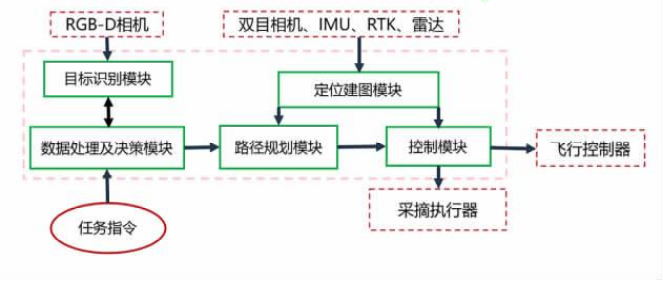

图 10 软件系统设计方案

Fig. 10 Software system design scheme

3 田间试验

3.1 基本性能试验

为检验运载无人车的动力性能,于 2024 年 3 月 1 日—3 日在广东省农业科学院果树研究所龙眼果园进行试验。通过在不同坡度的沙质土壤地表开展爬坡试验,测试运载无人车在不同载重下的最大爬坡角度,结果如表 2 所示。由表 2 可知,运载无人机的最大爬坡角度与其载重成反比,为保证其在沙质土壤地表具有良好的通过性,将其最大负载定为 45 kg。

表 2 运载无人车动力性能试验

Table 2 The power performance test of the unmanned cargo vehicle

序号	无人车载重质量/kg	最大爬坡角度/(°)
1	0	26
2	15	24
3	30	21
4	45	17
5	60	11

在稳定电压 24 V、最大电流 47 A、电机 1300 RPM/V、HQ7040 三叶桨、整体重量 4.5 kg 的试验条件下,测试采摘无人机整体性能,试验结果如下:

1) 悬停性能。油门百分比约为 46.6%,悬停时间约为 15.91 min,电调电流约为 6.29 A,电机转速约为 11639.7 r/min,电机输出功率约为 101.6 W,能量效率约为 65.4 %

2) 最大油门性能。飞行时间约为 3 min,电机转速为 19648.8 r/min,电机输出功率为 488.8 W,无人机总升力为 65 N,剩余载重为 2.43 kg,采摘执行器末端最大挂果质量为 0.1 kg,总体能源效率为 58.9%。

3) 整体性能。采摘无人机正常作业情况下,持续执行采摘作业的时间约为 11.9 min,最大倾斜角度为 64.3°,最大平飞速度为 29.3 m/s,抗风等级为 8 级,基本满足采摘无人机实际作业需求。

3.2 采摘作业试验

为进一步验证车载式无人机水果采摘系统自主作业的可行性,于 2024 年 3 月 6 日—15 日在华南农业大学农业工程楼附近开展田间试验。通过在龙眼仿真树上挂果模拟果园采摘环境,以减少其他因素对试验结果的影响。

作业前,采摘无人机起飞位置和采摘位置保持不变,起飞高度设定为 1.2 m,最大飞行速度为 1 m/s。龙眼仿真树距起飞点的水平距离为 1.6 m,假果挂放高度为 1.5 m。采摘试验分为 5 组,每组进行 10 次测试。当采摘执行器的剪夹机构对准龙眼假果时,判断为采摘成功,并记录采摘时长;若采摘时长超出 3 min,判断为采摘失败,不记录采摘时长。记录每组试验采摘成功次数和无人机从起飞到摘果瞬间的平均采摘时长。

试验结果如表 3 所示,可得采摘无人机的平均采摘成功率为 64%,平均采摘时长为 66.78 s。通过分

析可知,采摘成功率还与试验当天光照强度和户外风力大小有关,其光照强度影响采摘无人机的识别精度,户外风力过大会影响采摘无人机飞行稳定性。

表 3　采摘试验结果

Table 3　The picking test results

序号	天气	风速	采摘成功次数	平均采摘时长/s	采摘成功率/%
1	晴	1-3 级	6	67.2	60.0
2	晴	1-2 级	8	62.4	80.0
3	多云	1-3 级	5	70.2	50.0
4	多云	1-3 级	6	68.9	60.0
5	多云	1-3 级	7	65.2	70.0

4　结　论

1) 设计了一种适用于高空采摘任务的车载式无人机结构。通过对无人机动力元件进行计算和结构布局设计,减少了无人机重心偏移和低空飞行时下旋风产生扰流对采摘无人机飞行稳定性的影响,从而提高其在果园作业的稳定性,并采取运载无人车供电的措施,以解决无人机续航时间短的问题。

2) 制定了适用于簇状水果采摘的车载式无人机软件系统,该系统包括目标识别模块、定位导航模块和路径规划模块。通过各个模块的相互配合,实现了采摘无人机的自主采摘作业。

3) 基本性能试验结果表明,运载无人车在果园沙质土壤的地表通过性良好,采摘无人机的负载能力满足实际作业需求。采摘试验结果表明,在特定场景下,车载式水果采摘系统的平均采摘成功率为 64%,平均采摘时长为 66.78 s,验证了该系统自主采摘作业的可行性。通过分析可知,采摘成功率受自然光照和自然风场的影响,因此,后续车载式无人机水果采摘系统将针对不同环境下的采摘作业进行进一步改进和优化,继续提高采摘效率和采摘成功率。

参考文献:

[1] WANGZ H, XUN Y, WANG Y K ,et al. Review of smart robots for fruit and vegetable picking in agriculture [J]. International journal of agricultural and biological engineering, 2022, 15(1): 33-54.

[2] ZHOU H Y, WANG X, AU W, et al. Intelligent robots for fruit harvesting: recent developments and future challenges [J]. Precision agriculture, 2022, 23(5): 1856-1907.

[3] 韦慧玲,梁成斌,王金海,等.绳驱柔性机械手研究进展及其在农业机器人中的应用[J]. 智能化农业装备学报(中英文), 2024,5(4): 95-106.

[4] 纪超, 冯青春, 袁挺, 等. 温室黄瓜采摘机器人系统研制及性能分析[J]. 机器人, 2011, 33(6): 726-730.

[5] 刘继展, 吴硕. 草莓全程生产机械化技术与装备研究进展[J]. 农业机械学报, 2021, 52(5): 1-16.

[6] 郑刚, 刘佳, 李旭. 现代温室采摘机器人发展概况[J]. 农业工程技术, 2019, 39(31): 35-40.

[7] 曹英丽,张弘泽,郭福旭,等. 基于无人机遥感的农作物病害监测研究进展[J]. 沈阳农业大学学报, 2024, 55(5): 616-628.

[8] 郭文韬. 基于机器视觉的龙眼花果信息检测关键技术研究[D]. 广州: 华南农业大学, 2020.

[9] 郑思思, 王小花. 基于图像处理的视觉采摘机器人作业控制研究[J]. 农机化研究, 2024, 46(10): 21-26.

[10] 吴妮妮. 智能采摘机器人路径规划的设计与研究[J]. 农机化研究, 2024, 46(2): 65-69.

[11] 张超. 基于视觉引导的工业机器人应用研究[D]. 西安: 陕西科技大学, 2017.

[12] 罗昌志, 邸志峰, 向阳, 等. 基于机器视觉的蒜种识别夹取试验台设计与试验[J]. 农机化研究, 2024, 46(9): 72-81.

[13] 刘力维. 采摘机器人机械臂运动控制与目标抓取研究: 基于嵌入式和机器视觉技术[J]. 农机化研究, 2024, 46(4): 68-72.

[14] 王伟, 马浩, 徐金琦, 等. 多旋翼无人机标准化机体设计方法研究[J]. 机械设计与制造, 2014(5): 147-150.

[15] 王波, 侯中喜, 汪文凯. 小型电动垂直起降飞行器推进系统性能分析[J]. 国防科技大学学报, 2015, 37(3): 84-90.

[16] 雷瑶. Hex-rotor 无人机多旋翼流场数值模拟与试验研究[D]. 长春: 中国科学院大学(中国科学院长春光学精密机械与物理研究所), 2013.

[17] 喻辉. 重载四旋翼民用无人机设计与强度计算[D]. 成都: 中国民用航空飞行学院, 2017.

[18] 张超. 基于变桨距控制的四旋翼飞行器建模与设计[D]. 北京: 北京理工大学, 2016.

[19] 郭亚静. 农业无人机智能机器学习系统: 基于人工智能和深度学习[J]. 农机化研究, 2023, 45(3): 237-240,259.

[20] 谢嘉, 吴家桢, 李永国, 等. 采摘无人机研究综述[J]. 制造业自动化, 2022, 44(10): 72-75.

[21] 吴良军, 杨洲, 洪添胜, 等. 荔枝树枝力学特性的试验研究[J]. 农业工程学报, 2012, 28(16): 68-73.

[22] 吴良军, 杨洲, 段洁利, 等. 龙眼树枝修剪机具刀片切割力的影响因素试验[J]. 农业工程学报, 2012, 28(24): 8-14.

[23] 郑永军, 江世界, 陈炳太, 等. 丘陵山区果园机械化技术与装备研究进展[J]. 农业机械学报, 2020,51(11): 1-20.

[24] 赵立军, 李金广, 杨斌, 等. 山地电动履带底盘设计与仿真分析[J]. 拖拉机与农用运输车, 2024, 51(1):

30-37.
[25] 戚玲珑, 高建瓴. 基于改进 YOLOv7 的小目标检测[J]. 计算机工程, 2023, 49(1): 41-48.
[26] 廖龙祥, 陈学海, 杨光友. 基于 GNSS-RTK 水田平地机的设计与试验[J]. 农机化研究, 2024, 46(7): 131-135, 140.
[27] SHALAL N, LOW T, MCCARTHY C, et al. Orchard mapping and mobile robot localisation using on-board camera and laser scanner data fusion - Part B: Mapping and localisation[J]. Computers and electronics in agriculture, 2015, 119: 267-278.
[28] ZHUANG M, LI G, DING K X. Obstacle avoidance path planning for apple picking robotic arm incorporating artificial potential field and a algorithm[J]. IEEE access, 2023, 11: 100070-100082.
[29] 赵航. 基于 pixhawk 的多旋翼无人机避障飞行系统研发[D]. 北京: 北方工业大学, 2017.
[30] 吕辉, 李立君, 赵青, 等. 剪切式油茶花采摘末端执行器设计与实验[J]. 农机化研究, 2024, 46(4): 134-139, 14.

Design and Experiment of Vehicle-mounted UAV Cluster Fruit Harvesting System

Shi Linlin[1], Wu Kaixuan[1], Zhou Haobo[4], Mai Yuju[1], Lin Hengyi[1], Chen Hengxu[1], Li Jun[1,2,3]

(1. The College of Engineering, South China Agricultural University, Guangzhou 510642, China; 2. Guangdong Laboratory for Lingnan Modern Agriculture, Guangzhou 510642, China; 3. State Key Laboratory of Agricultural Equipment Technology, Beijing 100083, China; 4. Shenzhen Lanhe Technology Co., Ltd., Shenzhen 518000, China)

Abstract: Due to the existing picking robots represented by robotic arms are not suitable for picking tasks in tall tree canopies or cluster fruits such as litchi and longan of mountain orchards. Introduced an aerial picking robot with UAV as a mobile carrier, combined the growth characteristics and planting mode of longan, proposed a cluster-based fruit picking strategy based on UAV, and designed a truck-mounted UAV fruit picking system. Through the calculation of UAV power components and the structural layout design, the influence of gravity shift of UAV and turbulence generated by cyclone during low-altitude flight on the stable flight of UAV was reduced. At the same time, according to the actual operation requirements, the structure design of carrying unmanned vehicles was optimized. Combined with target recognition based on YOLOv8s algorithm, mapping positioning based on LiDAR and IMU data fusion, path planning based on improved A* algorithm, PID controller for flight control and other modules cooperation, the automatic operation of the picking system was realized. The field experiment results showed that the system had good operation performance on the sandy surface of the orchard, and the maximum operation radius could reach 3.2 m. Under certain conditions, the average round-trip picking time of a bunch of longan fruit was 66.78 s, and the successful picking rate was 64%, which verified the feasibility of autonomous operation of truck-mounted UAV fruit picking system, and provided guidance for the design and application of aerial picking robot.

Key words: hilly orchard; cluster fruit; harvesting actuator; unmanned vehicle; autonomous operation

Simultaneous Task Execution and Formation Reconfiguration in Multirobot Systems

Xuanchun Yin, *Member, IEEE*, Huabin Hu, and Linlin Shi

***Abstract*— To combine the advantages of multirobot task allocation (MRTA) in *teams* and *formations*, we propose a novel dual task allocation approach for multirobot formations. This work ensures that the task execution of a single robot and the formation reconfiguration of multiple robots are carried out simultaneously. Considering these two scenarios, the Auction and Kuhn–Munkres Algorithms are used for task allocation. The former is used to assign tasks to suitable robots, considering the type of task and robot, and the cost of a collision-free path. The latter assigns the position set of the desired formation to the remaining robots. In addition, to adapt to the dynamic changes in the number of robots in the formation, the formation structure is redefined through the graph theory. Finally, this method successfully solved the formation reconfiguration problem when the robot left the formation after receiving the task or returned to the formation after completing the task. Simulation results show that our approach can achieve the desired functions while ensuring the stability of the formation and has a certain scalability for small-scale systems.**

***Index Terms*— Formation control, graph theory, multirobot system, task assignment.**

I. Introduction

DURING the past few decades, multirobot systems have found widespread application in both civilian and military fields, typical applications include cooperative localization [1], [2], motion capture [3], surveillance [4], search and rescue [5], cooperative manipulation [6], and mapping and exploration [7]. To complete complex tasks more efficiently and quickly, multirobot systems require a group of robots with different capabilities to collaborate. This is because multirobot systems with multiple functions allow them to achieve a wide range of real-world objectives that would be challenging or impossible for systems composed of identical robots. By leveraging the unique capabilities of each type of robot, they can work together to complete tasks that require diverse skills and expertise.

Multirobot systems, comprising small groups of robots, can be classified into two main categories based on the nature of the interactions involved [8]: *team* and *formation*. In a *team*, each robot competes with one another, aiming to minimize its local costs to achieve the goal. On the contrary to a team, robots in a *formation* always cooperate to complete some specific missions and maintain the consistency of certain robot in formation through communication. Thus, the distinction between a *team* and a *formation* in a multirobot system lies in the varying relationships between the robots.

In addition, compared to the *team*, *formation* needs to consider the formation and maintenance of the desired shape. In this article, the consensus theory is used in the proposed method to maintain and control the formation connectivity. Consensus is the process of reaching an agreement on a common value or state among team members through a communication network or sensors [9], [10], [11], [12]. It successfully achieves the goal of formation assembly and keeping. However, the scalability problem in formation control is not considered when the number of robots in the formation changes. This can be divided into two scenarios: one is the passive process of robots passively leaving the formation, and the other is the active process in which the robots leave or join the formation due to mission requirements.

For example, when some robots within a formation lose communication with the formation due to a fault, it results in a change in the number. Cheng and Wang [13] considered this situation and investigated the fault tolerance ability for multirobot formation, allowing their model to continue completing the given mission by reorganizing the formation when some members fail. This article studies the passive process. In [14], an active process has been studied. The authors proposed the Veteran Rule to solve the scalability problem without changing the control parameters/gains in the whole formation system. In this article, the active processes are considered, and how the formation shape changes when robots leave or join the formation is studied. Based on this, the terms *formation* and *team* are reinterpreted to fit this article. *Formation* refers to a group of robots that form a desired formation and accomplish a specific mission as a whole, while *team* refers to a group of robots selected by the task allocation algorithm to leave the formation to perform some tasks.

To achieve superior and efficient performance in both team and formation, the most crucial step is multirobot task allocation (MRTA) [15], [16], [17], [18]. Multirobot systems achieve complex tasks through MRTA, which assigns tasks to robots according to their capabilities and improves the overall system

Received 29 April 2024; revised 7 February 2025; accepted 28 February 2025. Date of publication 1 April 2025; date of current version 11 April 2025. This work was supported in part by the National Natural Science Foundation of China under Grant 62303188 and Grant 61773171 and in part by Guangdong Natural Science Foundation Project under Grant 2024A1515011252. The Associate Editor coordinating the review process was Dr. Pritam Paral. *(Corresponding authors: Xuanchun Yin; Linlin Shi.)*

The authors are with the College of Engineering, South China Agricultural University, Guangzhou 510642, China (e-mail: xc_yin@scau.edu.cn; huabin_hu@stu.scau.edu.cn; lynnshi@scau.edu.cn).

Digital Object Identifier 10.1109/TIM.2025.3556831

performance by optimizing the overall objective function of the system.

In *teams*, MRTA aims to reasonably allocate tasks to randomly distributed robots throughout the workspace so that they can achieve optimal or suboptimal solutions without conflicts, cooperatively or competitively. This enables multirobot teams to perform multiple tasks simultaneously. Mayya et al. [19] present a centralized resilient task allocation framework for the heterogeneous multirobot system to ensure that each task is assigned to the most suitable robots in the presence of external perturbations. To solve the simultaneous multiagent task allocation problem, Wang et al. [20] designed a novel consensus-based timetable algorithm (CBTA) to meet the requirements and minimize the average start time of tasks. In these studies, the authors focus on task allocation without considering the problem of collision-free path planning to ensure that the robot reaches the assigned task. In real-world scenarios, multirobot teams balance minimizing overall cost with searching for collision-free paths to obtain a conflict-free solution. For example, in the multiagent pickup and delivery (MADP) problem, Chen et al. [21] designed the marginal-cost-based task assignment algorithm (MCA) and the regret-based MCA (RMCA). These algorithms can perform task assignments and path planning simultaneously by using real collision-free costs to ensure that each robot can carry multiple packages at the same time. In addition, Forte et al. [22] proposed a comprehensive framework to address the problem of multirobot task assignment (MRTA), planning, and coordination for heterogeneous fleets of robots, which are subject to noncooperative tasks posted online.

Similar to teams, MRTA benefits multirobot formations. Specifically, MRTA ensures that the reconfiguration process is carried out efficiently and effectively by assigning locations to the robots based on their state and proximity to the desired positions. Michael et al. [23] proposed a distributed market-based coordination algorithm to achieve distributed formation control and merging and splitting of groups. Gao et al. [24] proposed an adaptive hybrid particle swarm optimization and differential evolution algorithm to decouple the problem of multi-UAV reconfiguration into task assignment and control input optimization of UAVs. The path planning of the multiple unmanned surface vehicles (MUSVs) formation reconfiguration method, which considers the optimal allocation based on both total distance and simultaneity, is considered in [25]. In essence, MRTA plays a crucial role in multirobot formation, enabling the formation to adapt to environmental changes and task requirements to achieve the desired configuration efficiently.

To combine the advantages of MRTA in both *team* and *formation*, in this article, we propose a novel dual task allocation approach for multirobot formations where different types of robots have different capabilities and can only perform homogeneous tasks. An illustration of the proposed method is shown in Fig. 1. In the multirobot formation that has been assembled and is executing a preset mission, there are a total of n UAVs, including one leader-UAV (L-UAV) and $n-1$ follower-UAVs (F-UAVs). As a central server, L-UAV is responsible for planning the path from the start point of

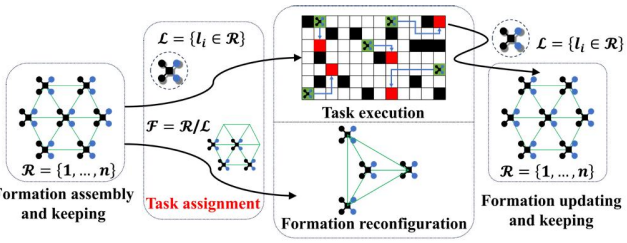

Fig. 1. Illustration of the proposed method. A group of UAVs assembles into the desired formation and moves across the workspace. When the tasks are released, the formation selects the UAVs to perform these tasks using the first task assignment algorithm. Then, after the second task assignment algorithm assigns the desired positions of the UAVs in the formation, the remaining UAVs initiate the formation reconfiguration to form a new shape. Finally, once the UAVs assigned to the task complete their tasks, they return to the formation and resume an initial shape with the other UAVs in the formation.

formation to the desired goal and assigning the tasks and inner-formation positions for suitable F-UAVs. It is always in formation and is not assigned any tasks. Contrary to L-UAV, each F-UAV follows L-UAV by the consensus-based leader-follower formation control strategy until they are assigned tasks. When the tasks are released, the Auction algorithm [26] is used to select the suitable F-UAVs to perform them. Then, after the Kuhn–Munkres algorithm [27] assigns the desired formation position to the remaining UAVs, the formation reconfiguration is triggered to rebuild a new shape. Finally, when the assigned F-UAVs complete their own tasks and return to the formation, the formation reconfiguration is triggered once again.

In simulations, the results of the proposed method under different undirected graph topologies are compared. This demonstrates that our method ensures formation stability even when the number of robots or tasks changes and is scalable for small-scale formations. Additionally, it ensures the realization of formation reconfiguration when multiple sets of tasks are released asynchronously. Finally, the proposed method is implemented in a UAV cruise scenario, proving that it can be used in complex scenarios and efficiently achieve the desired functions. The major contributions of this article are summarized as follows.

1) This work is dedicated to solving the problem of formation reconfiguration when robots leave the formation after receiving the task or return to the formation after completing the task. To ensure that the task execution of a single robot and the formation reconfiguration of multiple robots are carried out simultaneously, we propose a novel dual task allocation approach for the multirobot system by combining the advantages of MRTA in teams and formations. This method can be applied in complex environments, effectively combines the advantages of teams and formations, and improves the efficiency of the system.
2) The formation reconfiguration of the proposed method is triggered by the change in the number of robots within the formation, which is achieved through a redefinition of the formation structure according to graph theory. This method effectively ensures the formation stability by maintaining the distances between F-UAVs and

L-UAV at the preset value both before and after changing the formation shape.

The remainder of this letter is organized as follows. In Section II, the necessary notation and theory are provided. Then, the algorithms of the proposed dual task allocation approach for the multirobot formations are presented in Section III. In Section IV, we conduct simulations to test the performance. Finally, Section V concludes this work.

II. Problem Formulation

Consider that a group of robots randomly distributed in the workspace assembles into the desired formation and moves toward the goal. Once the tasks are released, several suitable robots are selected by task assignment to carry them out. Subsequently, the remaining robots form a new formation through formation reconfiguration and keep it until the assigned robot returns to the formation and triggers formation reconfiguration once again. Note that as long as the robot can communicate with the leader robot, it is considered to be within the formation range. However, being in the formation range does not necessarily mean that the robot has returned to the formation, and other constraints must also be met. Each robot can only perform specific tasks due to its limited capabilities. Moreover, each robot can only be assigned to one task per task assignment. Therefore, the instance is considered an online single task, single robot, instantaneous assignment (ST-SR-IA) MRTA problem [15].

A. Formula Definition

We use $\mathcal{R} = \{1, 2, \ldots, n\}$ to denote the set of indices of n robots that are initially randomly distributed in the workspace. Then the F-UAVs are assembled into a desired regular polygon formation using a formation control approach, with the L-UAV at the center. Each robot is identified by a tuple $r_i = \langle s_i, h_i, f_i \rangle$, where s_i represents status information of the robot i, h_i represents its type of platform (implemented function, carried sensors, etc.), and f_i represents the return flag of the robot i. $f_i =$ true if robot i is returning to the formation and $f_i =$ false, otherwise. When the robot is removed from the task execution list $\mathcal{L}$, f_i is reset to false. Let q_c be the position of the center of the formation. $\Pi = \{1, 2, \ldots, m\}$ denotes the set of indices of m randomly distributed tasks that are executed by robots which are specified by task assignment. Each task is identified by a tuple $\pi_j = \langle p_j, h_j \rangle$, where p_j represents the position of task i, and h_j is its information on the type (of robot needed to complete it).

Let $\mathcal{L} = \{l_i \in \mathcal{R}\}$ be the list of task execution, denoting the set of indices of the robots assigned tasks. $|\mathcal{L}|$ is the cardinality of $\mathcal{L}$. $\mathcal{F} = \{f_i \in \mathcal{R}\}$ denotes the set of indices of the remaining robots in the formation, which is initialized to $\mathcal{R}$ at the beginning, indicating that the tasks are not released, and all robots are assembled into a desired formation. $|\mathcal{F}|$ is the cardinality of $\mathcal{F}$. In general, $\mathcal{F} = \mathcal{R}/\mathcal{L}$ is the different set of $\mathcal{R}$ and $\mathcal{L}$.

B. Task Assignment

The scope of this article is limited to scenarios where each robot is capable of assigning and executing only one task at a time. This article does not explore the possibility of a single robot performing multiple tasks simultaneously, or the possibility of multiple robots jointly performing a task. We define μ_{ij} to denote whether task j is assigned to robot i or not. $\mu_{ij} = 1$ if assigned and $\mu_{ij} = 0$, otherwise.

For the multirobot system, where different types of robots have different capabilities, each type of robot can only perform homogenous tasks. To ensure efficient task assignment, a robot-task matching matrix, denoted by O, is created, which outlines the tasks that each robot is capable of performing. Its elements o_{ij} can be computed as

$$o_{ij} = \begin{cases} 1, & \text{if } h_i = h_j \ \forall i \in \mathsf{R} \ \forall j \in \Pi \\ 0, & \text{otherwise.} \end{cases} \tag{1}$$

When assigning robots to tasks, it is essential to consider not only the suitability of the robot for the task but also the cost of the path from its current position to reach the task. This means evaluating factors such as the distance the robot needs to travel, any obstacles it may encounter along the way, and the time it takes to complete the task. In our method, the path cost of two cases is considered: 1) the short-path cost of robot navigation during formation reconfiguration, and 2) the long-path cost of the robot leaving the formation and reaching the task.

In the first case, the task type is not considered because any F-UAV within the formation can reach the designated formation position when formation reconfiguration is triggered. There are an equal number of tasks and robots, which create a perfect matching problem. Then, the objective function to minimize the total travel distance for the robots from their current position to reach the desired position is computed as

$$\min \sum_{i \in \mathcal{R}} \sum_{j \in \Pi} \mu_{ij} \cdot \text{cost}_{ij} \tag{2}$$

s.t.

$$\sum_{i \in \mathsf{R}} \mu_{ij} = 1 \quad \forall j \in \Pi \tag{3}$$

$$\sum_{j \in \Pi} \mu_{ij} = 1 \quad \forall i \in \mathsf{R} \tag{4}$$

$$\sum_{i \in \mathsf{R}} \sum_{j \in \Pi} \mu_{ij} = m \tag{5}$$

$$m = n \tag{6}$$

where cost_{ij} is defined as the cost of the Euclidean distance between the robot i and task j. Constraint (3) requires that each task is assigned to precisely one robot; (4) implies that each robot can accept only one task at a time; (5) and (6) guarantees that all robots are assigned to tasks, and all tasks are assigned. For the aforementioned cases, the Kuhn–Munkres algorithm [27] is used to implement task assignments and optimize the performance of formation reconfiguration.

In the second case, both the task type and the cost of avoiding obstacles outside the formation are considered. It can be defined as a single-assignment problem in which at most one task can be assigned to a single robot. Furthermore, it is an imperfect matching problem as well, where the total number of robots is greater than the total number of tasks (tasks are

not assigned to the leader), that is $n > m$, and the number of robots of a type is greater than the number of tasks of the same type, ensuring that all tasks can be assigned. Otherwise, some tasks will be idle after the task assignment when $n \leq m$. These idle tasks can wait for the F-UAVs to complete their own task and be allocated through the second assignment. The objective function can be written as

$$\min \sum_{i\in \mathsf{R}} \sum_{j\in \Pi} \mu_{ij}(O) \cdot \text{cost}_{ij}^{\text{avoid}} \tag{7}$$

s.t.

$$\sum_{i\in \mathsf{R}} \mu_{ij}(O) = 1 \quad \forall j \in \Pi \tag{8}$$

$$\sum_{j\in \Pi} \mu_{ij}(O) \leq 1 \quad \forall i \in \mathsf{R} \tag{9}$$

$$\sum_{i\in \mathsf{R}} \sum_{j\in \Pi} \mu_{ij}(O) = m \tag{10}$$

$$m < n \tag{11}$$

where $\mu_{ij}(O)$ denotes that the task j is assigned to the robot i under the premise of considering the robot-task matching matrix O and $\text{cost}_{ij}^{\text{avoid}}$ represent the cost of travel distance of the robot i to the task j to consider obstacle avoidance. According to constraint (8), every task must be assigned to only one robot; (9) represents that each robot can only be assigned a maximum of one task; (10) and (11) guarantees that the number of robots assigned to the task is exactly m, which is less than n. Equation (7) is implemented by an Auction algorithm [26] to achieve optimal allocation. In this article, the Kuhn–Munkres algorithm and the Auction algorithm are utilized to implement the proposed method for task allocation.

C. Graph Theory

The multirobot system with a limited range of communication is modeled as a simple undirected graph $G = (V, E)$, where $V = \{v_1, v_2, \ldots, v_n\}$ represents the set of nodes and $E = \{(v_i, v_j)\} \subseteq V \times V$ represents the set of undirected edges. The set of neighbors of node i is denoted by $N_i = \{v_j \in V \mid (v_i, v_j) \in E\}$. More specifically, the robots are equivalent to the nodes of an undirected graph, and the communication links are equal to the edges [28]. Therefore, the elements of the adjacency matrix A can be defined as

$$a_{ij} = \begin{cases} 1, & \text{if } (v_i, v_j) \in E \ \& \ v_i \text{ and } v_j \\ & \text{are communicating} \\ 0, & \text{otherwise.} \end{cases} \tag{12}$$

It is important to note that the set of nodes in the undirected graph modifies as the system runs, and the set of edges changes accordingly. Fig. 2 illustrates the network topologies of the undirected graph used in this work [20].

Typically, there is no edge between the robots in $\mathcal{L}$ and other robots, and they are also removed from the set of nodes when they leave the formation. Given the circumstances as mentioned above, the communication matrix C is designed, in which its elements can be written as

$$c_{ij} = \begin{cases} 1, & \text{if } v_i \text{ and } v_j \text{ are communicating} \\ 0, & \text{otherwise.} \end{cases} \tag{13}$$

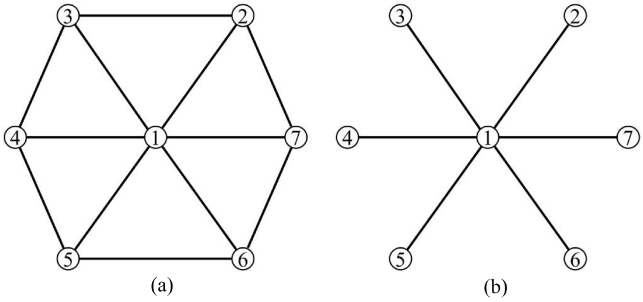

Fig. 2. Network topologies of the undirected graph. (a) Circular. (b) Star.

It is not considered in C if the robot cannot exchange information with the leader. The communication matrix C focuses on all robots communicating with the leader in the formation range, that is, the number of robots within the range of formation. Therefore, $|C|$ express its dimension, defining the number of robots (including the leader) that communicate with the leader directly or indirectly. However, the adjacency matrix A considers the variation of nodes and edges of the graph when the assigned robots leave or enter the formation range.

D. Formation Control

The consensus-based leader–follower formation control approach is a well-known formation strategy that emphasizes the maintenance of a stable state by regulating the relative position and velocity between the leader and the followers. Its goal is to establish a desired formation, where the followers maintain a fixed position with respect to the leader, ensuring a smooth and coordinated motion of the entire group. Each robot is designed as a second-order dynamic system model

$$\begin{cases} \dot{x}_i = v_i \\ \dot{v}_i = u_i \end{cases} \tag{14}$$

where x_i and v_i are the position and velocity of robot i, respectively; and the control input u_i is its acceleration which can be timely controlled. Here, the consensus-based formation controller [12] is as follows:

$$u_i(t) = \alpha \cdot \sum_{j\in N_i} a_{ij} \cdot \left(x_j(t) - x_i(t) - \tilde{x}_{ij}(t)\right) + \beta \cdot \sum_{j\in N_i} a_{ij} \cdot \left(v_j(t) - v_i(t) - \tilde{v}_{ij}(t)\right) \tag{15}$$

where $\tilde{x}_{ij}(t) = x_j^*(t) - x_i^*(t)$ and $\tilde{v}_{ij}(t) = v_j^*(t) - v_i^*(t)$ denote the desired relative position and velocity of robot i with respect to robot j, respectively; $x_i^*(t)$ and $x_j^*(t)$ are the offset of robot i and robot j determined by the formation shape, respectively; $v_i^*(t)$ and $v_j^*(t)$ are their desired velocity, respectively.

This article also utilizes the artificial potential field method [29] to plan the path for the robots, aiming to achieve obstacle avoidance and collision avoidance between robots. To be specific, the attractive potential field of the goal to the robot i, the repulsive potential field of the obstacle to the

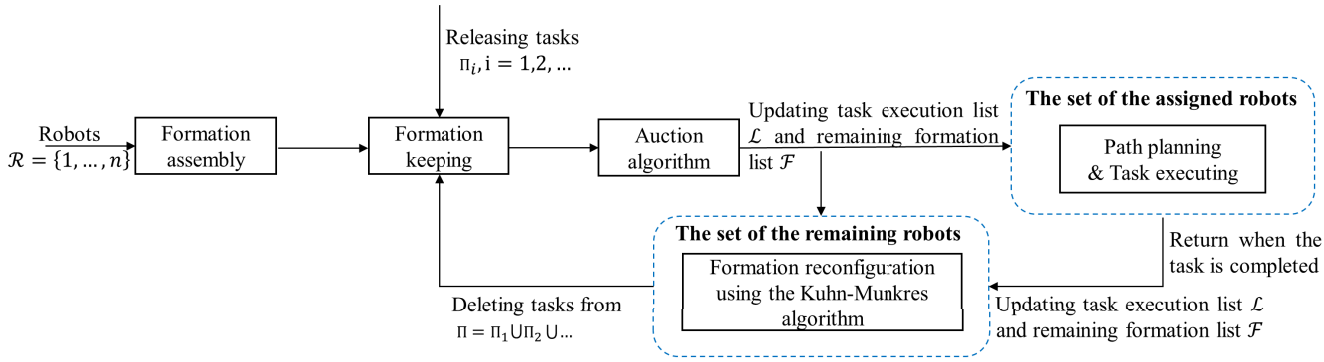

Fig. 3. System architecture. The system depends on three crucial modules: task assignment, task execution, and formation reconfiguration.

robot i, and the repulsive potential field between robot i and robot j are as follows:

$$U_i^a = \begin{cases} K_a \cdot d_a \cdot d(p_i, p_g) - \frac{1}{2} \cdot K_a \cdot d_a^2, & d(p_i, p_g) > d_a \\ \frac{1}{2} \cdot K_a \cdot d^2(p_i, p_g), & d(p_i, p_g) \le d_a \end{cases} \tag{16}$$

$$U_i^o = \begin{cases} 0, & d(p_i, p_o) > d_o \\ \frac{1}{2} \cdot K_o \cdot \left(\frac{1}{d(p_i, p_o)} - \frac{1}{d_o} \right)^2 \cdot d^2(p_i, p_g), & d(p_i, p_o) \le d_o \end{cases} \tag{17}$$

$$U_i^r = \begin{cases} 0, & d(p_i, p_j) > d_r \\ K_r \cdot \frac{1}{e^{d(p_i, p_j)} - e^{d_r}}, & d(p_i, p_j) \le d_r \end{cases} \tag{18}$$

where d_a, d_o, and d_r are potential field boundary distance; K_a, K_o, and K_r are positive control gains constant; $d(p_i, p_g)$, $d(p_i, p_o)$, and $d(p_i, p_j)$ represent the Euclidean distance of robot i to goal, obstacle, and robot j, respectively. Hence, the final control input of the robot i in the formation can be expressed as the result of the collaborative effect of consensus theory and artificial potential field methods, which are specifically expressed as

$$u_i^f = u_i + u_i^a + u_i^o + u_i^r \tag{19}$$

$$u_i^a = \begin{cases} -K_a \cdot d_a \cdot \overrightarrow{n_{ig}}, & d(p_i, p_g) > d_a \\ -K_a \cdot d(p_i, p_g) \cdot \overrightarrow{n_{ig}}, & d(p_i, p_g) \le d_a \end{cases} \tag{20}$$

$$u_i^o = \begin{cases} 0, & d(p_i, p_o) > d_o \\ K_o \cdot \left(\frac{1}{d(p_i, p_o)} - \frac{1}{d_o} \right) \cdot \frac{d^2(p_i, p_g)}{d^2(p_i, p_o)} \cdot \overrightarrow{n_{io}} \\ \quad + K_o \cdot \left(\frac{1}{d(p_i, p_o)} - \frac{1}{d_o} \right)^2 \cdot d(p_i, p_g) \cdot \overrightarrow{n_{ig}}, \\ d(p_i, p_o) \le d_o \end{cases} \tag{21}$$

$$u_i^r = \begin{cases} 0, & d(p_i, p_j) > d_r \\ K_r \cdot \frac{e^{d(p_i, p_j)}}{\left(e^{d(p_i, p_j)} - e^{d_r} \right)^2} \cdot \overrightarrow{n_{ij}}, & d(p_i, p_j) \le d_r \end{cases} \tag{22}$$

where $\vec{n}_{ig}$, $\vec{n}_{io}$, and $\vec{n}_{ij}$ represent the unit vector from robot i to goal, obstacle, and robot j, respectively. Equation (20) represents the attractive force from the goal to robot i. Equation (21) represents the repulsive force that robot i receives from the obstacle, while (22) represents the repulsive force between robots i and j. In short, through (19), the path planning of the formation can be realized while ensuring obstacle avoidance and collision avoidance.

In this article, the task execution of a single robot and the formation reconfiguration of multiple robots are considered simultaneously. For a single robot performing a task, it is generally controlled by the resultant force of APF, that is,

$$u_i^f = u_i^a + u_i^o + u_i^r. \tag{23}$$

However, for the remaining robots in the formation, (19) can be used to express the final control input of a single robot. It is worth noting that the change in the number of robots in the formation caused by the leaving or joining of some assigned robots makes the undirected graph of the whole formation change accordingly. Specifically, the change in the number of robots in the formation affects the communication matrix C and the adjacency matrix A, which in turn impacts the consensus-based formation control strategy. The details are given in Section III-C.

III. Method

To ensure efficient and effective performance, the system heavily relies on three critical modules of the proposed method: task assignment, allocation of tasks to appropriate robots to minimize the cost function; task execution, supervision of the status of robots while performing tasks; and formation reconfiguration, dynamic adjustment of the formation according to changes in the number of robots in the formation. The system architecture of the proposed method is shown in Fig. 3. According to the abovementioned architecture, we summarize the main ideas of the method and highlight the following algorithms:

1) *Task Assignment:* The auction algorithm is used to select appropriate robots within the formation to execute tasks, and then the remaining robots trigger the formation reconfiguration by the Kuhn–Munkres algorithm (see Algorithm 1 and its description in Section III-A).

Algorithm 1 Dual Task Allocation Approach

Require: Robot set $\mathcal{R}$, task set Π

1: // Initialize the list of task execution $\mathcal{L}$
2: $\mathcal{L} \leftarrow auctionAlgorithm(\mathcal{R}, \Pi)$
3: // Initialize the list of remaining robots $\mathcal{F}$
4: $\mathcal{F} \leftarrow \mathcal{R}/\mathcal{L}$
5: **while** $\mathcal{L} \neq \emptyset$ **do**
6: // Release new tasks
7: **if** $\Pi_k \neq \emptyset$ **then**
8: $\mathcal{L}_k \leftarrow auctionAlgorithm(\mathcal{F}, \Pi_k)$
9: // Update the list of task execution $\mathcal{L}$
10: $\mathcal{L} \leftarrow \mathcal{L} \cup \mathcal{L}_k$
11: // Update the list of remaining robots $\mathcal{F}$
12: $\mathcal{F} \leftarrow \mathcal{R}/\mathcal{L}$
13: // Update task set Π
14: $\Pi \leftarrow \Pi \cup \Pi_k$
15: **end if**
16: // Path planning and task execution for each robot in $\mathcal{L}$
17: *taskExecution*()
18: // Formation reconfiguration of the remaining robots using the Kuhn-Munkres Algorithm
19: *formationReconfiguration*()
20: **end while**

Algorithm 2 Task Execution (Line 17 of Algorithm 1)

Require: Robot status s_i, task π_{r_i}, task execution list $\mathcal{L}$, return flag f_i, formation center q_c.

1: $f_i \leftarrow false$ // Persistent variable
2: **if** robot i in $\mathcal{L}$ **and** $f_i = false$ **then**
3: **if** $pathplanning(s_i, \pi_{r_i})$ **then**
4: **if** *completeTask*() **then**
5: $f_i \leftarrow ture$
6: **endif**
7: **endif**
8: **endif**
9: // Update the state of the robot that completes tasks and returns to formation
10: **if** robot i in $\mathcal{L}$ **and** $f_i = ture$ **then**
11: **if** $pathplanning(s_i, q_c)$ **then**
12: **if** *returnFormation*() **then**
13: delete i from $\mathcal{L}$
14: $\mathcal{F} \leftarrow \mathcal{R}/\mathcal{L}$
15: delete π_{r_i} from Π
16: $f_i \leftarrow false$
17: **endif**
18: **endif**
19: **endif**

2) *Task Execution:* The status information will change accordingly with the robot when it performs at different stages. This article utilizes this property to determine when formation reconfiguration is triggered (see Algorithm 2 and its description in Section III-B).
3) *Formation Reconfiguration:* The formation reconfiguration of the remaining robots, when the assigned robots leave or return to the formation, is realized by redefining the formation structure through graph theory (see Algorithm 3 and its description in Section III-C).

A. Dual-Task Allocation Approach

Assuming that a group of UAVs are randomly distributed in the workspace, they start assembling through the communication link between each other. Then, they form the desired formation using the formation control strategy. Moreover, UAVs with different functions form a multi-UAV system and each F-UAV is capable of handling only one task at a time. After establishing the desired formation, the UAVs maintain their shape and perform a preset mission, either stationary or moving toward a target.

Algorithm 1 shows the pseudocode for the proposed method. At the beginning of the algorithm, task set Π is an empty set, and the remaining UAVs set $\mathcal{F}$ is set to the robot set $\mathcal{R}$.

In the process, once the tasks are released, the system proceeds to the next stage. The central server utilizes the auction algorithm to assign tasks in the task set to the suitable F-UAV to minimize the cost function, sequentially initializing the list of the task execution $\mathcal{L}$ and the remaining UAVs $\mathcal{F}$ (lines 1–4 in Algorithm 1). The auction algorithm selects the suitable F-UAV based on the type of F-UAV required to perform the task and the path cost required by its current location to reach the task. After that, the algorithm enters the main while loop (lines 5–20 in Algorithm 1). The assigned F-UAVs are guided to the goal by the path planning algorithm and execute their tasks (line 17 in Algorithm 1). This step is implemented by Algorithm 2. According to the change of the task execution list $\mathcal{L}$ and the state of the assigned F-UAVs, meanwhile, the formation consisting of the remaining UAVs triggers the formation reconfiguration, where the position of the new shape is assigned by the Kuhn–Munkres algorithm (line 19 in Algorithm 1). Algorithm 3 is responsible for implementing this step. During the execution of the main while loop, it is crucial to keep track of any new tasks that may be released (lines 7–15 in Algorithm 1). These tasks must be added to the task set Π to ensure they are properly accounted for. Additionally, the list of task execution $\mathcal{L}$ and the remaining UAVs $\mathcal{F}$ must be updated to reflect any changes to the task set. This ensures that all tasks are appropriately assigned and executed and that the system operates efficiently.

B. Task Execution

To distinguish the movement phases of F-UAVs outside the formation, a return flag f_i is designed for each UAV, which indicates whether the UAV is heading to the task from the formation or returning to the formation from the task. It is the persistent variable set as false initially (line 1 in Algorithm 2). But the return flag f_i only works when the UAV i is in the task execution list $\mathcal{L}$ (lines 2 and 10 in Algorithm 2). When suitable F-UAVs are selected to perform tasks, they are added to the task execution list $\mathcal{L}$ and then guided to their tasks from their current position by the Path Planning Algorithm (line 3 in Algorithm 2). Once the F-UAV reaches the designated goal,

Algorithm 3 Formation Reconfiguration (Line 19 of Algorithm 1)

Require: Robot set $\mathcal{R}$, task execution list $\mathcal{L}$, robot status s_i.

1: $C \leftarrow calcCommunicationMatrix(\mathcal{R})$
2: $\mathcal{F} \leftarrow \mathcal{R}/\mathcal{L}$
3: // Calculate the adjacency matrix
4: **if** $\mathcal{L} = \emptyset$ **and** $|C| = n$ **then**
5: $A \leftarrow calcAdjacencyMatrix(\mathcal{R})$
6: **endif**
7: **if** $\mathcal{L} \neq \emptyset$ **and** $n - |\mathcal{L}| < |C| \leq n$ **then**
8: $A \leftarrow calcAdjacencyMatrix(\mathcal{R})$
9: $A(\mathcal{L},:) \leftarrow 0$
10: $A(:,\mathcal{L}) \leftarrow 0$
11: **endif**
12: **if** $\mathcal{L} \neq \emptyset$ **and** $|C| \leq n - |\mathcal{L}|$ **then**
13: $A \leftarrow calcAdjacencyMatrix(\mathcal{F})$
14: **endif**
15: new_formation $\leftarrow creatRegularPolygon(|\mathcal{F}|)$
16: desired_formation $\leftarrow KMAlgorithm(\mathcal{F}$, new_formation)
17: consensusControl(A, desired_formation)

it begins executing the task until completion, after which its return flag is set to true (lines 4–6 in Algorithm 2).

After completing its task, the F-UAV returns to the formation from its goal. In this phase, certain conditions (such as direct or indirect communication with L-UAV) must be met before it returns to the formation. Only then will the return flag be set to false (lines 11–18 in Algorithm 2).

C. Formation Reconfiguration

In this article, the formation reconfiguration of the multi-UAV system needs to consider the variation of the task execution list $\mathcal{L}$ and the communication matrix C with the operation of the system. This is critical to ensure efficient and effective formation reconfiguration of the multi-UAV system. It can be divided into five categories.

1) No tasks are released or all assigned F-UAVs return to the formation. The formation maintains its original shape and continues the designated preset mission.
2) The F-UAVs assigned to the task remain in the formation after the tasks are released. The remaining UAVs stay in the position of the formation as before while the assigned F-UAVs gradually leave the formation.
3) All assigned F-UAVs leave the formation after the tasks are released. At this moment, the remaining UAVs trigger formation reconfiguration to form a new formation.
4) The assigned F-UAVs complete their task and enter the formation range. The formation, consisting of the remaining UAVs, reorganizes to the new formation and reserves suitable positions for the returning F-UAVs.
5) The assigned F-UAVs return to the formation. They move to the positions reserved for them under the influence of the formation control strategy.

All the above cases are achieved by redefining the formation structure through graph theory. Algorithm 3 covers all the cases mentioned above and has been implemented accordingly:

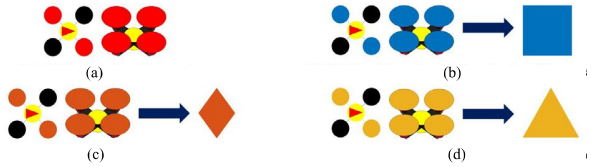

Fig. 4. Graphical symbols used in the 2-D and 3-D demonstrations. (a) L-UAV is not assigned any task. (b) F-UAVs of type-A are assigned tasks of the same type. (c) F-UAVs of type-B are assigned tasks of the same type. (d) F-UAVs of type C are assigned tasks of the same type.

lines 4–6 discuss case 1); lines 7–11 address cases 2) and 4); lines 12–14 cover cases 3) and 5). At the start of the algorithm, it is necessary to obtain the number of UAVs within the range of formation by computing the communication matrix C (line 1 in Algorithm 3). In addition, to calculate the adjacency matrix A, the set of UAVs $\mathcal{R}$ and the list of remaining UAVs $\mathcal{F}$ are also needed (line 2 in Algorithm 3). Then, according to the changes of the task execution list $\mathcal{L}$ and the number of UAVs within the range of formation $|C|$, different formation shapes are created by calculating the adjacency matrix A at different stages (lines 3–14 in Algorithm 3). Based on the number of remaining UAVs and the properties of regular polygons, a set of positions for the new formation is obtained (lines 15 in Algorithm 3). These positions are assigned to the appropriate remaining UAVs using the Kuhn–Munkres algorithm (lines 16 in Algorithm 3). Finally, the formation reconfiguration is realized by consensus control (line 17 in Algorithm 3). In Algorithm 3, a particular case is not considered. This refers to the UAVs being neither in the remaining formation list $\mathcal{F}$ nor in the task execution list $\mathcal{L}$, that is, $\mathcal{R}/(\mathcal{F} \cup \mathcal{L}) \neq \emptyset$.

IV. Simulations and Results

For multirobot formations, the formation shape is designed as the regular polygons, and its specific shape is determined by the number of F-UAVs. For example, when there are six F-UAVs, the formation will converge into a regular hexagon. At the same time, there is only one L-UAV in the formation, which is located at the center of the formation. Furthermore, we define d as the desired distance between the L-UAV and each F-UAV, and d_c as the maximum communication distance between each UAV. In these simulations, all relevant parameters are presented in Table I. When the selected F-UAV travels from its current position to the goal or returns to the formation, the improved artificial potential field method is used to plan its path. In addition, there are three different types of F-UAVs to perform corresponding tasks. Fig. 4 shows the graphical symbols used for the 2-D and 3-D demonstration. Among them, L-UAV is not assigned any tasks, while different types of F-UAVs are only assigned tasks of the corresponding types, which are indicated by different shapes and colors.

A. Test 1: Demonstration

Assume that the demonstration scenario of the proposed method involves randomly distributed UAVs assembling into the desired formation centered on L-UAV and waiting for task release. Except for the UAVs assigned to the task, other UAVs only move within the formation, while the multi-UAV

TABLE I
SIMULATION PARAMETERS UNDER DIFFERENT TESTS

	α	β	K_a	K_o	K_r	d_a(m)	$d_o(m)$	$d_r(m)$	$d(m)$	$d_c(m)$
Test 1	1	1	3	0.5	0.5	2	1	1	3	5
Test 2	2	1	0.5	1	0.5	1	1	1	3	5
Test 3	2	1	0.5	1	0.5	1	1	1	3	5
Test 4	2	1	0.5	0.5	0.5	1	1	1	3	5

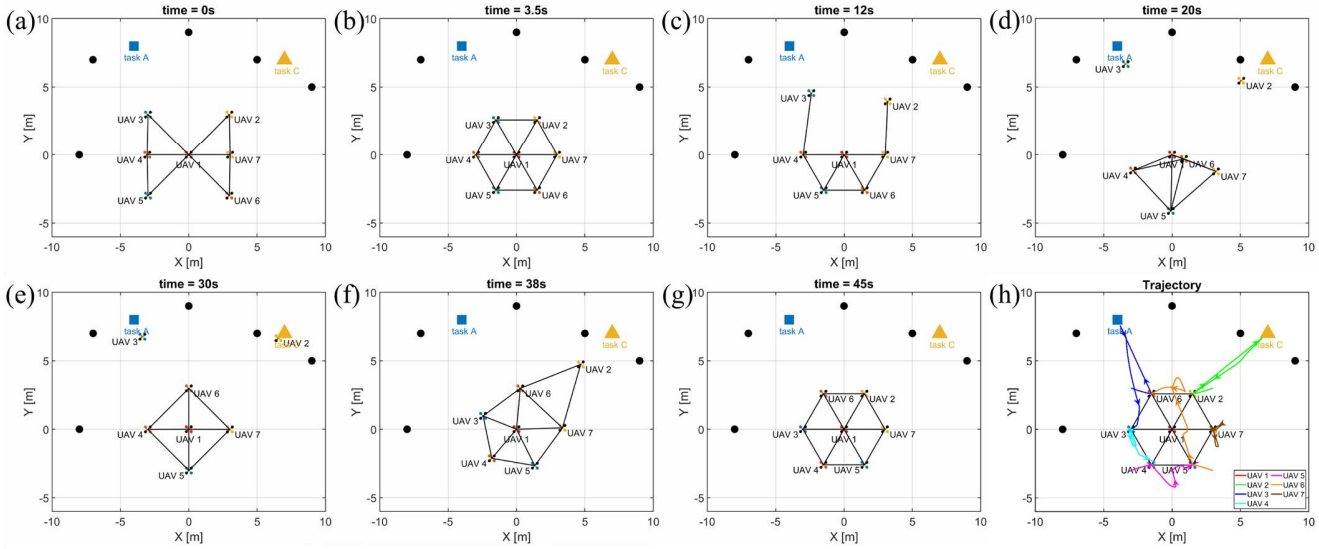

Fig. 5. Demonstration of the proposed method on the multirobot system under the circular network. (a)–(g) Key video frame of the proposed system demonstration. (h) Trajectory of each UAV during the demonstration.

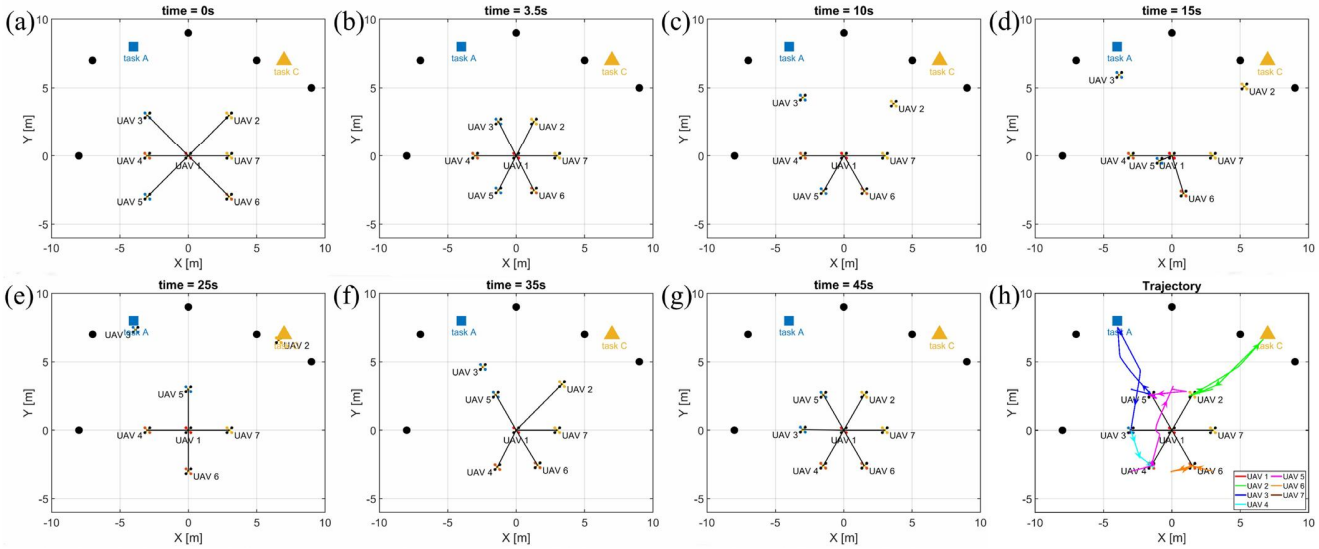

Fig. 6. Demonstration of the proposed method on the multirobot system under the star network. (a)–(g) Key video frame of the proposed system demonstration. (h) Trajectory of each UAV during the demonstration.

system as a whole remains stationary during the execution of the program. Figs. 5 and 6 depict the key video frame of the demonstration of our proposed approach under different network topologies of the undirected graph, as well as the trajectory of each UAV during the demonstration. This visual representation provides a comprehensive overview of how our approach works and the movement of each UAV in this process. Figs. 7 and 8 display the Euclidean distance between each UAV and the L-UAV over time.

There is 1 L-UAV and 6 F-UAVs, as well as two tasks in these demonstrations. Take the demonstration under the circular network as an example. At $t = 0$ s [Fig. 5(a)],

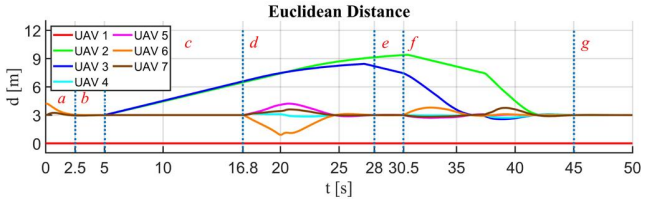

Fig. 7. Curve of the Euclidean distance between each F-UAV and L-UAV as a function of time under the circular network. In phase a, the multirobot system assembles into a desired formation. In phases b, e, and g, formation maintains the current desired shape. In phase c, tasks are released, and the assigned F-UAVs go to their targets to perform their task, and the remaining UAVs are still in place. In phases d and f, the assigned F-UAVs eventually leave and return to the formation, respectively. In phase d, the remaining UAVs begin to reconfigure and form a new desired formation, while phase f also includes the UAVs that have returned to the formation.

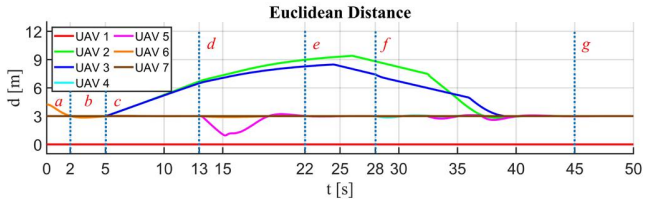

Fig. 8. Curve of the Euclidean distance between each F-UAV and L-UAV as a function of time under the star network.

F-UAVs are distributed around L-UAV, and then assembled to form the initial regular polygon (phase a in Fig. 7) and maintains this shape (Fig. 5(b); phase b in Fig. 7). The tasks are released at $t = 5$ s. At the same time, the F-UAVs assigned to the task through the auction algorithm gradually leave the formation range, while the remaining UAVs remain in place (Fig. 5(c); phase c in Fig. 7). When all assigned F-UAVs have departed from the formation, the remaining UAVs initiate a formation reconfiguration process (Fig. 5(d); phase d in Fig. 7). During this process, positions of the desired shape are assigned to suitable remaining UAVs using the Kuhn–Munkres algorithm, followed by maintaining the current formation (Fig. 5(e); phase e in Fig. 7). Until the assigned F-UAVs complete their tasks and return to the formation (the conditions for indirect or direct communication with L-UAV have been met), the formation reconfiguration is triggered once again (Fig. 5(f); phase f in Fig. 7). Finally, the multirobot formation reforms the initial formation (Fig. 5(g); phase g in Fig. 7) and until a new set of tasks is released. Under the star network, Figs. 6 and 8 have similar results.

As shown above, formation reconfiguration is triggered when the F-UAVs assigned to the task leave the range of the formation or return to the formation. Whenever the remaining UAVs reform and stabilize their formation through formation reconfiguration, the L-UAV and F-UAVs maintain at the set values ($d = 3$ m). Therefore, the proposed method can achieve the intended purpose: once the tasks are released, several F-UAVs in the UAV formation can be dispatched to perform these tasks, while the remaining formation reforms the shape and continues to perform the previous mission. The designated F-UAV can return to the formation after completing its task and meeting the necessary conditions.

As shown in Figs. 7 and 8, in phases d and f of the circular network, all F-UAVs in the formation have position changes and the formation takes a long time to stabilize. However, in the star network, only a few of them change, so the desired formation will be formed quickly. Specifically, under the circular network, since the F-UAVs assigned a task communicate with every UAV within its communication range (equivalent to an edge of the undirected graph), they will trigger formation reconfiguration when they completely leave the formation. In this process, the remaining UAVs need to communicate with each other, making it take a long time for the formation to stabilize. When the assigned F-UAVs return to the formation, they have similar results. However, it is different in the star network, the assigned F-UAVs only have connections with the L-UAV, and certain UAVs that do not change their position, such as UAV 4 and UAV 7, will not have redundant movements. When they leave the formation, the formation reconfiguration is triggered if communication with the L-UAV is not maintained. When returning to the formation, the L-UAV will determine whether they have entered the formation range and reserve a position for them.

The reason for the above conclusion is determined by the characteristics of the undirected graph of the two topological networks. For the circular network, as long as the assigned F-UAV can meet the communication distance with any UAV in the formation, it can be consistent with the realization state of the whole formation, to form the desired formation. In a sense, the circular network is a complete graph when all UAVs can communicate with each other. However, the star network only establishes a connection with the L-UAV.

Both topological networks have their own advantages. In this article, to ensure that the multi-UAV system can stably form the desired shape, the circular network is used as the undirected graph topology.

B. Test 2: Stability and Scalability

In this test, it is evaluated how variations in the number of tasks and UAVs involved affect the stability and scalability of the proposed method. It is worth noting that the formation scalability mainly refers to the adaptability of the system under different quantity conditions. The tasks are released at $t = 5$ s in the current test.

The Euclidean distance from each UAV to L-UAV under different numbers of UAVs and different numbers of tasks is shown in Fig. 9. This Euclidean distance is used to determine the stability of the formation under different numbers of UAVs and different numbers of tasks. The formation stability is defined as follows: when one or more F-UAVs leave or return to the formation, if the UAV formation can quickly form the desired formation shape based on the number of UAVs in the current formation, the UAV formation is considered stable. It has been observed that the timing of the first formation reconfiguration varies due to the fact that the F-UAVs assigned to the task leave the formation range at different times. The first formation reconfiguration is triggered when the last assigned F-UAV leaves. Moreover, since each F-UAV completes its task and returns to the formation at different times, the frequency of formation reconfiguration also

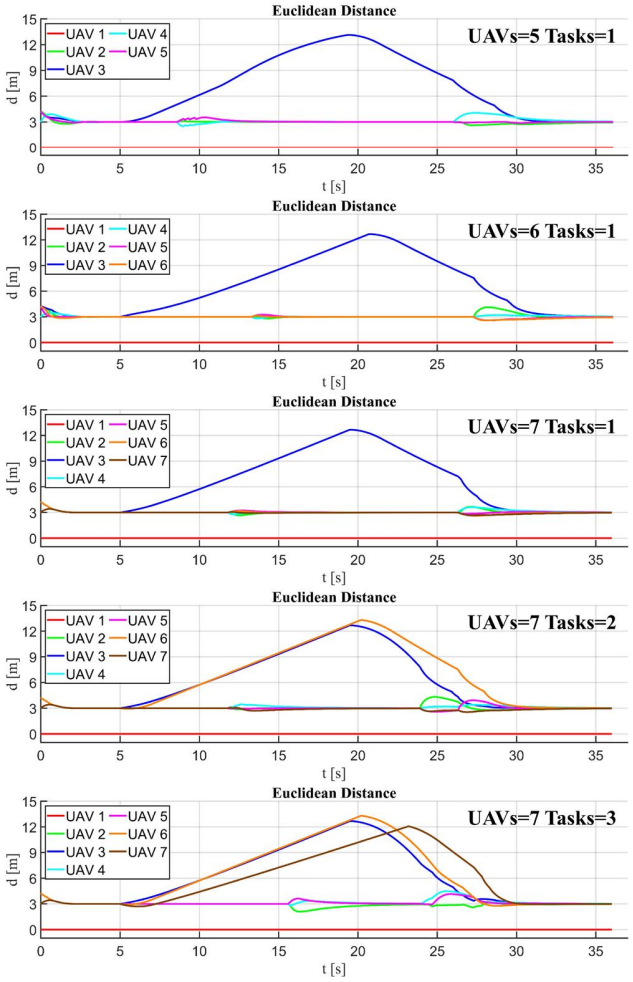

Fig. 9. Euclidean distance from each F-UAV to L-UAV under different numbers of UAVs and different numbers of tasks.

TABLE II
TOTAL RUNTIME AND AVERAGE RUNTIME UNDER DIFFERENT NUMBERS OF UAVS AND DIFFERENT NUMBERS OF TASKS

UAVs	Tasks	Total Runtime(s)	Average Runtime(s)
5	1	57.3587	11.4717
6	1	66.2867	11.0478
7	1	74.5623	10.6518
7	2	74.7758	10.6823
7	3	74.7762	10.6823

varies accordingly. Regardless of the number of robots and tasks involved, the proposed method ensures that the expected distance between the F-UAVs and L-UAV remains constant and guarantees the stability of the formation.

Table II displays the total and average runtime for the five cases in this test. As the number of UAVs increases, the total runtime of the system also increases, but when the number of tasks is fixed and the number of UAVs increases, the average runtime per UAV decreases accordingly. This means that an

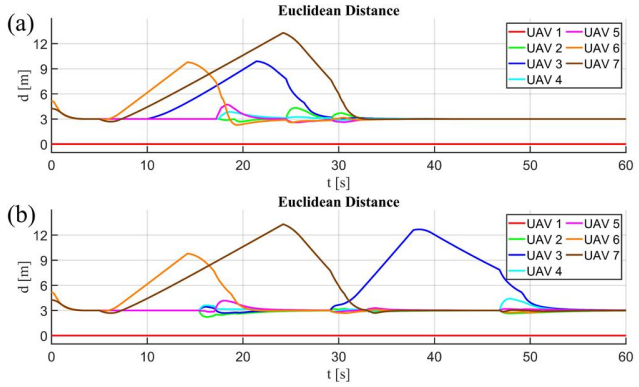

Fig. 10. Euclidean distance between each F-UAV and L-UAV when tasks are released asynchronously. In (a) and (b), the first task list has two task and is released at $t = 5$ s; the second task list is released at $t = 10$ s, and $t = 30$ s in (a) and (b), respectively, and has only one task.

increase in the number of UAVs can improve the performance of each UAV to a certain extent. However, only the number of tasks increases, the total and average runtime does not vary significantly. As a result, the proposed method is scalable for small-scale formations and can perform a certain number of tasks simultaneously.

C. Test 3: Task Asynchronous Release

In this simulation, the performance of the proposed method when tasks are released asynchronously is tested. In Fig. 10, the effectiveness of the proposed method is illustrated concerning the impact of releasing tasks asynchronously. In Fig. 10(a), the second task list is released before all UAVs selected in the first task release have left the formation. At this point, the formation reconfiguration has not yet been triggered. The second task list is released during the second formation reconfiguration in Fig. 10(b). The results show that no matter when the tasks are released, this method can ensure the realization of formation reconfiguration and stability of the formation.

D. Test 4: UAV Cruise Scenario

The proposed method underwent a test that involved a challenging application scenario, namely the UAV cruise scenario. More specifically, the UAV formation follows a predetermined route and executes tasks assigned during the flight, such as measurement, tracking, and localization. This scenario required this method to handle more tasks in a dense obstacle environment and demonstrate its ability to perform effectively and efficiently in complex situations. In actual situations, the route for the formation cruise is fixed so that obstacles can be reduced through advance preparation, while tasks are released randomly, and the generated path may encounter a large number of obstacles. Therefore, in this testing environment, the formation travels along a track with fewer obstacles, but there are numerous obstacles in other locations.

Fig. 11 displays the implementation of the proposed method in the UAV cruise scenario in a 3-D environment, which includes the map of the environment and the trajectory of each UAV. In this test, varying numbers of tasks are released at different intervals, and a total of six tasks are released four

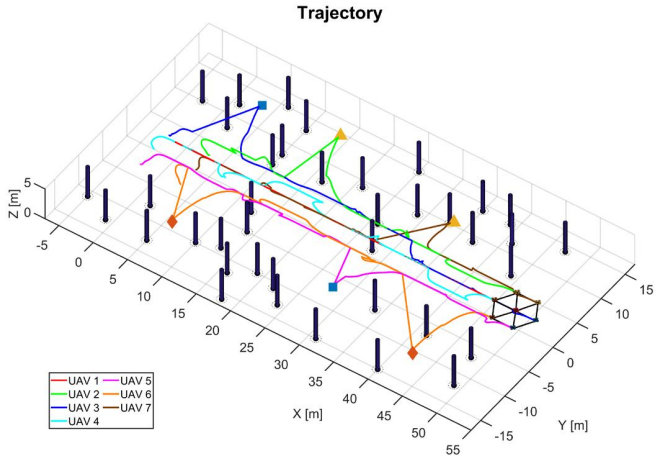

Fig. 11. Application of the proposed method in the UAV cruise scenario in a 3-D environment.

times. The results reveal that the UAV formation can choose the suitable F-UAVs to execute the task and guarantee that a new shape is reconstructed each time the task is released. Thus, the proposed approach can be implemented in complex scenarios and enhance system efficiency.

V. Conclusion and Future Work

In this letter, we propose a novel dual-task allocation approach for multirobot formations where different types of robots have different capabilities and can only perform homogeneous tasks, aiming to combine the benefits of both team and formation. This method enables the simultaneous achievement of task execution and formation reconfiguration. Initially, an auction algorithm is utilized to allocate tasks to suitable robots for task execution. Subsequently, the Kuhn–Munkres algorithm is applied to assign the necessary formation positions to the remaining robots in readiness for formation reconfiguration. Finally, the formation structure is redefined through graph theory to achieve formation reconfiguration. Simulation results are also presented, demonstrating the effectiveness of our proposed method. Our approach ensures formation stability even when the number of robots or tasks changes and is scalable for small-scale formations. Additionally, it can achieve the desired functions even when multiple sets of tasks are released asynchronously. Most importantly, this method can be applied in complex scenarios and improve system efficiency.

There are still several areas for improvement in this work. For example, an F-UAV may receive multiple tasks simultaneously, resulting in a multiassignment problem. Additionally, there are challenges in obstacle avoidance for multi-UAV systems and formation deformation in various scenarios. In future research, the application of this method will be extended from single-assignment problems to multiassignment problems, so that each F-UAV can be assigned a set of multiple tasks, making the entire system more efficient. The problem of obstacle avoidance and formation reconfiguration for multi-UAV systems in different scenarios will also be explored. Finally, it is important to address scalability concerns for the proposed method to be applied in large-scale systems.

References

[1] Y. Huang, C. Xue, F. Zhu, W. Wang, Y. Zhang, and J. A. Chambers, "Adaptive recursive decentralized cooperative localization for multirobot systems with time-varying measurement accuracy," *IEEE Trans. Instrum. Meas.*, vol. 70, pp. 1–25, 2021.

[2] D. Wang, H. Qi, B. Lian, Y. Liu, and H. Song, "Resilient decentralized cooperative localization for multisource multirobot system," *IEEE Trans. Instrum. Meas.*, vol. 72, pp. 1–13, 2023.

[3] S. Zhuge et al., "Markerless motion capture for humans through a multi-UAV system," *IEEE Trans. Instrum. Meas.*, vol. 73, pp. 1–12, 2024.

[4] O. Shorinwa, R. N. Haksar, P. Washington, and M. Schwager, "Distributed multirobot task assignment via consensus ADMM," *IEEE Trans. Robot.*, vol. 39, no. 3, pp. 1781–1800, Jun. 2023.

[5] J. Hu, P. Bhowmick, I. Jang, F. Arvin, and A. Lanzon, "A decentralized cluster formation containment framework for multirobot systems," *IEEE Trans. Robot.*, vol. 37, no. 6, pp. 1936–1955, Dec. 2021.

[6] W. S. Cortez, C. K. Verginis, and D. V. Dimarogonas, "A distributed, event-triggered, adaptive controller for cooperative manipulation with rolling contacts," *IEEE Trans. Robot.*, vol. 39, no. 4, pp. 3120–3133, Aug. 2023.

[7] P. Chand and D. A. Carnegie, "Mapping and exploration in a hierarchical heterogeneous multi-robot system using limited capability robots," *Robot. Auto. Syst.*, vol. 61, no. 6, pp. 565–579, Jun. 2013.

[8] S.-J. Chung, A. A. Paranjape, P. Dames, S. Shen, and V. Kumar, "A survey on aerial swarm robotics," *IEEE Trans. Robot.*, vol. 34, no. 4, pp. 837–855, Aug. 2018.

[9] A. Amirkhani and A. H. Barshooi, "Consensus in multi-agent systems: A review," *Artif. Intell. Rev.*, vol. 55, pp. 3897–3935, Jun. 2022.

[10] W. Ren, "Consensus based formation control strategies for multi-vehicle systems," in *Proc. Amer. Control Conf.*, Jun. 2006, pp. 4237–4242.

[11] W. Ni and D. Cheng, "Leader-following consensus of multi-agent systems under fixed and switching topologies," *Syst. Control Lett.*, vol. 59, nos. 3–4, pp. 209–217, 2010.

[12] Y. Wu, J. Gou, X. Hu, and Y. Huang, "A new consensus theory-based method for formation control and obstacle avoidance of UAVs," *Aerosp. Sci. Technol.*, vol. 107, Dec. 2020, Art. no. 106332.

[13] L. Cheng and Y.-J. Wang, "Fault tolerance for communication-based multirobot formation," in *Proc. Int. Conf. Mach. Learn. Cybern.*, vol. 1, Aug. 2004, pp. 127–132.

[14] Y. Ding, X. Wang, Y. Cong, and H. Li, "Scalability analysis of algebraic graph-based multi-UAVs formation control," *IEEE Access*, vol. 7, pp. 129719–129733, 2019.

[15] B. P. Gerkey and M. J. Matarić, "A formal analysis and taxonomy of task allocation in multi-robot systems," *Int. J. Robot. Res.*, vol. 23, no. 9, pp. 939–954, Sep. 2004.

[16] G. A. Korsah, A. Stentz, and M. B. Dias, "A comprehensive taxonomy for multi-robot task allocation," *Int. J. Robot. Res.*, vol. 32, no. 12, pp. 1495–1512, 2013.

[17] A. Khamis, A. Hussein, and A. Elmogy, "Multi-robot task allocation: A review of the state-of-the-art," in *Cooperative Robots and Sensor Networks*, vol. 604. Cham, Switzerland: Springer, 2015, pp. 31–51.

[18] H. Chakraa, F. Guérin, E. Leclercq, and D. Lefebvre, "Optimization techniques for multi-robot task allocation problems: Review on the state-of-the-art," *Robot. Auto. Syst.*, vol. 168, Oct. 2023, Art. no. 104492.

[19] S. Mayya, D. S. D'antonio, D. Saldaña, and V. Kumar, "Resilient task allocation in heterogeneous multi-robot systems," *IEEE Robot. Autom. Lett.*, vol. 6, no. 2, pp. 1327–1334, Apr. 2021.

[20] S. Wang, Y. Liu, Y. Qiu, and J. Zhou, "Consensus-based decentralized task allocation for multi-agent systems and simultaneous multi-agent tasks," *IEEE Robot. Autom. Lett.*, vol. 7, no. 4, pp. 12593–12600, Oct. 2022.

[21] Z. Chen, J. Alonso-Mora, X. Bai, D. D. Harabor, and P. J. Stuckey, "Integrated task assignment and path planning for capacitated multi-agent pickup and delivery," *IEEE Robot. Autom. Lett.*, vol. 6, no. 3, pp. 5816–5823, Jul. 2021.

[22] P. Forte, A. Mannucci, H. Andreasson, and F. Pecora, "Online task assignment and coordination in multi-robot fleets," *IEEE Robot. Autom. Lett.*, vol. 6, no. 3, pp. 4584–4591, Jul. 2021.

[23] N. Michael, M. M. Zavlanos, V. Kumar, and G. J. Pappas, "Distributed multi-robot task assignment and formation control," in *Proc. IEEE Int. Conf. Robot. Automat.*, May 2008, pp. 128–133.

[24] C. Gao, J. Ma, T. Li, and Y. Shen, "Hybrid swarm intelligent algorithm for multi-UAV formation reconfiguration," *Complex Intell. Syst.*, vol. 9, no. 2, pp. 1929–1962, Apr. 2023.

[25] J. Fan, Y. Li, Y. Liao, T. Ma, Y. Ge, and Z. Wang, "A formation reconfiguration method for multiple unmanned surface vehicles executing target interception missions," *Appl. Ocean Res.*, vol. 104, Nov. 2020, Art. no. 102359.
[26] D. P. Bertsekas, "The auction algorithm: A distributed relaxation method for the assignment problem," *Ann. Oper. Res.*, vol. 14, no. 1, pp. 105–123, Dec. 1988.
[27] H. Zhu, M. Zhou, and R. Alkins, "Group role assignment via a Kuhn–Munkres algorithm-based solution," *IEEE Trans. Syst., Man, Cybern., A, Syst. Humans*, vol. 42, no. 3, pp. 739–750, May 2012.
[28] K.-K. Oh, M.-C. Park, and H.-S. Ahn, "A survey of multi-agent formation control," *Automatica*, vol. 53, pp. 424–440, Mar. 2015.
[29] X. Fan, Y. Guo, H. Liu, B. Wei, and W. Lyu, "Improved artificial potential field method applied for AUV path planning," *Math. Problems Eng.*, vol. 2020, no. 1, 2020, Art. no. 6523158.

Xuanchun Yin (Member, IEEE) received the B.S. degree in mechanical engineering from Changchun University of Science and Technology, Changchun, China, in 2005, the M.S. degree in mechatronic engineering South China Agricultural University, Guangzhou, China, in 2012, and the Ph.D. degree in intelligent mechanical systems engineering from the Kagawa University, Takamatsu, Japan, in 2016.

He is currently an Associate Professor with the School of Engineering, South China Agricultural University. His research interests include haptics, human–robot interaction, teleoperation system, artificial intelligence, bioinspired robotics, medical robotics, and agricultural robotics.

Huabin Hu received the B.S. degree in engineering from South China Agricultural University, Guangdong, China, in 2022, where he is currently pursuing the M.S. degree with the College of Engineering.

His research interests include multirobot system and formation control.

Linlin Shi received the B.E. degree in electrical engineering and automation and the Ph.D. degree in control theory and control engineering from Zhejiang University of Technology, Hangzhou, China, in 2016 and 2022, respectively.

She is currently with the College of Engineering, South China Agricultural University, Guangdong, China. Her research interests include cooperative estimation and distributed control in multirobot systems.

frontiers | Frontiers in Plant Science

TYPE Original Research
PUBLISHED 22 January 2025
DOI 10.3389/fpls.2024.1518294

OPEN ACCESS

EDITED BY
Junfeng Gao,
University of Lincoln, United Kingdom

REVIEWED BY
Chao Qi,
Jiangsu Academy of Agricultural Sciences (JAAS), China
Zhili Zhang,
Chinese Academy of Sciences (CAS), China

*CORRESPONDENCE
Linlin Shi
lynnshi@zju.edu.cn

RECEIVED 28 October 2024
ACCEPTED 31 December 2024
PUBLISHED 22 January 2025

CITATION
Li J, Wu K, Zhang M, Chen H, Lin H, Mai Y and Shi L (2025) YOLOv8s-Longan: a lightweight detection method for the longan fruit-picking UAV. *Front. Plant Sci.* 15:1518294. doi: 10.3389/fpls.2024.1518294

YOLOv8s-Longan: a lightweight detection method for the longan fruit-picking UAV

Jun Li[1,2,3], Kaixuan Wu[1], Meiqi Zhang[1], Hengxu Chen[1], Hengyi Lin[1], Yuju Mai[1] and Linlin Shi[1]*

[1]College of Engineering, South China Agricultural University, Guangzhou, China, [2]Guangdong Laboratory for Lingnan Modern Agriculture, Guangzhou, China, [3]State Key Laboratory of Agricultural Equipment Technology, Beijing, China

Introduction: Due to the limited computing power and fast flight speed of the picking of unmanned aerial vehicles (UAVs), it is important to design a quick and accurate detecting algorithm to obtain the fruit position.

Methods: This paper proposes a lightweight deep learning algorithm, named YOLOv8s-Longan, to improve the detection accuracy and reduce the number of model parameters for fruitpicking UAVs. To make the network lightweight and improve its generalization performance, the Average and Max pooling attention (AMA) attention module is designed and integrated into the DenseAMA and C2f-Faster-AMA modules on the proposed backbone network. To improve the detection accuracy, a crossstage local network structure VOVGSCSPC module is designed, which can help the model better understand the information of the image through multiscale feature fusion and improve the perception and expression ability of the model. Meanwhile, the novel Inner-SIoU loss function is proposed as the loss function of the target bounding box.

Results and discussion: The experimental results show that the proposed algorithm has good detection ability for densely distributed and mutually occluded longan string fruit under complex backgrounds with a mAP@0.5 of 84.3%. Compared with other YOLOv8 models, the improved model of mAP@0.5 improves by 3.9% and reduces the number of parameters by 20.3%. It satisfies the high accuracy and fast detection requirements for fruit detection in fruit-picking UAV scenarios.

KEYWORDS

longan, lightweight network, attention mechanism, YOLOv8-Longan network, target detection

1 Introduction

Longan, a special fruit native to tropical and subtropical regions, is favored for its unique flavor and rich nutrition. However, longan has a relatively short ripening period, and timely picking is essential to ensure fruit quality. At present, longan is mainly harvested manually. However, the manual picking of tall longan trees has high labor intensity and high operation risk. Therefore, developing agricultural robots that can automatically pick longan has great economic value. Although some researchers have developed fruit harvesting robots (Yang et al., 2023, it is necessary to develop more adaptive harvesting robots according to the growth characteristics of large longan trees to improve picking efficiency and reduce labor costs to promote the development of modern agriculture.

Robotic picking is currently being studied by a wide range of scholars (Shi et al., 2023; Dairath et al., 2023). He et al. built a robotic vision servo system for tomato picking utilizing a depth camera and a six-degree-of-freedom manipulator. The system utilizes depth and color information of fruit targets and adopts a coordinated control strategy for the hand and eye at different distances (He et al., 2021). Liang et al. developed a facility-based cultivation grape-picking robot using a monocular camera and a distance-measuring sensor to identify clusters and locate the fruit branch cutting points for fast, efficient, and low-loss grape picking (Liang and Wang, 2023). However, robotic arm-type picking devices suffer from limited operating range, low picking flexibility, and poor maneuverability, which limit the advantages of automated picking. Aiming at the string fruit growth characteristics of tall longan trees, further development of more adapted harvesting robots is needed to improve picking efficiency and reduce labor costs.

Compared with traditional ground-based mechanical equipment, the unmanned aerial vehicle (UAV) has a wide range of application prospects in fruit-picking tasks due to their smaller size, good maneuverability, and strong adaptability to complex terrain (Chen et al., 2024a; Lu et al., 2024; Zhaosheng et al., 2022). Longan fruit in the fruit tree shows the characteristics of irregular, inconspicuous, and widely distributed string fruit growth characteristics, and its natural background is more complex, prone to multiple clusters of longan string fruits overlapping each other, as well as by the fruit tree branches and leaves cover and so on. In order to achieve accurate detection of longan string fruits, deep learning target detection techniques have been applied to string fruit detection in agricultural work scenarios due to their ability to extract complex patterns and regularities by learning a large amount of data (Li et al., 2021; Ding et al., 2024, 2022). Among them, Li et al. proposed an improved YOLOv7-litchi detection algorithm by integrating ELAN-L and ELAN-A modules based on lightweight ELAN on the backbone network, which makes the network structure lightweight and provides a theoretical basis for mechanized lychee harvesting (Li et al., 2024). Huang et al. proposed Triplet-Large Kernel Attention (TLKA). The TLKA module inherits the advantages of channel attention and large kernel attention, and TLKA-YOLOv7 outperforms all other research models in grape string detection and segmentation and obtains more competitive results in yield prediction (Huang and Li, 2023). Chen et al. proposed an improved YOLOv7-based multi-task deep convolutional neural network (DCNN) detection model MTD-YOLOv7 with two additional decoders for detecting tomato fruit cluster ripeness based on YOLOv7 (Chen et al., 2024b). Liu et al. (2024) proposed the MAE-YOLOv8 model using YOLOv8s-p2 as the baseline and introduced MPDIoU as the regression loss function to accurately detect Qing crisp plum in the actual complex orchard environment. Meanwhile, YOLOv8 is compared with other YOLO series models. In the Backbone network part, the YOLOv8 model uses the DarkNet-53 network structure, uses C2f to replace the C3 module, and uses the faster SPPF module. In the Neck network part, the YOLOv8 model uses the PAN-FPN network structure that removes the convolution structure in the upsampling stage. In the Head network part, YOLOv8 uses the Decoupled-Head network structure to separate the classification and detection heads. The YOLOv8 model is an anchor-free model, which directly predicts the center of the object rather than the offset of the known Anchor box. These improvements make YOLOv8 show higher performance and accuracy in object detection tasks, which are more widely studied by scholars (Sun, 2024; Jiang et al., 2023; Wang et al., 2024).

The above research is dedicated to optimizing deep learning models to improve their ability to detect string fruits. However, in the practical problems of agricultural automated picking tasks, when the fruit-picking UAV performs the longan-picking task, limited by the endurance, computing resources, and dynamic characteristics of fast flight, a lightweight and high-precision object detection model is needed.

In response to the above challenges, the key issues addressed in this paper are mainly divided into two aspects: i) model lightweight and ii) recognition and detection accuracy improvement. Specifically, the model is lightweight to solve the problem of the limited endurance of UAVs. The high demand for complex neural networks for computing resources will increase energy consumption and affect the operation time and identification and detection efficiency of UAVs. The improvement of detection accuracy is to ensure that the UAV can accurately identify and locate the target fruit in the process of rapid flight, reduce the recognition error, and improve the picking accuracy. Due to the irregular, inapparent, and widely distributed characteristics of longan bunches on the fruit tree, traditional detection methods often have difficulty balancing between real-time performance and accuracy.

To this end, the YOLOv8s-Longan model is proposed in this paper. In this paper, we propose a novel solution to realize longan picking using the fruit-picking UAV. It will help to improve object detection accuracy for the vision-based fruit-picking UAV in natural environments. A dataset of UAV-collected longan images is built to train and evaluate object detection models. The main contributions of this paper are listed in the following three parts.

1. Considering the limited computing power and fast flight speed of the UAV, this paper first proposes a lightweight deep learning model, named YOLOv8s-Longan, to obtain real-time fruit location in complex backgrounds.

2. For model lightweight, the Average and Max pooling attention (AMA) attention module is designed and integrated into the DenseAMA and C2f-Faster-AMA modules on the proposed backbone network to reduce the number of parameters and the number of calculations to make the network lightweight.
3. For detection accuracy, a novel Inner-SIoU loss function is designed, and the cross-stage local network structure VOVGSCSPC module is integrated into the neck network, which improves the model's ability to accurately locate the target longan and facilitates the UAV to move more stably to the designated location for picking.
4. The proposed model is actually developed on the UAV and occupies 18.1 MB of storage memory, which can process 45 to 50 images per second, and the average recognition accuracy of the real longan orchard scenario is 87.5%. It can meet the lightweight and accurate recognition of the longan fruits by the fruit-picking UAV.

2 Materials

2.1 Image acquisition equipment

In this paper, the structure of the independently developed and designed fruit-picking UAV is shown in Figure 1. An RGB-D camera named RealSense D435i is installed for image acquisition, which combines the features of a color camera and an infrared camera. To enhance the model's generalization, the images of Shek Kip and Chuliang longan are collected. To fully restore the real scene of UAV picking longan and the complexity of the orchard environment, the images within the range of 400–700 mm (near view) and 700–1,100 mm (far view) from the longan string are selected as the dataset. The dataset includes images taken under various lighting conditions, such as full sun and backlight, to ensure the acquired images are not disturbed by artificial shadows or lights.

2.2 Image dataset preprocessing

2.2.1 Image filtering

The 1,070 collected images were screened and reviewed, and images with high-definition and rich details were selected. Images with poor quality, severe exposure, and only a single string of fruit were eliminated to ensure the accuracy and stability of the subsequent algorithm.

2.2.2 Image flipping and brightness adjustment

Self-programmed image left–right flip and brightness adjustment algorithms are used to expand the image data to ensure the diversity of image data. In this way, the dataset is expanded from the original 438 longan images to obtain 2,460 images, and Table 1 shows the statistics of the categories and numbers of images in the dataset.

2.2.3 Image annotation

For 2,460 images, manual annotation and classification label definition are performed, where string fruit means a string of longan from the first to the last branch on the fruiting mother branch. The annotated dataset is divided according to the ratio of the training set to the test set (4:1), and 1,968 training images and 492 test images are obtained. As shown in Table 2, the number of images and annotation information contained in the dataset are counted, and the images of the test set are grouped according to the set standards to prepare for the grouping test of the network model and to examine the effectiveness of the network model in various interference cases.

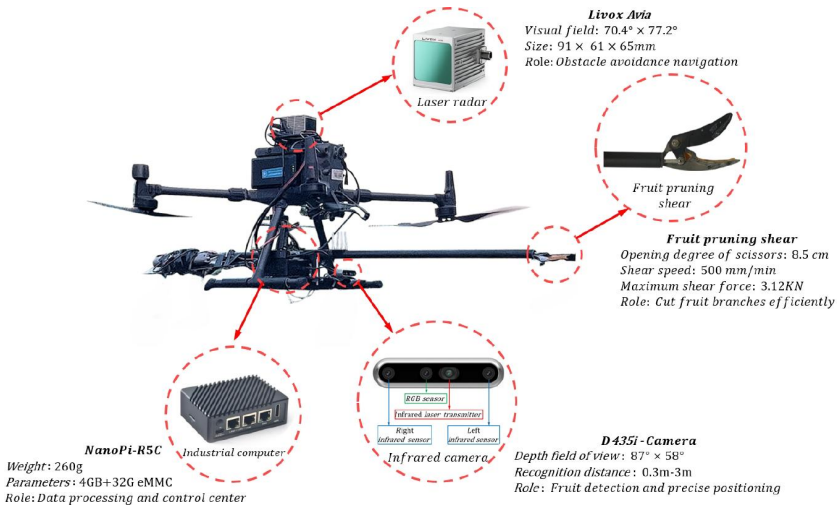

FIGURE 1
The structure of the fruit-picking UAV. UAV, unmanned aerial vehicle.

TABLE 1 Image categories and number.

Influence factor	Image category	Number of images
Original image	/	438
Flip degree	Left and right flip	438
Light conditions	Very highlights (flag = 0.3:0.4) Highlights (flag = 0.5:0.8) Shadows (flag = 1.2:1.5) Polar shadows (flag = 2.5:3.0)	1,584

TABLE 2 Details of the dataset.

	Number of images	Number of bounding boxes
Total dataset	2,460	34,302
Train dataset	1,968	28,554
Test dataset	492	5,748

3 The YOLOv8s-Longan detection method

3.1 Overall network structure

To improve the performance of the deep learning visual model for longan string fruit picking, the algorithm in this study is based on the YOLOv8 detection model to construct a lightweight YOLOv8s-Longan model, which is composed of three main parts: the backbone, neck, and head. The overall structure is shown in Figure 2. The detailed procedure of YOLOv8s-Longan is shown in Algorithm 1. The backbone serves as the backbone network of the model, consisting of the DenseAMA module, C2f-Faster-AMA module, and SPPF module. The input image is first passed through the densely connected DenseAMA module as the feature extractor to replace the first Conv and C2f combination module in the backbone network, which strengthens the feature learning ability of longan string fruit and mitigates the problem of insufficient features of longan string fruit in complex orchard environments. Then, the C2f-Faster-AMA module is used to replace the C2f module in the subsequent backbone network,

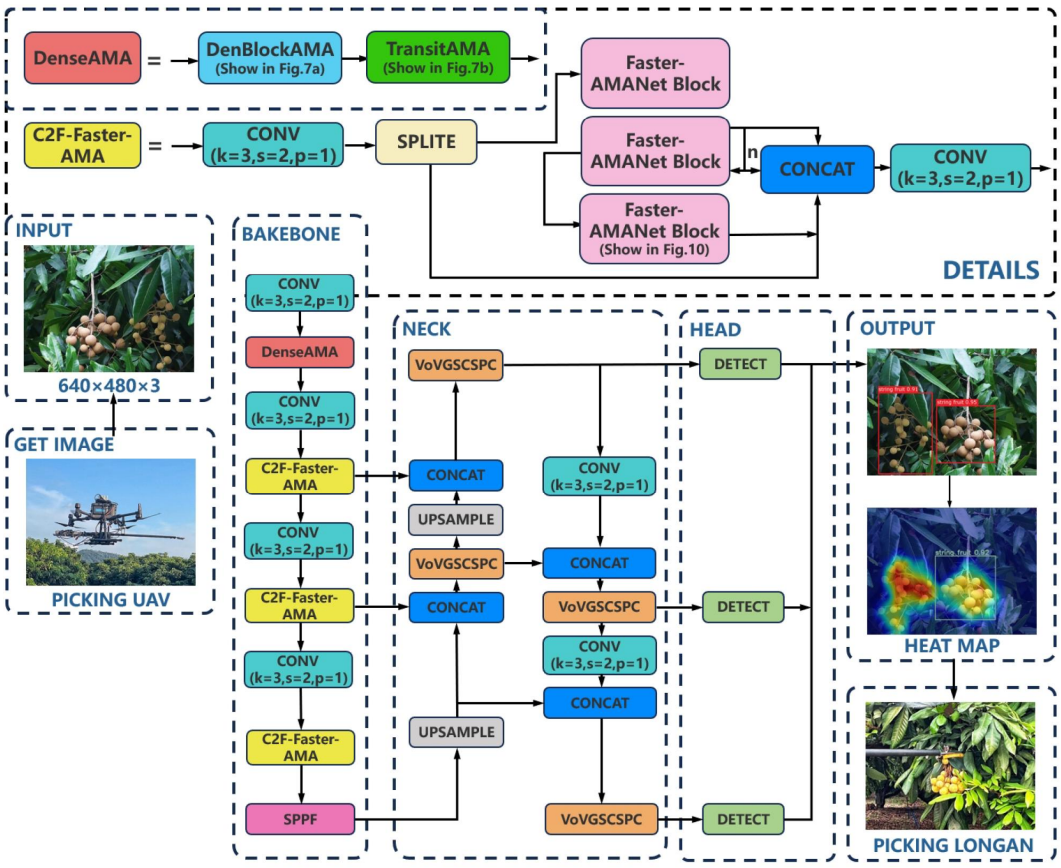

FIGURE 2
YOLOv8s-Longan network structure.

which can significantly reduce the amount of computation and memory access, thus lightening the backbone network and improving the inference speed of the model, which is conducive to the real-time detection of longan string fruit by the UAV during flight. Finally, the multiscale features are fused through the SPPF module of the backbone network. The features of the same longan string fruit feature map at different scales are fused to enrich the semantic features of the longan string fruit feature map, improve the attention given to important details of the string fruit features, and enhance the quality of the features obtained by the model.

Require: image size $\mathbb{S}$; Learning rateλ; Number of epochs $\mathbb{T}$.

Ensure: Pixel label

1: The Mosaic data augmentation strategy is used to concatenate the four images to generate a brand new image.

2: **for** $t = 1$ to $\mathbb{T}$ **do**

3: Feature maps with higher semantics are generated by Equations 3 and 4 through the DenseAMA module in Backbone.

4: The C2f-Faster-AMA module is used to lighten the Backbone network and improve the inference speed of the model by Equation 5.

5: The SPPF module is used to fuse multi-scale features.

6: The features of longan sting fruit at different scales are extracted through the VOVGSCSPC module in Neck by Equations 6 and 7.

7: The Inner-SIoU loss function is used to calculate the loss by Equations 8-21.

8: **end for**

9: Perform label prediction for each pixel.

10: **Output:** each pixel label.

Algorithm 1. Lightweight detection method of YOLOv8s-Longan.

The neck is used as the pyramid multiscale feature fusion structure of the model, and the different scales of longan string fruit feature maps output by the backbone are fused to different degrees. The cross-stage local network structure of the VOVGSCSPC module is designed through the aggregation method to replace the C2f module in the neck to reduce the complexity of its network structure and make the YOLOv8s-Longan model easy to deploy to the terminal equipment of the fruit-picking UAV.

The head is used as the model detection output, and the bounding box is generated for the longan string fruit feature maps of different scales output by the neck. The Inner-SIoU loss function is used as the loss function of the target bounding box to improve the positioning ability and prediction accuracy of the target box so that the UAV can more accurately and quickly detect the position information of the longan string in the process of flight.

3.2 Improvement of the backbone network

3.2.1 Proposed the AMA attention module

Longan fruits usually grow in the form of string fruits and show irregular, inconspicuous, and widely distributed features on the fruit trees. Moreover, the natural background of longan string fruits is complicated, and multiple clusters of longan string fruits overlap with each other, as well as being shaded by the branches and leaves of the fruit trees.

Meanwhile, different levels of longan feature maps usually have different background noise distributions and also generate redundant information due to differences in scale and location of longan string fruit feature maps. Therefore, in this paper, feature fusion is used to suppress the background noise of individual longan string fruit feature maps and generate more discriminative feature representations. In order to suppress the interference of negative information such as multiple cluster occlusion of longan string fruits and occlusion of fruit tree branches and leaves, the authors propose an AMA module, which is weighted by average pooling and maximum pooling, to reduce the negative impact of redundant information and noise on the network, improve the network's attention to longan string fruits, and help the model to focus on the most distinguishable and important features in the input.

The structure of the AMA attention module is shown in Figure 3. First, one-dimensional convolution is used to replace the fully connected layer, effectively reducing the weight parameters and increasing the inference speed, where W, H, and C are the width, height, and channel size of the feature vector, respectively. Then, global average pooling (GAP) and global maximum pooling (GMP) are performed on the last convolution output to aggregate the convolution features without dimensionality reduction.

Subsequently, channel feature learning is performed with the same dimension, and one-dimensional convolution is used to quickly capture the cross-channel information interaction between each channel and its nearly K adjacent channels. Thus, there is a non-linear mapping between K and C, as in Equations 1 and 2.

$$C = \omega(K) = \left| \left(\frac{gK - b}{a} \right)^{\frac{1}{0.35}} \right|, \tag{1}$$

$$K = \varphi(C) = \left| \left(\frac{aC^{0.35} + b}{g} \right) \right|, \tag{2}$$

where $a = 2$, $b = 1$, and $g = 4$.

The activation value of the one-dimensional convolution is calculated by the sigmoid activation function, and different weights are obtained to show the relevance and importance of the longan string features between channels. Finally, the learnable weight

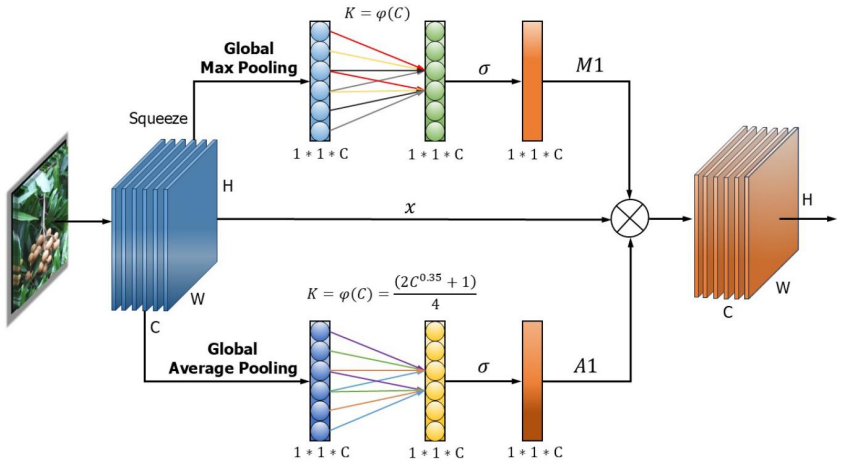

FIGURE 3
Structure of the AMA attention module. AMA, Average and Max pooling attention.

coefficients (A1, M1) of each channel are generated by GAP and GMP. Then, the weight of each channel is weighted to the original input feature map to complete the recoding of each channel feature so that the important features are assigned large weights to be enhanced, and the effective longan string fruit features are enhanced. Instead, the negative environmental features of ineffective nature are assigned a small weight to suppress.

The AMA attention module avoids information loss caused by mapping the input longan features to low dimensions. Additionally, it can capture cross-channel interactions effectively, better capture the important feature information of the target to be detected, enhance the feature extraction ability of the network, and make the model use global features to distinguish the image information level. In addition, this AMA attention module has fewer parameter requirements, which avoids the excessive complexity of the model and compensates for the loss in accuracy caused by the model being lightweight, increasing the effectiveness of channel learning attention and leading to obvious performance gains in the network. It is beneficial to integrate into the subsequent DenseAMA and C2f-Faster-AMA modules more effectively and improve the module's longan string fruit feature extraction ability.

3.2.2 Proposed the DenseAMA module

In the detection of missed fruit in the agricultural field, the longan background image usually has the problems of unobvious features, complexity, and redundancy. Using the feature extraction module C2F developed based on natural view images may lead to insufficient extracted longan string fruit feature information, which limits the performance of the model in detection tasks. To this end, a densely connected DenseAMA module is proposed as a feature extractor to replace the first Conv and C2f combination module in the backbone network, which is used to extract features of various scales from the input image, and the output of each layer is directly connected with the input of all subsequent layers. This connection makes the information flow of the network more sufficient, helps to prevent the vanishing gradient problem, and can use low-level features to supplement high-level features.

In computer vision, the main idea of DenseNet is to build dense connections, that is, to promote the reuse of features by connecting features between different channels (Jia et al., 2023; Cai et al., 2022). These properties allow DenseNet to maintain low model parameters and computational costs. The dense connection mechanism of DenseNet is shown in Figure 4, and its expression is below.

$$X_l = W_l * [X_0, X_1, \ldots, X_n, \ldots, X_{L-1}], \tag{3}$$

X_n is the feature output of each layer through the convolutional network, W_l is the weight of each dense layer, where l is the layer index, and $*$ is the composite function of operations such as batch normalization (BN), rectified linear unit (ReLU), pooling, or convolution.

DenseNet has multiple DenseBlocks, the inner layers of each DenseBlock are densely connected DenseLayer modules (by superposition rather than addition), and the dense blocks of different DenseBlocks are downsampled by transition layers. In this paper, the original DenseNet121 is used as the basic structure, and the H-swish activation function and the AMA attention mechanism are connected in the DenseBlock and transition layers to obtain the DenseAMA module.

Moreover, the H-swish (Sunkari et al., 2024; Mercioni and Holban, 2020) activation function has a low computational cost and comprises simple multiplication and addition operations, which can be calculated faster in model inference and training. The equation is shown in Equation 4:

$$\begin{aligned} \text{HardSwish}(x) &= x \times \text{HardSigmiod}(x) \\ &= x \times \frac{\text{ReLu6}(x+3)}{6} \\ &= x \times \begin{cases} 1, & x \le 2 \\ \frac{x}{6} + \frac{1}{2}, & -3 \le x \le 3 \\ 0, & x \le 3 \end{cases} . \end{aligned} \tag{4}$$

It shows that H-swish activation functions have strong similarities in terms of upper and lower boundaries, smoothness, and monotonicity. After replacing the sigmoid activation function

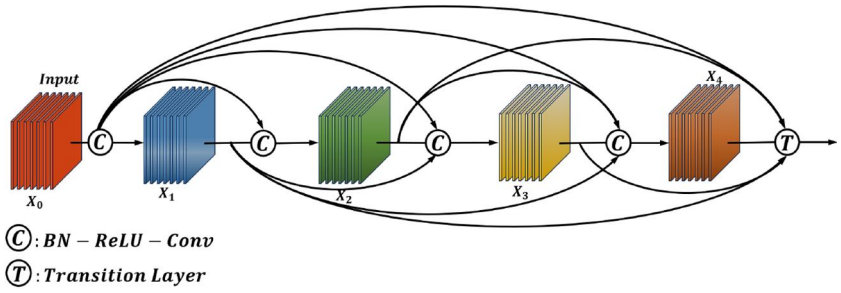

FIGURE 4
Schematic diagram of the DenseNet structure.

with the H-swish activation function, the number of parameters and the calculations in the model can be effectively reduced. When the backpropagation algorithm is trained, the H-swish activation function has a lower gradient saturation problem, which means that it is easier to train in the deep neural network, which can effectively enhance the feature extraction ability and eliminate the potential accuracy loss. Therefore, the H-swish activation function is more suitable for improving mode performance.

The DenseAMA module consists of three stages, where the first and second stages form the DenseLayerAMA layer and the third stage forms the TransitAMA layer, as shown in Figure 5. In the first stage, a BN operation is performed on the input longan feature map, and the H-swish activation function is used to activate the feature map. Then, a 1 × 1 convolution kernel is used to reduce the number of parameters.

The second stage is similar to the first. The input feature map is batch normalized and activated by the H-swish activation function. Then, a 3 × 3 convolution kernel is used to convolve the feature map. Finally, to reduce the number of parameters and calculations in the model as much as possible, the AMA attention mechanism module designed in this paper is added after the 3 × 3 convolution operation in the second stage, and the AMA attention module is used to extract features of the string fruit feature map to enhance the utilization ability of longan string fruit features. The DenseLayerAMA layer structure is shown in Figure 5A.

The TransitAMA layer in the third stage first inputs the feature map for the BN operation and uses the H-swish activation function for activation. It is processed by the AMA attention mechanism, and the average pooling operation is performed on the processed feature map to reduce the size of the input feature map by half. It can better reduce the spatial dimension of the feature map and the number of calculations and increase the receptive field size to better capture global information. The transition layer of the third stage connects the two adjacent dense blocks of the first and second stages to each other, which reduces the size of the feature map and plays the role of a compression model. The network structure of the TransitAMA layer is shown in Figure 5B.

The DenseAMA module is used to replace the first Conv and C2f combination modules in the backbone network. The DenseAMA module can effectively take advantage of feature reuse while retaining the original string fruit feature information and significantly enhancing its semantics, making the low-level features richer and more detailed, and generating feature maps with higher semantics. This method helps to alleviate the problem that the longan string fruit features in agricultural scenes may be submerged by redundant background information when the depth of the model increases so that the UAV can accurately and effectively identify longan string fruit during flight and improve the adaptability to complex environments.

3.2.3 Proposed C2f-Faster-AMA module

Although the accuracy of the YOLOv8 algorithm is improved compared with that of the previous version, the model is relatively complex and has a large number of parameters. When deploying the model in the field, the requirements for equipment performance are too high, and the model is not suitable for fruit-picking UAV terminal equipment. Therefore, the C2f module is improved to reduce the number of parameters and the model size, which

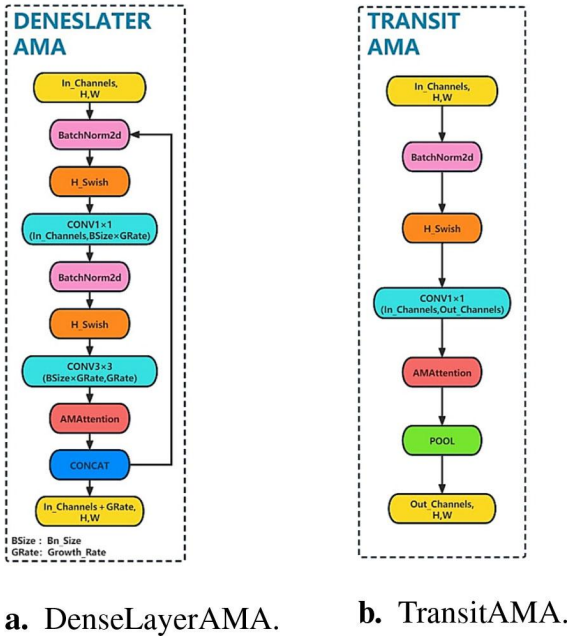

FIGURE 5
Local structure diagram of the DenseAMA module. **(A)** DenseLayerAMA. **(B)** TransitAMA.

overcomes the shortcomings of the YOLOv8 network in that the number of model parameters is too large and deployment is difficult.

Therefore, the simpler C2f-Faster-AMA module is proposed with the PConv convolution way to replace the last three C2f modules in the backbone network. By reducing the computations and memory access to extract features effectively, it can dynamically learn the relationships between different parts of the input, better understand the relationships and dependencies between longan data, and improve the performance of the YOLOv8s-Longan model.

Inspired by the FasterNet network, the bottleneck in the C2f module is replaced by Faster-Block, which reduces FLOPs while maintaining high FLOPS. The structure of the Faster-Block module is shown in Figure 6A.

Faster-Block consists of PConv and regular Conv modules. The PConv module can reduce both computational redundancy and memory access. The working principle of the PConv module is shown in Figures 6B, C. It shows that PConv only applies conventional Conv for spatial feature extraction on the part of the input channels, and the remaining channels remain unchanged. For consecutive or regular memory access, we compute the first or last consecutive c_p channel as a representative of the entire feature map. Without loss of generality, the input and output feature maps have the same number of channels, as shown in Equation 5.

$$h \times w \times 2c_p + k^2 \times c_p^2 \approx h \times w \times 2c_p \tag{5}$$

where h, w, and c_p represent the height, width, and number of channels of the feature map, and k represents the size of the convolution kernel.

The Faster-AMANet block module is obtained by integrating the AMA attention mechanism into the FasterNet block and replacing the bottleneck in C2f to obtain the C2f-Faster-AMA module. The C2f-Faster-AMA module is used to replace the last three C2Fs in the backbone network, which can reduce the redundant calculation and memory access of the model, extract spatial features more effectively, and better understand the connections and dependencies between longan data. Thus, the lightweight and real-time detection of the YOLOv8s-Longan model is ensured, so the UAV can adjust its flight attitude according to the detection results of the vision model in real-time and realize safe and stable picking work. The C2f-Faster-AMA module structure is shown in Figure 6D.

3.3 Integration into the neck structure of VOVGSCSPC

By integrating the cross-stage local network structure of the VOVGSCSPC module designed by the fusion method, the C2f module in the neck part is replaced to fuse multiple longan string feature maps of different scales better (Xu et al., 2023; Zhu et al., 2024). The VOVGSCSPC module can extract richer semantic information, and multiscale feature fusion can help the model better understand the

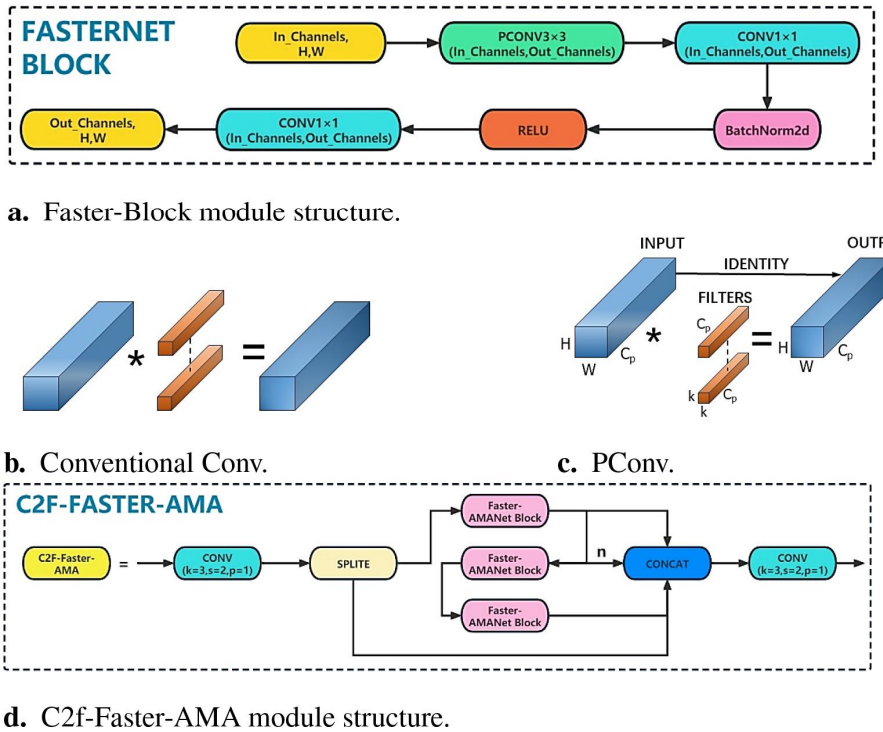

FIGURE 6
The specifics of the C2f-Faster-AMA module. **(A)** Faster-Block module structure. **(B)** Conventional Cony. **(C)** PCony. **(D)** C2f-Faster-AMA module structure.

global and local information of the longan image and improve the perception and expression ability of the model.

To further reduce the model complexity, through the idea of ResNet, the VOVGSCSPC module is introduced to replace the original C2f module. The VOVGSCSPC module uses a cross-stage local network designed by the aggregation method, and the structure is shown in Figure 7. In GSBottleneck, the idea of a residual is adopted. The output is obtained by adding the residual of the input feature map after two GSConv convolutions and one DWConv depth convolution.

The above process is expressed as

$$GSB_{out} = F_{GSC}\left(F_{GSC}\left(\alpha(X_{C_1})_{\frac{C_1}{2}}\right)\right) + \alpha(X)_{\frac{C_1}{2}}, \tag{6}$$

$$VOVGSCSPC_{out} = \alpha\left(Concat\left(GSB_{out}, \alpha(X_{C_1})\right)\right), \tag{7}$$

where C_1 is the number of channels of the input feature map X_{C_1}, α is the conventional convolution, GSB_{out} is the output of GSBottleneck, and $VOVGSCSPC_{out}$ is the final output of this module. The VOVGSCSPC neck structure balances the accuracy and speed of the model well and reduces the complexity of the calculation and network structure, making the YOLOv8s-Longan model lightweight and easier to deploy for fruit-picking UAV terminal equipment while maintaining sufficient accuracy and utilization of the extracted features.

3.4 Improvement of the Inner-SIoU loss function

The angle between the real bounding box and the predicted bounding box is ignored in different detection tasks to compensate for the existing IoU loss function, resulting in weak generalization ability and slow convergence speed in the training process, which easily results in a poor model. In this paper, the InnerSIoU loss function is proposed to capture the location information of defects more accurately and further improve the robustness of the algorithm.

In the Inner-SIoU, the use of an auxiliary bounding box is proposed to calculate the loss to accelerate the bounding box regression process, and the scale factor ratio is introduced to control the scale of the auxiliary bounding box. By using auxiliary bounding boxes of different scales for different datasets and detectors, we can overcome the limitations of existing methods in terms of their generalizability.

As shown in Figure 8A, the Ground truth and Anchor boxes are b^{gt} and b, respectively. (x_c^{gt}, y_c^{gt}) is the center point of the GT box and the center point of the inner GT box, while the center point of the Anchor box and the inner Anchor box is denoted by (x_c, y_c). The width and height of the GT box are denoted by w^{gt} and h^{gt}, respectively, while the width and height of the Anchor box are denoted by w and h, respectively. The variable "ratio" corresponds to the scaling factor and is typically in the range [0.5, 1.5]. The relevant formulas are shown in Equations 8 and 14, which describe the adjustment process of the Anchor box with respect to the GT box. In these formulas, the Anchor box is scaled and displaced by the scaling factor ratio.

$$b_l^{gt} = x_c^{gt} - \frac{\omega^{gt} \times ratio}{2},\ b_r^{gt} = x_c^{gt} + \frac{\omega^{gt} \times ratio}{2}, \tag{8}$$

$$b_t^{gt} = y_c^{gt} - \frac{h^{gt} \times ratio}{2},\ b_b^{gt} = y_c^{gt} + \frac{h^{gt} \times ratio}{2}, \tag{9}$$

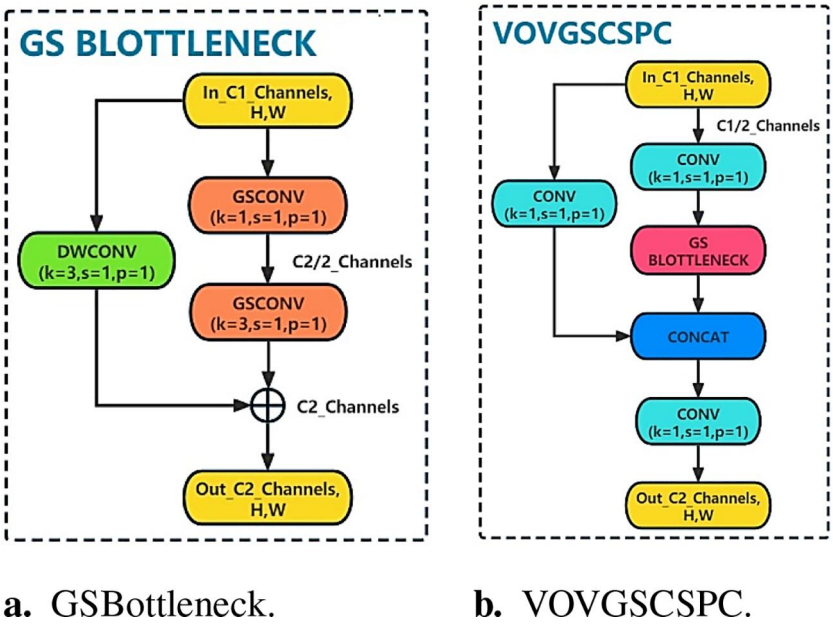

a. GSBottleneck. **b.** VOVGSCSPC.

FIGURE 7
VOVGSCSP module structure. **(A)** GSBottleneck. **(B)** VOVGSCSPC.

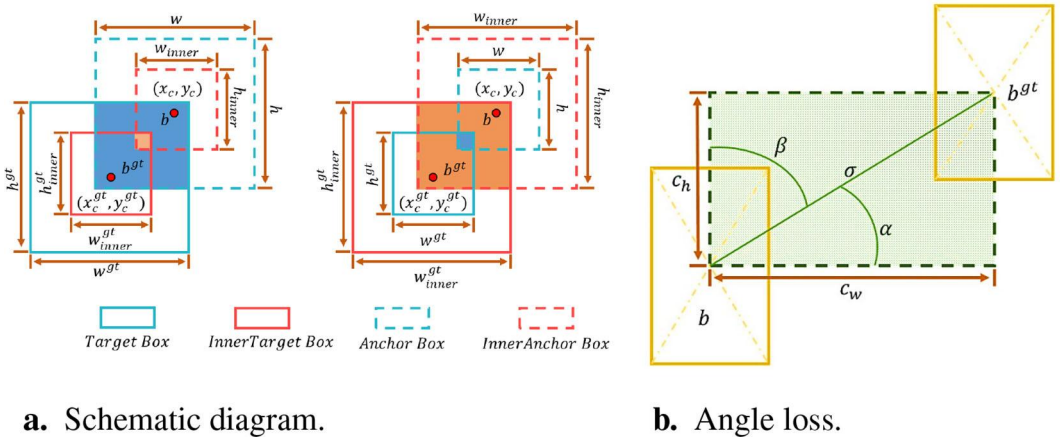

FIGURE 8
The specifics of the Inner-SIoU. **(A)** Schematic diagram. **(B)** Angle loss.

$$b_l = x_c - \frac{\omega \times ratio}{2},\ b_r = x_c^{gt} + \frac{\omega \times ratio}{2}, \tag{10}$$

$$b_t = y_c - \frac{h \times ratio}{2},\ b_t = y_c^{gt} + \frac{h \times ratio}{2}, \tag{11}$$

$$inter = \left(\min\left(b_r^{gt}, b_r\right) - \max\left(b_l^{gt}, b_l\right)\right) \times \left(\min\left(b_b^{gt}, b_b\right) - \max\left(b_t^{gt}, b_t\right)\right), \tag{12}$$

$$union = \omega^{gt} \times h^{gt} \times ratio^2 + \omega \times h \times ratio^2 - inter, \tag{13}$$

$$IoU^{inner} = \frac{inter}{union}. \tag{14}$$

The Inner-SIoU loss function inherits some characteristics of IoU and has unique characteristics. The range of Inner-SIoU and IoU loss functions is the same, which is [0, 1]. Since there is only a scale difference between the auxiliary bounding box and the actual bounding box, the loss function is calculated in the same way. Therefore, the Inner-IoU bias curve shows a similar trend to the IoU bias curve.

Additionally, the Inner-SIoU loss function redefines the loss index by the angle of the regression vector, which comprises three functions: angle loss, distance loss, and shape loss (Dong and Duoqian, 2023; Lawal et al., 2023). Here, the angle loss is defined as

$$\Lambda = 1 - 2\sin^2\left(\arcsin x - \frac{\pi}{4}\right), \tag{15}$$

$$x = \frac{c_h}{\sigma} = \sin\alpha, \tag{16}$$

$$\sigma = \sqrt{\left(b_{c_x}^{gt} - b_{c_x}\right)^2 + \left(b_{c_y}^{gt} - b_{c_y}\right)^2}, \tag{17}$$

$$C_h = \max\left\{b_{c_y}^{gt}, b_{c_y}\right\} - \min\left\{b_{c_y}^{gt}, b_{c_y}\right\}, \tag{18}$$

where $\left(b_{c_x}^{gt}, b_{c_y}^{gt}\right)$ are the real bounding box coordinates, $\left(b_{c_x}, b_{c_y}\right)$ are the predicted bounding box coordinates and a is the vector Angle. The angle loss is shown in Figure 8B.

The distance loss is defined as Equations 19 and 20:

$$\Delta = \sum_{t=xy}\left(1 - \exp^{-\gamma\rho_t}\right). \tag{19}$$

where

$$\rho_x = \left(\frac{b_{cx}^{gt} - b_{cx}}{c_w}\right)^2, \rho_y = \left(\frac{b_{cy}^{gt} - b_{cy}}{c_h}\right)^2, \gamma = 2 - \Lambda \tag{20}$$

The shape loss is defined in Equations 21 and 22:

$$\Omega = \sum_{t=\omega,h}\left(1 - \exp^{-\omega_t}\right)^{\theta}. \tag{21}$$

where

$$\omega_w = \frac{|w - w^{gt}|}{\max\{w, w^{gt}\}}, \omega_h = \frac{|h - h^{gt}|}{\max\{h, h^{gt}\}}, \tag{22}$$

where ω and h are the width and height of the predicted bounding box, respectively; ω^{gt} and h^{gt} are the width and height of the true bounding box, respectively. In summary, the loss function of Inner-SIoU is

$$L_{Inner-SIoU} = 1 - IoU^{inner} + \frac{\Delta + \Omega}{2}, \tag{23}$$

When α tends to 0, the angle cost Λ will also tend to 0, which means that the influence of Λ on the Inner-SIoU is greatly reduced. When α tends to 3.14/4, Λ takes the maximum value, which means that it has the greatest impact on the Inner-SIoU. This approach fully considers the angle between the real bounding box and the predicted bounding box, improving the target box localization ability and prediction accuracy.

4 Experimental results and analysis

In this paper, 1,070 images of the longan dataset from the Longan Garden of the Guangdong Academy of Agricultural

Sciences are used. After manual screening, annotation, and data expansion, 2,460 longan dataset images are obtained for model training and evaluation. The dataset contains images captured by fruit-picking UAV cameras with different lighting conditions, densities, angles, and longan species, which cover a wide range and have strong generalizability.

This experiment classifies the selected fruit-picking UAV aerial images, of which 1,968 are used for training and 660 are used for testing. The quantity of data and the size distribution of labels for each category in the training set are shown in Figure 9. The number of labels in each category varies, and the quantity of data between the corresponding categories varies greatly. In addition, most of the points in the label size distribution map are clustered in the bottom-left corner, while a few points are also clustered in the middle part and the top-right corner. This shows that the longan image dataset contains a large number of small- and partially medium-sized objects with diverse sizes, which is consistent with the background and problems studied in this paper.

The experiment is based on the Ubuntu 18.04 operating system, and the environment is Python3.9, CUDA11.7, and Pytorch2.0. The main specifications are as follows: CPU: AMD EPYC 7402 CPU @ 2.80 GHz; GPU: GPU NVIDIA RTX A4000 16G; RAM: Crucial DDR4 3200 1218G; Mechanical hard disk: WD HC550 16TB; Solid-state drive: SAMSUNG 980 1TB; Motherboard: Supermicro H12SSL.

In order to further validate the robustness of the model and avoid the interference of chance factors on the experiments, this section adopts a fivefold cross-validation method to test the system performance, which randomly and evenly divides the longan string fruit dataset into five subsets. Each experiment uses four of the subsets (1,968 sheets) for training and the remaining one (492 pairs) for testing, and the cross-validation is repeated five times to ensure that each subset is validated once as a test set. To ensure the validity of cross-validation, this experiment ensures that there are no images of the same case between the five subsets when dividing the dataset, i.e., to ensure that there are no overlapping cases between the training set and the test set.

To verify the effectiveness of the proposed model algorithm, we conduct a series of lateral comparison experiments and perform comparative ablation analysis on the corresponding improvement points to verify the advancement of the YOLOv8s-Longan model.

Under the same hyperparameters, the experiments are trained, verified, and tested on the basis of the original model, the training epochs are set to 100, the initial learning rate is 0.01, and the termination learning rate is $1e{-}4$.

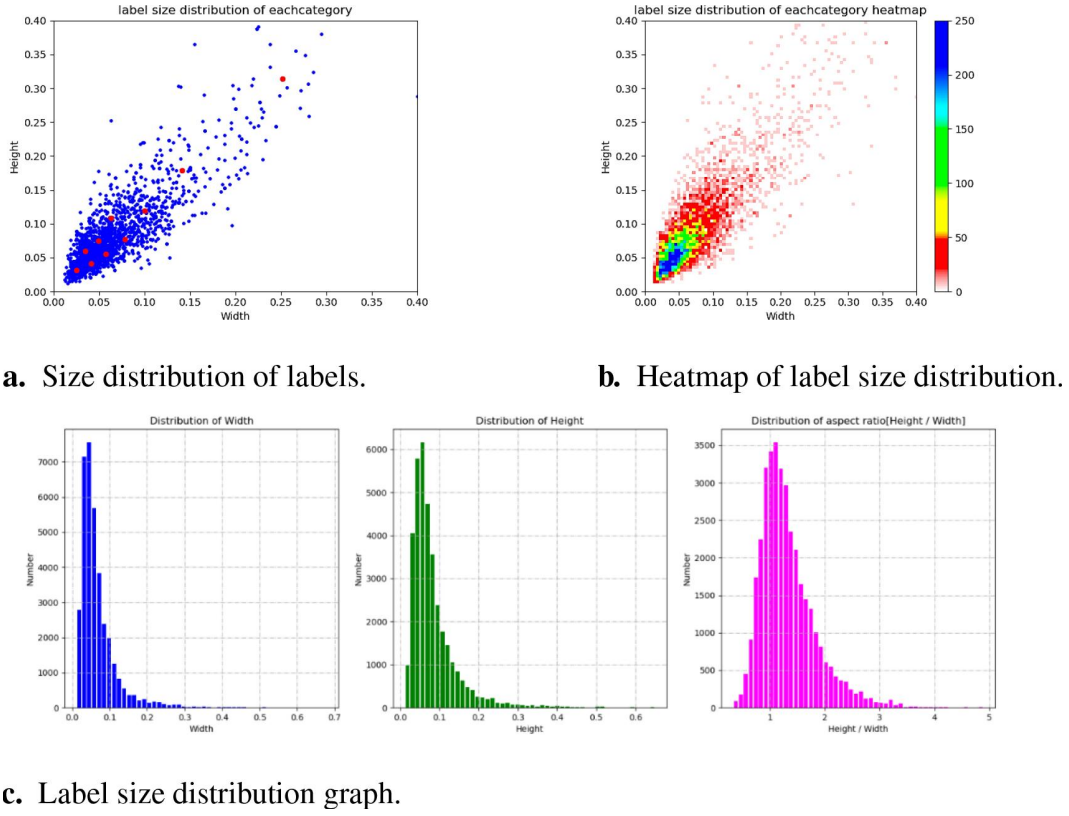

FIGURE 9
Data size of each category and label size distribution. **(A)** Size distribution of labels. **(B)** Heatmap of label size distribution. **(C)** Label size distribution graph.

4.1 Experimental evaluation index

To effectively and intuitively demonstrate the improvement effect of YOLOv8 in this paper, the mean average precision (mAP), the number of model parameters (Params), the total floating-point operations (GFLOPs), and the frame rate of refresh [Frames Per Second (FPS)] are used as the evaluation indexes of model performance (Zhou et al., 2024). The evaluation metrics contain precision, deployability, and speed, which are defined as shown in Table 3.

Efficient ECA channel attention mechanism, which only adds a small number of parameters but obtains performance gains, has some limitations in dealing with global context dependencies and channel spatial relationships. The DenseCBMA module incorporates the CBAM attention mechanism, adding the spatial attention mechanism on the basis of retaining the original channel attention mechanism, optimizing the network from both the channel and spatial aspects, and improving the feature extraction effect of the model from both the channel and spatial perspectives at the same time. Each DenseNet variant module replaces the first set of Conv-C2f modules in the YOLOv8 backbone network, and the experimental results are shown in Table 4.

4.2 DenseAMA module comparison results

The DenseAMA module is built based on the DenseNet module architecture and introduces the AMA attention mechanism module and the H-wish activation function, which are weighted by average and maximum pooling. The DenseNet, DenseAMA, DenseCA, DenseECA, and DenseCBMA modules are also selected for comparison with other DenseNet variants. The DenseAMA module is proposed on the infrastructure of DenseNet and aims to improve the generalization performance of the classifier through adaptive convolutional kernel tuning while enhancing the flow of information and gradients throughout the network. The DenseCA module introduces the CA attention mechanism in the DenseNet network, which focuses on the attention on the channel dimension, and although it may not be as good as the other 384 attention mechanisms for the case of a small number of channels, it can improve the detection accuracy of the model in scenarios with a large number of channels. The DenseECA module incorporates the efficient ECA channel attention mechanism, which not only adds a small number of parameters but also obtains performance gains, but it has some limitations in dealing with global context dependencies and channel spatial relationships. The DenseCBMA module incorporates the CBAM attention mechanism, adding the spatial attention mechanism on the basis of retaining the original channel attention mechanism, optimizing the network from both the channel and spatial aspects, and improving the feature extraction effect of the model from both the channel and spatial perspectives at the same time. Each DenseNet variant module replaces the first set of Conv-C2f modules in the YOLOv8 backbone network, and the experimental results are shown in Table 4.

Table 4 shows that the DenseAMA module improves the mAP@0.5 by 0.9% compared to the DenseNet module with essentially no change in the number of parameters and the amount of computation. Compared to the rest of the DenseNet variant modules, mAP@0.5 improves by 0.83% on average, thus proving the effectiveness of the DenseAMA module in terms of accuracy.

TABLE 3 Experimental evaluation indicators.

Indicator Type	Evaluation indexes	Description
Accuracy	mAP@0.5	During the last 10 epochs of model training, the average AP of all images under each category was calculated when the threshold IoU was set to 0.5.
	mAP@0.5–0.95	During the last 10 epochs of model training, the average AP of all images under each category was calculated when the threshold IoU was set to 0.5–0.95.
	Recall	Proportion of positive longan string fruit samples successfully identified by the model.
Deployability	Parameters (m) GFLOPs (G)	The number of parameters in the model. The number of floating-point operations, which measures the computational complexity of the model.
Speed	FPS (img/s)	Refresh frame rate, which indicates how many images are reasoned per second.

4.3 C2f-Faster-AMA module comparison results

The C2f-Faster-AMA module is built based on the C2f module architecture and introduces the FasterNet and AMA attention mechanism modules. Meanwhile, comparing other residual modules, C2f, C2f-Faster-AMA, C2f-DCNV2, and C2f-DBB residual modules are selected for comparison experiments. The C2f module adopts the concept of multi-level gradient extraction, which enhances the depth of feature extraction and improves the detection accuracy of the model. The C2f-Faster-AMA module is proposed on the basis of FasterNet and aims to reduce the model parameters while maintaining accuracy. The C2f-DCNV2 module adopts a two-branch structure to effectively fuse shared and context-aware weights and aggregate high-frequency local information. The C2f-DBB block aims to improve the feature extraction capability of the network by combining multiple branches for feature extraction using convolutional kernels of different sizes, which are merged or spliced together to form a more master-rich representation. The C2f module is replaced by each residual module in the backbone network, and the experimental results are shown in Table 5.

As shown in Table 5, compared to the C2f module, the C2f-Faster-AMA module has 9.8% less computation, 12.7% fewer parameters, and 1.4% improvement in mAP@0.5. Compared to other C2f residual modules, mAP@0.5 improves by 0.67% on average. Thus, the C2f-Faster-AMA module is superior in terms

TABLE 4 Comparison results of the performance of different DenseNet variants.

Variant module	Cross-validation	GFLOPs (G)	Parameters (m)	Recall	mAP@0.5	mAP@0.5–0.95
DenseNet	AVG	35.30	11.10	0.766	81.1%	47.6%
+CA	AVG	+2.70	+0.10	0.754	80.9%	46.4%
+ECA	AVG	+0.12	+0.06	0.759	81.2%	47.1%
+CBMA	AVG	+2.90	+0.10	0.767	81.5%	47.4%
+AMA	AVG	+0.53	+0.08	0.779	82.0%	48.8%

of the number of parameters, the amount of computation, and the prediction accuracy.

4.4 Inner-SIoU loss function comparison results

To verify the effectiveness of the loss function Inner-SIoU, the improved Inner-SIoU loss function was compared with Complete Intersection over Union (CIOU), Distance Intersection over Union (DIOU), Extended Intersection over Union (EIOU), and Generalized Intersection over Union (GIOU) in a comparison experiment, and the results are shown in Table 6.

Table 6 shows that the model with the Inner-SIoU loss function performs the best, leading the model with the CIOU loss function by 1.7%, which is an average improvement of 1.2% over the other models. In terms of recall, Recall Inner-SIoU still maintains the best recall with an improvement of 2.26% compared to the original model. Under the comprehensive evaluation, the improved loss function is effective, and Inner-SIoU not only improves the detection accuracy but also improves the recall of the model.

4.5 Ablation experiment

To analyze the detection performance of the proposed YOLOv8s-Longan algorithm on a dataset of 2,460 UAV aerial longan images, YOLOv8s is the baseline model and does not use pretraining parameters for the models before and after improvement. On the premise of maintaining the same experimental configuration, the detection performance of the proposed YOLOv8s-Longan algorithm improves. The input image resolution is set to the input size of the image taken by the D435i depth camera, which is 848 × 480.

Therefore, an ablation experiment is designed for the UAV aerial longan image dataset, and the experimental parameters are described in Section 4. A comparison of the ablation experimental results of the proposed method is shown in Table 7. Model 1 represents the original structure of YOLOv8s, Model 2 represents the integration of the DenseAMA module structure in the front of the YOLOv8s backbone, and Model 3 represents the replacement of the C2f module with the C2f-Faster-AMA module in the back of the YOLOv8s backbone. Model 4 represents the replacement of the original YOLOv8's neck network with the VOVGSCSPC module of the C2f module, model 5 represents replacing the loss function CIOU in the original YOLOv8s with the improved Inner-SIoU loss function, model 6 represents replacing the backbone overall network structure of the YOLOv8s by combining the DenseAMA module with the C2f-Faster-AMA module, model 7 represents replacing the backbone network of the model 6 with the VOVGSCSPC module to replace the C2f module in the neck network of model 6, and model 8 represents the YOLOv8s-Longan model structure of this paper.

According to Table 7, integrating the DenseAMA module structure in the front of the YOLOv8s backbone can improve the mAP@0.5 of the model by 1.6%, and replacing the C2f module with the C2FFast-AMA module in the back of the YOLOv8s backbone can improve the mAP@0.5 of the model by 1.4%. Additionally, the combination algorithm of the DenseAMA module and C2F-Fast-AMA module improved the mAP@0.5 of the original YOLOv8s model by 2.3%, thus showing a performance superposition effect. After C2f in the neck network is replaced with the VOVGSCSPC module, the loss function CIOU in the original network structure is changed to the Inner-SIoU loss function to improve global performance. Compared with those of the original YOLOv8s model, the parameters of the proposed YOLOv8s-Longan model are reduced by 20.3%, and the number of calculations in the model is reduced by 2.08%. With the same number of training steps (100 iterations), the recall rate increases by 6.3%, and the prediction accuracy mAP@0.5 increases by 3.9%. It shows that the proposed method not only improves the detection accuracy but also successfully realizes the lightweight nature of the model to meet real-time and accuracy requirements.

TABLE 5 C2f residual module performance comparison results.

Residual Module	Cross-validation	GFLOPs (G)	Parameters (m)	Recall	mAP@0.5	mAP@0.5–0.95
C2f	AVG	28.4	11.1	0.751	80.4%	46.8%
C2f-DCNV2	AVG	27.1	11.2	0.767	81.2%	47.3%
C2f-DBB	AVG	34.5	13.7	0.759	81.0%	47.2%
C2f-Faster-AMA	AVG	25.6	9.7	0.755	81.8%	47.8%

TABLE 6 Comparison results of the performance of different loss functions.

Loss function	Cross-validation	Recall	mAP@0.5	mAP@0.5–0.95
CIOU	AVG	0.751	80.4%	46.8%
DIOU	AVG	0.751	81.1%	46.9%
EIOU	AVG	0.773	81.0%	47.6%
GIOU	AVG	0.765	81.1%	47.1%
Inner-SIoU	AVG	0.768	82.1%	47.7%

CIOU, Complete Intersection over Union; DIOU, Distance Intersection over Union; EIOU, Extended Intersection over Union; GIOU, Generalized Intersection over Union.

4.6 Different comparison algorithms

To further verify the efficiency and adaptability of the YOLOv8s-Longan model proposed in this paper for longan string fruit target detection and positioning, the YOLOv8s-Longan model is selected to compare with YOLOv5, YOLOv6, and YOLOv8, which are classic models in the current object detection field. As a mature real-time detection model, YOLOv5 uses Mosaic data enhancement in the input and Focus structure in the Backbone network, which has a good balance between speed and accuracy. YOLOv6 further improves efficiency by introducing RepVGG and EfficientRep modules. As the latest version of the YOLO series, YOLOv8 uses deeper DarkNet-53 as the backbone network and replaces the C3 module in YOLOv5 with the C2f module, which has made significant improvements in lightweight and performance and has strong representability. By comparing the n and s versions of the YOLOv5 and YOLOv8 series proposed by Ultralytics, and the n and s versions of the commonly used YOLOv6 series, six performance indicators are selected. Namely, the amount of computation (GFLOPS), the number of parameters, recall, mAP@0.5 and mAP@0.5–0.95, and FPS are recorded, and the data are shown in Table 8 and Figure 10.

According to the comparative experimental results in Table 8, the improved YOLOv8s-Longan model proposed in this paper has higher mAP@0.5 and mAP@0.5–0.95 detection accuracies than other classical models, and the average accuracy of the other mAP@0.5 models increases by 4.72%. The parameters of the improved algorithm in this paper are lower than those of other classical models, the parameters of the YOLOv8s-Longan model are only half of those of the YOLOv6s model, and the parameters of the YOLOv8s-Longan model are reduced by 23.6% on average compared with those of other models with the same specifications. From the perspective of various indicators, the improved model algorithm in this paper has the best comprehensive performance and has good detection ability for longan string fruit images. This model not only improves detection accuracy but is also lightweight and can meet real-time and accurate requirements, demonstrating the obvious superiority of the YOLOv8s-Longan target detection model.

To better show the effectiveness of the improved algorithm, various classical accuracy detection models and the YOLOv8s-Longan model in the training process are compared with the changes in four indicators: accuracy, recall rate, mAP@0.5, and mAP@0.5–0.95. The experimental results are shown in Figure 10. With an increase in the number of iterations, all the comparison algorithms can finally reach convergence, but the four indicators of the improved YOLOv8s-Longan model are significantly greater than those of all the classical detection models. A comparison of the mAP@0.5 and mAP@0.5–0.95 curves is shown in Figures 10C, D. The mAP of the improved algorithm is greater than that of the original YOLOv8s benchmark model when training for 100 rounds, which proves that the YOLOv8s-Longan model in this paper can effectively improve the ability to detect longan bunk fruit compared with the original benchmark model.

The Longan Garden of the Guangdong Academy of Agricultural Sciences was used to test some of the 1,070 longan

TABLE 7 Comparative results of ablation experiments for YOLOv8s-Longan.

Model	Cross-validation	GFLOPs (G)	Parameters (m)	Recall	mAP@0.5	mAP@0.5–0.95	FPS (img/s)
YOLOv8s	AVG	28.8	11.1	0.751	80.4%	46.8%	115
YOLOv8s + DenseAMA	AVG	35.3	11.1	0.779	82.0%	48.8%	46
YOLOv8s + C2f-Faster-AMA	AVG	25.6	9.7	0.755	81.8%	47.8%	110
YOLOv8s + VOVGSCSPC	AVG	25.2	10.3	0.775	82.0%	47.7%	113
YOLOv8s + Inner-SIoU	AVG	28.8	11.1	0.768	82.1%	47.4%	114
YOLOv8s + DenseAMA + C2f-Faster-AMA	AVG	32.1	9.8	0.780	82.7%	48.4%	43
YOLOv8s + DenseA + C2f-Faster-AMA + VOVGSCSPC	AVG	28.2	8.8	0.778	82.6%	48.3%	45
YOLOv8s-Longan	AVG	28.2	8.8	0.798	84.3%	50.2%	45

10.3389/fpls.2024.1518294

TABLE 8 Comparative experimental results of classical models for object detection.

Model	Cross-validation	GFLOPs (G)	Parameters (m)	Recall	mAP@0.5	mAP@0.5–0.95	FPS (img/s)
YOLOv5n	AVG	7.8	2.65	0.743	79.5%	44.1%	272
YOLOv5s	AVG	24.2	9.15	0.750	79.9%	45.7%	119
YOLOv6n	AVG	13.1	4.5	0.720	78.9%	43.5%	292
YOLOv6s	AVG	44.9	16.4	0.749	79.7%	44.9%	116
YOLOv8n	AVG	8.2	3.0	0.745	79.1%	45.0%	262
YOLOv8s	AVG	28.8	11.1	0.751	80.4%	46.8%	115
YOLOv8s-Longan	AVG	28.8	8.8	0.798	84.3%	50.2%	45

dataset images to evaluate the effect before and after the improvement more intuitively. Comparing Figure 11 shows that except for YOLOv6s in Figure 11D and YOLOv8s-Longan in Figure 11G, there is no missing detection in the upper-right corner of the dense longan string fruit scene; other detection models fail to detect longan string fruit in the upper-right corner of the figure. Additionally, compared with Figures 11D, G, the overall accuracy of the YOLOv8s-Longan model in image detection is much greater than that of the YOLOv6s model, and the prediction accuracy of the YOLOv6s model increases by 21.1% on average. The improved model has higher detection accuracy, and the detection performance is significantly improved.

To further explore the improvement of the YOLOv8s-Longan model algorithm, a heatmap visualization comparison and analysis of the detection effect are performed, and the specific results are shown in Figure 12.

Specifically, Figures 12A, D show the heatmap visualization comparison of the YOLOv5 model, in which Figure 12A only vaguely identifies the approximate position of the longan string fruit, and Figure 12D only identifies the center position of the right

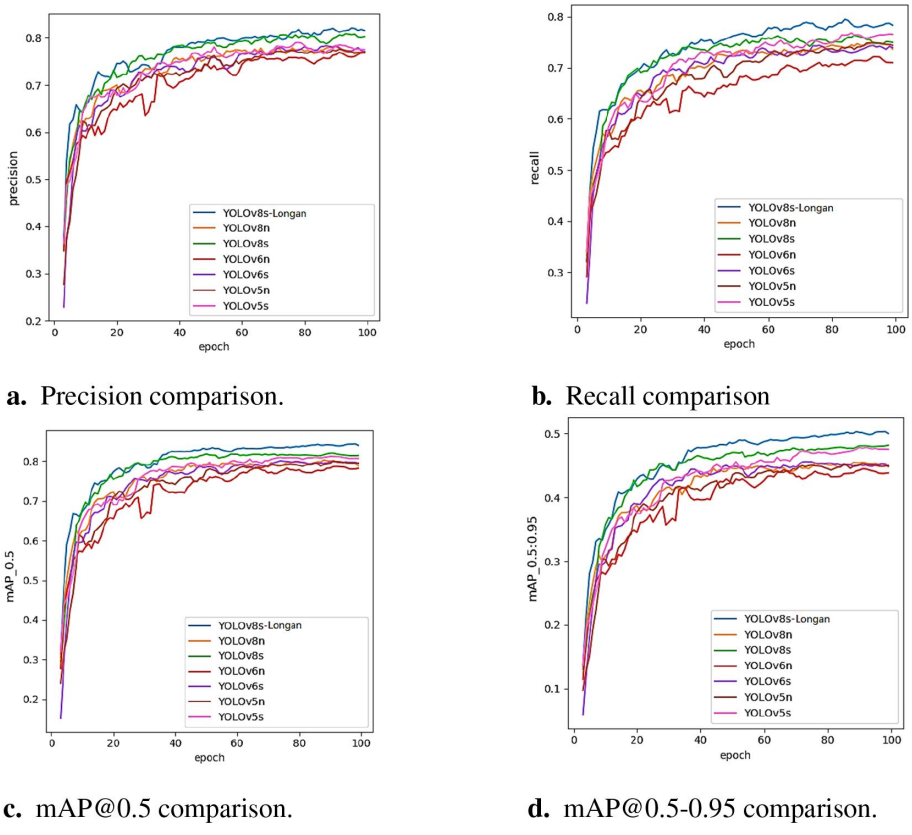

FIGURE 10
Comparison of object detection algorithms' indicators. **(A)** Precision comparison. **(B)** Recall comparison. **(C)** mAP@0.5 comparison. **(D)** mAP@0.5-0.95 comparison.

10.3389/fpls.2024.1518294

a. YOLOv5n. **b.** YOLOv6n. **c.** YOLOv8n.

d. YOLOv5s. **e.** YOLOv6s. **f.** YOLOv8s.

g. YOLOv8s-Longan detention results in dense longan string fruit scene.

FIGURE 11
Prediction comparison of different network models for identification. **(A)** YOLOv5n. **(B)** YOLOv6n. **(C)** YOLOv8n. **(D)** YOLOv8n. **(E)** YOLOv6s. **(F)** YOLOv8s. **(G)** YOLOv8s-Longan detention results in dense longan string fruit scene.

longan string fruit but does not identify the left longan string fruit. Figures 12B, E show the heatmap visual comparison of the YOLOv6 model. This group of figures can only identify the center position of the right longan string fruit and has obvious false detection of the surrounding green leaf environment. A heatmap of the YOLOv8 model is shown in Figures 12C, F. In Figure 12C, the approximate position of the longan string fruit on the left and right sides is fuzzy, but the surrounding green leaves are clearly misidentified. Figure 12F shows the approximate identification of the peripheral outline of the longan string fruit on the right. Figure 12G shows a heatmap visual comparison between the YOLOv8s-Longan model and other classical detection models. The improved YOLOv8s-Longan model can perfectly identify the irregular peripheral contour of longan string fruit, and there is no false detection of the surrounding green leaves or other interference objects. Therefore, the YOLOv8s-Longan model performs well in improving object detection accuracy and solving the problems of missed and false detections, which significantly improves the object detection task.

4.7 Detection effects in different natural scenes

In this section, the performance of the YOLOv8s-Longan model under different lighting conditions is evaluated in detail. In the frontal illumination environment, Figures 13A, B demonstrate that the model can accurately identify the target at different distances, far and near. Figures 13C, D are in the backlight condition; the model is still able to accurately identify the longan string fruit without being affected by the light intensity. As shown in Figures 13A, C, the recognition of longan strings in long-distance scenes proves that the model can maintain accurate detection of longan string fruit regardless of the lighting environment or scene distance. Comprehensive Figure 13 shows that

10.3389/fpls.2024.1518294

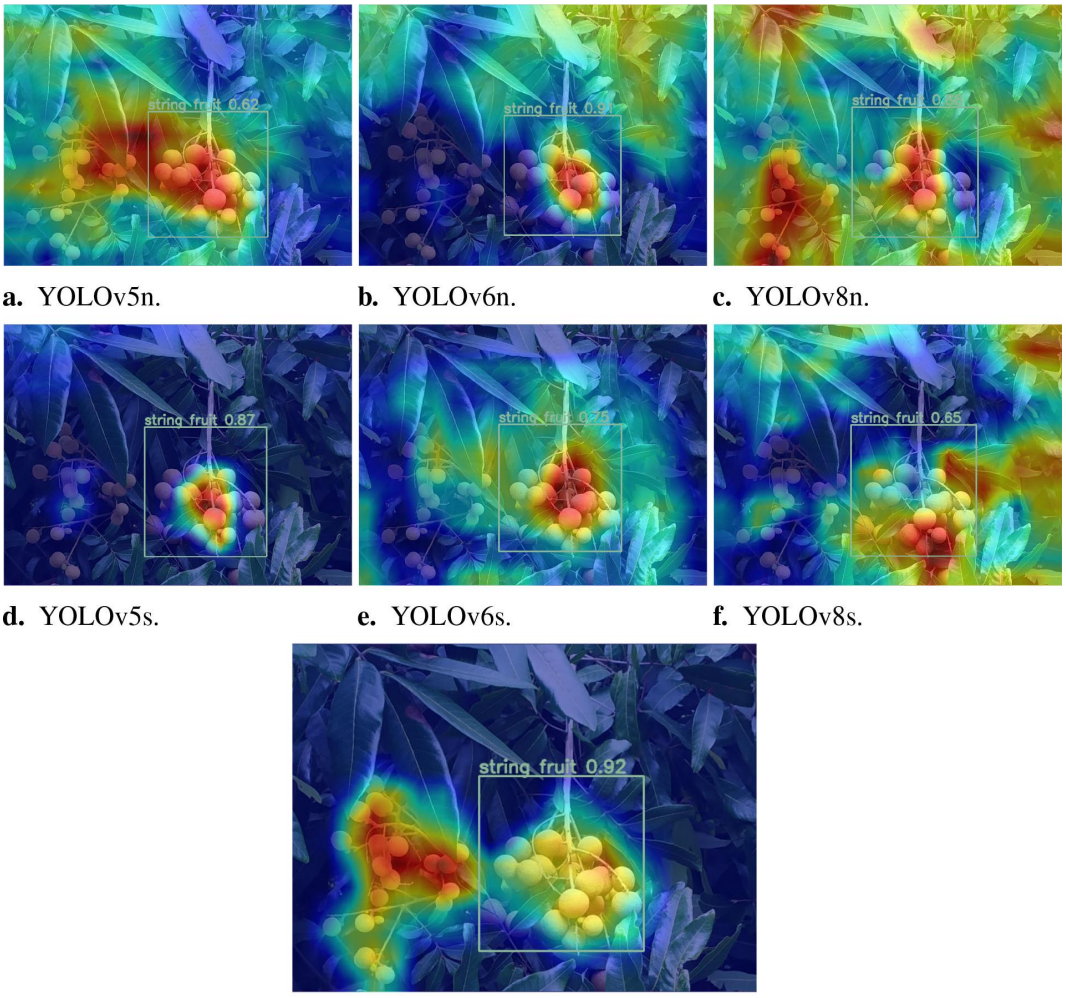

a. YOLOv5n. **b.** YOLOv6n. **c.** YOLOv8n.

d. YOLOv5s. **e.** YOLOv6s. **f.** YOLOv8s.

g. YOLOv8s-Longan heat map for longan string fruit prediction.

FIGURE 12
Comparison of heatmaps for prediction of longan fruit recognition by different network models. **(A)** YOLOv5n. **(B)** YOLOv6n. **(C)** YOLOv8n. **(D)** YOLOv8n. **(E)** YOLOv6s. **(F)** YOLOv8s. **(G)** YOLOv8s-Longan heat map for longan string fruit prediction.

the YOLOv8s-Longan model shows strong robustness regardless of the changes in lighting conditions or near and far scenes and successfully realizes the accurate detection of targets under different environmental conditions.

In order to verify the robustness of the YOLOv8s-Longan model for the recognition of different longan varieties, especially the detection ability of the model for different longan varieties in the same environment, Figures 14A, B show the detection results for the Chuliang longan, while Figures 14C, D show the detection results for the Shixia longan. There were obvious differences in the color, size, and shape of the two longan fruits, and different appearance characteristics were reflected at different distances and light conditions. Based on Figure 14, it can be seen that the model can accurately identify longan string fruit, which indicates that the YOLOv8s-Longan model shows excellent generalization performance in identifying different longan varieties.

4.8 The real-time deployment test

To verify the practical deployment capability of the proposed YOLOv8s-Longan model for the UAV, in this experiment, DJI M300 RTK model UAV and Intel RealSense D435i camera are selected, and the YOLOv8s-Longan model is deployed to the NanoPi-R5C-Combo onboard computer. The performance of string fruit recognition is tested on Chuliang and Shixia longan scenes in the longan garden of the Guangdong Academy of Agricultural Sciences. The test scenario is shown in Figure 15, and the recognition results are shown in Table 9.

During the actual test, the NanoPi-R5C-Combo on-board computer deploys the lightweight model with a parameter count of 8.83M with 18.1 MB of memory, and the model can process 45 to 50 images per second, which can meet the real-time recognition of longan string in real-time by the UAV. From Table 9, the

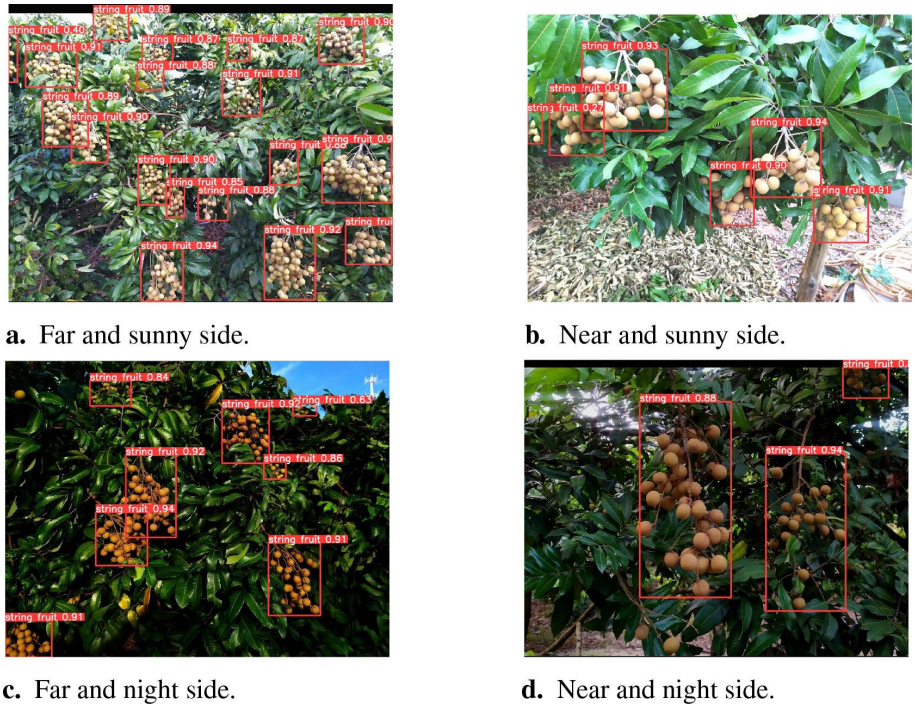

a. Far and sunny side.

b. Near and sunny side.

c. Far and night side.

d. Near and night side.

FIGURE 13
Comparison of detection results under different environmental conditions. **(A)** Far and sunny side. **(B)** Near and sunny side. **(C)** Far and night side. **(D)** Near and night side.

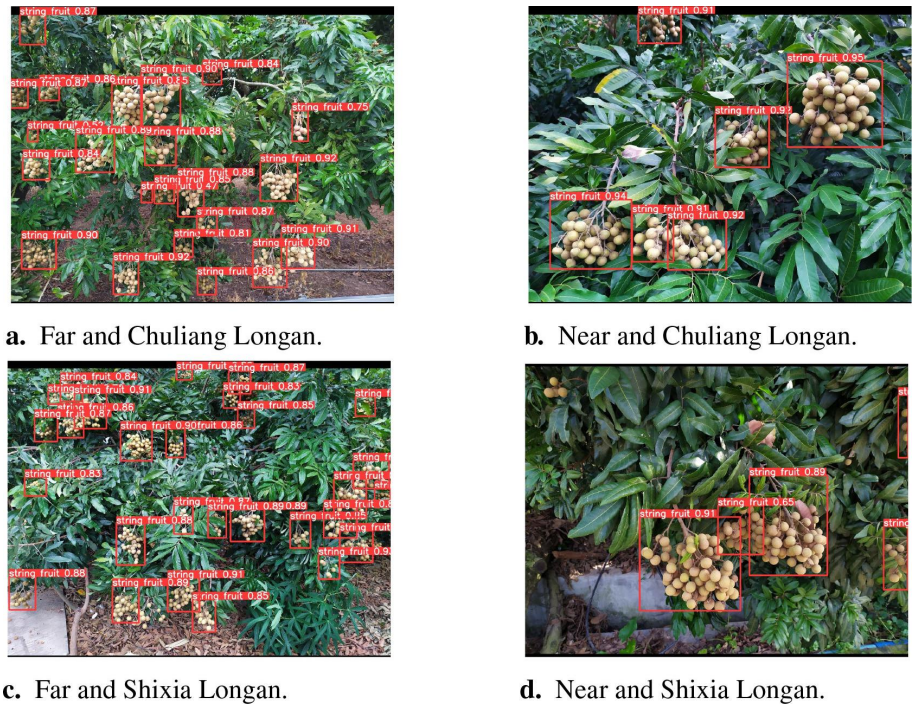

a. Far and Chuliang Longan.

b. Near and Chuliang Longan.

c. Far and Shixia Longan.

d. Near and Shixia Longan.

FIGURE 14
Comparison of the detection results for different longan varieties. **(A)** Far and Chuliang Longan. **(B)** Near and Chuliang Longan. **(C)** Far and Shixia Longan. **(D)** Near and Shixia Longan.

TABLE 9 Recognition results of YOLOv8s-Longan model in different natural scenes.

Different natural scenes	Number of true longan string clusters	Identify the correct number of longan string clusters	Identifying the wrong number of longan string clusters	Accuracy
Close, sunny side	7	7	0	100%
Close, night side	9	8	1	88.9%
Far, sunny side	15	13	2	86.7%
Far, night side	17	14	3	82.3%

FIGURE 15
The UAV test scenario. UAV, unmanned aerial vehicle.

YOLOv8s-Longan model has good recognition and detection results for both Chuliang and Shixia longan varieties in different natural scenarios. Among the 48 clusters of identified longan string, 42 clusters of string are accurately identified, and the average recognition accuracy of the YOLOv8s-Longan model is 87.5%, which can satisfy the need of the UAV for lightweight and accurate recognition of longan string. Among the six clusters of longan string that were missed, four clusters of string are occluded by the transition of longan string in front of them and thus identified as one cluster of longan string by the model; the other two clusters of string are missed because they are located inside the center of the fruit tree under cloudy conditions, which prevented them from being accurately identified by the model.

5 Conclusion

In this paper, a fast and accurate detection scheme based on deep learning is proposed for the UAV aerial longan image dataset. First, the Intel RealSense D435i depth camera is mounted on the fruit-picking UAV to collect longan string fruit data. Second, in order to reduce the computing requirements and memory usage of airborne computing equipment and improve the fast and accurate detection accuracy of longan string fruit, the YOLOv8s-Longan deep learning model is proposed.

The experimental results show that the recall and mAP@0.5 of the improved model proposed in this paper increase by 6.3% and 3.9%, respectively, on the longan string fruit dataset, and the parameter quantity of the improved model decreases by 20.3%. Compared with the other three YOLO series classical algorithms, the improved model algorithm in this paper is feasible, which improves the detection accuracy of longan string fruit targets and greatly reduces the number of missed and false detections of occluded targets.

In the future, the training speed of the model and the ability of the object detection model to resist environmental interference will be further improved, and the robustness, generalization ability, and application prospect of the model will be enhanced. In future work, we will analyze the maturity and disease and insect pests of longan string fruit through the model and provide customized picking strategies, which will help to improve the yield and quality of longan, promote the income growth of fruit farmers, and promote the sustainable development of longan cultivation industry.

Data availability statement

The raw data supporting the conclusions of this article will be made available by the authors, without undue reservation.

Author contributions

JL: Conceptualization, Funding acquisition, Writing – original draft. KW: Formal analysis, Methodology, Software, Writing – original draft. MZ: Data curation, Methodology, Visualization, Writing – review & editing. HC: Software, Supervision, Validation, Writing – review & editing. HL: Data curation, Software, Writing – review & editing. YM: Data curation, Validation, Writing – review & editing. LS: Funding acquisition, Supervision, Writing – review & editing.

Funding

The author(s) declare financial support was received for the research, authorship, and/or publication of this article. This work was supported in part by the National Natural Science Foundation

of China under Grants 52375094 and 62303188, the Guangdong Laboratory for Lingnan Modern Agriculture under Grant NT2021009, the China Agriculture Research System under Grant CARS-32, the open competition program of top ten critical priorities of Agricultural Science and Technology Innovation for the 14th Five-Year Plan of Guangdong Province (2022SDZG03), and the Discipline Construction Project of South China Agricultural University in 2023 under Grant 2023B10564002.

Conflict of interest

The authors declare that the research was conducted in the absence of any commercial or financial relationships that could be construed as a potential conflict of interest.

Generative AI statement

The author(s) declare that no Generative AI was used in the creation of this manuscript.

Publisher's note

All claims expressed in this article are solely those of the authors and do not necessarily represent those of their affiliated organizations, or those of the publisher, the editors and the reviewers. Any product that may be evaluated in this article, or claim that may be made by its manufacturer, is not guaranteed or endorsed by the publisher.

References

Cai, L., Li, H., Dong, W., and Fang, H. (2022). Micro-expression recognition using 3d densenet fused squeeze-and-excitation networks. *Appl. Soft Comput.* 119. doi: 10.1016/j.asoc.2022.108594

Chen, H., Chen, H., Huang, X., Zhang, S., Chen, S., Cen, F., et al. (2024a). Estimation of sorghum seedling number from drone image based on support vector machine and yolo algorithms. *Front. Plant Sci.* 15, 1399872. doi: 10.3389/fpls.2024.1399872

Chen, W., Liu, M., Zhao, C., Li, X., and Wang, Y. (2024b). Mtd-yolo: Multi-task deep convolutional neural network for cherry tomato fruit bunch maturity detection. *Comput. Electron. Agric.* 216, 108533. doi: 10.1016/j.compag.2023.108533

Dairath, M. H., Akram, M. W., Mehmood, M. A., Sarwar, H. U., Akram, M. Z., Omar, M. M., et al. (2023). Computer vision-based prototype robotic picking cum grading system for fruits. *Smart Agric. Technol.* 4, 100210. doi: 10.1016/j.atech.2023.100210

Ding, Y., Zhang, Z., Hu, H., He, F., Cheng, S., and Zhang, Y. (2024). "Multi-feature fusion: Graph neural network and cnn combining for hyperspectral image classification," In: *Graph Neural Network for Feature Extraction and Classification of Hyperspectral Remote Sensing Images*. (Springer, Singapore).

Ding, Y., Zhang, Z., Zhao, X., Cai, W., Yang, N., Hu, H., et al. (2022). Unsupervised self-correlated learning smoothy enhanced locality preserving graph convolution embedding clustering for hyperspectral images. *IEEE Trans. Geosci. Remote Sens.* 60, 1–16. doi: 10.1109/TGRS.2022.3202865

Dong, C., and Duoqian, M. (2023). Control distance IoU and control distance iou loss for better bounding box regression. *Pattern Recognit.* 137, 109256. doi: 10.1016/j.patcog.2022.109256

He, C., Deng, C., Li, N., and Miao, Z. (2021). "Design of vision control system of tomato picking robot," in *2021 40th Chinese Control Conference (CCC) (IEEE)*. Shanghai, China, 26-28 July 2021, 4267–4271.

Huang, Z., and Li, G. (2023). "Detection and segmentation of grape bunch by integrating channel attention and large kernel attention," in *2023 International Conference on Image Processing, Computer Vision and Machine Learning (ICICML) (IEEE)*. Chengdu, China, 03-05 November 2023, 695–698.

Jia, J., Lei, R., Qin, L., Wu, G., and Wei, X. (2023). ienhancer-dcsv: Predicting enhancers and their strength based on densenet and improved convolutional block attention module. *Front. Genet.* 14, 1132018. doi: 10.3389/fgene.2023.1132018

Jiang, H., Hu, F., Fu, X., Chen, C., Wang, C., Tian, L., et al. (2023). Yolov8-peas: a lightweight drought tolerance method for peas based on seed germination vigor. *Front. Plant Sci.* 14. doi: 10.3389/fpls.2023.1257947

Lawal, O. M., Zhu, S., and Cheng, K. (2023). An improved yolov5s model using feature concatenation with attention mechanism for real-time fruit detection and counting. *Front. Plant Sci.* 14, 1153505. doi: 10.3389/fpls.2023.1153505

Li, C., Lin, J., Li, Z., Mai, C., Jiang, R., and Li, J. (2024). An efficient detection method for litchi fruits in a natural environment based on improved yolov7-litchi. *Comput. Electron. Agric.* 217, 108605. doi: 10.1016/j.compag.2023.108605

Li, D., Sun, X., Elkhouchlaa, H., Jia, Y., Yao, Z., Lin, P., et al. (2021). Fast detection and location of longan fruits using UAV images. *Comput. Electron. Agric.* 190, 106465. doi: 10.1016/j.compag.2021.106465

Liang, J., and Wang, S. (2023). "Key components design of the fresh grape picking robot in equipment greenhouse," in *2023 International Conference on Service Robotics (ICoSR) (IEEE)*. Shanghai, China, 21-23 July 2023, 16–21.

Liu, Q., Lv, J., and Zhang, C. (2024). Mae-yolov8-based small object detection of green crisp plum in real complex orchard environments. *Comput. Electron. Agric.* 226. doi: 10.1016/j.compag.2024.109458

Lu, C., Nnadozie, E., Camenzind, M. P., Hu, Y., and Yu, K. (2024). Maize plant detection using uav-based rgb imaging and yolov5. *Front. Plant Sci.* 14, 1274813. doi: 10.3389/fpls.2023.1274813

Mercioni, M. A., and Holban, S. (2020). "P-swish: Activation function with learnable parameters based on swish activation function in deep learning," in *2020 International Symposium on Electronics and Telecommunications (ISETC) (IEEE)*. Timisoara, Romania, 05-06 November 2020, 1–4.

Shi, Y., Jin, S., Zhao, Y., Huo, Y., Liu, L., and Cui, Y. (2023). Lightweight force-sensing tomato picking robotic arm with a "global-local" visual servo. *Comput. Electron. Agric.* 204, 107549. doi: 10.1016/j.compag.2022.107549

Sun, X. (2024). Enhanced tomato detection in greenhouse environments: a lightweight model based on s-yolo with high accuracy. *Front. Plant Sci.* 15. doi: 10.3389/fpls.2024.1451018

Sunkari, S., Sangam, A., Suchetha, M., Raman, R., Rajalakshmi, R., Tamilselvi, S., et al. (2024). A refined ResNet18 architecture with swish activation function for diabetic retinopathy classification. *Biomed. Signal Process. Control* 88, 105630. doi: 10.1016/j.bspc.2023.105630

Wang, L., Wang, G., Yang, S., Liu, Y., Yang, X., Feng, B., et al. (2024). Research on improved yolov8n based potato seedling detection in uav remote sensing images. *Front. Plant Sci.* 15. doi: 10.3389/fpls.2024.1387350

Xu, C., Wang, Z., Du, R., Li, Y., Li, D., Chen, Y., et al. (2023). A method for detecting uneaten feed based on improved YOLOv5. *Comput. Electron. Agric.* 212, 108101. doi: 10.1016/j.compag.2023.108101

Yang, Y., Han, Y., Li, S., Yang, Y., Zhang, M., and Li, H. (2023). Vision based fruit recognition and positioning technology for harvesting robots. *Comput. Electron. Agric.* 213, 108258. doi: 10.1016/j.compag.2023.108258

Zhaosheng, Y., Tao, L., Tianle, Y., Chengxin, J., and Chengming, S. (2022). Rapid detection of wheat ears in orthophotos from unmanned aerial vehicles in fields based on yolox. *Front. Plant Sci.* 13, 851245. doi: 10.3389/fpls.2022.851245

Zhou, Z., Hu, Y., Yang, X., and Yang, J. (2024). Yolo-based marine organism detection using two-terminal attention mechanism and difficult-sample resampling. *Appl. Soft Comput.* 153, 111291. doi: 10.1016/j.asoc.2024.111291

Zhu, L., Li, X., Sun, H., and Han, Y. (2024). Research on CBF-YOLO detection model for common soybean pests in complex environment. *Comput. Electron. Agric.* 216, 108515. doi: 10.1016/j.compag.2023.108515

agronomy

MDPI

Article

HPS-RRT*: An Improved Path Planning Algorithm for a Nonholonomic Orchard Robot in Unstructured Environments

Meiqi Hu [1], Qinpeng Huang [1], Jiamin Cai [1], Yu Chen [1], Jun Li [1,2,3] and Linlin Shi [1,*]

[1] College of Engineering, South China Agricultural University, Guangzhou 510642, China; 15259855839@stu.scau.edu.cn (M.H.); h2716867388@stu.scau.edu.cn (Q.H.); c13533895601@stu.scau.edu.cn (J.C.); chenyu219@scau.edu.cn (Y.C.); autojunli@scau.edu.cn (J.L.)
[2] Guangdong Laboratory for Lingnan Modern Agriculture, Guangzhou 510642, China
[3] State Key Laboratory of Agricultural Equipment Technology, Beijing 100083, China
* Correspondence: lynnshi@scau.edu.cn

Abstract: Path planning is a fundamental challenge for autonomous robots, particularly in unstructured environments, where issues such as low search efficiency, suboptimal path quality, and local optima often arise. To address these challenges and enable a nonholonomic orchard robot to accomplish tasks safely and efficiently, this paper proposes a novel HPS-RRT* algorithm based on hybrid exploration and optimization mechanisms to enhance path planning performance. A hybrid sampling strategy adapted to the environmental characteristics is proposed to improve the search efficiency, and an extended step size based on Lévy distribution is designed to balance exploration and optimization. Moreover, a pruning strategy is incorporated to reduce redundant points during the search process, enhancing the efficiency of the exploration tree and reducing unnecessary expansion. Furthermore, a novel leader-based sparrow optimization algorithm is proposed to ensure that the planned path is suitable for the nonholonomic orchard robot. It can overcome the limitations of traditional smoothing methods by simultaneously optimizing curvature and path length. Compared with existing RRT*-based algorithms in environments of varying complexity, the proposed HPS-RRT* reduces the final path length by 1.7% to 27%, improves planning efficiency by 77.7% to 93.3%, and enhances path smoothness by 27.9% to 41.7%, while maintaining a 100% success rate. Furthermore, its feasibility for a nonholonomic orchard robot is validated through a multi-target planning task with curvature constraints.

Keywords: path planning; path optimization; unstructured environments; rapidly exploring random tree (RRT); autonomous orchard robot

Academic Editors: Marco Fontanelli and Lorenzo Gagliardi

Received: 17 February 2025
Revised: 9 March 2025
Accepted: 13 March 2025
Published: 14 March 2025

Citation: Hu, M.; Huang, Q.; Cai, J.; Chen, Y.; Li, J.; Shi, L. HPS-RRT*: An Improved Path Planning Algorithm for a Nonholonomic Orchard Robot in Unstructured Environments. *Agronomy* **2025**, *15*, 712. https://doi.org/10.3390/agronomy15030712

1. Introduction

Currently, orchard robots, such as weeding robots, harvesting robots, and spraying robots, have garnered significant attention from researchers. Compared with traditional open-field environments, such as those for rice and corn, the unstructured nature of orchard environments poses greater challenges for the autonomous navigation of orchard robots. Orchards in southern China are more concentrated in hilly areas, where the ground is undulating, and has more slopes, with angles that range from 5° to 20° [1]. Consequently, large machinery struggles to operate in such environments, resulting in a relatively low level of automation in the orchard planting industry. The integration of autonomous navigation technology is essential for the widespread adoption of smart agricultural machinery. Agricultural machinery automatic navigation technology is a core aspect of smart agricultural equipment and serves as one of the solutions to the aforementioned challenges [2]. The

development of autonomous navigation technology for orchard robots enables machinery to operate along optimized paths, improving operational quality and efficiency, making it an effective solution to this challenge.

Path planning is a crucial supporting tool for deploying autonomous driving systems in engineered environments and is one of the key technologies for achieving autonomous movement [3]. Path planning is a non-deterministic polynomial time ("NP") hard problem [4] which has the task of finding a continuous path connecting a system from an initial to a final goal configuration [5]. Traditional methods such as simulated annealing, artificial potential field, and fuzzy control methods were initially applied to path planning. Kun Shi et al. improved the simulated annealing algorithm's process in 2024 [6], enhancing the efficiency and optimality of path planning. Wang Siming et al. proposed an improved artificial potential field method in 2018 [7], which addressed issues such as unreachable goals and slow convergence in traditional artificial potential field methods by introducing virtual target points and improving the repulsive force function. Sawsan Abdel-Latif El-Teleity et al. designed a hierarchical behavior-based control strategy in 2011 [8], combining four different reactive behaviors using a fuzzy supervisor to achieve autonomous navigation for mobile robots. However, these methods often fail to effectively utilize global information, leading to unreachable targets and local optima. Graph-based methods, such as the A* algorithm, grid-based methods, and their improved variants, face efficiency decline and limited adaptability in unstructured orchard environments, making them inadequate for orchard path planning requirements. Yulun Zhu et al. in 2024 [9] proposed an escape route planning method based on the improved A* algorithm. In 2020, Ajeil, F.H. [10] et al. introduced an improved algorithm based on ant colony age, termed Age-Based Ant Colony Optimization (ABACO), into the standard ant colony optimization framework. ABACO is integrated with grid-based modeling of static and dynamic environments to tackle the path planning problem. Gong et al. [11] integrated Jump Point Search into the traditional A* algorithm to reduce memory usage and improve efficiency. These methods all face the issues mentioned above.

Among various path planning algorithms, sampling-based motion planning algorithms are widely favored for their suitability in large environments, fast search speed, and robust obstacle avoidance capabilities. Rapidly Exploring Random Trees (RRT) [12] and Probabilistic Roadmap (PRM) [13] are two commonly used sampling-based motion planning algorithms. Although widely used in path planning, experiments reveal that these algorithms cannot guarantee optimality and perform inefficiently in complex environments such as orchards. The RRT algorithm uses a strategy of uniformly and randomly sampling the entire state space, which is beneficial for searching unexplored portions. However, sampling in some unnecessary areas will slow down the algorithm's convergence rate and waste a lot of computing time. In addition, the length of the planned path and the shortest path will differ greatly [14]. In order to avoid blindness in the search process, LaValle and Kuffner in 2001 [15] put forward the idea of goal bias, which improves exploration efficiency. Their extensions, RRT* and PRM*, ensure asymptotic optimality but suffer from slow convergence and require extensive sampling to achieve optimal solutions. For example, Sertac Karaman et al. proposed a sampling-based algorithm based on the Rapidly Exploring Random Graphs (RRGs) method in 2012 [16] that solves this problem with probabilistic completeness and asymptotic optimality guarantees. Lei Ye et al. proposed the CBQ-RRT* algorithm in 2024, introducing the CreateConnectNode optimization method, which effectively addresses the path-smoothing issue at the intersection of expanding trees [17]. In 2023, Lei Ye et al. proposed the IKB-RRT algorithm, which incorporates an improved artificial potential field method, a sampling technique for motion control parameters of robotic configurations, and a path optimization strategy for dual-tree con-

nectivity, achieving obstacle avoidance while ensuring path smoothness [18]. Bio-inspired intelligent methods, such as Genetic Algorithm, Artificial Neural Networks, Ant Colony Optimization, and Particle Swarm Optimization (PSO), are closely aligned with natural biological properties and ecological mechanisms, offering higher intelligence and efficiency. For example, Yue Li et al. in 2023 [19] proposed a fusion algorithm based on the improved genetic algorithm and the dynamic window approach, enhancing the robot's ability to avoid dynamic obstacles and quickly solve for shorter and smoother robot paths. A. Zhu et al. in 2006 [20] proposed a neural network-based approach to task assignment, using a self-organizing map (SOM) for a multi-robot system in dynamic environments subject to uncertainties. Razif Rashid et al. in 2016 [21] proposed the ant colony optimization (ACO) technique to solve the mobile robot path planning (MRPP) problem. Li Zheng et al. in 2023 [22] proposed a particle swarm optimization algorithm based on the artificial potential field method. This approach generates the robot's planned path by adjusting the inertia weight parameters and particle position vector sorting (rPSO), which is then improved using the artificial potential field method. In addition, in 2014, M. Rickert and colleagues introduced the EET algorithm for motion planning [23], which balances optimality and efficiency by effectively utilizing spatial information. J. D. Gammell et al. in 2014 [24] introduced the Informed RRT* algorithm. This method enhances both convergence speed and solution quality by focusing the search on a subset of the sampling space through a precise approach. However, these methods are less suitable for unstructured environments like hilly orchard terrains. The traditional full-coverage job path planning algorithm has problems, such as not being smooth enough and having a large curvature fluctuation, which leads to unsteady running and a low working efficiency of the robot trajectory tracking [25].

Deep learning (DL) has become a novel artificial intelligence methodology in the last few years. In 2024, Ben Hazem published a paper detailing the development process of the DQL algorithm [26]. The artificial neural networks (ANNs) could enhance the self-learning of systems to obtain the required output. In 2022, Cui Jichao [27] published an article that integrated deep learning theories to enhance motion path planning and obstacle avoidance for mobile robots, significantly improving their autonomy. Although path planning algorithms based on Q-learning and deep Q-learning demonstrate strong capabilities in many tasks, their model training requires substantial time and computation, making them challenging to apply in resource-constrained environments and less adaptable to environmental changes. To clarify the characteristics and limitations of various path planning algorithms for easier discussion, we have summarized them in Table 1.

Table 1. The characteristics and limitations of various path planning algorithms.

Algorithms	Characteristics	Limitations	Reference Index
Simulated annealing	The annealing process in physics, avoids local optima	Slow convergence, challenging parameter tuning	[6]
Artificial potential field method	Attractive source, repulsive source, strong real-time	Path lacks smoothness, oscillation, local optima	[7]
Fuzzy control method	Adaptation to nonlinear systems	Designing fuzzy rules requires expertise	[8]
A* algorithm	Heuristic function, static environment, shortest path	Poor path smoothness, excessive turning points	[9]
Grid-based method	Static obstacle environment with grid discretization	Poor path smoothness, low path quality, efficiency	[10]
RRT	Rapidly exploring random trees, real-time path update	Poor path smoothness, challenging parameter tuning	[12]

Table 1. *Cont.*

Algorithms	Characteristics	Limitations	Reference Index
PRM	Graph-based search algorithm, high-dimensional space	Not well-suited for narrow environments	[13]
Genetic algorithm	Simulates natural selection and genetic variation	Premature convergence, slow convergence	[17]
Artificial neural network	Data training, pattern recognition, decision-making	Requires large training data, low interpretability	[18]
Ant colony algorithm	Ant foraging, pheromone	Slow convergence, local optima	[19]
Particle swarm optimization	Bird foraging, information sharing among particles	Challenging parameter tuning	[20]
EET	Extended tree, adaptable to dynamic environments	Highly complex with extensive algorithmic details	[21]
Deep learning	Feature extraction, large-scale real-time decision-making	Needs extensive labeled data, poor model interpretability	[24]

To address issues such as low search efficiency, poor path quality, local optima, and unreachable goals in existing path planning algorithms, this paper proposes a novel path planning algorithm for the nonholonomic orchard robot. The algorithm, which is an improved RRT* using hybrid sampling, branch and leaf pruning, and the improved sparrow search algorithm, called HPS-RRT* (H: Hybrid, P: Prune, S: Sparrow), enhances the classical RRT* framework by incorporating hybrid exploration and optimization mechanisms to improve efficiency and trajectory quality in unstructured environments. The main contributions of this paper are summarized as follows:

1. To enhance search efficiency in orchard path planning, the proposed HPS-RRT* algorithm employs a hybrid sampling strategy that selects appropriate sampling methods based on environmental characteristics, achieving overall sampling optimality. Additionally, it utilizes an extended step size based on Lévy distribution instead of a fixed step size [28], balancing exploration efficiency and optimality.
2. To reduce the proportion of redundant points during the search process, this paper innovatively designs a pruning strategy that eliminates redundant nodes, guiding the exploration tree in the correct direction. This enhances extension efficiency and decreases the ratio of unnecessary expansion points.
3. To address the issues of path smoothness and quality in traditional path planning algorithms, this paper proposes a leader-based sparrow optimization algorithm. This approach effectively resolves the limitation of conventional smoothing algorithms, which struggle to optimize curvature while considering path length.

The rest of this paper is as follows. Section 2 presents the traditional RRT algorithm and the RRT* algorithm. In Section 3, we show the detailed design of the proposed HPS-RRT* algorithm. The comparison results and an orchard robot experiment are presented in Section 4 to show the effectiveness of the HPS-RRT*. Conclusions and future directions of research are given in Section 5.

2. Materials and Methods

2.1. Traditional RRT Algorithm

The Rapidly Exploring Random Tree (RRT) is a path planning tree that grows from the start to the goal point. Starting from the initial point, the algorithm performs random sampling in the space, identifies the nearest point on the tree that can be connected without obstacles, connects it to the sampled point, and adds the sampled point to the tree. This

process continues until the area near the goal is explored. However, this method does not guarantee an optimal path. The RRT algorithm's expansion steps are as follows:

1. Define the starting point x_{init}, the goal point x_{goal}, and initialize the random tree T.
2. Generate a random sample point x_{rand}.
3. Find the nearest node x_{near} on the random tree to x_{rand}. In Figure 1, x_{near} corresponds to the starting point x_{init}.
4. Extend from x_{near} by a step size S to generate a new node x_{new}. Perform collision detection for x_{new}. If no collision occurs, add x_{new} as a child node. If a collision is detected, repeat step 2.
5. Check if x_{new} has reached the goal point x_{goal} or if the maximum iteration count is reached. If either condition is satisfied, stop the expansion; otherwise, continue expanding.
6. Repeat steps (2) to (5) until the goal point x_{goal} is found.
7. Once the goal point x_{goal} is found, backtrack from the goal point to the starting point through the parent nodes to form the path. In Figure 1, the red line segments represent the path obtained in this example.

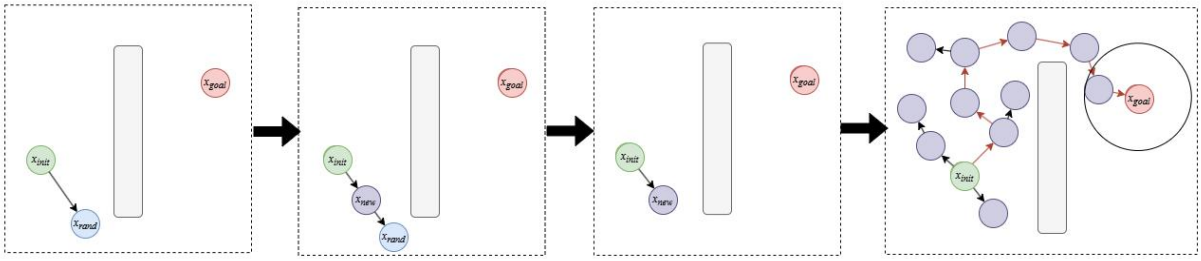

Figure 1. RRT algorithm principle diagram.

In Figure 1, gray rectangles represent obstacles, the green sphere x_{init} is the starting point, the red sphere x_{goal} is the goal point, the blue sphere x_{rand} is the randomly sampled point, the purple sphere x_{new} is the newly generated node, and the red path represents the final planned trajectory. The black circle indicates that the node has reached the vicinity of the target point.

2.2. RRT-Algorithm Based on RRT*

The RRT algorithm can only find a feasible path but does not guarantee an optimal one. The RRT* algorithm enhances the RRT by adding two steps, reconnection and optimization, which improve the quality and efficiency of path planning. The following explains these additional steps in the RRT* algorithm:

1. The initial steps are similar to the RRT algorithm.
2. Find the nearest node $x_{\min}$ to x_{new} in the random tree T, and calculate the cost $cost(x_{min}, x_{new})$ from x_{min} to x_{new}.
3. For nodes x_{near} within a certain range of x_{new} in the random tree T, calculate the cost $cost(x_{near}, x_{new})$ for connecting through x_{near}. Choose the connection with the minimum cost, as illustrated in Figure 2.
4. Add x_{new} to the random tree T and update the connection relationships and cost information between nodes.
5. Optimize certain nodes in the random tree T toward the goal x_{goal} by adjusting connections and cost information to improve path quality, as illustrated in Figure 3.
6. If x_{new} reaches the goal x_{goal}, identify a feasible path and terminate the algorithm.

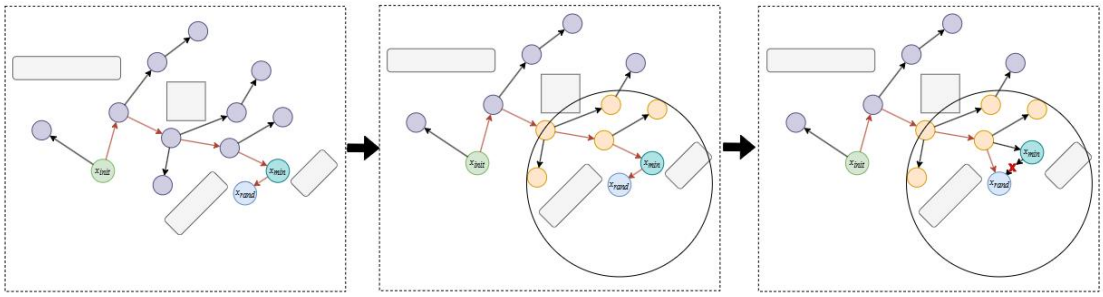

Figure 2. RRT reconnection.

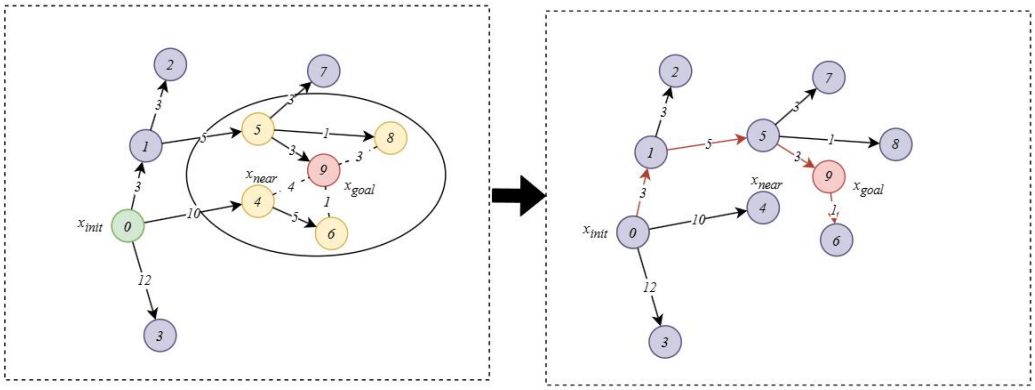

Figure 3. RRT optimization.

In Figure 2, the gray rectangle represents obstacles, the green spherical point x_{init} is the initial point, the cyan spherical point x_{min} is the node closest to x_{rand}, the orange spherical point enclosed by the circle represents the nodes x_{near} within a certain range of x_{rand}, and the red path represents the reconnected path.

In Figure 3, the green spherical point x_{init} is the initial point, the red spherical point x_{new} is the optimized target node, and the nodes x_{near} around the goal node are enclosed by an elliptical shape. Through computation, it is found that the cost from node 0 to node 6 was originally 15, but after optimization, the cost from node 0 to node 6 is reduced to 12, resulting in an optimized path.

The RRT* algorithm improves path quality and length through reconnection and optimization. However, since it does not alter the random sampling strategy, it still faces the same challenge as the RRT algorithm: low search efficiency in complex environments.

3. The Proposed HPS-RRT* Algorithm

As a classic sampling-based search algorithm, RRT* is widely used in robotic path planning; however, it suffers from low exploration efficiency, suboptimal final paths, and limitations in practical navigation applications. In this paper, the HPS-RRT* algorithm addresses these issues by employing hybrid sampling, Lévy distribution step sizes, and pruning strategies, significantly enhancing the exploration efficiency of RRT*. The sampling and connection process is outlined in Figure 4:

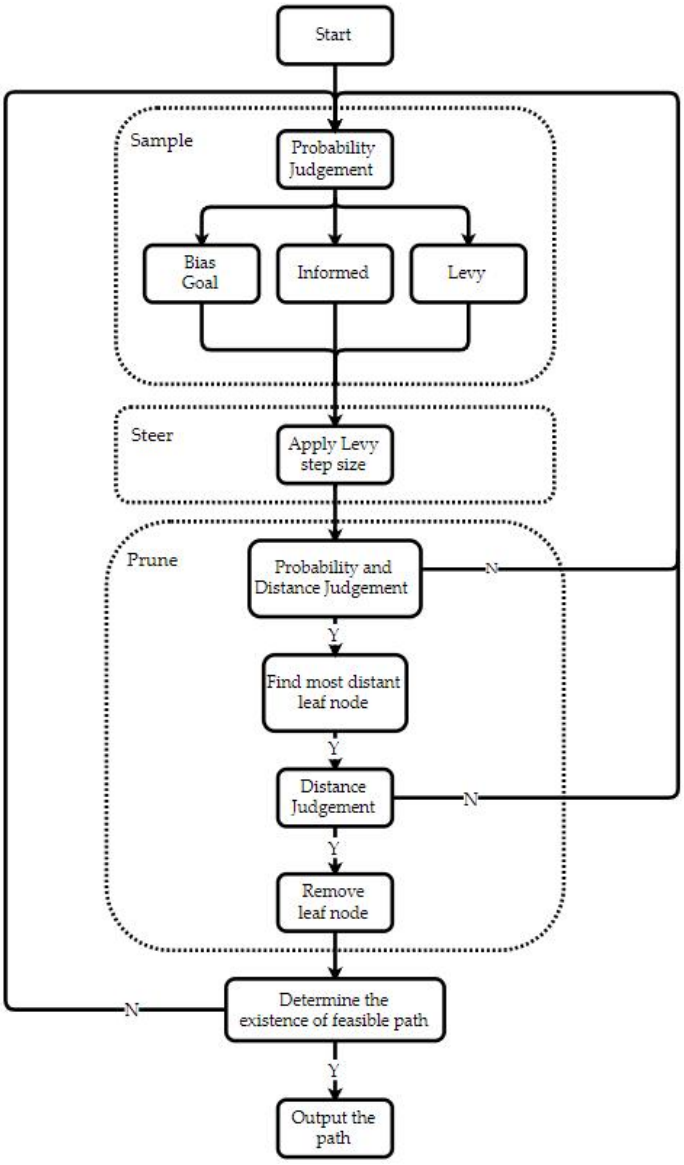

Figure 4. Flowchart of the HPS-RRT* algorithm.

Additionally, this paper presents a leader-based sparrow optimization algorithm to tackle the issues of non-optimal paths and poor smoothness. This method ensures rapid convergence while accommodating curvature constraints, enabling an optimization process with varying priorities. Consequently, the optimized path achieves the maximum curvature constraint and optimal path length. HPS-RRT* exhibits the following innovative features:

1. Utilizes a hybrid sampling strategy to balance the strengths and weaknesses of various sampling methods, achieving overall sampling optimization.
2. Employs extended step sizes based on Lévy distribution instead of fixed step sizes, enhancing exploration efficiency while avoiding local optima.
3. Introduces the innovative strategy of pruning redundant nodes during exploration, guiding tree growth in the correct direction and further improving exploration efficiency.
4. Implements a leader-based sparrow optimization algorithm to address the limitation of traditional smoothing algorithms, which fail to optimize curvature while considering path length.

3.1. Hybrid Sampling Strategy

The traditional RRT* algorithm is characterized by slow convergence, blindness, and a tendency to become trapped in local optima. To address these shortcomings, HPS-RRT employs a hybrid sampling strategy that probabilistically selects from different sampling methods to balance their respective strengths and weaknesses. The sampling strategies utilized in HPS-RRT* are outlined in Table 2:

Table 2. Hybrid sampling strategy.

Method	Probability	Advantage	Disadvantage
Bias-goal	0.2	Fast convergence to the goal	Risk of local minima
Informed	0.4	Efficient optimization	High computation cost
Lévy	0.4	Strong global exploration	Weak path optimization

As shown in Table 2, each sampling strategy has its advantages and disadvantages.

The Bias-goal strategy includes a certain probability of directly selecting the goal point as a sample during the sampling process, allowing for a quicker approach to the target. However, this method is prone to becoming trapped in local optima and has lower search efficiency in complex and diverse environments.

Inspired by the Informed-RRT* algorithm, the Informed strategy narrows the sampling space during exploration. It focuses on the starting point n_{start} and the node n_{close} closest to the goal, constructing an ellipse with a semi-major axis of twice the distance between these two points. The sampling process within this ellipse is as follows:

1. Construct the ellipse based on n_{start} and n_{close};
2. Calculate the rotation angle θ of the ellipse using the following formula:

$$\theta = arctan\left(\frac{y_{close} - y_{start}}{x_{close} - x_{start}}\right) \tag{1}$$

Here, x_{start} and y_{start} represent the axis value of n_{start}, and x_{close} and y_{close} represent the axis value of n_{close}.

3. Sample within a horizontally oriented ellipse with the same semi-major and semi-minor axes as the constructed ellipse;
4. Apply the rotation matrix to the sampled points matrix to rotate it into the constructed ellipse, resulting in the actual sampled point coordinates, as given by the following formula:

$$\begin{bmatrix} x_{new} \\ y_{new} \end{bmatrix} = \begin{bmatrix} cos\theta & -sin\theta \\ sin\theta & cos\theta \end{bmatrix} * \begin{bmatrix} x \\ y \end{bmatrix} \tag{2}$$

where $\begin{bmatrix} x_{new} \\ y_{new} \end{bmatrix}$ represents the coordinates of the sampled points, $\begin{bmatrix} cos\theta & -sin\theta \\ sin\theta & cos\theta \end{bmatrix}$ is the corresponding rotation matrix, and $\begin{bmatrix} x \\ y \end{bmatrix}$ denotes the coordinates of the points within the horizontal ellipse.

This sampling strategy utilizes a smaller, effective sampling space, improving search efficiency and optimizing the path. However, frequent computations can consume significant computational resources, placing certain demands on the processing platform. Additionally, the strategy exhibits poor adaptability in complex obstacle regions, making it challenging to find feasible paths.

Lévy sampling is a sampling strategy that follows a Lévy distribution, characterized by its heavy-tailed probability distribution. In sampling, it manifests as frequent small-range

samples interspersed with occasional large-range samples, a process known as the Lévy flight strategy. The sampling procedure is as follows:

1. Set the shape parameter β and the scaling factor α to calculate the Lévy step length s_L. In a standard Lévy distribution, the formula for σ is as follows:

$$s_L = \frac{\alpha * u}{|v|^{\frac{1}{\beta}}} \tag{3}$$

where u and v are random variables, with $u \sim N(0, \sigma^2)$ and $v \sim N(0,1)$ $(0,1)$. The formula for σ is as follows:

$$\sigma = \left(\frac{\Gamma(1+\beta) * sin\left(\frac{\pi * \beta}{2}\right)}{\beta * \Gamma\left(\frac{1+\beta}{2}\right) * 2^{\left(\frac{\beta - 1}{2}\right)}} \right)^{\frac{1}{\beta}} \tag{4}$$

$$\Gamma(x) = \int_0^{\infty} t^{x-1} * e^{-t} dt \tag{5}$$

2. Calculate the closest node to the target point, denoted as n_{close}.
3. Using n_{close} as the reference point, move a distance s_L in a random direction D_r to obtain the sample point n_{new}. The formula is as follows:

$$n_{new} = n_{close} + D_r * s_L \tag{6}$$

The Lévy sampling strategy enhances algorithm adaptability in complex environments through localized sampling. Additionally, occasional large-range sampling helps to mitigate local optima, improving global optimality; however, it exhibits poor performance in local optimization.

Each sampling strategy has its advantages and disadvantages. The HPS-RRT* algorithm balances these by probabilistically selecting different sampling strategies at each step, allowing it to enhance path quality and adaptability in complex environments while maintaining convergence speed.

3.2. Lévy Step Size

The traditional RRT* algorithm employs a fixed step size, leading to low node expansion efficiency and poor robustness across different maps, making parameter tuning challenging. This paper proposes using a Lévy step size, characterized by frequent small movements and occasional large jumps. The small movements facilitate navigation through complex environments, enhancing search efficiency, while the large jumps help to escape local optima, improving path quality. The Lévy step size enhances algorithm robustness while maintaining exploration efficiency, exhibiting low parameter sensitivity and high adaptability to various maps and environments. Its specific expression is given in Equation (3). The parameter β typically ranges from 1 to 2; closer to 1 indicates a stronger heavy-tailed Lévy distribution with a higher probability of long-distance jumps, enhancing global search capability. Conversely, closer to 2 results in a distribution similar to a Gaussian distribution, with smaller random step sizes and fewer long jumps, favoring local exploration. In this algorithm, β is set to 1.5, balancing local searches with adequate global search ability.

To visually observe the distribution of Lévy step lengths, we performed 2000 iterations based on the aforementioned formula, yielding the distribution shown in Figure 5.

In Figure 5, it is evident that the Lévy step length distribution consists of frequent small steps and occasional large steps. This characteristic aids in cautious node connections through complex obstacle-laden areas during exploration. Moreover, the occasional large steps can help escape local optima, enhancing exploration efficiency.

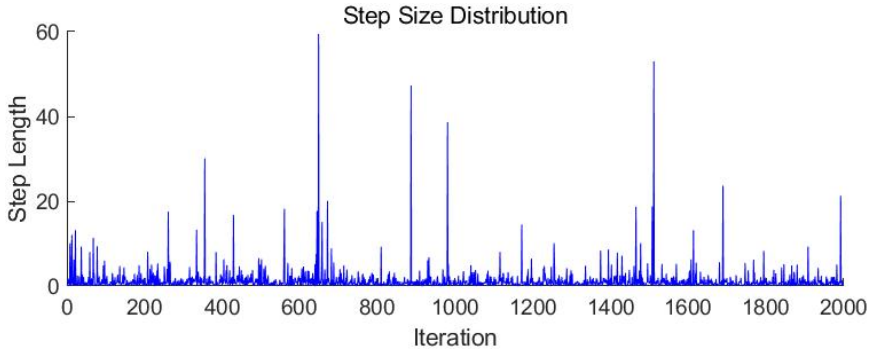

Figure 5. Lévy Step Size Distribution.

3.3. Leaf Prune

In the RRT* algorithm, each node connection is retained throughout the exploration process, which may lead to tree growth in incorrect or suboptimal directions. This can decrease exploration efficiency and increase the time required for path planning. To address this issue, HPS-RRT* introduces a pruning strategy inspired by ecological mechanisms in natural tree growth, such as apical dominance and lower branch degradation. This strategy aims to optimize the algorithm's exploration and convergence performance. The specific process is outlined as follows:

1. When connecting a new node n_{new}, if it is closer to the target than the nearest node n_{close}, a pruning decision is initiated.
2. After meeting certain probabilistic criteria, the process proceeds, simulating the uncertainty in tree growth.
3. The farthest node from n_{new}, labeled $n_{distant}$, is identified, and the distance to $n_{distant}$ is calculated.
4. If this distance exceeds half of the direct distance from the start point to the target, the $n_{distant}$ node is eliminated, simulating the degradation or wilting of lower leaves.

This strategy ensures stable tree growth during the initial exploration phase, allowing for comprehensive expansion and preventing premature convergence to local optima. In the later stages, as the tree approaches the target point, the pruning mechanism gradually directs the tree toward the target, reducing ineffective branches and enhancing algorithm efficiency. By removing nodes that are distant from the target, unnecessary search areas can be effectively minimized, conserving computational resources. The resultant effect is illustrated in Figure 6.

In Figure 6, n_{new} represents the new node, n_{close} denotes the nearest point to the target before connecting the new node, $n_{distant}$ is the farthest node from n_{new}, n_{start} indicates the starting point, and n_{goal} signifies the target point. Distances a and b correspond to the distances from n_{close} and n_{new} to the target, respectively. The circular shapes represent nodes, solid lines indicate actual connections, and dashed lines illustrate the pruning operation.

From the diagram, it can be observed that when $b < a$ and the distance and probability criteria are satisfied, a pruning operation is performed. The farthest node $n_{distant}$ from n_{new} and its connecting segments are pruned, as indicated by the dashed lines in Figure 6.

This visually demonstrates that the overall trend of the tree after pruning is more aligned with the target point, akin to the growth of terminal buds in branches. This improvement enhances the convergence rate during node expansion, directing the expansion closer to the target point and reducing the exploration of erroneous directions.

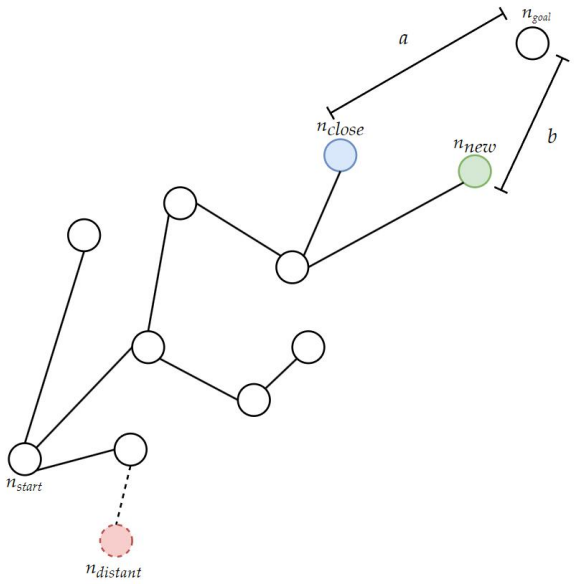

Figure 6. Pruning effect diagram. (*a* and *b* indicate the distance between the corresponding two nodes).

3.4. Leader-Based Sparrow Optimization Algorithm

Conventional RRT or RRT* algorithms often yield paths that are unsuitable for tracking by tracked robots in orchards. Some paths exhibit large curvature, failing to meet the maximum turning radius requirements of the tracked robots, which hinders effective tracking performance. Additionally, the generated paths are typically excessively long and not globally optimal, leading to increased operational costs and reduced efficiency for agricultural robots. This paper proposes an optimization strategy based on vehicle kinematic constraints—the improved sparrow search algorithm—to address this issue.

The sparrow search algorithm, as a heuristic swarm intelligence optimization method, is widely applied in various optimization scenarios. Its core idea is to simulate the foraging and anti-predation behaviors of sparrows, leveraging the collaboration and division of labor among individual members of the population to achieve effective global search and avoid local optima. In the conventional sparrow search algorithm, there are typically two roles: foragers and followers. Foragers are responsible for approaching the global optimum and enhancing solution diversity through random searches, simulating the foraging process of sparrows. On the other hand, followers focus on tracking the optimal solution while escaping from the worst solution, mimicking the anti-predation behavior and cooperative functionality of sparrows [29]. The sparrow search algorithm is characterized by strong global search capability, fast convergence speed, and fewer parameters that are easy to adjust. The general procedure is as follows:

1. Initialize the sparrow population;
2. Assign roles to the sparrows;
3. Execute functions based on assigned roles;
4. Calculate fitness and update the optimal solution;
5. Check if the maximum iteration count is reached; if so, output the optimal solution; otherwise, return to step 3 for further iterations.

In path optimization, two key metrics require significant attention: the maximum curvature (or smoothness) of the path, which affects its suitability for actual navigation tasks and is critical for the tracking performance of the robot, and the path length, where shorter paths can reduce navigation time costs and enhance operational efficiency. In conventional sparrow search algorithm implementations, optimizing both maximum curvature and path

length simultaneously may lead to paths with a greater maximum curvature after optimization compared to before. Additionally, while traditional path smoothing algorithms, such as B-spline optimization, can create smoother paths, they often overlook changes in path length, potentially resulting in an optimized path that is longer than the original. To comprehensively consider the two performance metrics mentioned above, ensuring that the maximum curvature of the path meets the robot's movement requirements while achieving a shorter and safer path, HPS-RRT* employs an improved sparrow search algorithm.

The HPS-RRT* algorithm integrates and enhances the sparrow search algorithm for path optimization by innovatively proposing a leader-based sparrow optimization algorithm. This approach aims to optimize curvature while ensuring path optimality. The optimization process is shown in Figure 7:

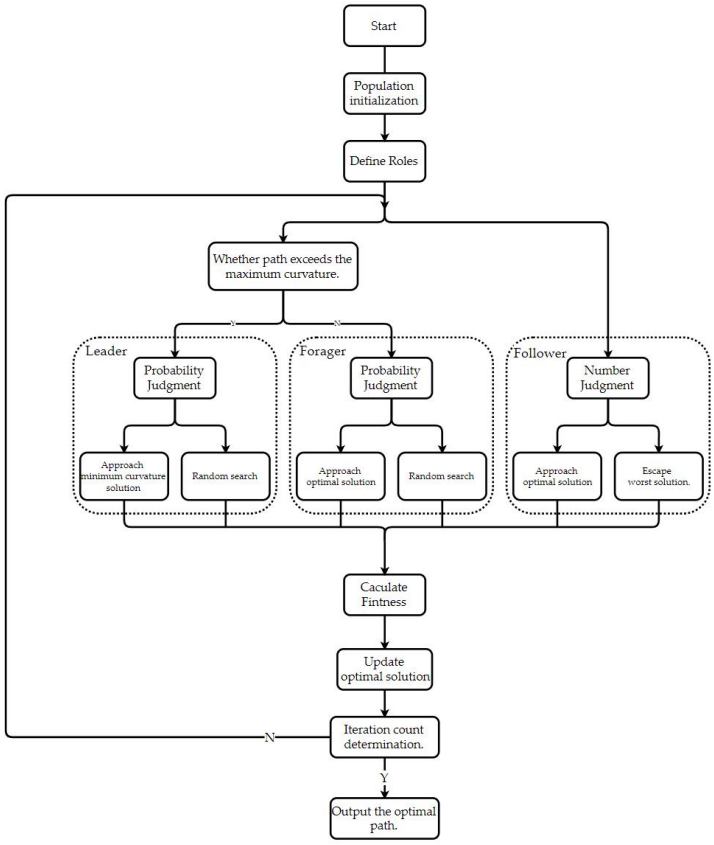

Figure 7. Flowchart of the leader-based sparrow optimization algorithm.

At the beginning of the optimization loop, the sparrow optimization algorithm calculates the fitness value based on the current path length and maximum curvature. The formula is as follows:

$$Fitness = \alpha_1 * L + \alpha_2 * Cur \tag{7}$$

where α_1 and α_2 represent the penalty weights, L denotes the path length, and Cur indicates the maximum curvature of the path.

Next, a population of sparrows is randomly initialized, where this initialization involves applying random perturbations to the control points of the existing path. This process yields sparrows with diverse solutions, which are then categorized into different roles proportionally.

During each optimization iteration, the algorithm checks whether the current path meets the maximum curvature constraint to ensure feasibility. If the constraint is not satisfied, the leader mechanism is triggered. In this case, the leader assumes the role of

the forager with a certain probability, guiding the population towards the solution with minimal curvature or conducting a random search.

The adjustment of control points in the path optimization can be expressed by the following formula:

$$P(x_{new}, y_{new}) = \begin{cases} P(x_{old}, y_{old}) + s_{rand} * \ D_{min}, p < 0.7 \\ P(x_{old}, y_{old}) + s_{rand} * \ D_{rand}, p \geq 0.7 \end{cases} \tag{8}$$

In this context, $P(x_{old}, y_{old})$ represents the original control points, while $P(x_{new}, y_{new})$ denotes the optimized control points. The parameter s_{rand} is a random number between 0 and 1, which should be adjusted according to the size of the map and the path. D_{min} indicates the direction of the solution with the minimum curvature and D_{rand} represents a random direction. Finally, p is a random probability between 0 and 1.

The leader mechanism effectively reduces the maximum curvature of the path, enhances path smoothness, and maintains solution diversity during the optimization process, thereby preventing convergence to local optima.

If the path satisfies the constraints, the forager will converge towards the optimal solution with a certain probability or explore in a random direction. This can be expressed by the following formula:

$$P(x_{new}, y_{new}) = \begin{cases} P(x_{old}, y_{old}) + s_{rand} * D_{opt}, p < 0.7 \\ P(x_{old}, y_{old}) + s_{rand} * D_{rand}, p \geq 0.7 \end{cases} \tag{9}$$

Here, $P(x_{old}, y_{old})$ represents the original control points, and $P(x_{new}, y_{new})$ denotes the optimized control points. s_{rand} is a random number between 0 and 1, D_{best} indicates the direction of the current optimal solution, D_{rand} represents a random direction, and p is a random probability between 0 and 1.

The forager's search allows the population to explore to a certain extent while simultaneously seeking the optimal solution, thereby enhancing the diversity of solutions.

The followers will either converge toward the optimal solution or evade danger by moving away from the worst solution. This can be expressed by the following formula:

$$P(x_{new}, y_{new}) = \begin{cases} P(x_{old}, y_{old}) + \ s_{rand} * D_{best}, p < 0.5 \\ P(x_{old}, y_{old}) + s_{rand} * D_{worst}, p \geq 0.5 \end{cases} \tag{10}$$

Here, $P(x_{old}, y_{old})$ represents the original control points, while $P(x_{new}, y_{new})$ denotes the optimized control points. s_{rand} is a random number between 0 and 1, s_{rand} indicates the direction of the current optimal solution, D_{worst} represents the direction to escape from the worst solution, and p is a random probability between 0 and 1.

The followers are responsible for maintaining the stability of the population's trend, with half of them approaching the optimal solution and the other half escaping the worst solution. This leads to an overall improvement in the population's direction.

At the end of each iteration, the fitness of each sparrow in the population is calculated, and the optimal and worst solutions are updated, continuing until the maximum number of iterations is reached.

The final optimized path obtained through the above optimization process achieves optimality while satisfying curvature constraints. The sparrow optimization algorithm demonstrates significant advantages in convergence speed and global optimization compared to traditional algorithms such as SA and PSO. Additionally, the improved sparrow optimization algorithm features a prioritized optimization process that allows for flexible

expansion and differentiated optimization of various path characteristics to meet diverse path requirements.

This algorithm has significant advantages over traditional path smoothing optimization methods, such as B-spline optimization, which often struggles to balance path length requirements and safety, leading to higher collision risks with obstacles. The improved sparrow optimization algorithm effectively addresses this issue by simultaneously optimizing path smoothness and globally optimizing path length to achieve an overall optimal solution.

4. Results and Discussion

To demonstrate the superiority of the HPS-RRT* algorithm, Map1, Map2, and Map3, as shown in Figure 8, were utilized as simulation maps of different complexity. Each map measures 1000 × 1000 and simulates different environments to assess the algorithm's performance in complex scenarios.

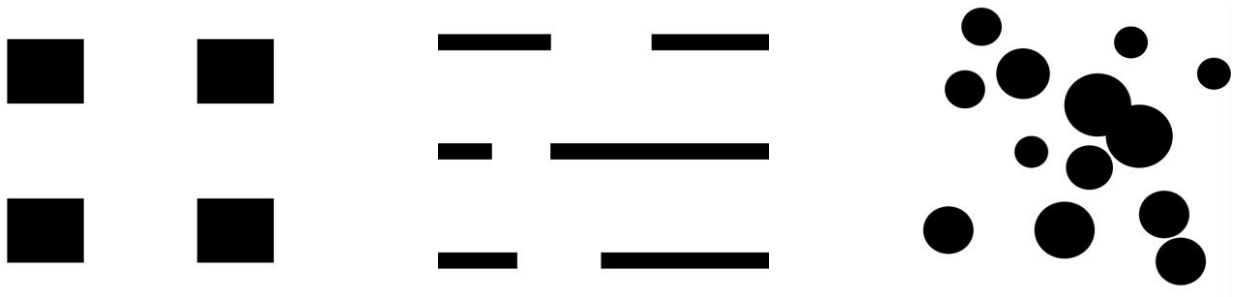

(**a**) (**b**) (**c**)

Figure 8. Illustrative diagram of experimental maps: (**a**) Map1; (**b**) Map2; (**c**) Map3.

In Figure 8, the white areas represent navigable regions, while the black areas indicate obstacles.

This experiment compares four algorithms: RRT*, Bias-RRT*, Connected-RRT*, and PRM*, with identical parameters across different maps. The parameters of the HPS-RRT* algorithm are shown in Table 3 and remain consistent in all subsequent experiments.

Table 3. HPS-RRT* parameter table.

Parameters	Symbol	Value
Step gain coefficient	α	100
Lévy shaping parameter	β	1.5
Initial population size of sparrows	ε	30
Number of iterations in the sparrow	i	1000

Bias-RRT* improves the traditional RRT by incorporating a fixed target-biased sampling probability, enhancing the likelihood of sampling near the target node. This approach accelerates the convergence by directly selecting the target node as a sampling point with a certain probability during random node generation, thereby expediting the path discovery process. Connected-RRT*, on the other hand, adopts a bidirectional strategy, simultaneously extending node trees from both the start and the goal points. This bidirectional expansion facilitates quicker connections between the two trees, significantly reducing path search time. PRM* differs from the RRT* algorithm in its planning process. It randomly distributes a certain number of nodes within the map and attempts to connect each node with others. If the distance between nodes is within a predefined range, the connection is considered valid; otherwise, it is discarded. Dijkstra's algorithm is then employed to find the optimal trajectory, with the resulting path chosen as the final output. As a graph-based

search algorithm, PRM* is applicable to high-dimensional spaces. However, its efficiency decreases significantly in environments with narrow passages or dense obstacles, and it may even fail to find a solution under such conditions.

4.1. Comparison of Map Performance

Figures 9–11 illustrate the performance of different algorithms on various maps. Green or blue line segments represent the expansion tree's attempted paths, while the red line segment indicates the final actual path. The red triangle marks the starting point, the blue triangle marks the goal, and the black regions represent obstacle areas.

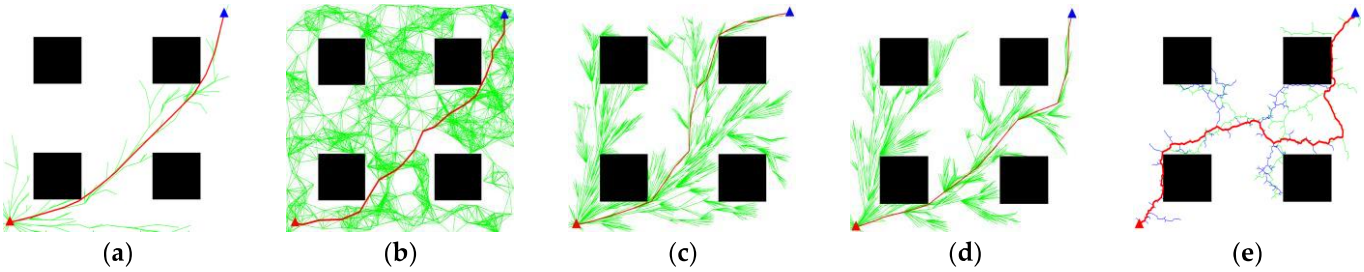

Figure 9. Path planning visualization for Map1: (**a**) HPS-RRT*; (**b**) PRM*; (**c**) RRT*; (**d**) Bias-RRT*; (**e**) Connected-RRT*.

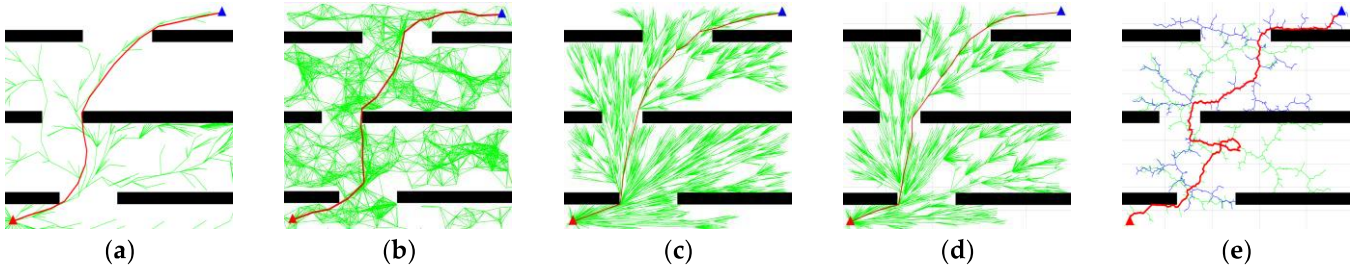

Figure 10. Path planning visualization for Map2: (**a**) HPS-RRT*; (**b**) PRM*; (**c**) RRT*; (**d**) Bias-RRT*; (**e**) Connected-RRT*.

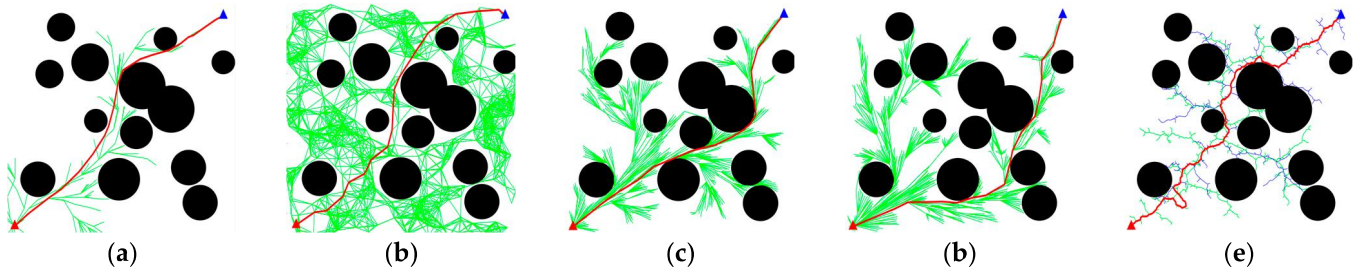

Figure 11. Path planning visualization for Map3: (**a**) HPS-RRT*; (**b**) PRM*; (**c**) RRT*; (**d**) Bias-RRT*; (**e**) Connected-RRT*.

A comparison of the different results shows that HPS-RRT* achieves faster convergence, with the shortest and smoother final paths, making it more suitable for trajectory tracking of the orchard crawler robot.

The performance comparison of different algorithms on various maps is presented in Table 4.

Table 4. Comparison of data across different maps.

Method	Map1				Map2				Map3			
	ALength	**ATime**	**SRate**	**ACur**	**ALength**	**ATime**	**SRate**	**ACur**	**ALength**	**ATime**	**SRate**	**ACur**
HPS-RRT*	1376.98	0.19	100%	0.10	1489.83	2.20	100%	0.10	1376.55	0.24	100%	0.08
PRM*	1410.12	0.31	98%	0.12	1533.25	0.18	91.00%	0.14	1437.11	0.13	100%	0.13
RRT*	1399.80	5.68	100%	0.17	1520.48	17.30	52.00	0.18	1398.44	5.79	100%	0.12
Bias-RRT*	1408.66	2.91	100%	0.17	1535.68	8.93	58%	0.16	1398.96	2.57	100%	0.13
Connect-RRT*	1873.21	2.80	100%	0.16	2118.43	4.19	98%	0.16	1831.43	3.20	93%	0.16

Here, "ALength" represents the average length of the effective paths discovered, "ATime" refers to the computation time from the start to the end of exploration to evaluate the algorithm's convergence performance, "SRate" indicates the average success rate of exploration, where success is defined as planning a collision-free path to the target point, and "ACur" refers to the mean maximum curvature, used to evaluate path smoothness.

As shown in Table 4, HPS-RRT* consistently demonstrates superior performance across various environments. Compared to RRT*, Bias-RRT*, and Connect-RRT*, it achieves improvements in path length by approximately 1.7%, 2.2%, and 27.0%, respectively, as well as in planning time by approximately 93.3%, 86.4%, and 77.7%. Moreover, HPS-RRT* consistently achieves a 100% success rate. In comparison with PRM*, while HPS-RRT* may have slightly higher planning times in certain maps, its path length is improved by approximately 3.1%. Additionally, HPS-RRT* shows significant enhancements in smoothness compared to all four algorithms, with improvements of approximately 27.9%, 39.7%, 39.0%, and 41.7% over PRM*, RRT*, Bias-RRT*, and Connect-RRT*, respectively.

To further validate the superiority of the HPS-RRT* algorithm, paired sample T-tests were conducted to compare its performance with RRT*, Bias-RRT*, Connected-RRT*, and PRM*, verifying the differences in various performance metrics.

The paired sample T-test, widely used in statistics to compare the means of two related samples, involves the following steps:

1. Perform a normality test: Verify that the samples follow a normal distribution; if satisfied, proceed to the next step;
2. Set the hypotheses: Define the null hypothesis H_0; the means of the two related samples are equal, indicating no difference. In the alternative hypothesis H_1, the means of the two samples are not equal, indicating a difference;
3. Calculate the means and standard deviations: Use the following formulas for mean $\overline{d}$ and standard deviation s_d:

$$\overline{d} = \frac{1}{n} * \sum_{i=1}^{n} d_i \tag{11}$$

$$s_d = \sqrt{\frac{1}{n-1} * \sum_{i=1}^{n} \left(d_i - \overline{d}\right)^2} \tag{12}$$

where d_i represents sample differences and n is the sample size.

4. Compute the T-value t and degrees of freedom d_f;

$$t = \frac{\overline{d}}{s_d / \sqrt{n}} \tag{13}$$

$$d_f = n - 1 \tag{14}$$

where $\overline{d}$ is the mean of differences, s_d is the standard deviation, and n is the sample size.

5. Determine the p-Value: Based on the computed t and d_f, find the corresponding p from the t-distribution table.
6. Compare with the significance level: If $p < \alpha$ (commonly 0.05), reject the null hypothesis H_0, concluding a significant difference in means; otherwise, accept H_1.

To quantify the magnitude of differences, Cohen's d is introduced, and calculated as follows:

$$d = \frac{(\overline{y_1} - \overline{y_2})}{\sigma_{pooled}} \tag{15}$$

$$\sigma_{pooled} = \left[\frac{(n_1 - 1) * s_1 + (n_2 - 1) * s_2}{n_1 + n_2}\right]^{\frac{1}{2}} \tag{16}$$

where $\overline{y_1}$ and $\overline{y_2}$ are sample means, s_1 and s_2 are standard deviations, and n_1 and n_2 are sample sizes.

The algorithm result data were subjected to normality tests, and all sample data passed the normality requirement. The null hypothesis H_0 was set as follows: the means of the two related samples are equal, indicating no difference. The alternative hypothesis H_1 was set as follows: the means of the two samples are not equal, indicating a significant difference. A significance level of p = 0.05 was chosen. Paired sample T-tests were conducted to compare the path length, planning time, and the maximum curvature of HPS-RRT* with RRT*, Bias-RRT*, Connect-RRT*, and PRM*. The results of the comparisons between each algorithm with HPS-RRT* are shown in Table 5.

Table 5. T-test results.

Performance Metrics	Comparative Method	Map1			Map2			Map3		
		t	*p*	*d*	*t*	*p*	*d*	*t*	*p*	*d*
Length	**PRM***	−7.860	0.000001	0.794	−5.115	0.000001	0.536	−6.921	0.000001	0.692
	RRT*	−4.818	0.000001	0.482	−4.199	0.000001	0.420	−2.24	0.000001	0.224
	Bias-RRT	−4.700	0.000001	0.470	−4.765	0.000001	0.626	−2.248	0.000001	0.225
	Connected-RRT*	−19.135	0.000001	1.933	−20.058	0.000001	2.026	−21.248	0.000001	2.125
Time	**PRM***	−8.146	0.000001	0.815	7.040	0.000001	0.704	4.104	0.000001	0.410
	RRT*	−28.539	0.000001	2.854	−10.071	0.000001	1.007	−21.213	0.000001	2.121
	Bias-RRT	−18.970	0.000001	1.897	−7.931	0.000001	0.793	−12.499	0.000001	1.250
	Connected-RRT*	−7.521	0.000001	0.752	−4.465	0.000001	0.447	−7.698	0.000001	0.77
Curvature	**PRM***	−0.803	0.000001	0.08	−4.303	0.000001	0.430	−9.757	0.000001	0.976
	RRT*	−4.540	0.000001	0.454	−6.399	0.000001	0.64	−5.034	0.000001	0.503
	Bias-RRT	−3.926	0.000001	0.393	−4.753	0.000001	0.475	−6.019	0.000001	0.602
	Connected-RRT*	−4.537	0.000001	0.454	−9.456	0.000001	0.946	−17.043	0.000001	1.704

A Cohen's d value less than 0.2 indicates a negligible effect size, values in the range [0.2, 0.5) indicate a small effect size, and values greater than 0.8 indicate a large effect size. As shown in Table 5, most Cohen's d values for HPS-RRT* compared to other algorithms are greater than 0.5. This indicates that the mean performance of HPS-RRT* is significantly different from, and substantially better than, the compared algorithms.

The HPS-RRT* algorithm employs a hybrid sampling strategy and a Lévy distribution step size optimized through a pruning strategy to significantly enhance the search speed for paths. Utilizing a leader-based sparrow optimization algorithm ensures that the paths not only meet the maximum curvature requirements of the robot but also minimize path length, achieving a global optimum. The experimental results demonstrate that the HPS-RRT* algorithm converges quickly, generates high-quality planned paths, and shows excellent adaptability to complex environments, outperforming the comparison algorithms and significantly exceeding the performance of traditional RRT* algorithms.

4.2. Experiment on Multi-Target Point Map in Orchard

To validate the effectiveness of the algorithm in orchard environments, the tracked robot shown in Figure 12 was employed for mapping. This robot is equipped with a MID360 LiDAR and a high-precision IMU for mapping and real-time localization. Additionally, it features a dual-line GPS system, enabling high-precision positioning for future experiments. The detailed kinematic parameters of this tracked robot are listed in Table 6.

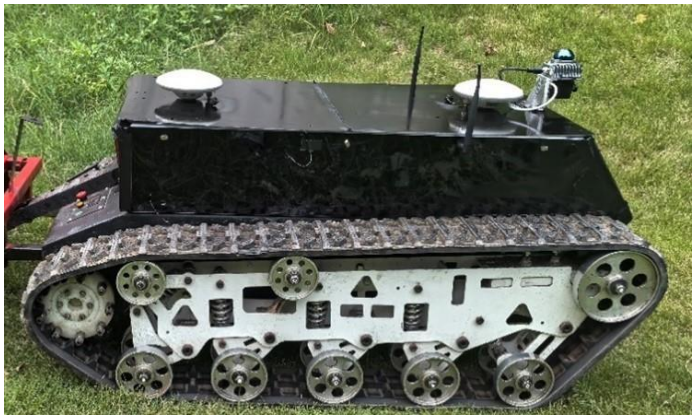

Figure 12. The nonholonomic orchard robot.

Table 6. The detailed kinematic parameters of this tracked robot.

Parameter	Value
Wheelbase (mm)	290
Maximum speed (km/h)	6
Maximum obstacle height (mm)	400

Based on the kinematic parameters of the tracked robot, the maximum wheel speed of the left and right tracks is 6 km/h, and the wheelbase is 290 mm. Assuming the robot performs a maximum radius turn where one track remains stationary and the other moves at maximum speed, the kinematic modeling is as follows:

To adapt to the complex terrain of agricultural environments such as orchards, this paper utilizes a tracked two-wheel robot model, which can also be regarded as a differential-drive robot. Its motion is determined by two independently controlled tracks. The simplified model of the tracked two-wheel robot chassis is shown in Figure 13:

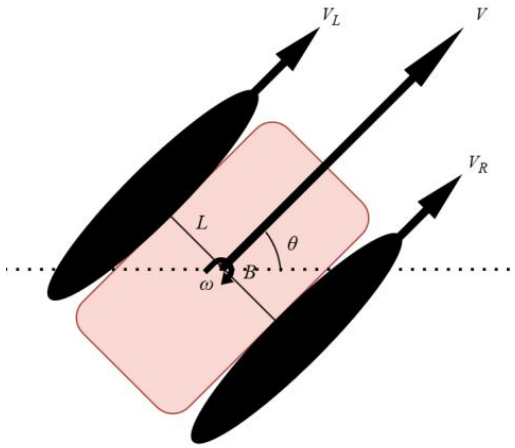

Figure 13. Simplified model of the tracked two-wheel robot chassis.

Here, L represents the track spacing (distance between the two tracks), V_L and V_R are the linear velocities of the left and right tracks, respectively, and θ denotes the robot's heading angle. B represents the robot's center, ω is the angular velocity, and V denotes the linear velocity of the robot's center. The calculations yield the following relationships:

The center velocity V and angular velocity ω are as follows:

$$V = \frac{V_L + V_R}{2} \tag{17}$$

$$\omega = \frac{V_R - V_L}{L} \tag{18}$$

The turning radius R and steering curvature k are as follows:

$$R = \frac{V}{\omega} = \frac{L*(V_L+V_R)}{2*(V_R - V_L)} \tag{19}$$

$$\mathrm{k} = \frac{\omega}{V} = \frac{2*(V_R - V_L)}{L*(V_L+V_R)} \tag{20}$$

Additionally, the robot's pose is updated in real-time using the following equations:

$$\dot{x} = V * cos\theta \tag{21}$$

$$\dot{y} = V * sin\theta \tag{22}$$

$$\dot{\theta} = \omega \tag{23}$$

According to Equations (17)–(20), the maximum steering curvature is 2.341 m^{-1}.

The mapping site is a pomelo orchard, with the arrangement of the trees illustrated in Figure 14. Figure 15 presents the 3D point cloud of the orchard.

Figure 14. Actual environment of the orchard.

In Figure 15, the colors correspond to the color bar on the right, representing the Z-axis data from smallest to largest, where the minimum value is 0 and the maximum is 2 m.

To ensure the planning results are clear and intuitive, the local part of the 3D point cloud data is dimensionally reduced and converted into a grid map. Regions with a Z-axis height greater than 0.1 m are defined as obstacles, as shown in Figure 16a. Additionally, to accommodate the actual volume of the orchard robot, obstacle expansion was applied, which expanded the volume of the obstacles to 2.5 times the original size, as illustrated in Figure 16b.

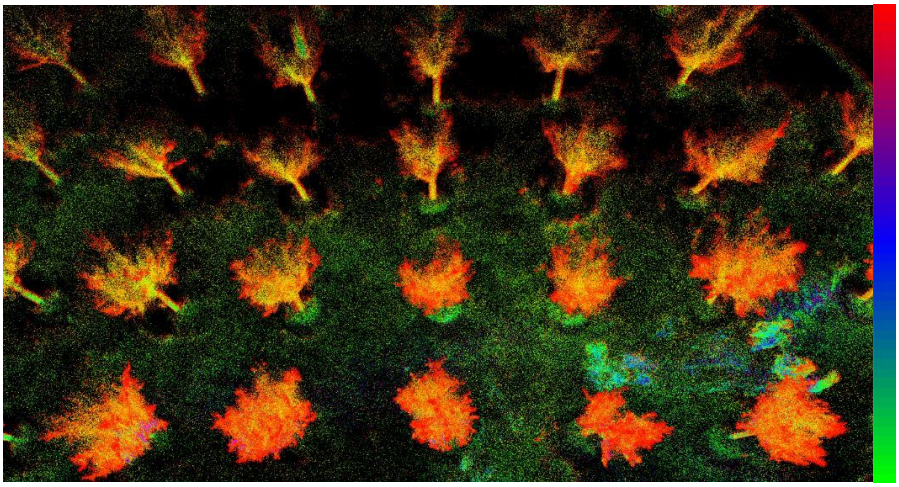

Figure 15. Three-dimensional point cloud of orchard.

(**a**) (**b**)

Figure 16. Two-dimensional map of orchard. (**a**) Before expansion; (**b**) after expansion.

In Figure 16, the white areas represent navigable regions, while the black areas indicate obstacles.

In the experiment, a series of target points were preset to simulate the path points required for actual fruit tree harvesting. Multi-objective planning was then performed sequentially based on these target points, as shown in Figure 17.

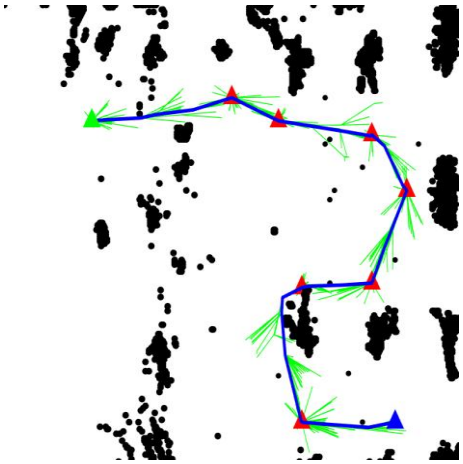

Figure 17. Orchard planning map.

In Figure 17, the green triangle represents the starting point, the blue triangle indicates the endpoint, the red triangles are path points, the black objects are obstacles, the green line segments show the exploration path, and the blue curve represents the actual path.

After conducting 100 experiments, the average maximum curvature of the final path was calculated as 0.35 m^{-1}, which is smaller than the tracked robot's maximum curvature of 2.341 m^{-1}, meeting its kinematic requirements. The final path was smooth, continuous, and collision-free, making it directly applicable to navigation in actual orchard operations. In all 100 experiments, HPS-RRT* successfully planned the path, demonstrating its robust performance in large, unstructured maps such as orchards. Additionally, the standard deviation of the maximum curvature is 0.1158, and the average planning time is 7.51 s.

To further evaluate the superiority of the HPS-RRT* planned path in practical navigation, a trajectory-tracking control experiment was designed based on the kinematic model of the orchard robot. The final results are shown in Figure 18.

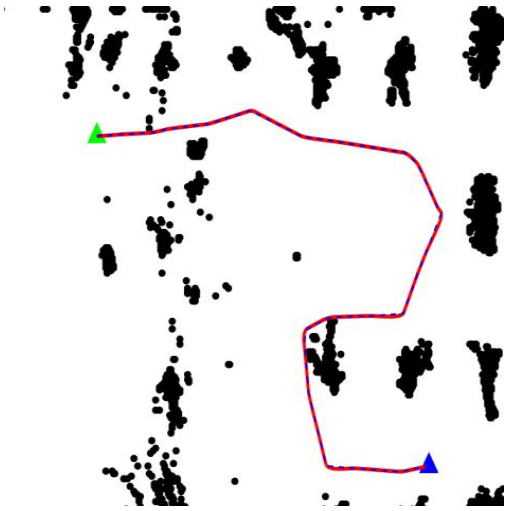

Figure 18. Trajectory tracking performance diagram.

In Figure 18, the green triangle represents the starting point, the blue triangle indicates the endpoint, the blue dashed line denotes the reference path, and the red solid line represents the tracked trajectory.

The figure intuitively shows that the tracked trajectory aligns well with the reference path, achieving a path overlap rate of 97.78%. This demonstrates that the path meets the practical navigation requirements of the orchard robot.

4.3. Robustness and Sensitivity Analysis of the Algorithm

Map3 is used as the baseline map to evaluate the algorithm's robustness and to conduct 100 experiments intuitively and effectively. In each experiment, 25 randomly sized obstacles are introduced as external disturbances to test the algorithm's performance under such conditions. The approximate planned paths are illustrated in Figure 19.

In Figure 19, the red line represents the planned path, the red triangle denotes the starting point, the blue triangle indicates the goal point, the black areas represent obstacles, and the white areas indicate feasible regions.

The performance metrics are summarized in Table 7, where "Basis" represents the baseline map and "Interference" represents the map with added disturbances.

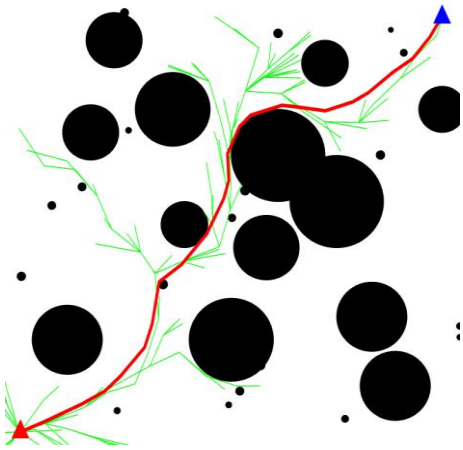

Figure 19. Path diagram.

Table 7. The performance metrics.

Map	Average Length	Average Time/s	Success Rate	Average Curvature
Basis	1376.55	0.24	100%	0.080
Interference	1405.59	0.27	100%	0.091

From Table 7, it can be observed that under certain external disturbances, the performance metrics of HPS-RRT* show minimal variations compared to the baseline. This demonstrates the strong robustness of the HPS-RRT* algorithm.

To further evaluate the sensitivity of various parameters in the HPS-RRT* algorithm, Map3 was selected as the experimental map. The experiments were conducted 100 times for four groups of algorithm parameters: A, B, C, and D. The specific parameters for A, B, C, and D are detailed in Table 8.

Table 8. Parameter combination table.

Group	α	β	ε	i
A	50	1.5	30	1000
B	100	1.25	30	1000
C	100	1.5	20	1000
D	100	1.5	30	500

The experimental results are shown in Table 9, where “Basis” represents the original parameters.

Table 9. Planning results.

Group	Average Length	Average Time/s	Success Rate	Average Curvature
Basis	1376.55	0.24	100%	0.080
A	1379.59	0.50	100%	0.096
B	1376.00	0.21	100%	0.094
C	1379.49	0.28	100%	0.095
D	1394.05	0.26	100%	0.135

As shown in Table 9, the impact on “Length” under different parameters ranges from approximately 0.04% to 1.2%, indicating a minimal effect. The impact on “Time” ranges from about 0.7% to 52.0%, showing a significant effect, while the impact on “Curvature” is around 16.7% to 40.7%, which is relatively small.

Thus, it can be concluded that adjusting the parameters of HPS-RRT* has a considerable effect on planning time. Different parameters should be selected for different maps to enhance planning efficiency, further demonstrating that HPS-RRT* is highly sensitive to parameter settings and requires careful selection to adapt to various environments.

5. Conclusions

To address the issues of low success rates, inefficient searches, poor path quality, and insufficient smoothness in existing path planning algorithms for unstructured environments like orchards, this study proposes the HPS-RRT* algorithm. To counter the low planning efficiency caused by the random sampling strategy in traditional RRT algorithms, a hybrid sampling strategy is employed, significantly improving planning speed and reducing ineffective sampling points. The HPS-RRT* algorithm utilizes an extended step size based on Lévy distribution to ensure both the efficiency and quality of the planned paths, thereby resolving the inefficiencies, rigidity, and collision issues associated with fixed step sizes. Additionally, to tackle the redundancy of ineffective nodes during the planning process, an innovative pruning strategy is introduced to eliminate redundant nodes during tree growth, enhancing search efficiency. To improve the smoothness of the final paths generated by traditional RRT algorithms, the proposed method incorporates a leader-based sparrow optimization algorithm, which optimizes both path curvature and length, allowing for direct application in path tracking.

The experimental results indicate that the proposed HPS-RRT* algorithm outperforms RRT, Bias-RRT*, Connect-RRT, and PRM algorithms in several aspects. The final path length was reduced by 1.7% to 27%, planning efficiency improved by 77.7% to 93.3%, and path smoothness increased by approximately 27.9% to 41.7%, achieving a success rate of 100%, while other algorithms occasionally experienced planning failures. The calculated average maximum curvature of the paths was 0.8 m^{-1}, confirming the feasibility of the HPS-RRT* algorithm for robotic applications in orchard environments.

In conclusion, the proposed HPS-RRT* algorithm effectively addresses path planning issues in unstructured environments such as orchards. However, it remains sensitive to parameter selection, making appropriate parameter tuning crucial across different map scenarios. Additionally, the HPS-RRT* algorithm has only been tested in static environments, lacking adaptability to dynamic scenarios. The experimental results also indicate that HPS-RRT* has high computational demands and relies on hardware performance, which may affect its application in real-time navigation.

In future work, we will attempt to utilize neural network algorithms such as reinforcement learning to optimize the sampling strategy's probabilities, enabling dynamic adjustments for different environments. Additionally, the algorithm will be extended to incorporate real-time dynamic obstacle avoidance by integrating predictive models or local obstacle avoidance strategies. Furthermore, we aim to explore the practical performance of HPS-RRT* across various hardware platforms, optimizing its operational efficiency.

Author Contributions: Conceptualization, M.H. and Q.H.; methodology, M.H. and J.C.; software, M.H.; validation, Q.H. and Y.C.; formal analysis, J.L. and L.S.; investigation, M.H. and Q.H.; resources, M.H. and Q.H.; data curation, M.H. and J.C.; writing—original draft preparation, M.H. and Q.H.; writing—review and editing, L.S.; visualization, M.H. and J.C.; supervision, Y.C. and J.L.; funding acquisition, L.S. All authors have read and agreed to the published version of the manuscript.

Funding: This work was supported by the Guangdong Basic and Applied Basic Research Foundation under Grant 2024A1515010135, the National Natural Science Foundation of China under Grant 62303188, and the 2024 Basic and Applied Research Project of Guangzhou Science and Technology Plan under Grant 2024A04J4140.

Institutional Review Board Statement: Not applicable.

Data Availability Statement: Data are contained within the article.

Conflicts of Interest: The authors declare no conflicts of interest.

References

1. Duan, Z.; Qiu, W.; Ding, W.; Liu, Y.; Ouyang, Y. Tilting stability analysis and experiment of the 3-DOF lifting platform for hilly orchards. *Int. J. Agric. Biol. Eng.* **2018**, *11*, 73–80. [CrossRef]
2. Zhang, M.; Li, X.; Wang, L.; Jin, L.; Wang, S. A Path Planning System for Orchard Mower Based on Improved A* Algorithm. *Agronomy* **2024**, *14*, 391. [CrossRef]
3. Liu, L.; Liu, H.; Li, J.; Wang, P.; Yang, X. Construction of Orchard Agricultural Machinery Dispatching Model Based on Improved Beetle Optimization Algorithm. *Agronomy* **2025**, *15*, 323. [CrossRef]
4. Chen, B.; Quan, G. NP-Hard Problems of Learning from Examples. In Proceedings of the 2008 Fifth International Conference on Fuzzy Systems and Knowledge Discovery, Jinan, China, 18–20 October 2008; Volume 2, pp. 182–186.
5. Karur, K.; Sharma, N.; Dharmatti, C.; Siegel, J.E. A Survey of Path Planning Algorithms for Mobile Robots. *Vehicles* **2021**, *3*, 448–468. [CrossRef]
6. Kun, S.; Yang, L.; Wu, Z.; Jiang, B.; Gao, Q. Multi-robot dynamic path planning with priority based on simulated annealing. *J. Frankl. Inst.* **2025**, *362*, 107396.
7. Wang, S.; Zhao, T.; Li, W. Mobile Robot Path Planning Based on Improved Artificial Potential Field Method. In Proceedings of the 2018 IEEE International Conference of Intelligent Robotic and Control Engineering (IRCE), Lanzhou, China, 24–27 August 2018; pp. 29–33.
8. El-Teleity, S.A.L.; Nossair, Z.B.; Mansour, H.M.A.K. Fuzzy logic control of an autonomous mobile robot. In Proceedings of the 2011 16th International Conference on Methods & Models in Automation & Robotics, Miedzyzdroje, Poland, 22–25 August 2011; pp. 188–193.
9. Zhu, Y.; Zhang, G.; Chu, R.; Xiao, H.; Yang, Y.; Wu, X. Research on escape route planning analysis in forest fire scenes based on the improved A* algorithm. *Ecol. Indic.* **2024**, *166*, 112355. [CrossRef]
10. Ajeil, F.H.; Ibraheem, I.K.; Azar, A.T.; Humaidi, A.J. Grid-Based Mobile Robot Path Planning Using Aging-Based Ant Colony Optimization Algorithm in Static and Dynamic Environments. *Sensors* **2020**, *20*, 1880. [CrossRef]
11. Gong, P.; Li, W.; Ma, Q.; Hu, W. Research on Path Planning for Unmanned Vehicles Based on Improved A* Algorithm. *J. Combin. Machine Tools Autom. Process* **2023**, *3*, 17–20,24.
12. Kazemi, M.; Gupta, K.K.; Mehrandezh, M. Randomized Kinodynamic Planning for Robust Visual Servoing. *IEEE Trans. Robot.* **2013**, *29*, 1197–1211. [CrossRef]
13. Kavraki, L.E.; Svestka, P.; Latombe, J.C.; Overmars, M.H. Probabilistic roadmaps for path planning in high-dimensional configuration spaces. *IEEE Trans. Robot. Autom.* **1996**, *12*, 566–580. [CrossRef]
14. Liu, H.; Zhang, X.; Wen, J.; Wang, R.; Chen, X. Goal-biased Bidirectional RRT based on Curve-smoothing. *IFAC-PapersOnLine* **2019**, *52*, 255–260. [CrossRef]
15. LaValle, S.M.; Kuffner, J.J., Jr. Randomized kinodynamic planning. *Int. J. Robot. Res.* **2001**, *20*, 378–400. [CrossRef]
16. Karaman, S.; Frazzoli, E. Sampling-based algorithms for optimal motion planning with deterministic μ-calculus specifications. In Proceedings of the 2012 American Control Conference (ACC), Montreal, QC, Canada, 27–29 June 2012; pp. 735–742.
17. Ye, L.; Li, J.; Li, P. Improving path planning for mobile robots in complex orchard environments: The continuous bidirectional Quick-RRT* algorithm. *Front. Plant Sci.* **2024**, *15*, 1337638. [CrossRef]
18. Ye, L.; Wu, F.; Zou, X.; Li, J. Path planning for mobile robots in unstructured orchard environments: An improved kinematically constrained bi-directional RRT approach. *Comput. Electron. Agric.* **2023**, *215*, 108453. [CrossRef]
19. Li, Y.; Zhao, J.; Chen, Z.; Xiong, G.; Liu, S. A Robot Path Planning Method Based on Improved Genetic Algorithm and Improved Dynamic Window Approach. *Sustainability* **2023**, *15*, 4656. [CrossRef]
20. Zhu, A.; Yang, S. A Neural Network Approach to Dynamic Task Assignment of Multirobots. *IEEE Trans. Neural Netw.* **2006**, *17*, 1278–1287.
21. Rashid, R.; Perumal, N.; Elamvazuthi, I.; Tageldeen, M.K.; Khan, M.A.; Parasuraman, S. Mobile robot path planning using Ant Colony Optimization. In Proceedings of the 2016 2nd IEEE International Symposium on Robotics and Manufacturing Automation (ROMA), Ipoh, Malaysia, 25–27 September 2016; pp. 1–6.
22. Zheng, L.; Yu, W.; Li, G.; Qin, G.; Luo, Y. Particle Swarm Algorithm Path-Planning Method for Mobile Robots Based on Artificial Potential Fields. *Sensors* **2023**, *23*, 6082. [CrossRef]
23. Rickert, M.; Sieverling, A.; Brock, O. Balancing Exploration and Exploitation in Sampling-Based Motion Planning. *IEEE Trans. Robot.* **2014**, *30*, 1305–1317. [CrossRef]

24. Gammell, J.D.; Srinivasa, S.S.; Barfoot, T.D. Informed RRT*: Optimal sampling-based path planning focused via direct sampling of an admissible ellipsoidal heuristic. In Proceedings of the 2014 IEEE/RSJ International Conference on Intelligent Robots and Systems, Chicago, IL, USA, 14–18 September 2014; pp. 2997–3004.
25. Kong, F.; Liu, B.; Han, X.; Yi, L.; Sun, H.; Liu, J.; Liu, L.; Lan, Y. Path Planning Algorithm of Orchard Fertilization Robot Based on Multi-Constrained Bessel Curve. *Agriculture* **2024**, *14*, 979. [CrossRef]
26. Ben Hazem, Z. Study of Q-learning and deep Q-network learning control for a rotary inverted pendulum system. *Discov. Appl. Sci.* **2024**, *6*, 49. [CrossRef]
27. Cui, J.; Nie, G. Motion Route Planning and Obstacle Avoidance Method for Mobile Robot Based on Deep Learning. *J. Electr. Comput. Eng.* **2022**, *2022*, 5739765. [CrossRef]
28. Tsallis, C. Lévy distributions. *Phys. World* **1997**, *10*, 42. [CrossRef]
29. Xue, J.; Shen, B. A novel swarm intelligence optimization approach: Sparrow search algorithm. *Syst. Sci. Control Eng.* **2020**, *8*, 22–34. [CrossRef]

Smart Agricultural Technology 10 (2025) 100752

Contents lists available at ScienceDirect

Smart Agricultural Technology

journal homepage: www.journals.elsevier.com/smart-agricultural-technology

An autonomous obstacle avoidance and path planning method for fruit-picking UAV in orchard environments

Jun Li [a,b,c], Haobo Zhou [e], Yuju Mai [a], Yuhang Jia [d], Zhengqi Zhou [f], Kaixuan Wu [a], Hengxu Chen [a], Hengyi Lin [a], Mingda Luo [a], Linlin Shi [a,*]

[a] College of Engineering, South China Agricultural University, Guangzhou, 510642, China
[b] Guangdong Laboratory for Lingnan Modern Agriculture, Guangzhou, 510642, China
[c] National Key Laboratory of Agricultural Equipment Technology, Beijing, 100083, China
[d] Guangzhou Xaircraft Technology Co., Ltd., Guangzhou, 510642, China
[e] Guangzhou Gaoqing Electromechanical Technology Co., Ltd., 510510, China
[f] Hunan University of Science and Engineering, Hunan, 425101, China

ARTICLE INFO

Keywords:
Fruit picking
Unmanned aerial vehicle
Path planning
Obstacle avoidance

ABSTRACT

In orchard environments, compared with picking robotic arms, improving the efficiency and safety of the fruit-picking unmanned aerial vehicle (UAV) becomes more challenging. In this paper, an autonomous obstacle avoidance and path planning method based on LiDAR data is proposed for the self-built fruit-picking UAV. First, a LiDAR static-dynamic dual map construction scheme is designed. Using the original point cloud data from LiDAR, a time-accumulated local point cloud map is generated to provide orchard obstacle information for path planning. Then, an improved hybrid A* algorithm based on the B-spline curve is proposed. This algorithm not only comprehensively takes into account the impact of surrounding branches on the flight of the picking UAV near the target fruit bunch, but also ensures that the planned path meets the specific action requirements of the picking UAV when picking the target fruit bunch. The experimental results demonstrate that the proposed map construction scheme significantly reduces the computational power requirements and collision detection time. Moreover, the path planning algorithm effectively guides the UAV and its attached picking actuator to successfully navigate around obstacles, enabling efficient picking of the target fruit bunch. Indicating that the proposed method provides a feasible solution for task execution of the fruit-picking UAV in complex orchard environments.

1. Introduction

Longan is a vital crop in the hilly regions of southern China, with a two-thirds output of the world. Due to its pronounced seasonality, intense labor requirements, and significant costs, longan picking emerges as the most time-consuming and labor-intensive aspect throughout the entire fruit production cycle [15]. At present, longan predominantly hosts manual harvesting and ground equipment-assisted harvesting. Escalating labor costs and the gradual emergence of labor shortages necessitate the rapid development of efficient automatic fruit-picking robots [2,20,3]. The predominant approach for harvesting is to use robotic arms, which are limited by terrain topography and fruit tree height in hilly orchard areas [18,16]. In contrast, the unmanned aerial vehicle (UAV) offers notable operational benefits in intricate orchard terrains [19,6]. Its ability to operate at high altitudes grants it unrestricted access to fruit trees of varying heights and picking ranges, but there is little literature about the design of the UAV-based fruit-picking robot [14].

However, when navigating the intricate environment of fruit tree canopies, the UAV encounters challenges such as irregular obstacles and confined spaces. Achieving autonomous obstacle avoidance for such UAV traversing fruit tree canopies has thus become a pivotal challenge [12]. In recent years, a comprehensive system solution with a “perception, planning, control” framework has been developed through years of exploration for the autonomous obstacle avoidance flight of the UAV within orchards. At the perception level, sensors collect orchard environmental data, including information about fruit trees and the ground, and the raw data are processed. At the planning level, the processed data are further analyzed, and appropriate algorithms are selected to plan the

* Corresponding author.
E-mail address: lynnshi@scau.edu.cn (L. Shi).

https://doi.org/10.1016/j.atech.2024.100752
Received 18 September 2024; Received in revised form 16 December 2024; Accepted 24 December 2024

Available online 6 January 2025

passable path of the UAV. At the control level, the UAV is guided to move through the planned path based on corresponding control algorithms.

Visual sensors and LiDAR, as the two primary components of robotic perception systems, present significant differences in their typical usage scenarios. In the domain of visual sensors, [11] has demonstrated that quadcopter UAV equipped with monocular cameras can autonomously avoid collisions with obstacles in unstructured and unknown environments through visual information. Conversely, Wang et al. leveraged deep learning and depth cameras to perceive obstacle attributes by the UAV, including detection of object categories, profiles, and 3D spatial positions, in support of obstacle avoidance techniques [17]. However, RGB-D sensors are prone to recording significant noise and signals that are easily influenced by light, necessitating probabilistic filtering to reduce corresponding data uncertainty. This also intensifies the computational load on the processor. Additionally, commonly used visual sensors face limitations in terms of sensing range and resolution, posing challenges in reliably detecting obstacles in orchards, such as branches and wires. Miao et al. generated LiDAR data graphs using an image noise point filtering algorithm and employed an improved DBSCAN algorithm to cluster obstacles, achieving motion recognition and position detection of obstacles [9]. In contrast, LiDAR typically provides higher-resolution perception data but also requires high-resolution data that imposes greater computing power on the system, particularly on onboard computers. To address this challenge, Lee et al. proposed a method of creating probability grid occupancy maps based on sensor data to generate three-dimensional local dynamic maps (LDMs) of UAV perception systems [5]. This map employs a loop buffer as a data structure to reflect the flying environment of the UAV, ensuring low memory usage and fast running speed. Despite the extensive research in the field of LiDAR mapping, the efficacy of general mapping algorithms in overcoming irregular obstacles (such as branches) is suboptimal, while imposing a high demand on the UAV computing power that is often difficult to meet with traditional onboard UAV computers. Therefore, further research is valuable to enhance the applicability of LiDAR mapping algorithms and the accuracy of such systems for navigating orchard environments.

The positioning of the UAV is pivotal in perception systems, providing essential prerequisites for subsequent planning and control. Concerning the orchard, [1] evaluated the positioning accuracy of the low-cost GNSS receiver in mobile RTK mode for tracking logging trajectories in forest environments. It has pinpointed tree height, ground elevation, slope orientation, canopy elevation, and tree density as primary factors influencing GNSS performance. When integrated with LiDAR data, GNSSs exhibit high performance and the potential for precise navigation on roads during harvesting in commercial forests. Shalal et al. proposed a local orchard map construction method based on the fusion of camera and laser scanner data for tree trunk detection [10]. An orchard map is constructed based on the positions of tree and nontree objects in tree rows to enable accurate positioning of orchard mobile robots. Hiraoka et al. conducted dynamic positioning experiments in orchards and revealed that under specific environmental conditions, the positioning accuracy of RTK-GNSS and SA-GNSS can reach several tens of centimeters and several meters, respectively [4]. Through an agricultural robot simulator with orchard environmental information, it was demonstrated that vehicles based on RTK-GNSS can autonomously navigate without colliding with trees. This finding suggested that the integration of GPS and IMU odometry can meet the positioning needs of the UAV.

Regarding automated path planning and control, [13] proposed two dynamically feasible path planning and trajectory planning methods for omnidirectional mobile robots, namely, DB-RRT and FMDB-RRT. They integrated the convex hull characteristics of B-splines with the fast expansion ability of RRT to effectively realize safe, dynamically feasible, and improved trajectory plans. Li et al. proposed a quality-oriented UAV path planning algorithm, optimizing the A* algorithm using global static planning and local dynamic hierarchical planning while introducing dynamic exploration factors to form an efficient global-local mixed path planning strategy [7]. This approach significantly enhances the quality and execution efficiency of UAV's path planning. Zhu et al. presented a method based on an artificial potential field and the A* algorithm, focusing on the application of six degrees of freedom robotic arms in apple picking [21]. Through kinematic analysis, the introduction of an artificial potential field (APF), the combination of the A* algorithm, and the use of the IRRT algorithm to improve path smoothness, this method has been validated in simulation experiments for its obstacle avoidance effect in complex environments. Li et al. proposed a path planning and navigation method for dense jujube planting robots based on the improved A* algorithm and dynamic window method (DWA) [8]. Through such real-time global and local path planning, the average navigation positioning deviation of traditional algorithms is reduced, thereby providing high-precision path navigation for plant protection operations in dwarf dense jujube orchards in southern Xinjiang. Despite extensive research in the field of path planning, relatively few studies have focused on path planning for UAVs picking fruits, and it is difficult for traditional path planning algorithms to meet the special action requirements of UAVs picking fruits.

Fig. 1. Distribution of Hardware Modules for Longan FP-UAV.

Inspired by the previous work, this paper aims to propose an obstacle avoidance and picking path planning method for the self-built fruit-picking unmanned aerial vehicle (FP-UAV). The main contributions are listed below.

(1) Considering the growth characteristics of standard longan orchards, a LiDAR map construction scheme is designed first. This scheme accumulates time data to generate a local point cloud map and skillfully a static-dynamic dual map, which is used to acquire environmental information. It minimizes the computational demands to satisfy the real-time obstacle avoidance needs of the FP-UAV.

(2) To adapt to the action demands of longan picking, based on the static map, we propose an improved A* hybrid algorithm based on the B-spline. This algorithm can generate obstacle avoidance routes that adapt to global static obstacles, avoiding collisions between the FP-UAV and static obstacles during the picking process. Additionally, based on the dynamic map, we design the DWA dynamic window algorithm for obstacle avoidance planning concerning local dynamic obstacles.

(3) Through the proposed method, the self-built FP-UAV can accurately perceive obstacles in an orchard and effectively navigate around them in obstacle avoidance path planning. It provides a feasible and efficient solution for the FP-UAV for the first time, which can independently pick longan in an orchard environment.

2. Construction of the FP-UAV platform

This paper describes the development of an FP-UAV designed based on the growth characteristics of longan. The hardware system of the FP-UAV encompasses a perception device (Livox Avia solid-state LiDAR), a control device (Intel NUC 11PAH-i7 onboard computer), a picking actuator, and a platform (Dji M300 RTK), shown as Fig. 1.

The FP-UAV is primarily designed for longan picking and has specific and corresponding requirements for load capacity and flight stability. In

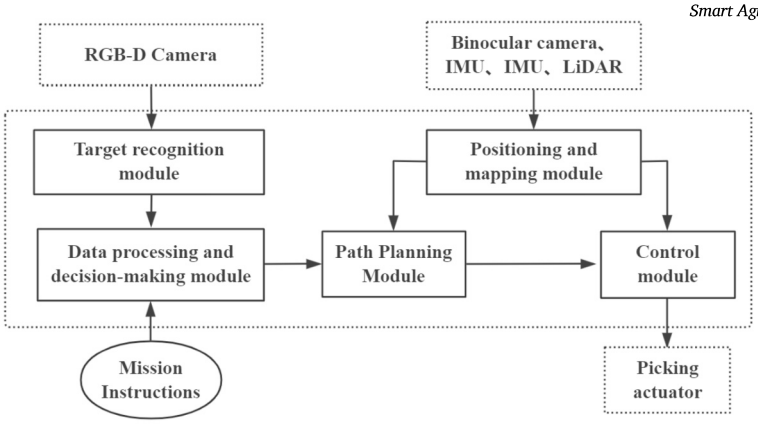

Fig. 2. A software system design scheme for the FP-UAV.

Fig. 3. Information transmission process of the FP-UAV.

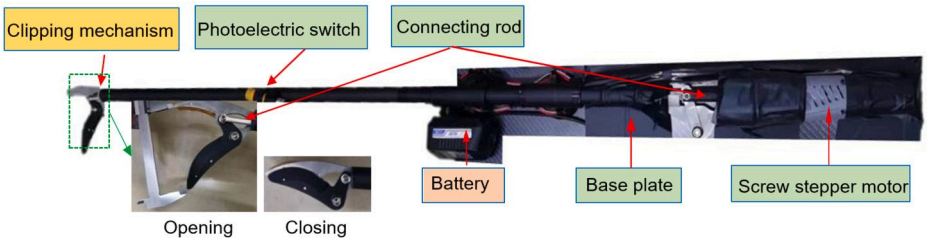

Fig. 4. The picking actuator and its components.

this paper, the Dji M300 RTK was chosen as the flight platform; it features dimensions of 810 × 670 × 430 mm and a maximum load capacity of 2.7 kg. The picking and control devices are securely connected to the UAV through a support frame, weighing a total of 1.6 kg and evenly distributed beneath the UAV. When the picking device clamps longan clusters within 1 kg, the FP-UAV can maintain stability and meet the load requirement of the FP-UAV. The sensing device is installed directly above the UAV using an expansion bracket, ensuring that the LiDAR laser source is positioned at the center of the radar surface. This arrangement prevents the body from obstructing the laser beam, thus preventing the detection of environmental information.

Based on the hardware design of the FP-UAV, a software system design scheme is further proposed for the FP-UAV, as shown in Fig. 2. It can ensure that the FP-UAV can fly safely and perform tasks efficiently in the orchard environment.

Specifically, the target recognition module focuses on the precise identification of the location of the fruit and feeds the positioning data back to the decision module to guide the subsequent picking action. The positioning and mapping module solves the positioning problem of the FP-UAV in the orchard environment, and generates an effective orchard environment information map to provide support for navigation tasks. The path planning module is responsible for planning the optimal route, considering the obstacle avoidance strategy, and enhancing the operational autonomy of the FP-UAV. The flight control module performs precise attitude adjustment and path tracking to ensure flight stability. The picking execution module completes specific fruit picking tasks.

2.1. Perception and control devices

The proposed sensing device, control device framework, and communication process are illustrated in Fig. 3. The FP-UAV employs the Livox Avia solid-state LiDAR. This sensor offers advantages in terms of volume and weight, weighing only 498 g, making it lightweight and convenient for UAV installation and disassembly. It also exhibits excellent performance, generating a noise rate of only 3ppm along with a very low error rate. The LiDAR includes an IMU sensor, enabling effective output of inertial parameters such as the attitude angle and speed in the orchard environment. The airborne computer utilizes an Intel NUC 11pahi7 with an Intel Core™ i7-1165g7 processor featuring 4 cores and 8 threads, with a maximum turbo frequency of 4.70 GHz, providing robust computing performance. It is compact, lightweight, and has low power consumption at only 40 W, making it highly suitable for mobile devices with a modest load to accomplish tasks such as sensor data reception, information processing, and output.

2.2. Picking actuator

The picking actuator is a crucial component in an FP-UAV, which typically consists of both a hardware structure and a control system. In the design of the picking actuator, factors such as the shape and growth characteristics of the targeted fruit, the UAV's payload, and the balance requirements for the mounting device must be considered. In this paper, cluster fruits such as longan and litchi fruits were picked. The hardware structure of the picking actuator for FP-UAV is depicted in Fig. 4 and in-

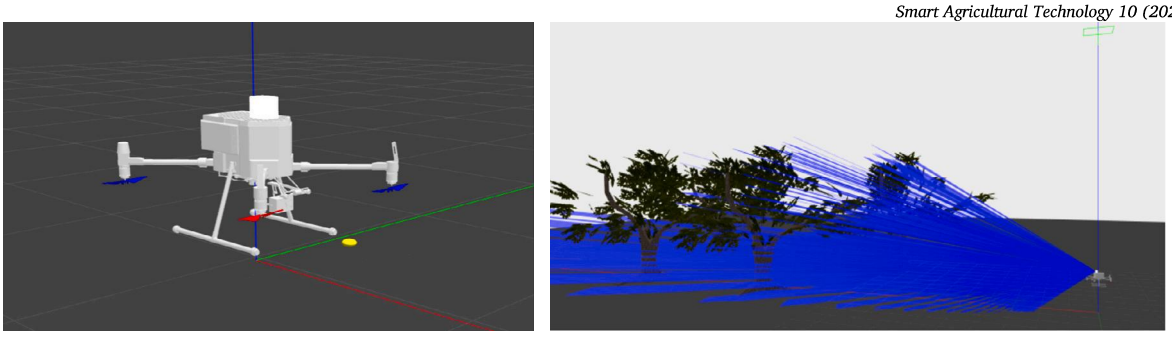

(a) The FP-UAV model. (b) Orchard environment.

Fig. 5. Simulation model and environment.

cludes the integrated clip mechanism, photoelectric switch, connecting rod, battery, base, and screw motor. Based on the shape characteristics of longan fruit clusters, considering the efficiency of harvesting, the ideal cutting position for longan fruit clusters is selected as the fruit-bearing main branch. Through sampling tests, it was found that the diameter of the longan fruit-bearing main branch is within the range of 4−10 mm, and the maximum cutting force required is about 0.9 KN. The harvesting device increases the speed and thrust of the screw motor to improve the cutting speed and cutting force of the harvesting actuator, thus ensuring effective cutting of the longan fruit-bearing main branch. The integrated clip mechanism has an opening of 8.5 cm, and the cutting speed is about 500 mm/min. The maximum cutting force is about 3.12 KN, which is sufficient to cut the longan main branch. According to the operation characteristics, the fruit-bearing main branch is cut off while holding the fruit, and moved to the collection box. Therefore, the cutting and clamping mechanism is equipped with a sharp scissors on the upper surface and a clamping mechanism on the lower bottom surface. Considering the effective load of the UAV, the total mass of the harvesting device is 1.2 kg. Considering the balance of the FP-UAV, the center of gravity of the harvesting device is aligned with the horizontal center of gravity of the FP-UAV, and most of the weight is located at the center of gravity position. String fruit picking by the picking actuator primarily involves the manipulation of the clip mechanism's opening and closing. The control system utilizes an Arduino control board to output high- and low-frequency signals, controlling the expansion and contraction of the stepping screw motor. This action drives the clip mechanism to open and close, ultimately realizing string fruit picking using the picking actuator.

2.3. Simulation environment of the FP-UAV

To verify the feasibility of the proposed system, as well as the stability and performance of the proposed algorithm, a simulation test system was constructed to simulate the actual flight ability of the picking UAV in an actual orchard environment and to ensure the safety of the system test. Considering the type of multirotor UAV and the requirement of matching the control logic of the simulator with the algorithm, a rotor simulation in Ubuntu platform. The operating system used in the simulation environment of this article is Ubuntu 18.04, and the ROS version is Melodic.

The Rotors simulation platform, developed by a research team at ETH Zurich, focuses on the simulation of multi-rotor UAVs, supporting multi-axis aircraft, such as four-rotor, six-rotor, and so on. By using Universal Robot Description Format(URDF) to create a multi-rotor UAV model, Simulation Description Format(SDF) to describe the fruit tree model of the simulation scene. And the solid state LiDAR model provided by the Rotors simulation platform was used to build the simulation model successfully. Ultimately, the URDF description file of the UAV simulator in the Rotors simulation platform was modified, and the motor installation position was adjusted to seamlessly integrate the DJI M300RTK simulation model, as depicted in Fig. 5(a). Additionally, a fruit tree model was incorporated into the simulator to represent the orchard environment, as shown in Fig. 5(b).

3. Target fruit detection and localization

3.1. Data acquisition and preprocessing

In this paper, 1070 Longan data set images provided by Longan Park of Guangdong Academy of Agricultural Sciences were used. After manual selection, labeling and data extension, 2460 Longan dataset images were obtained for model training and evaluation, of which 1968 were used for training and 660 were used for testing.

3.2. Fruit detection model

In order to achieve the working requirements of high accuracy, low consumption and real-time operation, YOLOv5n is used as the detection model in this paper. The structure of YOLOv5n is shown in Fig. 6, which is divided into backbone network, neck network and head network. Specifically, CSPDarknet is used as the main feature extraction module in the backbone network, and the computational complexity is reduced through the CSP structure while maintaining the efficiency of feature extraction. The CSP structure enhances the feature extraction ability of the network by performing residual stacking in the backbone part and a small amount of processing in the residual side part. A combined structure of FPN (Feature Pyramid Network) +PAN (Path Aggregation Network) is used in the neck network. FPN transmits strong semantic features in a top-down manner, while PAN transmits strong localization features in a bottom-up manner. This structure helps the model to capture objects at different scales and improve the detection ability of small objects. An auxiliary structure training method is proposed in the head network, which can improve the accuracy by increasing the training cost without affecting the inference time.

3.3. Experimental analysis and discussion

In order to further verify the accuracy and adaptability of the YOLOv5n model selected in this paper for longan string fruit target detection, the YOLOv5n model algorithm is compared with the classical model of target detection. It is evaluated with the classical models (YOLOv6 and YOLOv8). Six performance indicators such as amount of computation (GFLOPs), number of Parameters (Parameters), recall rate, mAP@0.5 and mAP@0.5-0.95 are selected for recording, and the data are shown in Table 1.

According to the comparative experimental results in Table 1, the detection accuracy of the YOLOv5n model selected in this paper is higher than that of the n version classic model of the YOLOv6 and YOLOv8 series, and slightly lower than that of the s version classic model of the YOLOv5 series. Compared with models with the same n specifications, the number of parameters of the selected algorithm in this paper is significantly lower than that of other classical models, and the number of

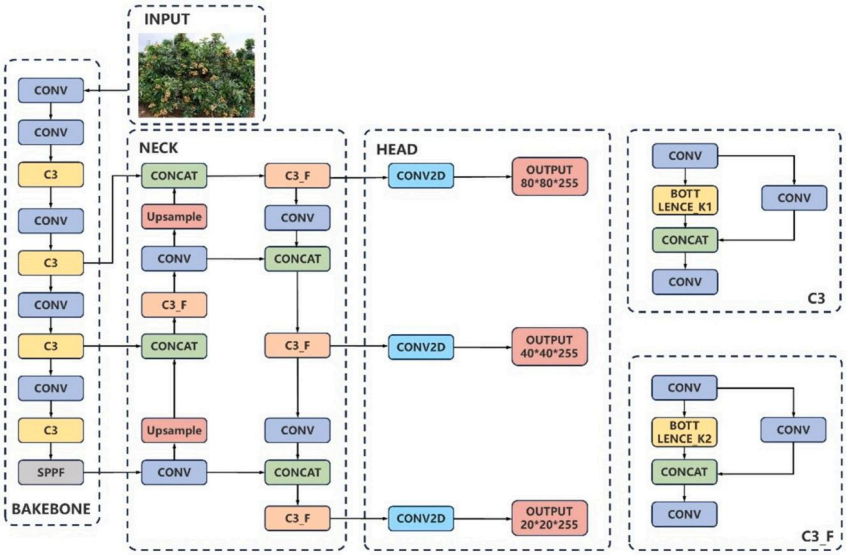

Fig. 6. YOLOv5n network structure diagram.

Table 1
Comparative experimental results of classical models for object detection.

Model	GFLOPs (G)	Parameters (m)	Recall	mAP@0.5	mAP@0.5 – 0.95	FPS (img/s)
YOLOv5n	**7.8**	**2.65**	**0.741**	**79.5%**	**45.3%**	**89**
YOLOv5s	24.2	9.15	0.762	80.3%	47.6%	38
YOLOv6n	11.9	42.3	0.698	78.2%	44.5%	90
YOLOv8n	8.2	3.01	0.741	79.4%	45.1%	84

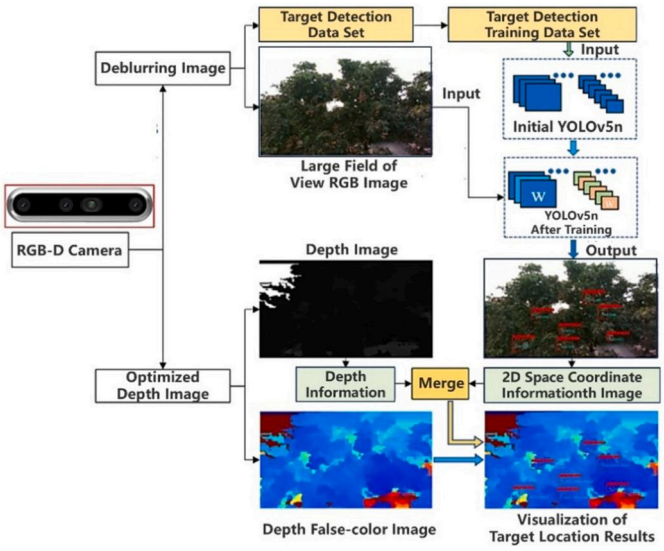

Fig. 7. Object detection and localization system scheme.

parameters of YOLOv5n model is only one third of that of YOLOv5s model. At the same time, compared with YOLOv6n, YOLOv5n model is only one-sixteenth of YOLOv6n model. From the perspective of various indicators, the YOLOv5n model selected in this paper has the best comprehensive performance, and has excellent recognition ability for longan string fruit images. And in the case of maintaining a high FPS (number of images processed per second), YOLOv5n model can meet the requirements of real-time and accuracy, and provide accurate information support for the spatial coordinates of the target fruit required for subsequent path planning.

3.4. Target fruit location

In order to give the UAV the ability to quickly detect and locate multiple targets in a wide field of view, this paper uses the YOLOv5n model to accurately identify and locate the target fruit of longan. By combining the target plane position information obtained by YOLOv5n model and the depth information obtained by RBG-D camera, the camera coordinate system is transformed into the world coordinate system with the UAV as the reference, so as to obtain accurate 3D position information of longan string fruit in a complex orchard environment. The specific workflow is shown in Fig. 7.

In this paper, we first calibrate the intrinsic parameters of the RGB-D camera carried by the picking UAV to improve the accuracy of image processing. The RGB image, depth image and depth pseudo-color image captured by the camera comprehensively reflect the details of the target longan and its surrounding environment. Based on these images, this paper selects fruit tree canopy images suitable for large field of view as the detection data set, and further subdivides them into training sets for the preliminary training of YOLOv5n model to create a detection model with weight parameters. After that, the preprocessed clear RGB image is input into the trained YOLOv5n model, which is responsible for outputting the bounding box information of longan string fruit. Next, these detections are combined with the information in the depth image to determine the exact position of the fruit in 3D space. Finally, the external parameter calibration of the camera was carried out, and the camera coordinate system was transformed into the world coordinate system with the UAV as the reference, so as to realize the precise positioning of the target longan string fruit in the global scope. The actual operation effect is shown in Fig. 8.

Through this process, the system can not only effectively realize multi-target recognition in complex environments, but also accurately obtain the position of the target in space, which provides reliable data support for the navigation and picking action of the UAV. This comprehensive application based on deep learning and image processing

Fig. 8. Longan skewfruit detection and localization.

technology greatly improves the efficiency and accuracy of UAV tasks in orchards.

4. Obstacle avoidance and picking motion planning method

In this section, the obstacle avoidance and picking motion planning method is proposed of the FP-UAV, encompassing orchard environment mapping and obstacle avoidance and picking path planning.

To address the challenge of orchard environment mapping, we utilize LiDAR to collect original point cloud data, organize the point cloud data using a KD-Tree structure, and finally construct a static-dynamic dual map by creating a time-accumulated local point cloud map. The objective is to formulate a mapping strategy that is well suited for orchard environments and minimizes computational demands, thereby realizing practical obstacle information for FP-UAV path planning.

Addressing the challenge of integrating obstacle avoidance and picking motion planning, we design a path generation algorithm based on the B-spline improved A* algorithm for global planning utilizing a static map. The proposed algorithm fully adjusted the distance threshold of path reconstruction according to the orchard environment to ensure the pose of the end of the FP-UAV during flight, and was suitable for path planning in orchard environment. Additionally, for local planning, the DWA dynamic window algorithm, combined with the dynamic map, guides the picking robot to avoid dynamic obstacles in real-time.

4.1. Local map construction

In the orchard canopy environment, constructing a grid map using ray casting is time-consuming, especially when considering small and irregular obstacles that require the division of the sensed area into small grid elements. This process increases construction time and poses challenges in meeting the real-time obstacle avoidance needs of the UAV. Currently, the development of LiDAR technology is rapidly advancing, and the false alarm rate of the Livox-avia radar is extremely low ($< 0.0003\%$), which allows for direct use of the raw point cloud data for obstacle avoidance planning. Therefore, this paper utilizes the non-repeating scan of the Avia LiDAR and proposes a map building strategy suitable for the orchard environment, providing information on orchard obstacles for the FP-UAV's path planning.

Considering that the original point cloud data are unordered, we employ a KD-Tree to organize the original point cloud, aiming to increase the collision detection efficiency. Due to the huge amount of point cloud data, up to 7,200,000 points are generated per second, and it continues to grow exponentially over time, by accumulating point cloud data and building maps based on a time threshold, we can reduce the impact of historical point cloud data on obstacle avoidance planning. This approach is implemented to mitigate the impact of historical point cloud data on obstacle avoidance planning, to achieve real-time and efficient obstacle avoidance for the UAV navigating the orchard environment.

4.1.1. A temporally accumulated local point cloud map

A time accumulation local map, that is, the point cloud scanned most recently, is used as the local map of the FP-UAV. By accumulating point clouds within a certain period, a point cloud with sufficient resolution can be produced to identify obstacles in an orchard.

By comparing point clouds accumulated over different time periods in Fig. 9, the experiment has shown that point clouds accumulated within 100 ms are insufficient for determining tree bodies. Point clouds accumulated within 500 ms can recognize the outline of the tree body but struggle to effectively identify small branches. However, point cloud maps accumulated within 1000 ms can better display the outline of the tree body and the edges of small branches. In summary, in this paper, a cumulative time of 1000 ms (1 s) was applied.

To minimize the volume of the point cloud data, a resolution of 10 cm was used to downsample the original point cloud. Notably, the downsampling resolution used here differs from the resolution occupied by the grid map, ensuring that it does not impact the detection of obstacles below the resolution. This step successfully optimizes the point cloud data, enhancing the efficiency of subsequent obstacle avoidance planning.

4.1.2. A static-dynamic dual map

To effectively manage the static and dynamic information of the orchard environment, we introduced two K-Trees. One tree maintains the static environment of the orchard, and the other tree is used for dynamic updating. The point cloud data generated according to the cumulative time are stored. The update rules are shown in Fig. 10. Based on the accumulation time of point clouds, we set the number of point cloud frames received for each point cloud map to 10 frames. When a new point cloud frame arrives, it is downsampled at a specified resolution and added to the first local map until it is filled. After the first local map is full, a new point cloud scan is added to the second KD-Tree. At this point, the first KD-Tree serves as the static map, while the second functions as the dynamic map. Upon reaching the full capacity of the second local map, the first local map is emptied, and a new point cloud scan is added to it. Then, the second local map serves as the static map, and the first becomes the dynamic map. This process is iterated to achieve the alternating updates of static and dynamic maps.

The proposed optimization strategy enables effective management of static and dynamic information in the orchard environment, ensuring comprehensive consideration of both static and dynamic obstacles, such as fruit trees, in picking obstacle avoidance planning.

Algorithm 1 KD-tree local map construction.

Require: Point Clouds NewPoints in the new scan
Ensure: KD-Tree
Set parameter $H = 10$, $N = 2$
if $PointsInputNum \geq H \times N$ **then**
  $PointsInputNum = 0$
  $KDTreeInputNum = 0$
else
  $KDTreeInputNum = KDTreeInputNum/H$
end if
if $PointsInputNum \mod H = 0$ **then**
  Cloud.Clear()
  Cloud = NewPoints
else
  Cloud.add(NewPoints)
end if
CloudFilterd = VoxelGridFilter(Cloud);
KDTree[KDTreeInputNum].build(Cloud);
$PointsInputNum = PointsInputNum + 1$;

In Algorithm 1, parameter H is the number of point cloud frames received for each point cloud map, N represents setting two KD-Tree, and VoxelGridFilter function is used for downsampling.

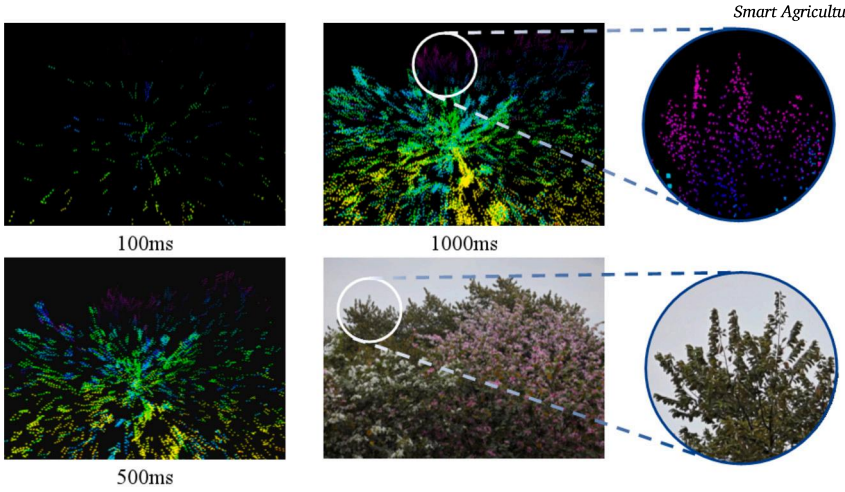

Fig. 9. Point cloud scanning at varying accumulation times.

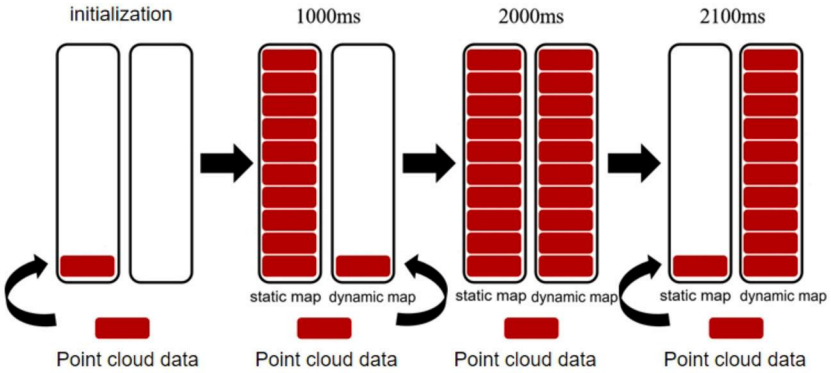

Fig. 10. Alternating updates of static and dynamic maps.

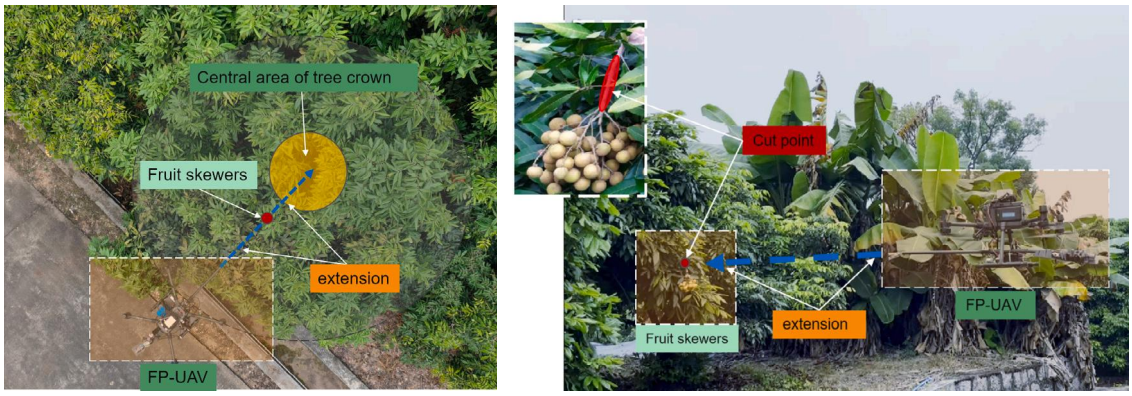

(a) Vertical view. (b) Lateral view.

Fig. 11. Schematic diagram of the FP-UAV.

4.2. Obstacle avoidance picking path planning

In this paper, the test sites were all located in standardized orchards, and all the fruit tree canopies were regarded as annular surfaces. In contrast to other UAVs, when planning the obstacle avoidance path of an FP-UAV, it is necessary to consider the impact of the branches around the target fruit cluster on the flight of the FP-UAV and to satisfy the active requirements of the FP-UAV when picking the target fruit cluster. For this purpose, we will define an extension line, the blue dashed line in Fig. 11, which is determined through the center of the tree and the target fruit string. The generated path should ensure that the end of the path is tangent to the extension line. When approaching the target fruit string, the UAV is roughly aligned with the extension line of the tree trunk to successfully complete the picking task.

To address the challenges faced by FP-UAV in picking target fruits, a path planning system suitable for FP-UAV autonomous obstacle avoidance picking was established. A hybrid A* algorithm based on the B-spline curve was proposed for global path planning. The algorithm aims to guide the FP-UAV to pick the target fruit while avoiding obstacles. Path planning systems comprehensively consider the impact of static and dynamic obstacles on the flight of FP-UAV in an orchard environment and consider the action requirements of FP-UAV when picking the target fruit string. The corresponding implementation process is shown in Fig. 12.

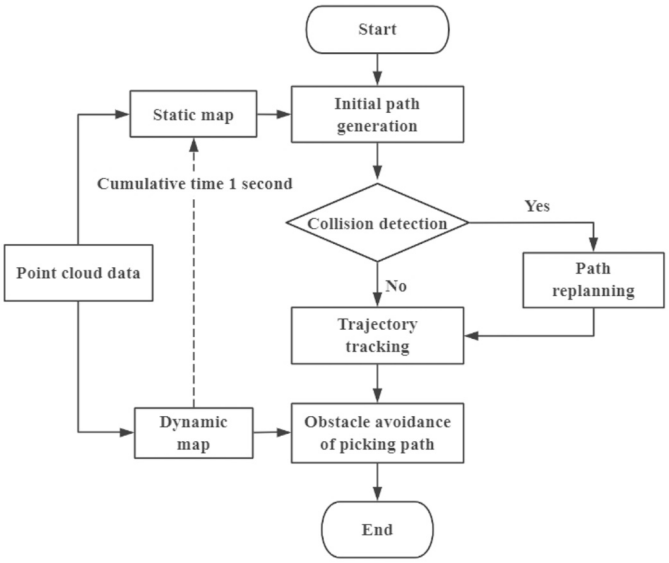

Fig. 12. Flowchart of the path planning system.

4.2.1. Initial path generation

Considering standardized orchard operations with FP-UAVs, the majority of obstacles, such as branches and leaves requiring avoidance, are often located near the target fruit string. This interference has impacts the path planning capability of the FP-UAV. It is a key problem to ensure that the end route of the generated path is close to the extension line between the target fruit string and the tree trunk when realizing successful picking of the target fruit string by an FP-UAV. In this paper, an improved A* hybrid algorithm based on the B-spline curve is proposed. First, the initial path is directly generated by the improved quasiuniform B-spline curve algorithm.

The B-spline curve is designed to generate a smooth curve through a set of specified points. This curve possesses the property of a convex hull and maintains the end tangent to the control point. In the context of path planning, the B-spline curve is employed to smooth the generated global path, ensuring continuity.

The algorithm introduced in this paper generates the initial path by improving the quasiuniform B-spline curve algorithm. To meet the action requirements of the FP-UAV, the algorithm uses the characteristic that the end of the B-spline curve is tangent to the control point. The start point and end point are strategically selected, the target point and the point on the extension line are selected and added to the control point sequence. This ensures that the end path of the generated initial path is aligned with the extension line between the target fruit string and the trunk.

The detailed process of path planning for the FP-UAV in orchards is shown below. It utilizes an improved A* algorithm based on B-spline curves to meet the requirements of precise fruit picking and obstacle avoidance. The process is divided into the following stages:

Step 1: Determination of initial control points. First, the starting and ending point of the path planning are determined, namely the current position (x_0, y_0, z_0) of the FP-UAV and the target fruit string position (x_n, y_n, z_n). To ensure that the ending point of the path is precisely aligned with the target fruit string and take into account the specific direction requirements of the fruit picking, an additional control point $(x_{n-1}, y_{n-1}, z_{n-1})$ is located on the extension line of the target fruit string and the tree trunk. At the same time, based on the Avia LiDAR obtained scanning data of the orchard environment, the Avia LiDAR image contour lines are recognized and expanded, and the corner points, $(x_1, y_1, z_1), (x_2, y_2, z_2), \ldots, (x_{n-2}, y_{n-2}, z_{n-2})$, are added to the control point sequence to ensure that the initial pathway waypoints fall within the convex hull of the control points, achieving obstacle avoidance for static obstacles.

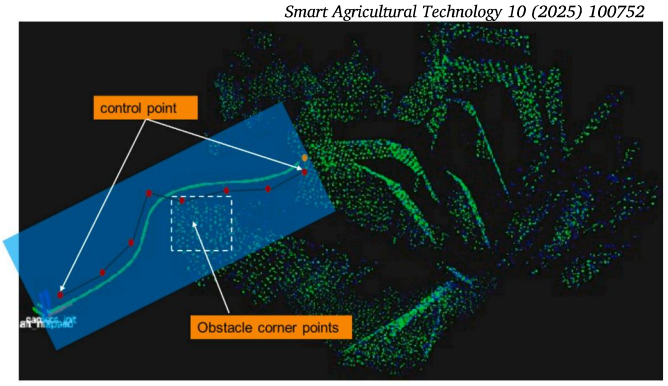

Fig. 13. Schematic diagram of the control points based on the B-spline curve.

Step 2: Determination of node vectors and degrees. The length of the node vector and the degree of the curve $d(d = 2)$ are related to the number of control points n. In this paper, a third-order quasi-uniform B-spline curve is proposed and the node vector will contain $n + d + 1$ elements. The selection of a third-order curve is mainly based on its smoothness and flexibility, as well as its ease of adjusting the influence of control points on the path shape.

Step 3: Calculation of B-spline basis functions. The basis function $N_{i,p}(u)$ is

$$N_{i,p}(u) = \frac{u - u_i}{u_{i+p} - u_i} N_{i,p-1}(u) + \frac{u_{i+p+1} - u}{u_{i+p+1} - u_{i+1}} N_{i+1,p-1}(u), \quad (1)$$

where $p = 3$, is the order of the basis function, and the index i represents the i-th control point in the sequence of control points. The function $N_{i,3}(u)$ recursively calculated according to the De Boor-Cox formula to assign weights to each control point in the curve construction and thereby determine the specific shape of the path.

Step 4: Generation of B-spline curves. By using the control points and corresponding basis functions, the coordinates of each point on the curve are calculated to form a smooth initial path. In this step, special attention is paid to utilizing the characteristic of the B-spline curve end point being tangent to the control point to meet the specific direction requirements of the fruit picking action end.

Step 5: Path Discretization. This step aims to ensure that the path avoids these obstacles by leveraging the convex hull property of the quasi-uniform B-spline curves. Then, the generated quasi-uniform B-spline curves are discretized into a series of path points, providing a basis for subsequent collision detection and path adjustment.

Step 6: Path Optimization and Collision Detection. After generating the initial path, collision detection is performed for each path point to ensure the feasibility of the path. If a collision is detected, the affected path segment is replanned using the A* algorithm until a final path is found that avoids obstacles and satisfies the picking requirements.

Through the above detailed steps, the path planning strategy proposed in this paper can effectively cope with the complex situation in the orchard environment, realize the path planning of the UAV fuselage and the picking actuator, and ensure that the FP-UAV can complete the picking task safely and effectively.

Using the convex hull of the B-spline curve, the obstacle information near the target fruit cluster is extracted and expanded upon based on the static map incorporating the time-integrated point clouds. After the obstacle information is processed by expansion, the extracted key corner points are added to the sequence of control points to ensure that the UAV avoids these obstacles and makes the planned path fall within the safe area, as shown in Fig. 13.

4.2.2. Collision detection

After adding a new point cloud frame to the local map, collision detection on the tracking path is crucial to ensure that the FP-UAV is safely flying. To adapt to the traffic conditions of an FP-UAV in an orchard, we

establish appropriate collision detection conditions. These conditions include coincidence, distance threshold, and flight space parameters, which are listed below.

(1) Coincidence: For each waypoint in the tracking path, determine whether the point coincides with any laser scanning point in the local map. This condition enables detection of whether the path intersects with the actual point cloud data in the environment.

(2) Distance threshold: Calculate the distance between each waypoint in the tracking path and the nearest point in the local map, and evaluate whether the distance is greater than the safety distance threshold. By setting the threshold, the UAV can maintain a sufficient distance from the environment during flight to avoid collisions.

(3) Flight space: For each waypoint in the tracking pathevaluate judge whether it exceeds the specified flight space range at the z-axis altitude. This condition is used to limit the vertical flight range of the UAV to ensure safe flight at different altitudes.

By comprehensively considering the above three conditions, effective collision detection can be conducted, ensuring the safe flight of the FP-UAV in orchards. Accurate and timely collision detection enhances the ability of an FP-UAV to respond rapidly to environmental changes, ensuring its flight safety.

4.2.3. Path replanning

In the presence of intricate obstacle information around the target fruit string and when the FP-UAV encounters collision detection failure during path execution, indicating that the initial path is no longer viable. Thus, we implement an intelligent path replanning algorithm. The fundamental concept of this algorithm is to generate a new path based on real-time positioning information from the FP-UAV, the current environmental status, and the location of the operational target point. This process ensures that the FP-UAV can effectively and safely accomplish the picking task in the complex obstacle avoidance environment of the orchard.

In the initial stage, the A* algorithm excels in narrow channels and diverse environments, swiftly identifying feasible paths. Employed at the forefront of heuristic path planning, the A* algorithm initiates searches from the starting point, estimating surrogate values for each search node to guide the direction closer to the target point coordinates. The objective during this stage is to rapidly generate a global path satisfying the obstacle avoidance requirements for an FP-UAV navigating an intricate orchard canopy environment.

However, considering the complexity of the orchard environment, the A* algorithm may not fully account for dynamic obstacles and the irregular shape of fruit trees. This limitation hinders the ability of this approach to ensure the proximity of the path to the extension line of the target fruit string and trunk. To address this, the B-spline algorithm is introduced later in the global path. A distance threshold D is incorporated to determine when to transition from the A* algorithm to the improved B-spline curve algorithm. The expression of the distance threshold D is

$$D = \sqrt{(x_k - x_i)^2 + (y_k - y_i)^2 + (z_k - z_i)^2}, \tag{2}$$

where (x_k, y_k, z_k) is the extension node, which is currently being considered by the A * algorithm when searching for a path, and (x_i, y_i, z_i) is the target fruit position. In this paper, we set $D = 0.5$ m according to the orchard environments.

As the path generated by the A* algorithm approaches the target position, the system transitions to the B-spline algorithm, better aligning with the orchard's action requirements. This technique ensures that the FP-UAV is in the ideal position upon reaching the target fruit string. By introducing the B-spline curve into the global path, this hybrid strategy brings the path closer to the extension line of the target fruit string and trunk. Thus, under various complex environments, waypoint paths can be generated to meet the action requirements of an FP-UAV when picking a target fruit string, enhancing the robustness of FP-UAV autonomous obstacle avoidance picking, as shown in Fig. 14.

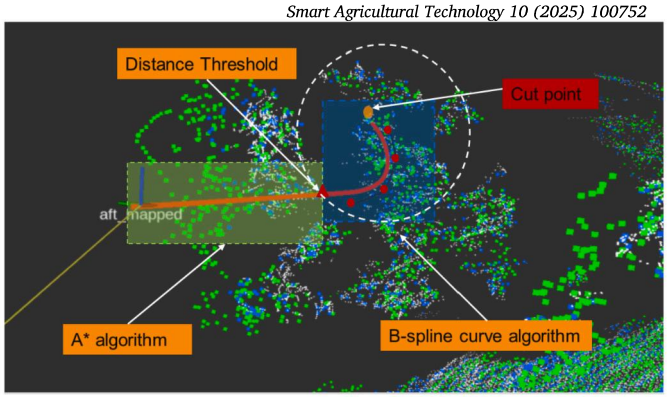

Fig. 14. The picking path planning of the proposed method.

4.2.4. Obstacle avoidance of the picking path

In orchards, the dynamic obstacle avoidance of an FP-UAV is highly important for ensuring an efficient and safe picking task. Therefore, the improved dynamic window approach (DWA) algorithm is proposed to adapt to real-time changes in orchard environments, especially in the presence of dynamic obstacles.

Algorithm 2 Obstacle avoidance picking path planning.

Require: Static map, dynamic map, start and end pose
Ensure: The path connecting the starting point and the ending point
Set $threshold = 10$
if $collision\_detection(initial\_goal\_path, static\_obstacles)$ **then**
  $Final\_goal\_path = ReplanPath(start, goal, threshold)$
  while $distance(current, goal) > threshold$ **do**
    $ReplanPath = aStarPath$
  end while
$ReplanPath = BSplinePath$
else
  $Final\_goal\_path = initial\_goal\_path$
end if
while $robot\_current\_pose! = goal\_pose$ **do**
  $dynamic\_map = update\_dynamic\_map()$
  $(best\_trajectory, best\_velocity) = DWA\_Algorithm(robot\_current\_pose, target\_velocity, dynamic\_map)$
  $move\_robot(Final\_goal\_path, robot\_current\_pose, best\_velocity)$
end while

Initially, dynamic obstacle information in the environment, including position and speed, is gathered through various sensors, such as visual sensors and LiDAR. Concurrently, real-time status data of the FP-UAV, encompassing key information such as position, speed, direction, and dynamic constraints, are obtained. Leveraging the sensing data, the velocity space of the FP-UAV is defined by incorporating the velocity values around the current velocity and potential angular velocity values. It establishes fundamental motion parameters for subsequent path planning.

The core of the DWA algorithm is to generate the dynamic sampling window. Leveraging the current velocity space and information about dynamic obstacles, the system generates the feasible motion range of the robot. This dynamic sampling window highlights the potential speed and direction the robot might adopt in the next time step. Subsequently, through trajectory evaluation, collision detection is executed for each combination of speed and direction. This process ensures that the chosen trajectory is secure, meaning that the robot will not collide with dynamic obstacles during movement. Factoring in collision risk, the optimal trajectory is determined by selecting the velocity and direction combination with the minimum collision cost. This trajectory guides the FP-UAV to move efficiently and safely in the orchard, gradually approaching the target fruit cluster.

In practical transit, the real-time update mechanism of the DWA algorithm ensures the real-time adjustment of the dynamic window and

Fig. 15. Longan orchard.

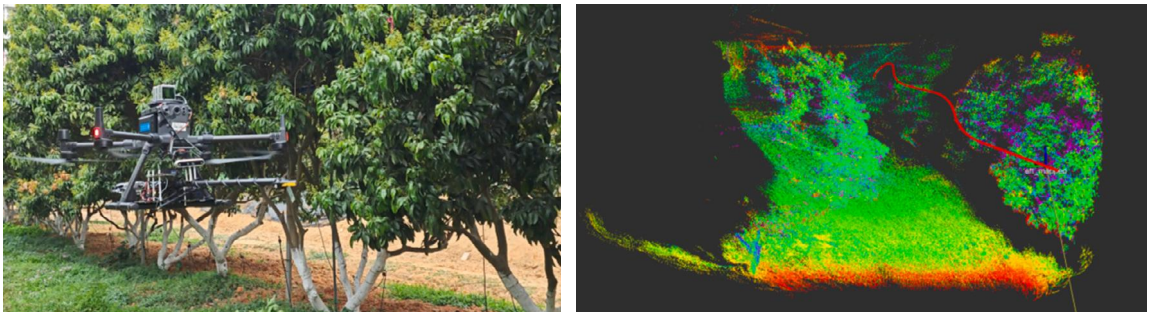

(a) Collect orchard environment information. (b) High-resolution and high-precision 3D maps.

Fig. 16. The FP-UAV obstacle avoidance picking scene.

trajectory to adapt to environmental changes and the movement of dynamic obstacles. This hybrid strategy fully considers the complexity of the orchard environment and ensures the robustness of the system in dynamic scenes so that the FP-UAV can successfully complete the picking task.

By integrating the DWA algorithm, the FP-UAV can effectively avoid dynamic obstacles in complex and changeable orchard environments and provide a safe and reliable path planning strategy for orchard picking tasks.

5. Experiment and discussion

To verify the hardware and software design of the mapping and obstacle avoidance experiments of the FP-UAV were conducted in the longan orchard of the College of Horticulture, South China Agricultural University and the longan orchard of the Guangdong Academy of Agricultural Sciences. The real experimental environment is shown in Fig. 15, which can simulate the obstacle avoidance scene of an FP-UAV during the picking process.

In this paper, the system parameters are configured as follows: when constructing a local map, the point cloud's downsampling resolution is set to 10 cm; to account for potential slight reductions in obstacle size due to downsampling, the safety gap between the FP-UAV and obstacles is set to 600 mm based on the wheelbase of the M300RTK UAV, which is 895 mm.

In the obstacle avoidance picking path planning module, the dynamic speed limit is set to 1 m/s, and the acceleration is set to 1 m/s^2. The fixed integration time (ts) for each expansion is 0.6 s. An image of the experimental site is shown in Fig. 16(a). Due to the characteristics of LiDAR systems, high-resolution and high-precision 3D maps of the environment can also be constructed, as depicted in Fig. 16(b).

5.1. Map construction experiment by FP-UAV

5.1.1. Verification of map construction effect

This experiment was conducted in the orchard of the Agricultural Science Institute for map building testing. The experimental environment is the real environment of the orchard, which meets the initial intentions of the project and is conducive to detecting the map building effect.

While flying between rows of fruit trees, the FP-UAV collects point cloud data using an Avia LiDAR. It then downsamples the point cloud data using a voxel grid filter to reduce the data volume while retaining the shape features of the point cloud. The Avia LiDAR contains 72000 points per frame, and after the downsampling operation, it will be reduced to $3000-4000$ points. Then, two time-iterative KD-Tree data structures are used to organize the point cloud and form a static-dynamic local map. Finally, the local map is converted to the global coordinate system through coordinate system transformation.

The comparison of the effect mapping after downsampling is shown in Fig. 17. From Fig. 17(a), it shows the effect of accumulating the original point cloud within 1000 ms, while Fig. 17(b) shows the effect of accumulating the point cloud after downsampling by voxel grid filter within 1000 ms. By comparison, it can be seen that the downsampled point cloud still retains the shape characteristics and detailed information of the obstacles within the field of view, and its point cloud quantity has decreased significantly compared to the original point cloud.

The mapping effect is shown by the detail local map iteration in the Fig. 18. Specifically, the blue point cloud in Fig. 18(a) represents a static map organized by the KD-Tree data structure, with the number of point clouds remaining constant during the cycle. The green point cloud in Fig. 18(b) represents the dynamic map organized by the KD-Tree data structure. During the cycle, the number of point clouds increases as new point cloud frames are scanned. Fig. 18(c) shows a partial map of the whole area, covering both static and dynamic information. The outline of fruit trees and greenhouses is clearly visible in the map, which can directly reflect the shape characteristics and location information of dynamic obstacles and small obstacles.

The above experiments show that the map construction method proposed in this paper can effectively reflect the feature information of obstacles in the orchard, and provide the maximum possible environmental information of the orchard while reducing the computing pressure of the airborne computer, providing a basis for the UAV picking and obstacle avoidance planning.

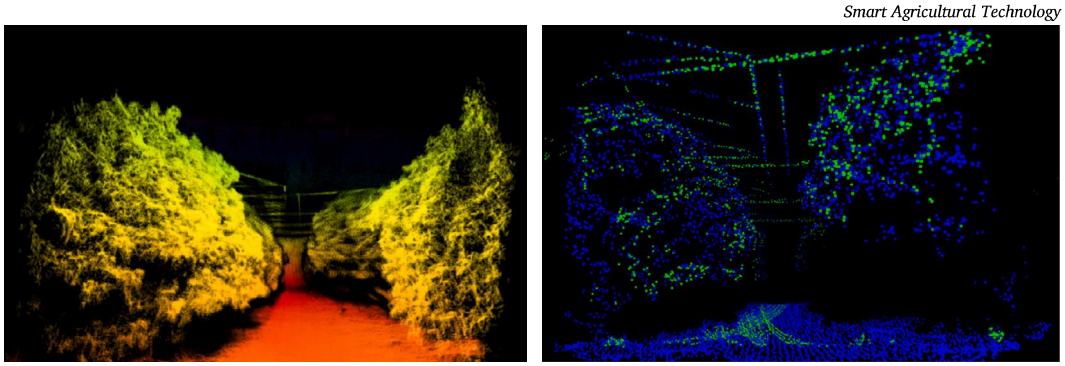

(a) Raw Point Cloud. (b) Downsampled point cloud.

Fig. 17. Comparison of point cloud downsampling effect.

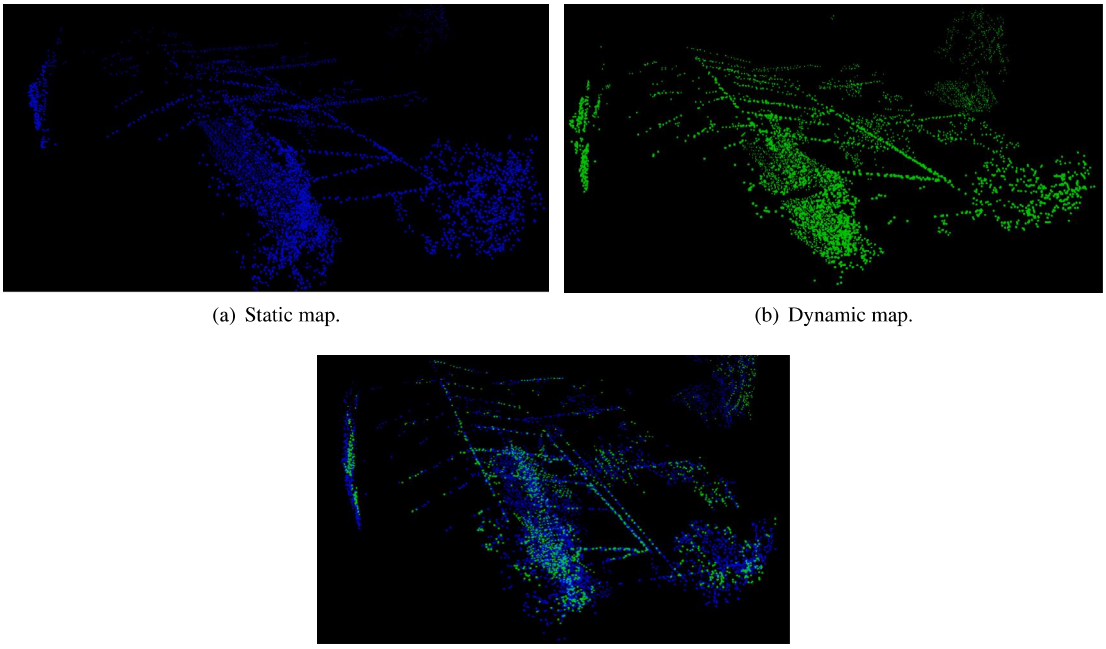

(a) Static map. (b) Dynamic map.

(c) Local map.

Fig. 18. Local staic-dynamic mapping effect.

5.1.2. Comparison of map construction methods

We compare the proposed map construction strategy with that of OctoMap. OctoMap is a type of occupancy grid map widely used in various applications and serves as the foundation for Euclidean Signed Distance Functions (ESDF) maps. A comparative experiment was conducted in the orchard of the Academy of Agricultural Sciences. In this paper, an OctoMap grid map was constructed within a fixed time of 10 s at different resolutions (2 cm, 5 cm, and 10 cm), as illustrated in Figs. 19(a), (b), and (c), respectively. The effect of the map construction scheme proposed in this paper is shown in Fig. 19(d). The data show that when constructing an updated map at a 10 cm resolution, the map failed to display the shape of the fruit trees within the fixed 10 s construction time. At 2 cm and 5 cm resolutions, the fruit contour can be displayed within a 10 s fixed construction time, but accurately reflecting the characteristics of fruit branches at the edge is still challenging.

The update process for the OctoMap raster map is time-consuming, particularly when scanning high-resolution or outdoor areas, in which the update time significantly increases. It is because, for each newly scanned laser point, all the grids on its rays need to be updated. In contrast, the obstacle avoidance planning method directly utilizes laser point clouds, and the map construction time depends on the number of laser points in each frame. Consequently, the construction effect remains relatively consistent during each scan.

5.2. Obstacle avoidance picking experiment by FP-UAV

5.2.1. Moving personnel obstacle experiment

To assess the effectiveness of the obstacle avoidance system against typical dynamic obstacles, such as workers, in the orchard, experiments were conducted in the longan orchard of the Guangdong Academy of Agricultural Sciences. In this scenario, the FP-UAV flew toward the picking point position from a distance of 6 meters and a height of 3 meters, constructed a local map, and planned the picking path, shown in Fig. 20(a). While in flight, personnel suddenly appeared within the LiDAR data and were recorded as crossing the harvesting planning path, shown in Fig. 20(b). As depicted in the figures, the movement contours and morphological features of the personnel are clearly visible. After the personnel reached the safe range of the current planned path, collision detection conditions were triggered. With respect to the obstacle avoidance picking system, based on the current constructed point cloud map and the location information of the FP-UAV, we plan to avoid obstacles. The replanned path is indicated by the red curves in Fig. 20(a) and Fig. 20(b).

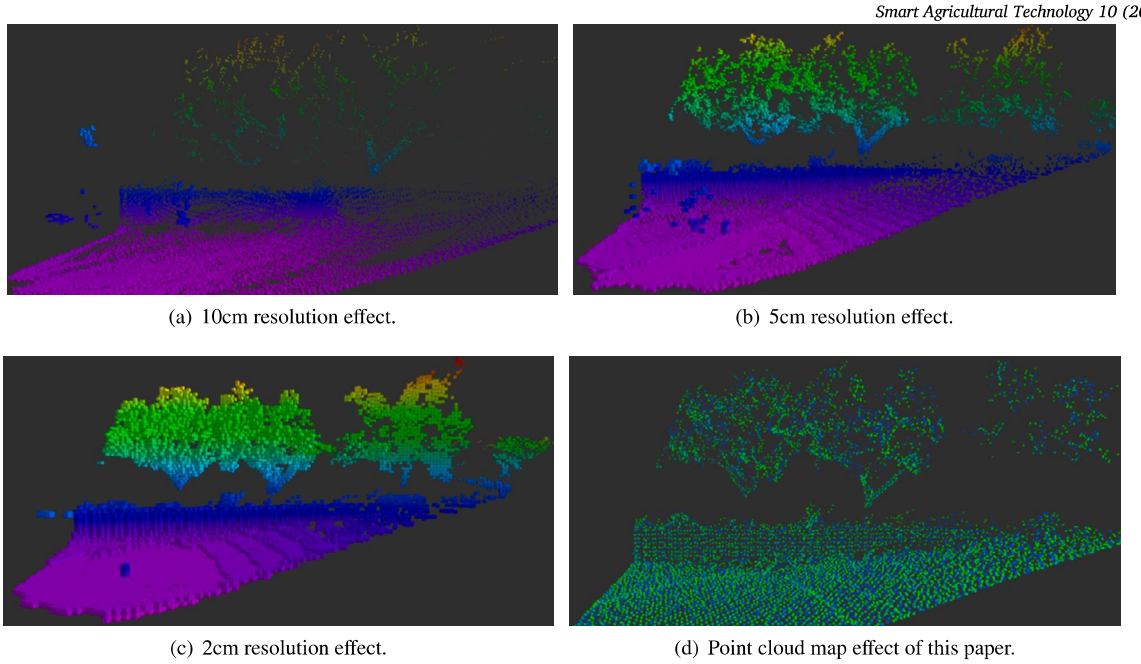

(a) 10cm resolution effect.

(b) 5cm resolution effect.

(c) 2cm resolution effect.

(d) Point cloud map effect of this paper.

Fig. 19. Comparison between the grid map and the point cloud map.

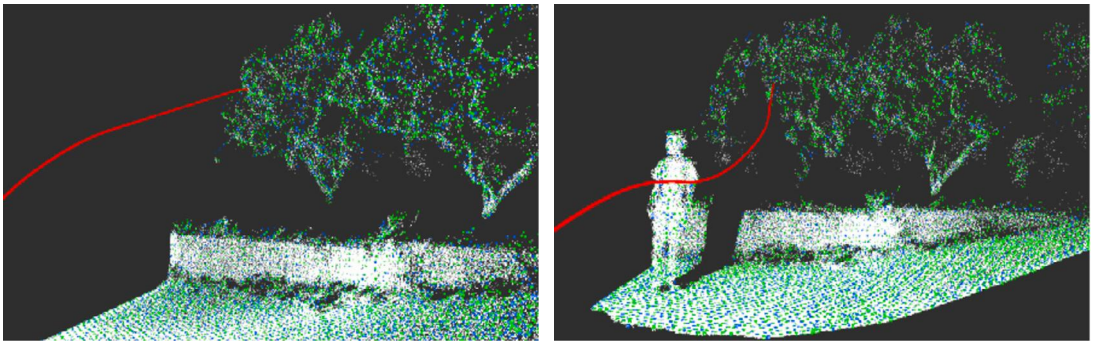

(a) Global path planning.

(b) Local path obstacle avoidance planning.

Fig. 20. Obstacle experiment for mobile personnel.

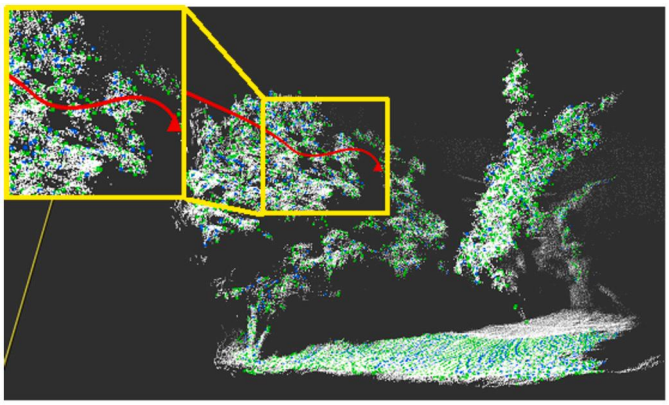

Fig. 21. Obstacle avoidance experiment outside the canopy of fruit trees.

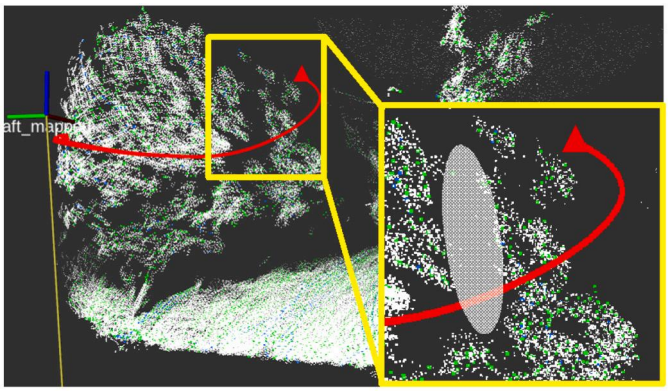

Fig. 22. Obstacle avoidance experiment at picking points at canopy intersections.

5.2.2. Picking points outside the canopy of fruit trees

In the orchard, the experiment initially simulated the picking operation outside the canopy of the longan tree. The FP-UAV operating point was set outside the longan tree in the longan garden of the Academy of Agricultural Sciences, at a height of 2 meters and a distance of 75 cm from the nearest tree crown, as indicated by the red triangle in Fig. 21.

After the FP-UAV receives the location of the operation point, the algorithm plans the obstacle avoidance picking path based on the real-time constructed local map, as shown by the red curve in Fig. 21. The white point cloud in the figure represents all the points received thus far, and the blue and green point clouds represent the static and dynamic parts of the constructed local map, respectively, for obstacle avoidance and

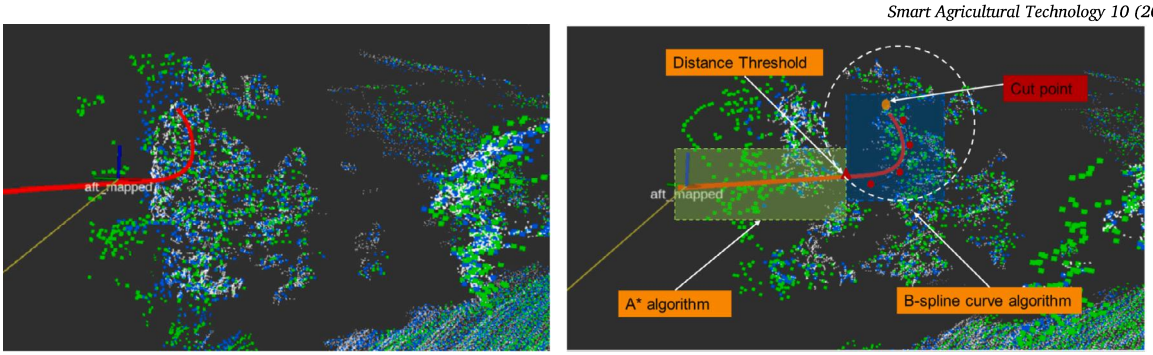

(a) Initial picking path. (b) Replanning picking path.

Fig. 23. Obstacle avoidance experiment at picking points at canopy intersections.

picking planning. The upper left side of the figure is the local side of the longan tree near the outer part of the canopy. The figure clearly shows that the LiDAR image clearly captured the outline of the longan tree canopy. Through the construction of a local map, an FP-UAV can use the map to conduct accurate obstacle avoidance and picking planning.

5.2.3. Picking point at the canopy intersection

In the orchard, picking at the intersection of longan tree canopies was simulated. The operation point of the FP-UAV is set at the intersection of two longan trees in the longan garden, which is 68 cm away from the nearest left and right tree crowns, as shown by the red triangle in Fig. 22. The elliptical area in the lower right corner represents an occluded area. Because this area is occluded by the front crown, there is no point cloud information. After the FP-UAV receives the location of the operation point, it replans the picking path to avoid obstacle based on the real-time constructed local map, as shown by the red curve in Fig. 22.

During the flight of the FP-UAV to the operation point, the local map updates the nearest point cloud of the FP-UAV in real time and detects collisions along the currently tracked planned path, as shown in Fig. 23(a) and Fig. 23(b). After the collision condition is triggered, the obstacle avoidance system again conducts obstacle avoidance planning based on the currently constructed point cloud map and the current position information of the FP-UAV, as denoted by the red path in Fig. 23. This process ensures that, when encountering obstacles or emergencies, the FP-UAV can adjust its path promptly to ensure the safety and efficiency of flight.

6. Conclusion

In this paper, we develop an autonomous obstacle avoidance picking method for the self-built FP-UAV in orchard environments, with a focus on exploring suitable orchard mapping strategies and obstacle avoidance picking motion planning based on the FP-UAV.

First, LiDAR was used to acquire the original point cloud data, and a time-accumulated local point cloud map was constructed ingeniously using the KD-Tree structure. This approach effectively mitigates the impact of historical point clouds on obstacle avoidance planning through time accumulation, thereby enhancing collision detection efficiency. To comprehensively manage static and dynamic information in orchard environments, a static-dynamic dual map is generated to ensure proper consideration of changes in fruit trees and the presence of dynamic obstacles in picking obstacle avoidance planning.

Considering obstacle avoidance and picking path planning, we develop an improved A* hybrid algorithm based on the B-spline curve. This algorithm ensures that the end route of the generated path closely aligns with the extension line between the target fruit string and the trunk, meeting the action requirements of the FP-UAV during fruit picking. Concurrently, by leveraging obstacle information from the dynamic map, this paper utilizes the DWA dynamic window algorithm to achieve dynamic obstacle avoidance path planning. Ultimately, this technique results in the realization of smooth and safe obstacle avoidance planning for UAV picking in complex orchard environments, ensuring seamless picking of the target fruit string.

Based on extensive experimentation, the proposed UAV obstacle avoidance system is shown to demonstrate favorable performance in real orchard environments, offering robust technical support for the efficient and safe application of FP-UAV in orchards. Future research could focus on further optimizing algorithms to enhance the robustness and applicability of the system.

CRediT authorship contribution statement

Jun Li: Writing – original draft, Funding acquisition, Conceptualization. **Haobo Zhou:** Writing – original draft, Visualization, Methodology. **Yuju Mai:** Writing – review & editing, Visualization, Data curation. **Yuhang Jia:** Software, Methodology. **Zhengqi Zhou:** Methodology, Investigation. **Kaixuan Wu:** Software, Formal analysis. **Hengxu Chen:** Investigation, Conceptualization. **Hengyi Lin:** Validation, Methodology. **Mingda Luo:** Validation. **Linlin Shi:** Writing – review & editing, Methodology, Funding acquisition.

Declaration of competing interest

The authors declare that they have no known competing financial interests or personal relationships that could have appeared to influence the work reported in this paper.

Acknowledgements

This work was supported in part by the National Natural Science Foundation of China under Grants 52375094 and 62303188, the Guangdong Laboratory for Lingnan Modern Agriculture under Grant NT2021009, the China Agriculture Research System under Grant CARS-32, the open competition program of top ten critical priorities of Agricultural Science and Technology Innovation for the 14th Five-Year Plan of Guangdong Province (2022SDZG03), and the Discipline Construction Project of South China Agricultural University in 2023 under Grant 2023B10564002.

Data availability

Data will be made available on request.

References

[1] O. Abdi, J. Uusitalo, J. Pietarinen, A. Lajunen, Evaluation of forest features determining GNSS positioning accuracy of a novel low-cost, mobile RTK system using LiDAR and TreeNet, Remote Sens. 14 (2022) 2856.
[2] R. Arikapudi, S.G. Vougioukas, Robotic tree-fruit harvesting with arrays of Cartesian arms: a study of fruit pick cycle times, Comput. Electron. Agric. 211 (2023) 108023.
[3] R. Bogue, Fruit picking robots: has their time come?, Ind. Robot 47 (2020) 141–145.

[4] R. Hiraoka, Y. Aoyagi, K. Kobayashi, Automatic travelling of agricultural support robot for a fruit farm. Verification of effectiveness of real-time kinematic-global navigation satellite system and developed a simulator for specification design, J. Agric. Eng. 54 (2023).
[5] J.W. Lee, W. Lee, K.D. Kim, An algorithm for local dynamic map generation for safe UAV navigation, Drones 5 (2021) 88.
[6] D. Li, X. Sun, S. Lv, H. Elkhouchlaa, Y. Jia, Z. Yao, P. Lin, H. Zhou, Z. Zhou, J. Shen, et al., A novel approach for the 3D localization of branch picking points based on deep learning applied to longan harvesting UAVs, Comput. Electron. Agric. 199 (2022) 107191.
[7] D. Li, W. Yin, W.E. Wong, M. Jian, M. Chau, Quality-oriented hybrid path planning based on a* and q-learning for unmanned aerial vehicle, IEEE Access 10 (2021) 7664–7674.
[8] Y. Li, J. Li, W. Zhou, Q. Yao, J. Nie, X. Qi, Robot path planning navigation for dense planting red jujube orchards based on the joint improved a* and DWA algorithms under laser SLAM, Agric. 12 (2022) 1445.
[9] Y. Miao, Y. Tang, B.A. Alzahrani, A. Barnawi, T. Alafif, L. Hu, Airborne LiDAR assisted obstacle recognition and intrusion detection towards unmanned aerial vehicle: architecture, modeling and evaluation, IEEE Trans. Intell. Transp. Syst. 22 (2020) 4531–4540.
[10] N. Shalal, T. Low, C. McCarthy, N. Hancock, Orchard mapping and mobile robot localisation using on-board camera and laser scanner data fusion–part b: mapping and localisation, Comput. Electron. Agric. 119 (2015) 267–278.
[11] A. Singla, S. Padakandla, S. Bhatnagar, Memory-based deep reinforcement learning for obstacle avoidance in UAV with limited environment knowledge, IEEE Trans. Intell. Transp. Syst. 22 (2019) 107–118.
[12] J. Su, X. Zhu, S. Li, W.H. Chen, AI meets UAVs: a survey on AI empowered UAV perception systems for precision agriculture, Neurocomputing 518 (2023) 242–270.
[13] Y. Sun, C. Zhang, C. Liu, Collision-free and dynamically feasible trajectory planning for omnidirectional mobile robots using a novel B-spline based rapidly exploring random tree, Int. J. Adv. Robot. Syst. 18 (2021) 17298814211016609.
[14] Y. Tang, M. Chen, C. Wang, L. Luo, J. Li, G. Lian, X. Zou, Recognition and localization methods for vision-based fruit picking robots: a review, Front. Plant Sci. 11 (2020) 510.
[15] Y. Tang, S. Dananjayan, C. Hou, Q. Guo, S. Luo, Y. He, A survey on the 5G network and its impact on agriculture: challenges and opportunities, Comput. Electron. Agric. 180 (2021) 105895.
[16] N.K. Uppalapati, B. Walt, A.J. Havens, A. Mahdian, G. Chowdhary, G. Krishnan, A Berry picking robot with a hybrid soft-rigid arm: design and task space control, in: Robotics: Science and Systems, 2020, p. 95.
[17] D. Wang, W. Li, X. Liu, N. Li, C. Zhang, UAV environmental perception and autonomous obstacle avoidance: a deep learning and depth camera combined solution, Comput. Electron. Agric. 175 (2020) 105523.
[18] L. Ye, J. Duan, Z. Yang, X. Zou, M. Chen, S. Zhang, Collision-free motion planning for the litchi-picking robot, Comput. Electron. Agric. 185 (2021) 106151.
[19] C. Zhang, J. Valente, L. Kooistra, L. Guo, W. Wang, Orchard management with small unmanned aerial vehicles: a survey of sensing and analysis approaches, Precis. Agric. 22 (2021) 2007–2052.
[20] H. Zhou, X. Wang, W. Au, H. Kang, C. Chen, Intelligent robots for fruit harvesting: recent developments and future challenges, Precis. Agric. 23 (2022) 1856–1907.
[21] M. Zhuang, G. Li, K. Ding, Obstacle avoidance path planning for apple picking robotic arm incorporating artificial potential field and a* algorithm, IEEE Access (2023).

证书号第6890456号

发明专利证书

发明名称：一种水果采摘无人机以及作业方法

发　明　人：李君;巫凯旋;李灯辉;周浩波;周峥琦;施琳琳;张美琪
麦超栋;江润鹏

专　利　号：ZL 2023 1 0038361.4

专利申请日：2023年01月10日

专利权人：华南农业大学

地　　址：510640 广东省广州市天河区五山路483号

授权公告日：2024年04月12日　　授权公告号：CN 116138039 B

国家知识产权局依照中华人民共和国专利法进行审查，决定授予专利权，颁发发明专利证书并在专利登记簿上予以登记。专利权自授权公告之日起生效。专利权期限为二十年，自申请日起算。

专利证书记载专利权登记时的法律状况。专利权的转移、质押、无效、终止、恢复和专利权人的姓名或名称、国籍、地址变更等事项记载在专利登记簿上。

局长
申长雨

国家知识产权局
2024年04月12日

其他事项参见续页

证书号第8238092号

专利公告信息

发明专利证书

发明名称：一种基于采摘无人机的减振平衡装置

专利权人：华南农业大学

地　　址：510640 广东省广州市天河区五山路483号

发 明 人：李君;麦煜炬;周峥琦;巫凯旋;林恒毅;陈恒旭;施琳琳
罗明达;王倩

专　利　号：ZL 2024 1 1919706.8　　授权公告号：CN 119705887 B

专利申请日：2024年12月24日　　授权公告日：2025年09月09日

申请日时申请人：华南农业大学

申请日时发明人：李君;麦煜炬;周峥琦;巫凯旋;林恒毅;陈恒旭;施琳琳
罗明达;王倩

国家知识产权局依照中华人民共和国专利法进行审查，决定授予专利权，并予以公告。

专利权自授权公告之日起生效。专利权有效性及专利权人变更等法律信息以专利登记簿记载为准。

局长
申长雨

国家知识产权局
2025年09月09日

华南农业大学2025批次大学生创新训练计划立项项目信息汇总表

编号	所属学院	项目名称	项目类型	拟立项级别	项目负责人	学号	项目其它成员	指导教师	职称	所属学院	备注
101	工程学院	番时捷——ROS赋能的樱桃番茄智选者	创新训练项目	国家级	李雅萱	202421120111	李熙微(202421120110)，赖炜健(202321210108)，蔡佳芸(202421310201)，洪芷芸(202321120106)，郑依桐(202421110130)	杨丹彤，张亚莉	副教授，副教授	工程学院，工程学院	
102	工程学院	基于光谱技术的茶园赤星病早期诊断研究	创新训练项目	国家级	卢洁莹	202421110117	谢铖涛(202321210220)，林子怡(202421110116)，徐悦(202421110124)，陈灿民(202329220101)	吴伟斌，罗霞	教授，高级实验师	工程学院，电子工程学院（人工智能学院）	
103	工程学院	柑橘天眼—基于UAV/UGV协同赋能的柑橘果实生长智能巡检系统	创新训练项目	国家级	黄子文	202321810211	吴宇航(202321210122)，陈惠志(202321810202)，李辉(202421810106)，崔桁彰(202434510206)	姜锐，施琳琳	助理研究员（自然），讲师	工程学院，工程学院	
104	工程学院	基于无人机遥感的烟草冠层实时检测与精准打顶系统研发	创新训练项目	国家级	张梓源	202321110128	邹雄峰(202421810230)，林填(202421510411)，陈鸿(202421510202)	马锐军	讲师	工程学院	
105	工程学院	AgroVisor：基于多模态感知的果园智慧巡检机器人	创新训练项目	国家级	罗东宇	202321120116	陈钲烨(202321120103)，吴诗瑶(202321120122)，陈嘉乐(202421210302)，陈杰(202421210202)，成祯(202421210205)	马锐军	讲师	工程学院	卢永根书院专项
106	工程学院	基于智能传感器的植保无人机雾滴漂移实时监测技术	创业实践项目	省级	卢奕铭	202321140115	林峻锋(202321810115)，张舒宝(202321810130)，陈佳洲(202219110401)，陈键斌(202321810103)，潘载轩(202321140119)	吕佳，申遂愿	讲师，副教授	工程学院，工程学院	
107	工程学院	巴戟天全自动化分拣抽芯一体机	创新训练项目	省级	张烨婷	202228210124	高炳业(202228110506)，王琅川(202421510326)，林佳霓(202421510316)，关双魁(202318410106)	孙振刚，孔莲芳	副教授，讲师	工程学院，工程学院	
108	工程学院	果园荔枝串果智能采收机器人开发	创新训练项目	省级	李思樘	202321510407	陈业(202221510304)，曾华(202221510126)，庄善精(202321110230)，朱晨(202421510430)，杨立成(202421810224)	黄光文	讲师	工程学院	
109	工程学院	AI Agent 领航：多模态数据融合打造水稻机械化生产大数据智慧管理平台	创新训练项目	省级	陈玥	202221120102	黄柔洁(202334310107)，陈正方(202334610203)，曹冰燕(2024211201011)，周童(202421110229)	廖娟	助理研究员（自然）	工程学院	
110	工程学院	稻田水渠清淤机器人	创新训练项目	省级	李籽昂	202319310112	吴韦翰(202321210219)，梁凯棱(202421810213)，王雨阳(202421110217)，吴小钰(202421110218)	赵润茂，胡炼	副教授，研究员（自然）	工程学院，工程学院	
111	工程学院	丰收利器·割前脱粒水稻收获机器人	创新训练项目	省级	吴子牛	202121410225	陈灿辉(202221410101)，孟娟(202221410122)，贺知礼(202221410205)，张丽萍(202421410232)，苏子杰(202421410124)	杨文武	副教授	工程学院	
112	工程学院	基于气象监测与智能调度的陈皮全程生晒系统	创新训练项目	省级	何金城	202321810209	邱智恒(202321810224)，杨安(202321810226)，杨子健(202321810228)，李金榜(202421810211)	周锡恩，莫嘉嗣	实验师，副教授	工程学院，工程学院	
113	工程学院	棕榈果多场景智能识别与品质分级系统设计	创新训练项目	省级	郭雨妍	202321210105	冯嘉燕(202321310204)，黄荣浩(202321810210)，仲伯伦(202221510228)	李杰浩	副教授	工程学院	
114	工程学院	基于图谱融合和深度学习的名优茶芽精准识别研究	创新训练项目	省级	李子豪	202321210109	叶靖锋(202221140127)，黄凯祥(202321510110)，邱子钊(202433140112)	吴伟斌，罗霞	教授，高级实验师	工程学院，电子工程学院（人工智能学院）	
115	工程学院	基于无人机的高陡边坡的复绿装置研制	创新训练项目	省级	黄文涛	202421810207	陈智源(202334210104)，尹学明(202421510125)，黄立煌(202421510208)	郑峰	讲师	工程学院	
116	工程学院	基于蜚蠊触须感知的仿生垄间跟随采运机器人	创新训练项目	省级	林炳钿	202321210112	曾梓颖(202421110221)，黄展鸿(202321110106)，钱梓涵(202321120118)	钟南	教授	工程学院	
117	工程学院	基于束带机构的香蕉套袋机构设计	创新训练项目	省级	林康敏	202221510314	张振凯(202221510329)，李庆东(202321810215)，陶旺强(202421810121)	王慰祖，段洁利	副教授，教授	工程学院，工程学院	
118	工程学院	基于无人机航拍图的甘蔗导航播种作业评估	创新训练项目	省级	梁倩怡	202321310312	李怡程(202323610213)，王浩然(202228110318)，陈长鑫(202321410203)，赖珈琦(202423220109)	张智刚	副教授	工程学院	
119	工程学院	用于荔枝采摘的绳驱机械臂的结构设计与运动控制	创新训练项目	省级	陈静宁	202318210201	陈锐(202321510202)，严甜甜(202421510425)，黄冰婷(202421510404)，王奇英(202421510419)，吴章硕(202413220121)	程碧懿，王红军	副教授，教授	工程学院，工程学院	
120	工程学院	稻海智驭——再生稻种收协同高效低损智能装备	创业实践项目	省级	郭博文	202421210305	郭嘉涛(202421210306)，陈炜佳(202421210304)，曹雅淇(202321110201)，曾志豪(202422210127)	曾山，卢家欢	研究员（推广型），副教授	工程学院，工程学院	
121	工程学院	基于ROS与智能监测的鸽棚自主换料机器人	创新训练项目	校级	罗康雅	202321510116	包宇翔(202321120101)，张沁(202425610230)，程荣杰(202421120105)，廖一飞(202421120114)	杨丹彤，吕辉雄	副教授，教授	工程学院，资源环境学院	
122	工程学院	基于北斗定位的多功能绿豆播种管理机	创新训练项目	校级	许峻威	202321510124	罗晓蓝(202321510318)，张凤仪(202421510426)，许朝阳(202421510120)	甄文斌	正高级实验师	工程学院	
123	工程学院	基于光谱技术的茶园土壤养分与重金属快速检测技术研究	创新训练项目	校级	钟培伟	202321210228	施博森(202421210321)，黄靖伦(202325710405)，黄相茗(202221210213)	罗远强，高婷	副研究员（自然），高级实验师	工程学院，资源环境学院	
124	工程学院	模块化播种器研制：气固耦合效应驱动的快换排种盘的设计与验证	创新训练项目	校级	梁心怡	202318710109	陈锦弘(202421210101)，江东升(202421810208)，杨家祺(202421410128)，刘雅雯(202421310216)	尹选春	副教授	工程学院	卢永根书院专项
125	工程学院	双极行星排拖拉机无极变速系统设计与制造	创新训练项目	校级	朱静怡	202321210229	陈欣然(202321210203)，宋锦浩(202321210314)，陈皓月(202439020102)	肖博一	讲师	工程学院	
126	工程学院	基于mppt算法与多能互补的鼢鼠振动干扰系统	创新训练项目	校级	邓锦途	202221110204	张钊珲(202421110225)，张坤鹏(202321120127)，李耿怡(202321120109)	贾瑞昌	讲师	工程学院	
127	工程学院	基于农用无人机的高效低飘粉状物料播撒装置	创新训练项目	校级	王旭楠	202421120120	李响(202421510109)，孙洪(202434410118)，李心玥(202421120109)，廖康宁(202421510112)	周志艳	教授	工程学院	卢永根书院专项
128	工程学院	坡地自动导航行驶模拟试验平台系统	创新训练项目	校级	覃桦升	202321140121	梁宇浩(202321310212)，吴嘉明(202321310223)，植秀炫(202421210328)	张闻宇	助理研究员（自然）	工程学院	
129	工程学院	基于乡村品牌赋能的双百行动助农产品包装设计开发	创新训练项目	校级	蓝鑫	202221410209	黄韵雯(202321410109)，刘泓佐(202321410215)，毛帅(202321410116)，程乐乐(202421410203)	郭涵	副教授	工程学院	

AiC

获奖证书

2025年第七届全球校园人工智能算法精英大赛
全国总决赛

优秀奖

赛道名称：产业命题赛-百度智能云AI应用赛

赛题名称：行业知识智能体应用

参赛院校：华南农业大学

参赛选手：卢广栋 吴浩铭 王灏

指导教师：施琳琳 邱亚龙

特发此证，以资鼓励！

2025-AIC-GM40BWM7Z

全球校园人工智能算法精英大赛组委会

2025年12月

中国技术经济学会
Chinese Society of Technology Economics

2025

首届全国人工智能应用创新大赛

证书编号：19116819883061452 82

★★★

一等奖

竞赛级别：通用赛道-全国赛-研究生组

作品名称：农业科技投入对农业生产效率的影响评估

获奖作者：卢广栋、吴浩铭、王灏

指导教师：施琳琳、申遂愿

获奖单位：华南农业大学

中国技术经济学会

2025年6月

CRAIC

获奖证书

HONORARY CERTIFICATE

华南农业大学 代表队：

在第二十七届中国机器人及人工智能大赛广东省选拔赛中，

表现优异，荣获 智能家居服务 项目

三等奖

参赛学生：莫艺峰，宁锦泰，邹俊涛

指导教师：施琳琳，周锡恩

特颁此证，以资鼓励。

广东省产教融合促进会

中国机器人及人工智能大赛
广东赛区组委会（代章）

二零二五年七月

证书编号：CRAIC202553OIUYNZ

AiC
2025 AIComp

获奖证书

2025年第七届全球校园人工智能算法精英大赛
省级选拔赛

二 等 奖

赛道名称：产业命题赛-百度智能云AI应用赛

赛题名称：行业知识智能体应用

参赛院校：华南农业大学

参赛选手：卢广栋 吴浩铭 王灏

指导教师：施琳琳 邱亚龙

特发此证，以资鼓励！

2025-AIC-S2QA6AK8

全球校园人工智能算法精英大赛组委会

2025年11月

获奖证书

参赛院校：华南农业大学

参赛学生：胡美棋、黄钦鹏、何泽基、林泽宏、黄龙生

指导老师：周锡恩、施琳琳

荣获"2025年睿抗机器人开发者大赛（RAICOM）全国总决赛"慧眼识果竞赛项目一等奖。

特发此证，以资鼓励！

工业和信息化部人才交流中心

2025年08月31日

证书编号：IITCHJRAIC25023114